ScuDo

Scuola di Dottorato ~ Doctoral School

WHAT YOU ARE, TAKES YOU FAR

Doctoral Dissertation

Doctoral Program in Mechanical Engineering (29^{th}cycle)

State Estimation and Control of Active Systems for High Performance Vehicles

By

Jyotishman Ghosh

******

Supervisor:

Prof. Nicola Amati, Politecnico di Torino

Doctoral Examination Committee:

Prof. Bruce Minaker, Reviewer, University of Windsor

Prof. Aldo Sorniotti, Reviewer, University of Surrey

Prof. Andrea Tonoli, Committee member, Politecnico di Torino

Prof. Subhash Rakheja, Committee member, Concordia University

Prof. Basilio Bona, Committee member, Politecnico di Torino

Politecnico di Torino

2017

Declaration

I hereby declare that the contents and organization of this dissertation constitute my own original work and does not compromise in any way the rights of third parties, including those relating to the security of personal data.

Jyotishman Ghosh
2017

* This dissertation is submitted to the Graduate School of Politecnico di Torino (ScuDo) in partial fulfillment of the requirements for the degree of Doctor of Philosophy.

To Ma, Baba, Kuttu and Italy

উৎসর্গ

"মা, বাবা, কুট্টু ও ইতালি"

Acknowledgements

During my doctoral studies, I have been extremely fortunate to have known a lot of people, who have assisted me in a myriad of ways.

I would like to start off by thanking both professors of the Mechatronics laboratory of Politecnico di Torino. Firstly, Prof. Nicola Amati, who graciously accepted to be my Ph.D. thesis tutor. During both my undergraduate and my doctoral studies, Nicola has been always there for me whenever I needed some clarifications regarding vehicle dynamics and vehicle sub-systems. Whether writing academic papers or preparing presentations, Nicola has always provided me with valuable feedback that has helped me improve my individual skills as a researcher. But apart from academic interactions, Nicola also taught me a lot of important life lessons and ways to interact with people within an office environment.

I shall be forever indebted to Prof. Andrea Tonoli, who was my primary supervisor for the majority of my doctoral research work. Everything that I have been able to achieve during my Ph.D. has been a direct consequence of the faith that Andrea has shown in me. At a time when I was a fresh M.Sc. graduate, he entrusted me with managing one of his most important industrial projects that was carried out with Automobili Lamborghini S.p.A. While he ensured that I had the freedom and autonomy to be able to work in a creative manner, at the same time he acted as guiding compass, nudging me in the right direction, whenever necessary. From writing patents and papers to preparing the winning presentation for the “My research in 3 minutes” contest, Andrea has always provided me with innovative ideas.

My heartfelt thanks to the thesis reviewers, Prof. Bruce Minaker and Prof. Aldo Sorniotti, for accepting to review my Ph.D. thesis and for finding time out of their busy schedules to provide me with invaluable comments. It was their critical feedback, that allowed me to augment the quality of the manuscript to an academic standard. Bruce read the thesis with immaculate attention, and his comments and correc-

tions were fundamental in correcting some inconsistencies that were present within the thesis. Aldo's insightful comments, that were derived from his vast experience on chassis control systems, provided me with an new idea for extending the work done on torque vectoring. I am also thankful to the other members of the doctoral examination committee, Prof. Basilio Bona and Prof. Subhash Rakheja for reading the thesis patiently, for their availability and for asking thoughtful questions during the thesis defence, that allowed me to reflect on the work done from a different perspective.

I was very fortunate to have been able to carry out my Ph.D. thesis with Automobili Lamborghini as the industrial partner. This was a once in a lifetime experience and I believe that very few automotive engineering Ph.D. students are able to get this level of exposure. At Lamborghini, I met a lot of amazing people, each of whom influenced my Ph.D. experience in their own special way. Firstly, thanks to Lorenzo Rinaldi for letting me work on this project and for letting me be a part of his team at R&D Vehicle Dynamics. In spite of being a student from a foreign land, I always felt at home while working at Lamborghini. Francesco Gallone was instrumental in the definition of overall framework of the entire research collaboration and we had some interesting brain storming sessions for understanding our system design targets or the 'soul' of the work. Antonio Toma was my partner-in-crime during a lot of activities at Lamborghini. I spent a majority of my time at Lamborghini working with him, where he assisted me in a number of ways, ranging from managing the research activity from the industrial side, preparing the experimental vehicle and the Hardware-In-the-Loop (HIL) setup, optimising the workflow, collecting data from test sessions to finally giving me a ride between Castelfranco Emilia - Sant'Agata Bolognese. We taught each other, a lot of things while working together and the collaboration resulted in a very positive experience. Giulio Tarquinio helped me understand the initial Rear Wheel Steering (RWS) system design requirements and played an important role in the sideslip observer validation during the first half of the project. Antonino Esposito, with his vast calibration experience, allowed me to understand subjective evaluation of vehicle handling. He was the first person to test our RWS system, and he gave valuable inputs on the control system design. Simone Moscatelli's and Giuseppe di Rosa's contributions were fundamental in the HIL test bench setup that led to further refinement in the control system design. Nicolo Piancastelli, Marco Mapelli, Ivan Pezzolla and Simone Campadelli were like the 'Avengers' of our team with their superhuman driving skills. Apart from their

ability to drive the vehicle beyond the limits, that helped in having a rigorous validation of the developed algorithms, their subjective feedback specifically from Nicolo and Ivan (un sette percento più di sottosterzo .. ahem.. Nicolo!) was the primary driving force behind the control system calibration. Luca Bertocchi, who also managed the project for a short period, taught me how to drive a 750 bhp vehicle on a frozen lake under low road grip conditions. Giovanni Caputi enlightened me with his vast knowledge of tire development and at the same time, Pugliese delicacies including the incredible 'Taralli'. Manuel Tassinari, who was like a big brother not only made sure that the vehicle was always ready for testing but he would always come up with incredible stories during the trips between the hotels and the proving grounds.

During my time in the Mechatronics laboratory, I was very lucky to have had many competent colleagues who made work interesting. Renato Galluzzi, our senior postdoc helped me out with a lot of practical things including microprocessor coding and sharing his wisdom on improving the quality of manuscript preparation. He was always available to give his guidance related to scientific and non-scientific matters. With Luca Castellazzi, I had a number of interesting discussions regarding vehicle dynamics and automotive systems in general. At the same time, managing the Squadra Corse together with him was a very positive experience as this allowed both of us to widen our leadership skills along with troubleshooting of practical issues. A big thank you to Gianluca Dara and Mirko De Giuseppe for their availability and support with the various electronic and embedded systems that I used during the last three years. Thanks also to Maria di Napoli for helping me out with the preparation of the "My research in 3 minutes" contest and giving the idea for the winning slide. Finally thanks to Yijun Xu, Qingwen Cui, Dario Gandini, Mario Silvagni, Sanjarbek Ruzimov, Claudio Sanguedolce, Valentino Mirabella, Weitao Chen and Simone Natoli for the interesting times spent in the lab during the last three years. I would also like to thank the HPC initiative at Politecnico di Torino for providing the computation resources required for the work involving deep learning. My heartfelt thanks to the HPC support staff for their availability and assistance with the setup of the High Performance Computer.

In 2016, I was able to carry out a part of the experimental work in the thesis at TU Darmstadt, Germany. I would like to thank Prof. Stefan Rinderknecht for inviting me to work in his lab and for introducing me to the impeccable German work culture. A big thank you to Rafael Fietzek and Stephane Foulard, who supervised my work

and made sure that I had everything that I needed to carry out my research and experimental work. With Rafael, I spent some very interesting times disassembling and mounting the suspensions of the test vehicle while losing the number six spanner countless number of times within the vehicle itself. The friendly atmosphere at the lab made my stay very much enjoyable. Plus the fact that the test vehicle was a BMW M3 meant that the testing sessions were thrilling.

Finally, I would to thank my family for their continued moral support during all the crises that I faced during my Ph.D. I knew that I could always turn to my father for words of wisdom and countless number of times he was there to guide me. His wise words motivated me to view adversities as opportunities to learn the art of tackling unfavourable situations and consequently, grow as a person. Additionally, I am also grateful to my father for the guidance that I received during manuscript and thesis preparation from the ground up. To my mother, I am ever so more grateful for always encouraging me during difficult times, for always morally supporting me, for her personal sacrifices for my sake and for her unconditional love. To my younger brother, thank you for being an intellectual peer for all these years. The passion that we share for cars, motorbikes and various other things has been always a source of funny interactions that has brought a smile on my face innumerable times. Lastly, I would like to thank the Italian Republic for welcoming me to their country with open arms. I came to Italy as teenager to start my university career and the warmth that I have received from the people of Italy in all these years is second to none. It is due to this warmth and affection that Italy now feels like my second home and it will always have a special place in my heart.

List of Patents and Publications

The work done during my Ph.D. has led to a number of patents and publications which are listed as follows:

Patents

1. Metodo di stima di un parametro di assetto di un veicolo (Method for the estimation of a parameter of a vehicle) Patent no. 102017000019122.
2. Virtueller Federwegsensor (Virtual sensors for the suspension deflection) - In the process of filing at the German patent office.

Publications

1. Ghosh, Jyotishman, Andrea Tonoli, and Nicola Amati. "Sideslip Angle Estimation of a Formula SAE Racing Vehicle." SAE International Journal of Passenger Cars-Mechanical Systems 9.2016-01-1662 (2016): 944-951.
2. Ghosh, Jyotishman, Andrea Tonoli, and Nicola Amati. "A Torque Vectoring Strategy for Improving the Performance of a Rear Wheel Drive Electric Vehicle." Vehicle Power and Propulsion Conference (VPPC), 2015 IEEE. IEEE, 2015.
3. Ghosh, Jyotishman, Andrea Tonoli, and Nicola Amati. "Improvement of Laptime of a Rear Wheel Drive Electric Racing Vehicle by a Novel Motor Torque Control Strategy". No. 2017-01-0509. SAE Technical Paper, 2017.
4. Ghosh, Jyotishman, Stéphane Foulard, and Rafael Fietzek. "Vehicle Mass Estimation from CAN Data and Drivetrain Torque Observer". No. 2017-01-1590. SAE Technical Paper, 2017.

Abstract

In recent days, mechatronic systems are getting integrated in vehicles ever more. While stability and safety systems such as ABS, ESP have pioneered the introduction of such systems in the modern day car, the lowered cost and increased computational power of electronics along with electrification of the various components has fuelled an increase in this trend. The availability of chassis control systems onboard vehicles has been widely studied and exploited for augmenting vehicle stability. At the same time, for the context of high performance and luxury vehicles, chassis control systems offer a vast and untapped potential to improve vehicle handling and the driveability experience. As performance objectives have not been studied very well in the literature, this thesis deals with the problem of control system design for various active chassis control systems with performance as the main objective.

A precursor to the control system design is having complete knowledge of the vehicle states, including those such as the vehicle sideslip angle and the vehicle mass, that cannot be measured directly. The first half of the thesis is dedicated to the development of algorithms for the estimation of these variables in a robust manner. While several estimation methods do exist in the literature, there is still some scope of research in terms of the development of estimation algorithms that have been validated on a test track with extensive experimental testing without using research grade sensors. The advantage of the presented algorithms is that they work only with CAN-BUS data coming from the standard vehicle ESP sensor cluster. The algorithms are tested rigorously under all possible conditions to guarantee robustness.

The second half of the thesis deals with the design of the control objectives and controllers for the control of an active rear wheel steering system for a high performance supercar and a torque vectoring algorithm for an electric racing vehicle. With the use of an active rear wheel steering, the driver's confidence in the vehicle

improves due a reduction in the lag between the lateral acceleration and the yaw rate, which allows drivers to push the vehicle harder on a racetrack without losing confidence in it. The torque vectoring algorithm controls the motor torques to improve the tire utilisation and increases the net lateral force, which allows professional drivers to set faster lap times.

Contents

List of Figures

List of Tables

Nomenclature

Abbreviations

2D	Two Dimensional
A/D	Analogue to Digital
ABS	Anti-lock Braking System
AI	Artificial Intelligence
ANN	Artificial Neural Network
AWD	All Wheel Drive
CAN	Controller Area Network
CG	Center of Gravity
cRIO	Compact Reconfigurable Input Output
DC	Direct Current
DLC	Double Lane Change
DLO	Deep Learning Observer
DOF	Degrees of Freedom
DYC	Direct Yaw Control
ECU	Electronic Control Unit
EKF	Extended Kalman Filter

EM	Electric Motor
ESP	Electronic Stability Program
FB	Feedback
FF	Feedforward
FWD	Front Wheel Drive
GPS	Global Positioning System
H-inf	H-infinity
HIL	Hardware in the Loop
IMU	Inertial Measurement Unit
K&C	Kinematics and Compliance
LPV	Linear Parameter Varying
LSTM	Long Short Time Memory
ML	Machine Learning
MPC	Model Predictive Control
NTC	Nardo Technical Center
OEM	Original Equipment Manufacturer
PI	Proportional Integral
PID	Proportional Integral Derivative
PSD	Power Spectral Density
R&D	Research and Development
RC	Roll Centre
RHP	Right Half Plane
RLS	Recursive Least Squares

RMS	Root Mean Square
RNN	Recursive Neural Network
RWD	Rear Wheel Drive
SCXV	Squadra Corse XV
SSC	Sliding Surface Controller
SUV	Sports Utility Vehicle
TV	Torque Vectoring
UKF	Unscented Kalman Filter

Symbols

α	Tire sideslip angle
β	Vehicle sideslip angle at CG
ΔF_y	Net increase in axle lateral force due to TV
$\delta_{FL,FR,RL,RR}$	Front left, front right, rear left, rear right wheel toe angles
δ_f, δ_r	Front, rear steering toe angles
δ_{roll}	Roll steer on the rear axis
$\dot{\psi}_{ref}(s)$	Reference yaw rate for the feedback controller
η	Drivetrain efficiency
$\hat{\beta}$	Estimate of vehicle sideslip angle at CG
$\hat{C}_t$	LSTM cell(s) candidate memory state vector
λ	RLS forgetting factor
μ	Global tire-road friction coefficient
μ_x	Longitudinal tire force divided by normal load on tire
μ_y	Lateral tire force divided by normal load on tire

ω	Frequency in rad/s
ω_c	Crossover frequency
$\omega_{FL,FR,RL,RR}$	Front left, front right, rear left, rear right wheel rotational velocities
ϕ	Roll angle
ψ	Yaw angle of the vehicle
ρ	Air density
σ	Actual wheel slip
σ_{des}	Desired wheel slip
τ_d	In-wheel motor to wheel reduction gear ratio
θ	Road grade angle
θ_e	Rotational speed of the engine
θ_{out}	Rotational speed of the transmission output
θ_w	Average rotational speed of the wheels
a	Front axle distance from CG
A_d	Discrete system matrix of the transmission model
$a_{f,x}$	Band pass filtered longitudinal acceleration
a_x	Longitudinal acceleration at CG
a_{yf}	Lateral acceleration at the front axle
a_{yr}	Lateral acceleration at the rear axle
a_y	Lateral acceleration at CG
b	Rear axle distance from CG
B_d	Discrete input matrix of the transmission model

B_y	Pacejka tire model stiffness factor
b_{in}, b_f, b_o, b_c	LSTM cell bias matrix of the input, forget and output gates and memory state
B_{roll}	Vehicle roll damping coefficient
$C(s)$	RWS Controller
C_d	Discrete output matrix of the transmission model
C_y	Pacejka tire model shape factor
C_{af}, C_{ar}	Front, Rear tire cornering stiffness
c_{red}	Reduced drivetrain rotational damping ratio
C_r	Coefficient of rolling resistance
C_t	LSTM cell(s) memory state(s)
D_y	Pacejka tire model peak factor
e	Euler's number
$e(s)$	Error signal in feedback loop
E_y	Pacejka tire model curvature factor
F	System model Jacobian
$F'_{Yin,out}$	Axle's inner, outer tire lateral force with TV
F_T	Traction force demand by driver
F_y	Tire lateral force
F_yf	Front axle lateral force
F_yr	Rear axle lateral force
$F_{aerodrag}$	Aerodynamics drag force on vehicle
F_{brake}	Braking force on vehicle

f_{ekf}	Non-linear system model of four DOF vehicle model
$F_{f,xwheel}$	Band pass filtered sum of wheel longitudinal forces
f_{in}, f_f, f_o	Activation function of the input, forget and output gates of LSTM cell
$F_{roadgrade}$	Component of vehicle weight along the vehicle longitudinal axis due to road grade
$F_{rollingresist}$	Rolling resistance force on vehicle
$f_{rollsteer}$	Non-linear function of roll angle to wheel toe due to roll
$f_{steerratio}$	Non-linear function of input steer by driver to wheel toe
$F_{traction}$	Longitudinal traction force on vehicle
F_{TVmax}	Amount of force generated by TV moment which gives the max. ΔF_y
$F_{x,wheel}$	Estimated sum of wheel longitudinal forces
F_{xi}	Longitudinal tire force on i^{th} wheel
$F_{yfl}, F_{yfr}, F_{yrl}, F_{yrr}$	Front left, front right, rear left, rear right tire lateral forces
F_{Yout}	Axle's outer tire lateral force without TV
$F_{zfl}, F_{zfr}, F_{zrl}, F_{zrr}$	Front left, front right, rear left, rear right tire normal forces
F_{zf}, F_{zr}	Front, rear axle normal loads
$G_{\frac{\dot{\psi}}{\delta_f}}$	Transfer function between yaw rate and front steering angle
$G_{\frac{\dot{\psi}}{\delta_r}tot}(s)$	Transfer function of yaw rate to rear steering angle with actuator dynamics
$G_{\frac{\dot{\psi}}{\delta_r}}$	Transfer function between yaw rate and rear steering angle without actuator dynamics
$G_{\frac{a_y}{\dot{\psi}}}$	Transfer function between lateral acceleration and yaw rate

$G_{act}(s)$	RWS actuator input/output transfer function
H	Output model Jacobian matrix for Kalman filter
h_t	LSTM cell(s) output vector
h_{cgrc}	Height of center of gravity from roll axis
h_{cg}	Height of center of gravity
h_{ekf}	Non-linear output model for four DOF vehicle model
h_{rcf}	Height of front suspension roll center from ground.
h_{rcr}	Height of rear suspension roll center from ground.
h_{rc}	Height of roll center from ground.
i_c	Constant transmission ratio
i_d	Differential ratio
$i_{j1/2}$	Transmission ratio of half transmission 1,2
I_w	Wheel rotational inertia
I_{xx}, I_{xz}, I_{zz}	Moment of inertia across the various planes as represented by their subscripts
J_e	Mass of inertia of the engine
J_{out}	Mass of inertia of the transmission output
J_v	Mass of inertia of the rest of the vehicle reduced on the wheels
K	Optimal Kalman gain matrix
k	Front to rear steering proportional constant
K_d	Derivative component of PID
K_p	Proportional component of PID
K_{brake}	Brake pressure to wheel force constant

$K_{M_{z,ssc}}$	SSC constant to guarantee SSC stability
k_{red}	Reduced drivetrain rotational stiffness ratio
K_{rls}	RLS optimal correction gain
$K_{roll,f}$, $K_{roll,r}$	Front axle, rear axles roll stiffness about the roll center.
$K_{rollsteer}$	Roll steering constant for vehicle roll angle
K_{roll}	Roll stiffness of the vehicle about the roll center
$K_{ssc\sigma}$	Slip SSC control gain
k_{st}	Slip SSC stability constant
L	Wheelbase
$L(s)$	Open loop transfer function
l_r	Relaxation length of tire
$L_{act}(s)$	Open loop transfer function with actuator dynamics
m	Vehicle mass
M_z	Yaw moment around CG
$M_{z,TVmax}$	Maximum yaw moment from outer layer control
M_{zPID}	Yaw moment from PID controller
M_{zSSC}	Yaw moment from SSC controller
$n(s)$	Noise in the feedback loop
o_i	Output of neuron, i
P_{brake}	Brake pressure
P_k	State error covariance matrix at the k^{th} sample
P_{rls}	RLS probability matrix
Q	Co-variance matrix of the process noise of a Kalman filter

R	Co-variance matrix of the measurement noise of a Kalman filter
r	Yaw rate of a vehicle at CG
r_w	Wheel rolling radius
R_ϕ	Roll rate of the sprung mass
$R_{in,out}$	Radius of inner, outer tire's force friction circle
S	Measurement / process noise cross covariance matrix
s	Laplace transformation variable
$S(s)$	Sensitivity function of the closed loop
S_{slip}	Sliding surface for wheel slip controller
S_x	Frontal Surface area of the vehicle
SV_y	Pacejka tire model offset factor
t	Track width of vehicle with TV control
$T(s)$	Complementary sensitivity function of the closed loop
$T_{c1/2}$	Clutch torque of the half transmission 1,2
$T_{e,corr}$	Corrected engine torque with drivetrain losses
$T_{EML,Rbrake}$	Braking left, right EM torque demand after slip control
$T_{EML,Rdrive}$	Driving left, right EM torque demand after slip control
$T_{EML,Rout}$	Left, Right motor reference torque before slip control
T_e	Engine torque output
T_{FB}	Electro-hydraulic friction brake demand
t_f, t_r	Front, Rear track width
T_{lim}	Limiting maximum electric motor torque available for TV

T_{req}	Torque demand by driver
T_r	Driving resistance torque
T_{wi}	Torque on i^{th} wheel
u	Longitudinal vehicle velocity
U_{in}, U_f, U_o, U_c	LSTM cell input from the previous time step output weighing matrix of the input, forget and output gates and memory state
V	Vehicle velocity vector at CG
v	Lateral vehicle velocity
v_k	Measurement noise of Kalman filter
v_i	i^{th} wheel's velocity across its plane
V_{lyp}	The Lyapunov function of the sliding surface S_{slip}
w_k	Process noise of Kalman filter
$w_{i,j}$	Weighing connection between neuron i and j
W_{in}, W_f, W_o, W_c	LSTM cell layer input weighing matrix of the input, forget and output gates and memory state
$x(t)$	States of the vehicle model at time t
x_k	State vector of transmission model at sample k
x_t	LSTM cell(s) input vector
y_{in}, y_f, y_o	Output of the input, forget and output gates of LSTM cell
y_k	Output vector of vehicle/transmission model at sample k
g	Acceleration due to gravity

Chapter 1

Introduction

1.1 Motivation

The modern day automobile not only represents a means of transport, but it also forms an integral part of human society. Since its invention in the early 20th century, it has been ingrained in our daily lives with the passage of time. While a majority of people still use it as a means of transport, to some their car reflects their personality while for a few others it symbolises freedom from their daily routines. Desires such as these have motivated car manufacturers to continuously develop and improve their vehicle's attributes such as styling, performance and safety. At the pinnacle of automotive excellence are 'Supercars', which are known for their outrageous styling coupled with mind boggling performance. The early supercars were known to have big engines coupled with lightweight bodies and low centres of gravity. All these factors allowed the vehicles to have extraordinary performance. While engine capabilities have rather slowly evolved in the last few years, engineers have started exploring other avenues that can lead to improvements in vehicle performance. Vehicle dynamics is one such avenue that has received special attention by auto-makers for improving the performance of their vehicles. With the advancement in electronics and the availability of faster processing capabilities, the introduction of active chassis control systems has given a significant boost to vehicle dynamics. It currently forms a big part of the research and development effort that goes into creating a modern day supercar. Active systems in vehicles are generally composed of a cluster of sensors, an Electronic Control Unit (ECU) and actuator(s). Much

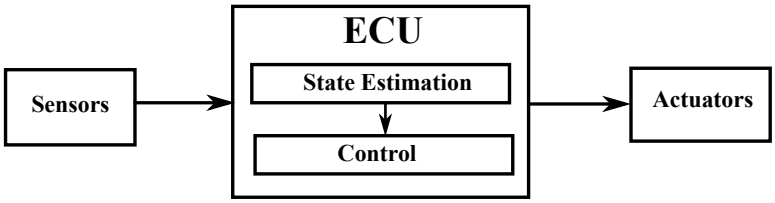

Figure 1.1 Schematic diagram of an active system.

like a biological system, the vehicle is able to sense its present state with the help of sensors that are mounted on it. The active system's ECU acts as its brain, which analyses the vehicle's state(s) and issues an order to the actuators to achieve a desired vehicle state. The actuators then move in order to follow the ECU's commands and physically realise the desired actuation.

History of Chassis Control Systems

Early applications of mechatronics systems in vehicles were mostly motivated by issues related to improving vehicle safety. Commercial applications involved the introduction of the Anti-lock Braking System (ABS) by several manufactures around 1971 [1]. This system helped vehicles avoid locking their wheels while braking, which drastically improved the vehicle's stopping distance during emergency situations. The system involves wheel speed signal acquisition from all four wheels through dedicated wheel speed sensors, processing the information in an ECU and activating/releasing the brake pads. The ECU works by releasing the brake pressure of an individual wheel when its locking is detected. Bosch later introduced the Electric Stability Program (ESP) as an extension to ABS for further augmenting vehicle handling safety [2]. Figure 1.2 shows the schematics of the ESP system. The Bosch ECU system includes traction control and anti-lock braking system for avoiding wheel locking or slipping thereby improving the vehicle lateral stability. Furthermore, the ESP system also monitors the vehicle states such as the sideslip angle and the yaw velocity and tries to keep their values within desired thresholds. All this computation takes place in the ESP ECU, which then activates the actuators when required. The actuators for the ESP system are the electro-hydraulic wheel braking circuit and the engine torque demand. By controlling the wheels' slips using the aforementioned two actuators, the ECU tries to control the vehicle's yaw rate and sideslip angle such that it stays within the limits of handling, thereby ensuring

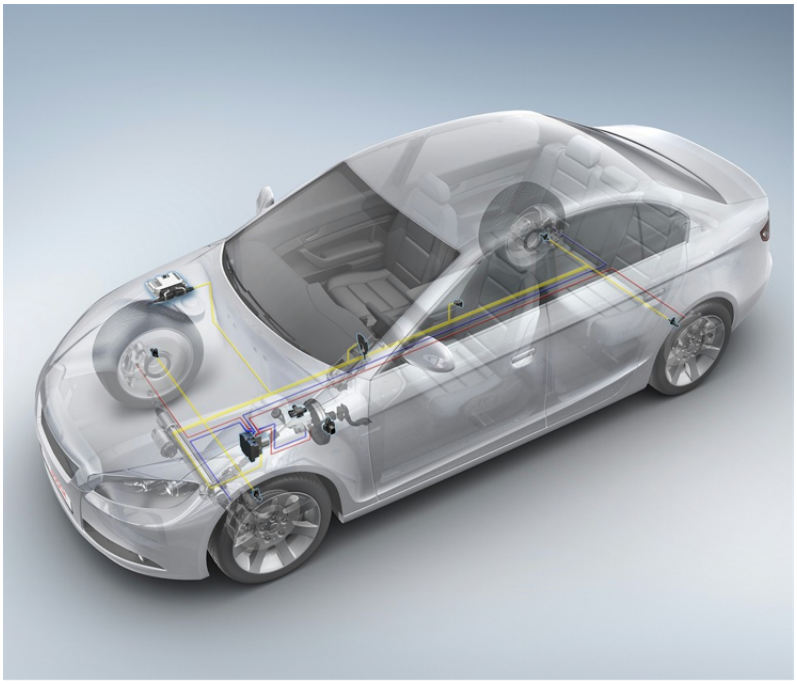

Figure 1.2 Schematic diagram of Bosch's ESP system (Source: products.bosch-mobility-solutions.com)

safety. Motivated by the potency of these active systems, governing bodies across Europe and the United States of America have made the presence of such active safety systems onboard a vehicle mandatory [3, 4].

An Overview of Various Automotive Chassis Control Systems

The ABS and the ESP systems are motivated by the augmentation of the vehicle stability and safety. As a result, the current generation systems are reactive in nature as they intervene only when the vehicle is operating beyond its stable operating conditions, for example, an excessive yaw rate or high wheel rotational acceleration. However, in modern vehicles active control systems are slowly gaining traction. Unlike reactive systems, active (or semi-active) systems work continuously in order to change the behaviour of a vehicle. Such systems typically work with sensors (real or virtual) which measure/estimate the vehicle states such as yaw rate and sideslip angle and then use a control logic to regulate the vehicle states with various sub-objectives. Figure 1.3 shows the various chassis control systems that are currently employed in high performance vehicles. Adaptive dampers work by changing the

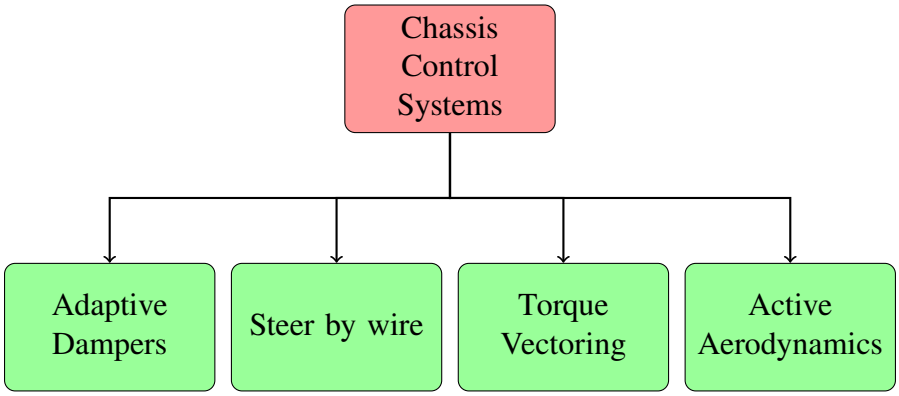

Figure 1.3 Active systems in modern vehicles.

Figure 1.4 Bugatti Veyron braking using its air brake (Source: https://www.yahoo.com/news/).

damping characteristics of the dampers in the four suspensions. The optimal damping for comfort is lower than the optimal damping for improving road holding. Thus, by varying the damping, one can toggle between control and handling objectives. Active aerodynamics work primarily to reduce the vehicle aerodynamic drag while accelerating, increasing the vehicle downforce while cornering and increasing the drag while braking. Such systems can be found in vehicles such as the Lamborghini Aventador and the Bugatti Veryon, which have an adjustable rear wing that also acts as an aero brake. A more interesting application could be seen in the Pagani Huayra, which uses active front flaps to alter the downforce on the inside and the outside wheel of a car while cornering. This kind of aero-vectoring leads to a better load distribution and an improvement in the grip level. The Lamborghini Huracan Performante also employs a similar solution. Torque vectoring (TV) involves uneven transfer of traction/braking torque across different wheels of a vehicle. This leads to

Figure 1.5 Pagani Huayra with active aerodynamics (Source: https://en.wikipedia.org/wiki/Pagani_Huayra).

the generation of a yaw moment around the vertical axis of the vehicle. When controlled, this yaw moment can be utilised to alter the lateral dynamics response of the vehicle and obtain better vehicle handling performance. Rear wheel steering (RWS) on the other hand works by directly steering the rear wheel of the vehicle. The rear wheel steer has very high sensitivity on the vehicle lateral dynamics and thus can be also used to achieve various vehicle handling performance targets. In the domain of lateral vehicle dynamics control, the control of the vehicle yaw rate and the vehicle sideslip angle are one of the primary objectives. Torque vectoring and rear wheel steering/all wheel steering by wire have high controllability of the vehicle yaw rate [5]. Thus, to improve the vehicle's handling performance while using active chassis control systems, torque vectoring and rear wheel steering offer the most interesting and effective solutions. An overview of the existing technologies on TV and RWS, their requisite states estimation for control systems design and their research gaps on the two technologies is presented in the following section.

1.2 Literature Review

Most active chassis control systems are composed of four main components i) Sensors that collect information about the vehicle's current state ii) A target behaviour generator for the controlled vehicle that acts as a reference signal for the control system iii) Control algorithm that combines information from the previous two components to generate the control command iv) Actuators that physically move to realise the control algorithm's commands. Production vehicles are equipped with a sensor

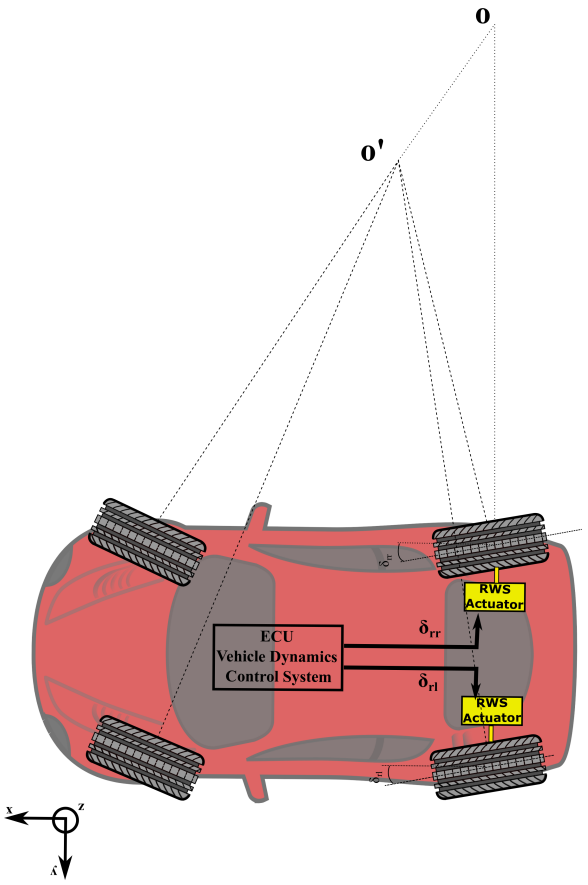

Figure 1.6 Schematics of a RWS system.

cluster present in the ESP system which includes a lateral and a longitudinal accelerometer, a yaw rate sensor, wheel speed sensors and steering angle sensor(s). Using state observers, unmeasurable states like the vehicle mass and the vehicle sideslip angles need to be estimated [6]. The design of the target controlled vehicle's behaviour depends upon the requirements of the auto-maker and a lot of it depends on the objectives of the active system. Normally, the target varies between increasing the vehicle's stability or agility. And finally once the desired behaviour has been decided upon by the designers and engineers, the behaviour is generally written down in the form of a simplified model that generates a reference yaw rate and/or sideslip angle to be followed by the control system. Various kinds of controllers can be used, each of which have their own advantages and disadvantages in terms of accuracy, ease of implementation and calibration etc. All these issues listed

above are studied and presented in the following subsections to obtain an idea of the state of the art. Research limitations from the literature review are then presented at the end of each subsection to clearly project the objective and scope of work.

1.2.1 Sideslip Estimation

As control algorithms are based on methods such as state feedback or sliding surface controllers, the knowledge of vehicle states such as sideslip angle and yaw angle rate is of paramount importance. While current series production automobiles are only equipped with inexpensive sensors that can measure accelerations and yaw rate, it is a challenging task to have an accurate measurement of the sideslip angle. Although it is possible to directly measure the slip angle of the vehicle very accurately using optical sensors, these devices are very expensive and are impractical for series production implementation [7]. In the past, researchers have made use of Global Positioning System (GPS) based techniques to measure the sideslip angle of the vehicle. Such techniques generally involve fusion of inertial sensor signals with the GPS signals. Researchers in [8, 9] have fused single and dual antenna GPS systems with IMU sensors using Kalman filters for the calculation of the sideslip angle. The effect of signal latency on the sideslip estimate error has also been presented. Such latency errors occur due to the fact that the velocity signals are obtained by the difference between two succesive signals received by the GPS module, which operates at 5 Hz or 10 Hz. Carrier based differential GPS was used in [10] to calculate the heading angle of a vehicle on a ractrack. The sideslip angle was subsequently calculated by subtracting the yaw angle of the vehicle that was computed as a solution to Wahb's problem. One major drawback for these GPS based systems is the need to have satellite signals at all times for accurate estimation. In urban environments and in tunnels, such systems are highly prone to errors due to loss of communication. Moreover, accurate GPS systems also tend to be expensive [11]. Yoon et al. in [11] presented a system that reduced the cost of GPS based sideslip measuring systems to around 500 dollars. A dual Kalman filter structure with a stochastically filtered magnetometer signal was used to compute the sideslip angle. Nevertheless, such sensors are still normally absent in production vehicles as of now.

Motivated by the issues listed above, researchers have tried to investigate indirect methods to measure sideslip angle, such as state observers. The dynamic model based approach uses state observers to get an estimate of the sideslip angle.

Table 1.1 State of the art: Sideslip Estimation.

Author	Observer type	Vehicle model	Validation type
Ray [12]	EKF	8 DOF, Pacejka	Simple experimental
Kim [13]	EKF	4 DOF, Pacejka	Constant velocity experimental
Best et al. [14]	EKF	4 DOF	Simulation
Baffet et al. [15]	EKF	Bicycle model	Sine sweep constant velocity experimental
Doumiati et al. [16]	EKF/UFK	Four wheel model, Dugoff tire model	Constant velocity experimental
Kim et al. [17]	EKF	Sensor fusion of a_x, a_y	Constant velocity experimental
Dakhlallah et al. [18]	EKF	3 DOF, Dugoff tire	Simple experimental
Bevly et al. [8]	Kalman filter	One and two antenna GPS with sensor fusion with IMU	Experimental
Ryu et al. [9]	Kalman filter	Two antenna + bicycle model+IMU fusion	Experimental
How et al. [10]	Kinematic relation of beta, heading, yaw	Carrier DGPS signals used to calculate β, attitude from Wahba's problem solution	Experimental
Yoon et al. [11]	GPS magnetometer low cost fusion	Dual Kalman filter, Stocastic filter for magnetometer disturbance rejection	Experimental
Grip et al. [19]	Non-linear vehicle observer	Bicycle model, friction estimation	Simple experimental
Gao et al. [20]	High gain observer	-	Sine sweep only
Hsu et al. [6]	Non-linear observer	Non-linear tire model, friction estimation via steer torque	Simple experiments
Abdulrahim [21]	Neural network	Array of accelerometers, no model	Experimental drifting
Ding et al. [22]	RLS	2 DOF modified Dugoff	Simulation

The state observer relies on sensor measurements from low-cost sensors such as gyroscopes and accelerometers to estimate the sideslip angle. The accuracy of this method relies heavily on a suitable modelling of the vehicle. The most crucial part of modelling the system is to successfully represent the tire cornering stiffness as incorrect modelling tends to generate steady state errors. The challenging task in the modelling of the tire's cornering stiffness is that its value is influenced by time varying parameters. Recent research has made use of adaptive Kalman filters to estimate the cornering stiffnesses. The cornering stiffness are considered as state variables in the Extended Kalman Filter (EKF) with a four degree of freedom vehicle model and the derivatives of the cornering stiffness are modelled as random Gaussian noise in [14]. An EKF based on a bicycle vehicle dynamics model and estimation of tire lateral and longitudinal forces with a sliding mode observer and variable variance-covariance matrices depending upon tire operating conditions is used in [15]. The above methods depend a great deal on correct parametrization of the variance-covariance matrices. Ray [12] used a Kalman-Bucy filter based on an eight degree of freedom model to estimate vehicle sideslip angle and tire lateral forces. However, due to estimation of eight states, the computational burden is substantial. Kim in [13] estimated the sideslip angle of a vehicle implementing an EKF with a four degree of freedom vehicle model and the magic tire formula. Dakhlallah et al. used a three degree of freedom vehicle model and a Dugoff tire model based EKF to estimate the sideslip angle at low velocities [18]. Doumiati et al. in [16] used an unscented Kalman filter based on a four degree of freedom vehicle model and a Dugoff tire model to estimate the sideslip angle for manoeuvres with more or less constant longitudinal velocity.

Apart from Kalman filter techniques, research with non-linear observers has been also carried out. Hsu et al. in [6] used the steering self-aligning torque measurement and a calibrated tire model to estimate the sideslip angle with a non-linear observer. However, the effect of the longitudinal forces on the reduction of the lateral forces due to combined slip tire characteristics and on the yaw rate dynamics was largely neglected. Grip utilised a non-linear observer to estimate the vehicle lateral velocity and the tire road maximum friction coefficient in [19]. A high gain observer was used in [20] along with a heuristics based algorithm to estimate the sideslip angle. Ding et al. presented a recursive least square algorithm to esitmate the sideslip angle and the tire-road friction coefficient [22]. The results were verified in simulation with a high degree of freedom vehicle model. For estimating the sideslip angle

of vehicles while 'drifting', a single layer neural network was trained and utilised in [21]. The algorithm required an array of accelerometers placed at different locations in the vehicle and the results were shown only for drifting manoeuvres.

Research Gaps in Sideslip Angle Estimation

Most of the work based on dynamic model based observers presented above involve techniques that estimate the sideslip angle for pure lateral slip conditions. Regarding their usage in performance vehicles, several issues arise that have not been covered in the aforementioned articles. These issues include the estimation of the sideslip angle during combined slip manoeuvres with strong excitations and harsh driving conditions such as drifting. Some articles do present the estimation results during combined slip conditions, but the validation is performed only on a few manoeuvres. Moreover, issues of error in sideslip angle due to variabilities such as tire wear, change of tires from summer tires to winter tires, etc., have never been addressed. Thus, there is a need for an algorithm that can robustly estimate the sideslip angle while accounting for all the variabilities mentioned above.

1.2.2 Mass Estimation

The latest research on active safety systems includes model based control algorithms that contain parameterized simple vehicle models. The control algorithm presented in [2] uses a bicycle model to compute the safety thresholds of the yaw rate that a vehicle should have. Once these limits are crossed, the active system intervenes to correct the vehicle yaw rate, and brings it back to the stable domain. Moreover, most of the safety algorithms utilise onboard vehicle state observers such a sideslip angle observer to estimate the vehicle sideslip angle, which is then used as an input for the state feedback controllers. The sensitivity to vehicle mass of such state observers is quite high and thus it is desirable to have an accurate estimate of the vehicle mass as an input parameter to such control or estimation algorithms [16, 23]. In order to develop accurate vehicle models for control design and vehicle state estimation, it is very important to have knowledge of the vehicle mass a priori. As a result, to take care of this variation, researchers have used information from other sensors such as GPS [7] or suspension deflection [24], to compensate for the error introduced due to the incorrect mass parameter used in the modelling process. However, if the mass

of the vehicle can be determined in real time as a slowly varying parameter, this could lead to a simpler system architecture and fewer required sensors onboard. The topic of vehicle mass estimation has been extensively studied by researchers in the past. Rajmani et al. used an adaptive observer for estimating the vehicle mass using vehicle vertical dynamics based methods [7]. The authors in [16, 25, 26] utilised suspension deflection sensors to estimate the vehicle mass. A majority of the previous research work focuses on modelling the vehicle longitudinal dynamics with simple models of force balance equations. Kidambi et al. presented an algorithm with Recursive Least Squares (RLS) estimation based on vehicle longitudinal dynamics [27]. The aerodynamic load is also considered in the modelling. The mass estimate converges within a 10% error margin. The algorithm assumes the presence of half shaft torque sensors onboard for the computation of the traction torque. Wragge-Morley et al. in [28] presented a Kalman filter based algorithm that utilises CAN information to produce the vehicle mass estimate. The algorithm's accuracy depends on the quality of the torque signal present onboard. McIntyre et al. used an adaptive least squares estimator to estimate the mass of a heavy duty vehicle [29]. Hong et al. in [30] used an Unscented Kalman filter and a vehicle dynamics model with tire-brush model to identify the vehicle mass during both longitudinal and lateral motion based on a driving situation detection algorithm. The mass estimation results are accurate; however, this method has two drawbacks. The first is that the algorithm mass estimate has a very slow convergence to its correct value and the second one is that the tire-brush tire model may not be sufficient to represent the vehicle motion in a variety of conditions, such as those involving combined slip. Vahidi et al. estimated the mass and the road grade angle for a heavy duty vehicle using a recursive least squares estimator with multiple forgetting factors [31]. However, the algorithm was found to be slow and not very accurate with its convergence when it was applied to passenger cars [32]. Similarly, Rezaeian et al. in [33] used a RLS algorithm to estimate the vehicle mass. They also assume that knowledge of driving torque is available. Fathy et al. presented an innovative idea of filtering the high frequency components of the regressor signals to eliminate the effect of road grade, aerodynamic drag or rolling resistance in [32]. However, as claimed in its conclusions, the algorithm is not robust to the effect of powertrain shuffle dynamics.

Research Gaps in Vehicle Mass Estimation

It is noticed that all the methods presented above either do not consider the transmission efficiency and dynamics or they require a dedicated wheel torque measuring sensor or other special sensors, which are unfortunately not available on production vehicles. As a result, for a real world application, they are certain to present errors when it comes to the vehicle mass estimate. Moreover, complex transmissions such as dual clutch transmissions have their own dynamics and variable efficiencies based on the operating conditions. The modelling of such effects are thus necessary to have an accurate estimate of the vehicle mass when utilising methods based on the vehicle longitudinal dynamics. Thus, an algorithm which is able to estimate the vehicle mass irrespective of the transmission efficiency and dynamics without the usage of non-production sensors is warranted.

1.2.3 Rear Wheel Steering

Rear wheel steering is an active system that is recently getting a lot of attention. Present day supercar manufacturers such as Porsche, Ferrari, Lamborghini and Lexus have implemented RWS systems in their vehicles to improve the handling performance. Many of the early RWS systems were either mechanical or hydraulic in nature. In the early 90's, most of Japanese OEMs introduced such systems in their vehicles. Honda's four wheel steering system varied the rear to front steer ratio as a function of the front steer angle. Mazda's system varied the front to rear wheel steering angle ratio as a function of the vehicle speed, which gave more vehicle agility at low speeds and more stability at high speeds. Nissan and Mitsubishi used feedback control and a hydraulic actuator system to steer the rear wheel as a function of the front steer aligning moment [34]. Currently, commercial RWS actuators are electrical in nature (electric motors and a trapezoidal spindle drive) due to ease of packaging, control and reliability.

Different control objectives have been achieved with RWS systems by researchers in the past. Sano et al. in [35] used a proportional feedforward controller to steer the rear wheels in the same direction as the front wheels to reduce the delay in vehicle lateral acceleration response. Fukui et al. in [36] proposed steering the rear wheels in the same direction for low frequency steer manoeuvres and in the opposite direction for high frequency steer inputs. This led to better vehicle stability during

Table 1.2 State of the art: Rear Wheel Steering.

Author	Controller	Objective
Furukawa, et al. [34]	Review article showing various strategies	
Sano et al. [35]	Proportional feedforward	Steer the rear wheels in the same direction as the front wheels to reduce the delay in vehicle lateral acceleration response
Fukui et al. [36]	Feedforward	Steering the rear wheels in the same direction for low frequency steer manoeuvres and in the opposite direction for high frequency steer inputs
Weichert et al. [37]	Inverse model FF	Follow reference β
Ackerman et al. [38]	Generic control law	Ideal steering dynamics and yaw stabilization
Hirano et al. [39]	H2/H-inf control	Follow first order systems ref. yaw rate and β
Fahmi et al. [40]	Sliding surface	Longitudinal, lateral dynamics and yaw motions controlled simultaneously
El Hajjaji et al. [41]	Fuzzy	Improve vehicle stability, reduce β
Higuchi et al. [42]	Optimal control	Minimise β
Nagai et al. [43]	H-inf	Follow 1st order systems ref. yaw rate and β
Palkovics [44]	Optimal quadratic programming	Follow desired β
Nagai et al. [45]	Linear + neural controller	Minimise β
Du et al. [46]	H-inf	Minimise β, yaw damping
Ono et al. [47]	Optimal control	Minimizes work load of each tire

lane changes. Ackerman presented a generic control law for achieving ideal steering dynamics and yaw stabilisation [38]. Hirano et al. in [39] used a robust control algorithm to control both sideslip angle and yaw rate. The desired sideslip angle and yaw rate were modelled as first order systems while the sideslip angle is estimated with a vehicle observer that is also presented in the article. Fahimi in [40] presents a sliding mode controller to achieve control of a four wheel steering vehicle that is robust to changes in longitudinal velocity. A fuzzy logic controller based system was presented in [41] where the authors improved the vehicle stability by minimising the sideslip angle to zero by feedback control. A similar approach was utilised in [42] by Higuchi et al., where the objective of minimising the sideslip angle was achieved by using optimal control. As a result, yaw damping was achieved and the yaw response of the vehicle was much more stable. An H_∞ controller was presented by Nagai et al. in [48] to obtain robust control of the active rear wheel steering, where the controller's task was to track the desired yaw rate and the desired sideslip angle, that were modelled as first order systems. Palkovics demonstrated the robustness of a control strategy to changing tire pressures by using quadratic programming to obtain the rear steer angles [44]. Nagai et al. presented a hybrid control structure with a combination of a linear and a neural network controller to track a zero sidelslip angle and improve the vehicle stability [45]. Du et al. in [46] used an H_∞ model following controller to control an active steering system to achieve zero sideslip angle and yaw damping. Ono et al. presented an optimal control strategy which aimed at equalising the work load of all four tires to increase the grip limit in [47].

All the above works have presented simulation results and they assume that the RWS actuators are ideal in nature, in a sense that they behave like an all-pass filter. In a real world application, RWS actuators have their own dynamics as well as inherent dead times. Veldhuizen in [49] presented a feedback control system design that took the dynamics of the actuators into consideration. The modelled actuators were electro-hydraullic in nature. The FB controller aimed to track the vehicle's desired yaw response, which was modelled as a first order system. The controller, however, suffered from issues related to the yaw rate sensor noise as well as the actuator bandwidth. The RWS controller implemented in the latest generation Porsche 911 Turbo consists of a feedforward controller that is designed to track a desired vehicle model's sideslip response [37]. The control is obtained by inverting the model of the actual vehicle to be controlled and inserting the desired vehicle sideslip angle value into the inverted model to obtain the rear wheel steering angle. Non-linearities

are accounted for by special functions that manage functionalities like the oversteer control.

Research Gaps in RWS Control

While many feedback algorithms have been presented in the state of the art, their main drawback is that they remain unimplementable in the real world due to the missing consideration of the actuator dynamics. Another issue is that experimental validation of the control system design is missing, as most articles present simulation results only. Most of the control systems are based on objective design criteria, but they do not present the subjective feeling of the vehicle with the implementation of the control system. As most high performance vehicles are tested and evaluated with the subjective feedback of the test drivers, the state of the art which leaves out this aspect, is missing a control system design, done by taking subjective feedback into account. Furthermore, the control of the transient response of the vehicle is missing from most of the works presented.

1.2.4 Torque Vectoring

Torque vectoring involves the uneven transfer of traction/braking torque on the different wheels of a vehicle. For a front wheel drive or a rear wheel drive vehicle, this would mean the transfer of torque between the left and the right wheel. For all wheel drive vehicles, it would mean left-right torque transfer within the two axles and a front axle to rear axle torque differential. Researchers have utilised various actuation systems to achieve Direct Yaw Control (DYC) by torque vectoring. One of the earliest and the simplest solutions was to use electro hydraulic brakes to have individual braking on four wheels [43, 48, 50–55]. While torque vectoring by braking requires very few changes in the actual hardware of the vehicle, it suffers from the fact that the vehicle slows down every time the brakes are applied to create a yaw moment.

Another actuation system that is utilised to achieve torque vectoring is an active differential [55–59]. Such differentials are generally electromechanical in nature, and unlike open differentials, they allow an uneven transfer of torque across the axles of a vehicle. These differentials are typically controlled via an input current to the electro-hydraulic system present in the differential [60]. The advantage that active

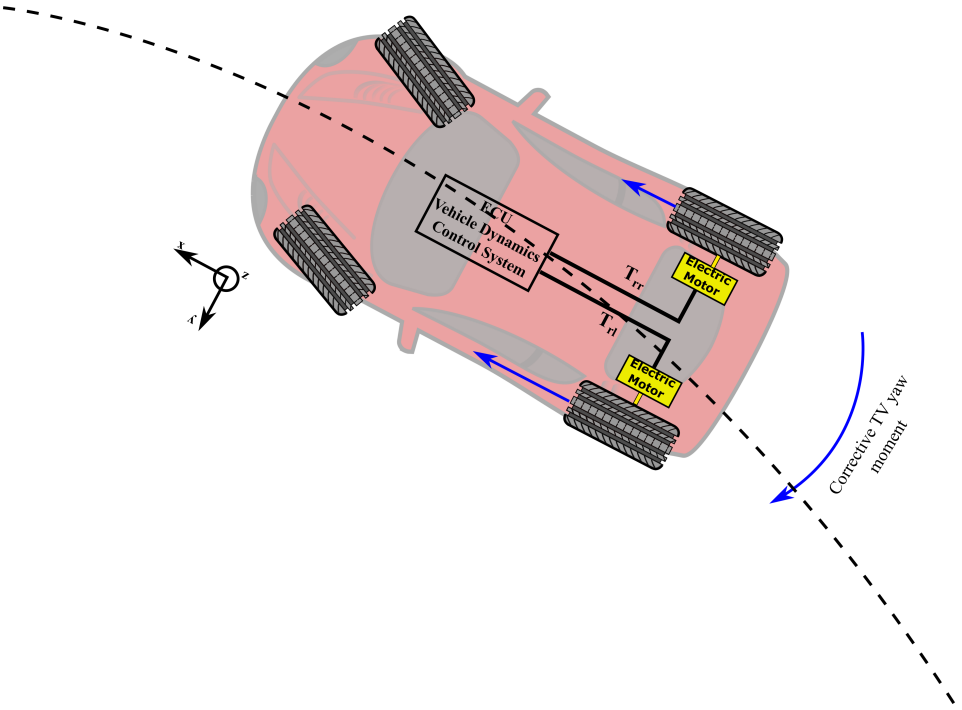

Figure 1.7 Torque vectoring by uneven torque distribution across the rear axle used to control the vehicle oversteer while cornering.

differentials present is that they can transfer torque to achieve DYC without having the need to brake the vehicle, which means that they are more energy efficient and the lateral dynamics control can be decoupled from the longitudinal dynamics control within the limits of the actuator saturation. However, torque vectoring differentials have performance limitations in terms of dynamic response, maximum allowable torque transfer and efficiency. In the domain of hybrid and electric vehicles, torque vectoring via two or more individually actuated electric motors is thus much more practical [61]. Vehicles equipped with in-wheel motors are able to exploit torque vectoring by unequal allocation of motor torques during traction or electric braking across the different wheels [57, 61–69]. The advantage of using electric motors for DYC is that the electric motors can generate torque almost instantaneously, which leads to a very crisp response and better controllability. Moreover, in full electric

vehicles the amount of torque differential between the left and the right wheels could theoretically be very high.

Various handling objectives have been realised by researchers using DYC control. A majority of the work involves improving vehicle stability by using DYC. Van Zanten in [2] controlled the yaw rate and the sideslip angles within a predetermined safety limit. The brakes are applied when the yaw rate or the sideslip angle becomes larger than the safe reference limit. Envelop control based on a phase plane analysis has been used to improve vehicle safety as well [52, 61, 63]. Chung et al. in [52] calculated the stable domain in the sideslip angle versus its derivative's phase plane and set the controller objective to keep the vehicle within this stable domain. As a result the vehicle sideslip angle does not reach large values even during high dynamic manoeuvres on low friction roads and the stability of the vehicle is enhanced. Another popular method of ensuring vehicle stability that has been used by many researches is to set the controller objective to guarantee a zero sideslip angle [43, 48, 54, 58]. Zheng et al. [54], within the optimal controller penalised a non-zero sideslip angle with a certain weight. As a result, the sideslip angle did not increase to large values.

Perhaps the most popular strategy for torque vectoring control is to impose a fixed understeering gradient using a feedback controller. To improve the vehicle stability, a handling behavior with a fixed understeering gradient is chosen such that the vehicle has either tunable understeer [51, 55, 59, 61, 62, 69] or neutral steering [53]. This leads to improved handling within stable limits, as an undertsteering gradient with lower slope can be chosen for highly understeering vehicles like an SUV [51, 59, 61, 62]. The feedback controller also ensures the avoidance of oversteer.

While stability objectives have been almost exhaustively researched, performance improvement in terms of driving dynamics has been seldom studied. A lower turning radius was imposed as an objective criteria in [65]. Cheli et al. in [56] imposed oversteer control as one of the control objectives. This led to faster lap times as well as ease of vehicle controllability. Other works have used torque vectoring to enlarge the grip limit of the vehicle [70, 71] using calculation methods based techniques. Along with simple torque vectoring, some articles have presented a more elegant solution by achieving torque vectoring through the control of individual wheels' longitudinal slips. This results in an automatic guarantee of wheel grip availability as wheels are controlled to stay within the saturation region and thus the available grip is maximised [54, 65, 72, 73]. Zheng et al. in [54] used a sliding mode con-

troller to control the slip of the individual tires. Siampis et al. in [72] used a model predictive control (MPC) controller to calculate the optimal tire longitudinal slips, that in turn created the desired DYC moment. It was demonstrated that the controller that controls the wheel slips performs better than the same controller with an objective to control just the wheel torques to obtain the same DYC moment.

Various types of controllers have been utilised for torque vectoring. All the aforementioned works involve the presence of a feedback controller. In addition to a feedback (FB) controller, some works have utilised a feedforward (FF) controller as well to improve the transient response of the whole control algorithm. While a static map based FF controller has been used in [56], a dynamic FF controller based on the inverted linear model of the vehicle was used by Canale et al. in [60]. De Novellis et al. in [51] utilised a combination of both the above controllers to improve the transient response. Moving on to the feedback controllers, a gain scheduled PID controller was applied in [51]. Similarly, a PI controller has been used in [58, 66]. In recent studies, sliding surface controllers (SSC) have become quite popular for their effectiveness in handling non-linear systems with relative ease [52, 54, 62, 69, 74]. An interesting comparison of various feedback controllers was presented in [61] where the authors compared a PID, an adaptive PID and a SSC controller. It was found that the PID-based controllers achieve very good vehicle performance in steady state and transient conditions, whereas the controllers based on the sliding-mode approach demonstrate a high level of robustness against variations in the vehicle parameters. Apart from these methods, more computationally expensive control methods such as optimal control and MPC have also been implemented by researchers. Quadratic programming has been used in [55, 73] to obtain the control allocation for the individual wheel slips and torques. LQR based optimal control is chosen in [43, 48, 63] as a FB controller with the vehicle yaw rate and the body sideslip angle as the two states to be controlled. Model predictive control has been demonstrated to be effective in [57, 72]. While the optimal control based techniques are quite good in terms of their performance, they require an accurate knowledge of all the vehicle states and substantial amount of onboard computation power.

Research Gaps in Torque Vectoring Control

The above articles mainly focus on the vehicle stability while an analysis on how TV can improve vehicle performance for high performance vehicles is missing. Issues

Table 1.3 State of the art: Torque Vectoring.

Author	Actuator	Controller	Objective
Ding et al. [50]	Brakes	Control law	Stability during evasive manoeuvres
Goggia et al. [62]	EM	Integral sliding mode	Impose understeer characteristic
De Novellis et al. [61]	EM	PID, IInd order sliding mode	Impose understeer characteristic
Geng et al. [63]	EM	LQR	Envelope control
De Novellis et al. [51]	Brakes, EM	PID	Impose understeer characteristic
Chung et al. [52]	Brakes	Sliding surface	Yawrate ref. 1st order sys., penalise β
Fujimoto et al. [64]	EM	Control law	Yawrate ref. 1st order sys., slip control
Siampis et al. [65]	EM	LQR, backstepping	Control slip, impose a desired turning radius
Cheli et al. [56]	Clutch	PI	Oversteer management
Osborn et al. [66]	EM	PI	Maintain vehicle path, maximise acceleration
Rubin et al. [57]	Active differential	MPC	Follow understeer gradient, upper limit β
Siampis et al. [72]	EM	MPC	Stabilisation of the vehicle near the limit of lateral acceleration
Canale et al. [60]	Active differential	Integral mode control	Follow ref. yaw rate from map
Croft et al. [58]	Differential	PI	Minimise β
Liu et al. [68]	EM	LPV	Follow ref model, improve stability
De Novellis et al. [59]	EM	Control allocation	Impose understeer characteristic
Bayar et al. [73]	EM	Sliding surface control	Follow slip and yaw rate reference for stability.

such as improvement of lap-time by the augmentation of the available tire grip and the reduction of the driver's effort, such as counter-steering and throttle modulation due to the control system's action has not been presented.

1.3 Objectives and Scope

The primary objective of the work presented in this thesis is to develop active chassis control systems with performance as the main goal. Traditionally, most of the mechatronic systems presented in literature tend to focus more on the stability aspect. As a result, performance gets a lower priority that safety. However, with high performance vehicles that are intended for sheer driving pleasure, the main objectives toggle from stability to agility as and when desired by the driver. The control systems to be designed should be fully integrable with existing production vehicles and should be tested extensively such that they work without strange effects during all sorts of driving conditions. Even during extreme driving conditions, such as drifting on a race track, the underlying control systems should function with the safe level of effectiveness as they would under normal driving conditions. The specific objectives are enumerated below:

1. **Estimation of Vehicle Sideslip Angle and Mass**:
    - The vehicle sideslip angle should be robustly estimated in real-time. The algorithm should work in driving conditions with combined slip conditions and also for extreme driving cases like drifting on a race track.
    - The estimation algorithm should not be computationally intensive, to facilitate onboard integration. The algorithm should only use sensors that are present on the vehicle as standard and whose signals are published on the vehicle CAN network. It should not require additional sensors on the vehicle, as for production vehicles, this is not a possibility due to financial reasons.
    - To improve the quality of the sideslip estimation algorithms and other control algorithms, a dedicated vehicle mass estimation algorithm should be also developed. Similar to the sideslip estimation algorithm, this algorithm should also only use information derived from the CAN network.

2. **Rear Wheel Steering Control**:

   - A robust yet simple control algorithm for the control of the RWS system should be developed for the prototype vehicle under study. The controller should work well in all driving conditions, and should have a fast response to improve the driving feeling.
   - The effect of the actuator dynamics and CAN delays should be considered in the control system design.
   - Moreover, as these kind of systems are mostly calibrated by the subjective feedback of racing drivers, a study should be made to translate the subjective feedback from the drivers into objective numbers for the facilitation of the controller calibration process.
   - The controller developed should be a complete module with provisions for handling extraordinary conditions, plausibility checks and hardware safety modules to prevent damage to the actuators due to improper use. The performance of the controller should be evaluated intensively with a variety of tests.

3. **Torque Vectoring Control**:

   - Development of a control algorithm for the torque vectoring control of an electric racing vehicle with the objective of improving the lap-time of the vehicle around a race track should be done. The algorithm should look to improve the total available grip of the vehicle so that the driver has more confidence to drive faster around a track.

1.4 Thesis Contributions

This thesis provides with several contributions in the field of vehicle state and parameter estimation and control of active chassis control systems. Most of the results have been validated with VI-CarRealTime simulations and subsequently with experimental data. The contributions of the thesis are listed as follows:

1. **Development of a sideslip angle estimation algorithm based on experimentally calibrated Pacejka tire model for higher accuracy.** The algo-

rithm uses only CAN-BUS data and works also for variable longitudinal speed conditions, such as a fast lap around a racetrack.

2. **Development of a sideslip angle estimation algorithm based on deep learning techniques.** The algorithm requires just CAN signals as input and it provides to the estimate of the sideslip angle in all situations including extreme conditions like drifting of a vehicle on a track or on ice/snow. Extensive validation with experimental track data demonstrates the robustness of the algorithm.

3. **Development of a fast and accurate vehicle mass estimation algorithm using a torque observer**. The algorithm uses a recursive least squares algorithm with a wheel torque observer to include the effect of the drivetrain dynamics in the parameter identification process. This introduces an improvement in the quality of the estimation as compared to traditional methods based on the engine torque estimate.

4. **Development of RWS control software.** A unique RWS control strategy is developed keeping the actuator dynamics and real world implementation concerns in mind. The controller is able to reduce double yaw rate peaks during lane change manoeuvres, which is an improvement over commercial RWS control software, that suffer from the problem of double yaw rate peaks. The controller is deployed on a prototype Italian supercar via a rapid prototyping ECU from National Instruments, and it is extensively tested and calibrated with both subjective and objective evaluations. An objective analysis of the test driver's subjective evaluation is also presented.

5. **Development of a TV control strategy for improvement of the laptime of an Electric Racing Vehicle.** The algorithm aims at improving the total available grip of the vehicle by active torque vectoring and wheel slip control. As a result, there is a significant improvement in the lap time as the driver is able to push the vehicle faster through corners without losing control of the vehicle due to the increase in grip. The results have been verified via simulations in VI-CarRealTime.

1.5 Dissertation Outline

The thesis is organised into two sections. The first section deals with the state and parameter estimation required as inputs for the controllers. The second section elaborates on the design of various controllers for active chassis systems. Chapters 2, 3 and 4 are part of the first section, whereas Chapters 5 and 6 form the second section. The brief description of all the chapters are presented below. The y-axis of the plots and other sensitive data are hidden in Chapters 2,3 and 5 to respect the confidentiality of data of the industrial partner.

Chapter 2: Sideslip Estimation with EKF

This chapter presents a sideslip estimation algorithm based on a rigid body vehicle model and an EKF. The algorithm is tested with experimental data to analyse the quality of the estimation.

Chapter 3: Sideslip Estimation with Deep Learning Observer

This chapter presents a sideslip angle estimation algorithm which is independent of a vehicle model. The algorithm is based on a deep learning technique and is shown to be robust with respect to tire-road friction coefficient, and it is also capable of estimating the sideslip angle accurately during drifting.

Chapter 4: Vehicle Mass Estimation

This chapter presents a vehicle mass estimation algorithm that requires only the data from the existing sensors present on board the vehicle. A torque observer is used to obtain the estimated the driving torque on the wheels and a recursive least squares estimator is used to estimate the mass of the vehicle.

Chapter 5: RWS Control

This chapter presents a control system from the rear wheel steering actuator of a prototype vehicle. The developed control algorithm is designed to reduce the lag between yaw rate and lateral acceleration, as well as to improve vehicle stability.

The designed algorithm is tested in simulation, HIL simulation, and on test tracks with a prototype vehicle.

Chapter 6: Torque Vectoring Control

This chapter presents a torque vectoring control algorithm for a rear wheel drive electric vehicle. The control algorithm is designed to improve the vehicle's laptime around a racetrack by improving the utilisation of the four tires.

Chapter 7: Conclusions

The conclusions from the work done in this thesis are presented along with the scope of future work.

Part I

Vehicle State Estimation

Chapter 2

Sideslip Angle Estimation I

2.1 A Look at the Problem

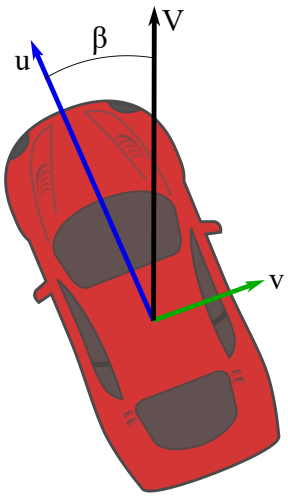

Figure 2.1 The sideslip angle β of a vehicle.

The sideslip angle of a vehicle is the angle between its total velocity vector and its longitudinal velocity vector. The knowledge of the vehicle sideslip angle is important from the point of view of vehicle dynamics, as it is one of the vehicle states that is perceived by the driver as an indicator of the vehicle's handling characteristics. It is also one of the desired controllable vehicle states as the vehicle sideslip provides information about the saturation of the tires and thus the proximity of the vehicle to

Table 2.1 Overview of sideslip angle estimation techniques.

β estimation Method	Advantages	Disadvantages
IMU integration	Inexpensive	Sensor drifts, integration errors
GPS	Accurate, robust on variable road conditions	Expensive, does not work in tunnels
Dynamic model observer	Inexpensive, works with onboard sensors	Requires accurate vehicle model, friction estimation

loss of control. Active systems such as torque vectoring or rear wheel steering are normally utilised to control the vehicle sideslip angle. As vehicle sideslip cannot be measured directly without very expensive sensors and very cumbersome instrumentation, there arises a need for the estimation of this vehicle state. Moreover, with the constraint of having only standard production vehicle sensors such as accelerometers, gyroscopes, steering angle and wheel speed sensors at one's disposal, the only possible estimation method is to use a dynamic vehicle model based observer. Such observers are based on vehicle models that are used to represent the vehicle's yaw rate and sideslip angle dynamics. The observer based on the dynamic model approach developed in this thesis is presented in the following sections.

2.2 Vehicle Modelling for Observer

2.2.1 Chassis Modelling

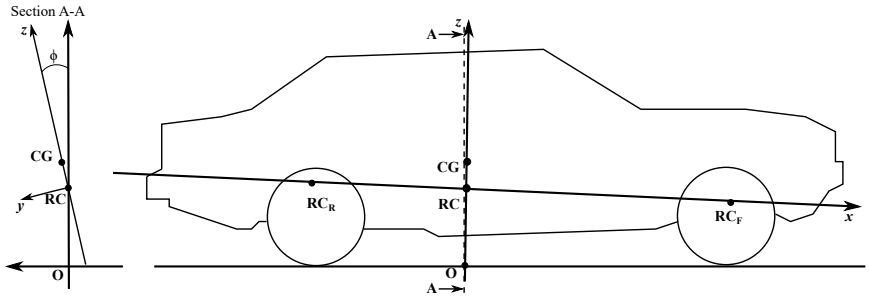

Figure 2.2 Frame of reference for the vehicle model after [75].

In order to have an accurate estimation of the sideslip angle with a dynamic model based observer, it is very important to have an accurate vehicle model. The

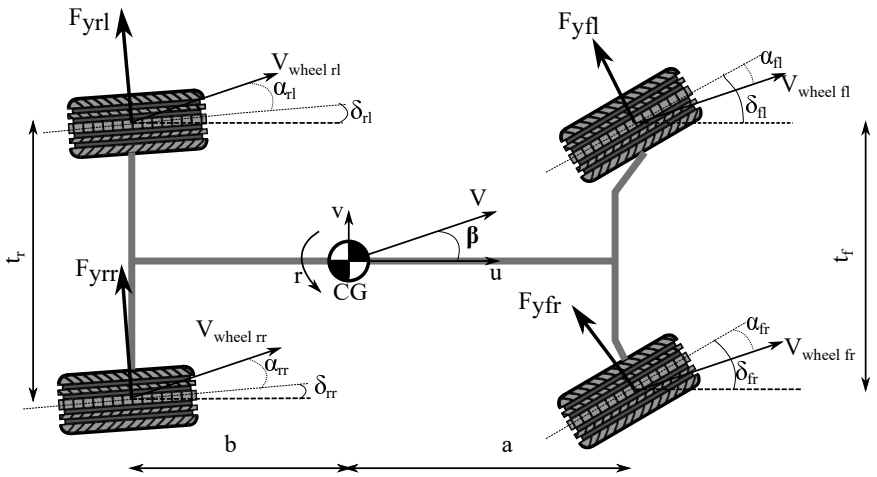

Figure 2.3 Free body diagram of the vehicle.

model should be complex enough to model the vehicle's dynamic behaviour up to a reasonable frequency. At the same time, it should not be overcomplicated; otherwise, the computational burden becomes higher. To model the vehicle, it is necessary to model the vehicle's chassis, tires and the steering system. The modelling of these subcomponents are presented below.

The overall dynamics for the vehicle can be formulated by taking into account all the forces and moments acting about the origin of the reference frame as mentioned in [75]. The frame of reference denoted by xyz can be seen in Figure 2.2. The axis x is the line passing through the roll centres of the front and rear suspensions. The axis z, that is perpendicular to x, passes through the centre of gravity CG and intersects x at RC, which from now on is defined as the roll center of the vehicle and is also considered as the origin of this frame of reference. The axis y is perpendicular to both x and z and passes through RC. As a result, a four degrees of freedom (DOF) model which includes the lateral velocity at RC v_{RC}, longitudinal velocity at RC u_{RC}, yaw rate r (angular velocity about z axis), and roll angle ϕ (rotation about x axis) dynamics can be used to represent the vehicle. The vehicle is represented with a four wheel model as shown in Figure 2.3.

The system can be represented by the following equations:

$$m\dot{v}_{RC} - mh_{cgrc}\ddot{\phi} = -mu_{RC}r + F_{yf}cos\delta_f + F_{yr}cos\delta_r + F_{xtot}sin\delta_r, \tag{2.1}$$

$$m\dot{u}_{RC} = mv_{RC}r - mh_{cgrc}r\dot{\phi} - F_{yf}sin\delta_f - F_{yr}sin\delta_r + F_{xtot}cos\delta_r, \tag{2.2}$$

$$I_{xx}\ddot{\phi} - I_{xz}\dot{r} - mh_{cgrc}\dot{v}_{RC} = mh_{cgrc}u_{RC}r - B_{roll}\dot{\phi} + (mgh_{cgrc} - K_{roll})\phi, \tag{2.3}$$

$$I_{zz}\dot{r} - I_{xz}\ddot{\phi} = aF_{yf}cos\delta_f - bF_{yr}cos\delta_r - bF_{xtot}sin\delta_r \tag{2.4}$$
$$+ (F_{yfl} - F_{yfr})sin\delta_f\frac{t_f}{2} + (F_{yrl} - F_{yrr})sin\delta_r\frac{t_r}{2},$$

where m is the mass of the vehicle, a and b are the distances of the front and rear axles from the CG, h_{cgrc} is the height of the CG above the roll axis, $F_{yfl}, F_{yfr}, F_{yrl}, F_{yrr}$ denote the tire-ground lateral forces on the front left, front right, rear left and rear right tires respectively, F_{yf}, F_{yr} denotes the sum of the left and right tire-ground lateral force on the front and rear axles respectively, δ_f represents the average front steering angle, δ_r the average rear roll steer angle, I_{xx}, I_{xz}, I_{zz} are the moments of inertia in the planes denoted by their subscript, t_f and t_r the front and rear track-width, K_{roll} the roll stiffness, B_{roll} the roll damping.

The vehicle that is the focus of this study has very stiff suspensions and a roll center that is quite close to the centre of gravity (0.1m). Thus, the roll angles during cornering are very small (around 1 degree for large lateral accelerations). This behaviour is typical of high performance vehicles. This allows one to make a simplifying assumption that the distance between the roll center and the center of gravity can be neglected. This vehicle model with the aforementioned simplification has been widely used in literature within sideslip angle observers based on dynamic model based techinques [12, 14]. Thus, it is assumed that the observer is not affected by this simplification of considering the RC and the CG velocities to be the same and the model is suitable for accurate sideslip estimation with an acceptable error limit. As a result, we assume that

$$u_{RC} \approx u, \tag{2.5}$$

$$v_{RC} \approx v. \tag{2.6}$$

The tangible parameters for the vehicle model are obtained as information known a priori. Such parameters include the vehicle sprung and unsprung mass, the track

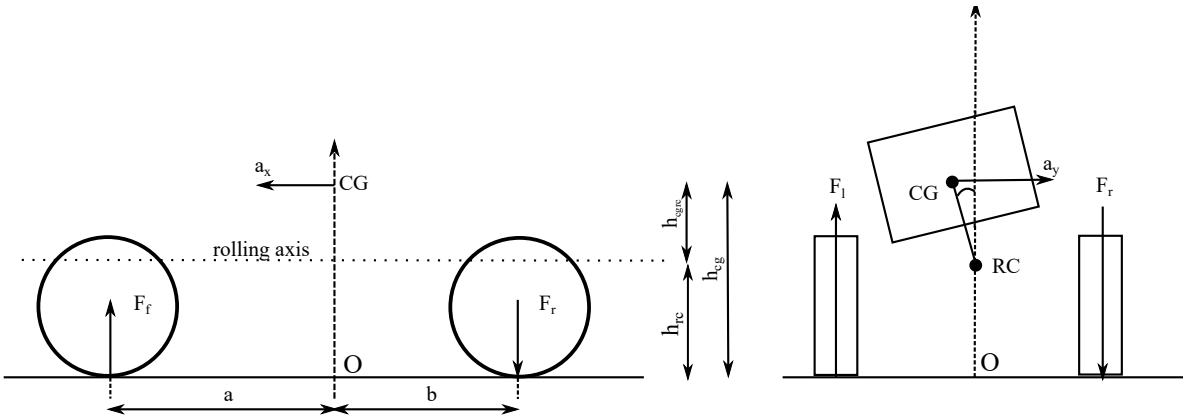

Figure 2.4 Longitudinal and lateral load transfer due to balance of the inertial forces.

widths and the wheelbase length. The inertia parameters and the height of the CG from the roll center are calculated using a parameter optimisation algorithm that fits the existing model to the outputs from the experimentally calibrated vehicle simulator model in VI-CarRealTime. The tire sideslip angles are obtained by using a kinematic relationship as shown below

$$\begin{aligned} \alpha_{fl} &= \frac{v + ar}{u - 0.5t_f r} - \delta_{fl}, \qquad \alpha_{fr} = \frac{v + ar}{u + 0.5t_f r} - \delta_{fr}, \\ \alpha_{rl} &= \frac{v - br}{u - 0.5t_r r} - \delta_{rl}, \qquad \alpha_{rr} = \frac{v - br}{u + 0.5t_r r} - \delta_{rr}, \end{aligned} \tag{2.7}$$

where $\delta_{fl,fr,rl,rr}$ represent the steer angle of the wheels represented by the subscripts.

As knowledge of the normal load on each tire is required for the lateral force computation, it is important to have a precise model to calculate the normal loads on all four tires. The normal load of a tire is composed of a static and a dynamic contribution. While the static contribution depends on the mass of the vehicle and the distance of the axles from the center of gravity, the dynamic contribution arises from the effect of load transfer due to lateral and longitudinal acceleration. The expression of the normal forces can be written down by considering a balance of the moments about the point O and about the rolling axis that passes through roll centre (RC) as follows [76]. The normal loads on the front and rear wheels of the vehicle

when going along a straight path are given by the expressions below:

$$F_{zf} = \frac{mgb - ma_x h_{cg}}{2L}, \tag{2.8}$$

$$F_{zr} = \frac{mga + ma_x h_{cg}}{2L}, \tag{2.9}$$

where L is the wheelbase.

The lateral acceleration at the CG causes a roll motion of the vehicle body in the x-z plane and also results in a load transfer from the inside wheel to the outside wheel. This allows the load transferred, $\triangle F_{\mathrm{zf}}$ and $\triangle F_{\mathrm{zr}}$ on the front and the rear axles, respectively as follows:

$$\triangle F_{zf} = a_y \frac{K_{\phi f} R_\phi + mgbh_{rcf}/L}{gt_f}, \tag{2.10}$$

$$\triangle F_{zr} = a_y \frac{K_{\phi r} R_\phi + mgah_{rcr}/L}{gt_r}, \tag{2.11}$$

where

$$R_\phi = \frac{mgh_{cgrc}}{K_{\phi f} + K_{\phi r} - mgh_{cgrc}}. \tag{2.12}$$

The final expression for normal load on each wheel considering the load transfer due to roll can be thus written as shown below:

$$F_{zfl} = F_{zf} - \triangle F_{zf}, \tag{2.13}$$

$$F_{zfr} = F_{zf} + \triangle F_{zf}, \tag{2.14}$$

$$F_{zrl} = F_{zr} - \triangle F_{zr}, \tag{2.15}$$

$$F_{zrl} = F_{zr} + \triangle F_{zr}. \tag{2.16}$$

2.2.2 Tire Modelling

The most important part of the vehicle modelling is the modelling of the tire ground forces. The quality of the sideslip estimate is highly sensitive to the accuracy of the tire model. The literature provides numerous tire models, starting from simple models such as the brush-tire model [77] and the Dugoff tire model [78]. The Pacejka's

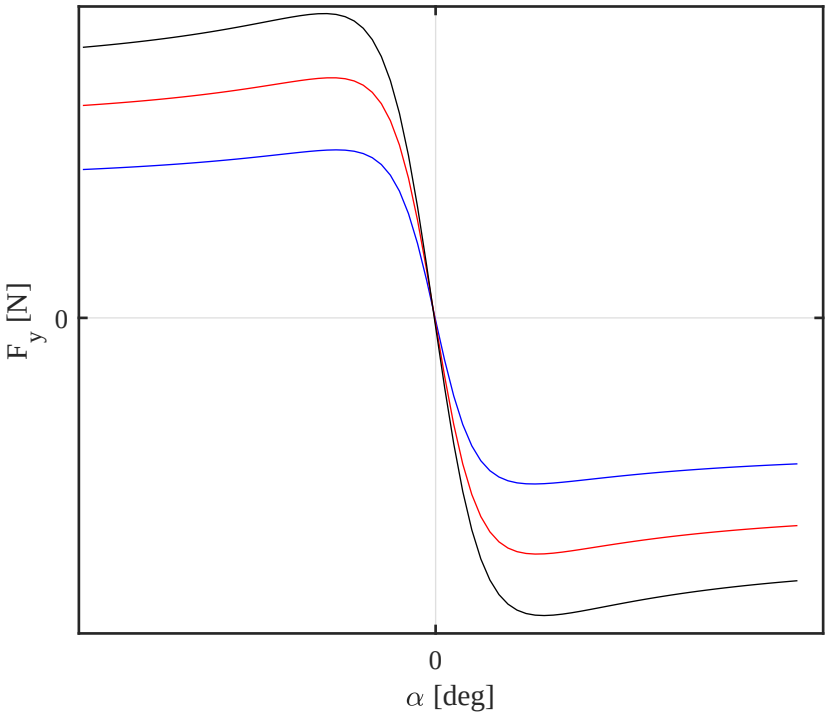

Figure 2.5 Tire lateral force characteristics as a function of tire sideslip angle for various normal loads on the tire (Black: 8000 N, Red: 6000 N, Blue: 4000 N.)

Magic formula is an empirical tire model and is known to be able to model the tire's non-transient behaviour to the closest extent. The tire lateral force is modelled as a function of the tire sideslip angle, the normal load on the tire, the camber angle of the tire, the tire-road friction coefficient and the longitudinal slip on the tire. Under conditions of pure lateral slip, the tire lateral force can be written as

$$F_y = D_y sin(C_y tan^{-1}(B_y\alpha_y - E_y(B_y\alpha_y - tan^{-1}(B_y\alpha_y)))) + SV_y. \tag{2.17}$$

The parameters in 2.17 namely D_y, C_y, B_y, E_y, SV_y are computed based on a set of sub-parameters. The complete set of equations of the model are shown in Appendix A. These parameters are provided by the vehicle OEM and they are obtained by fitting experimental data obtained from tire-test rigs that simulate the working range of the tire under standard driving conditions. For the longitudinal dynamics, only the effect of steering is modelled. The longitudinal dynamics due to traction/braking forces are modelled as a gain times the difference between the measured vehicle speed and the model's longitudinal velocity state.

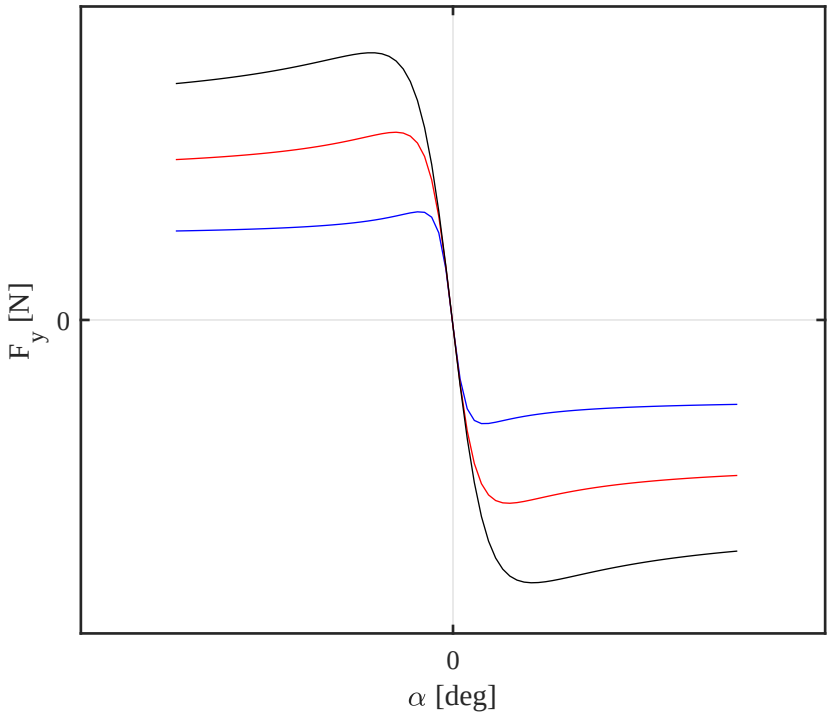

Figure 2.6 Tire lateral force characteristics as a function of tire sideslip angle for various tire road friction coefficients of the tire (Black: $\mu = 1$, Red: μ=0.7, Blue: μ=0.4.)

To model the effect of combined slip, lookup tables are used to reduce the lateral force as a function of the longitudinal acceleration. This is an approximation assuming that the four wheels will have similar longitudinal slips, due to four wheel drive. This is done to eliminate the estimation of the wheels longitudinal slips, which by themselves pose a challenge for an all-wheel drive vehicle with production sensors.

2.2.3 Steering System Modelling

While in multibody CAE simulation environments such as ADAMS, the behaviour of the steering system can be completely modelled by modelling the individual components, such a modelling is quite heavy for this application. A clever way to avoid such modelling is to store the whole behaviour of the steering as lookup tables that are functions of various vehicle states such as the body roll, the suspension jounce or rebound, etc. This can be done with the help of a Kinematics and Compliance machine, which can produce the kinematics look-up tables of the steering and the suspension. For the vehicle under study, these tables are available from the OEM.

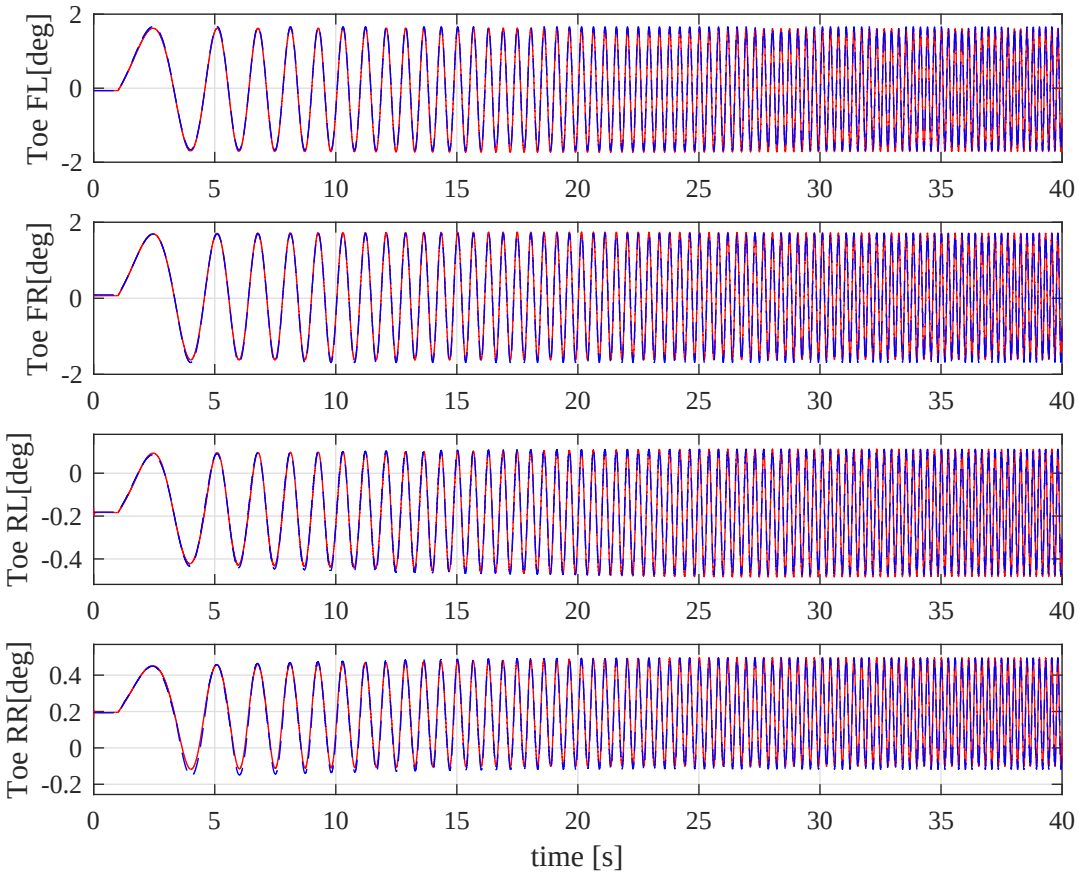

Figure 2.7 Validation of the modelling of the toe angles of the four wheels of the vehicle. The steering toe angle of the VI-CarRealTime model is shown in blue while the presented steering system model's toe angles are shown with red dashed lines.

However, since the vehicle model under study is a rigid body model and it has only four degrees of freedom, the effect of roll steer and the asymmetric right and left steer only is considered. All these properties are stored within lookup tables. As a result, the toe angle of a particular wheel, δ_{toe} is written as

$$\delta_{toe} = f_{steerratio}(\delta_{steerinput}) + f_{rollsteer}(\phi). \tag{2.18}$$

Figure 2.7 shows the validation of the toe angles of the model of the steering system with the toe angles of the VI-CarRealTime vehicle model. The VI-CarRealTime model contains the real vehicle's steering characteristics, that have been obtained as lookup tables from a K&C machine.

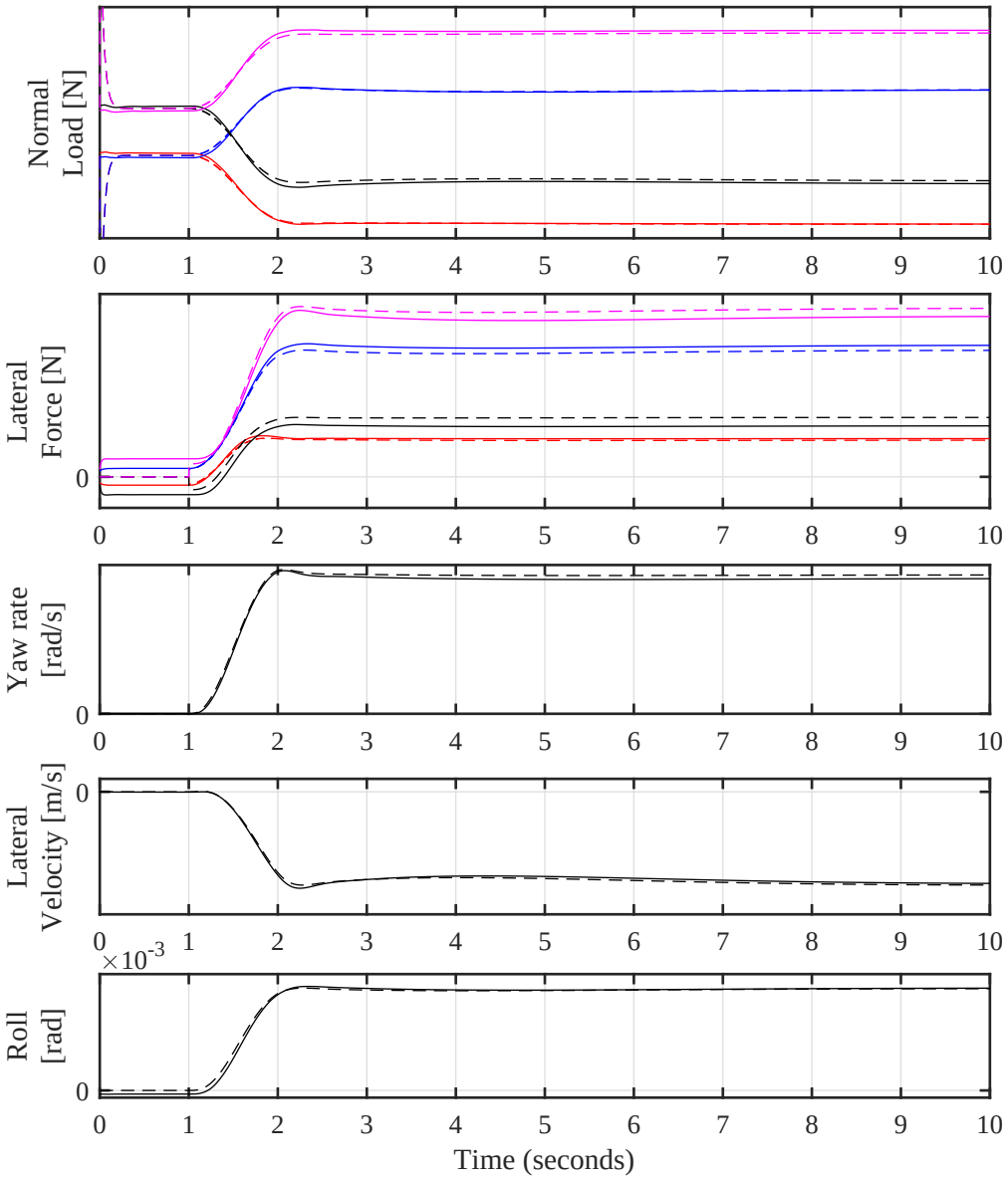

Figure 2.8 Validation of the 4 DOF (dashed lines) vehicle model with a multi-body VI-CarRealTime vehicle model(solid lines) which has been calibrated with the actual vehicle for a step steer manoeuvre. Blue- FL wheel, red- FR wheel, black- RL wheel, magenta- RR wheel.

2.2.4 Validation of the Vehicle Model

The developed four degree of freedom model is validated with the multi-body vehicle model in VI-CarRealTime obtained from the OEM. The multi-body model has been calibrated to match the actual prototype vehicle's behaviour. The matching of

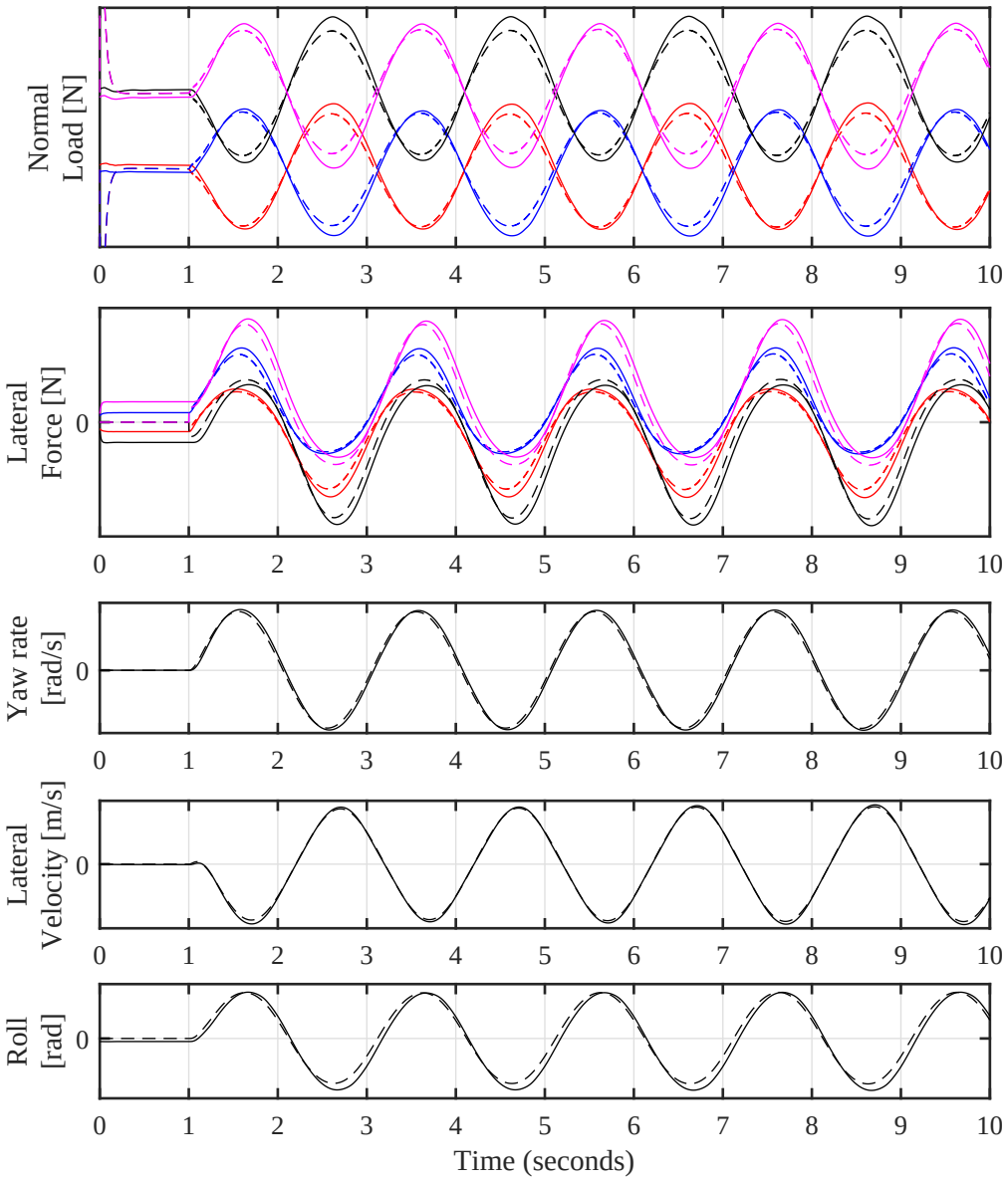

Figure 2.9 Validation of the 4 DOF (dashed lines) vehicle model with a multi-body VI-CarRealTime vehicle model(solid lines) which has been calibrated with the actual vehicle for a sine steer manoeuvre. Blue- FL wheel, red- FR wheel, black- RL wheel, magenta- RR wheel.

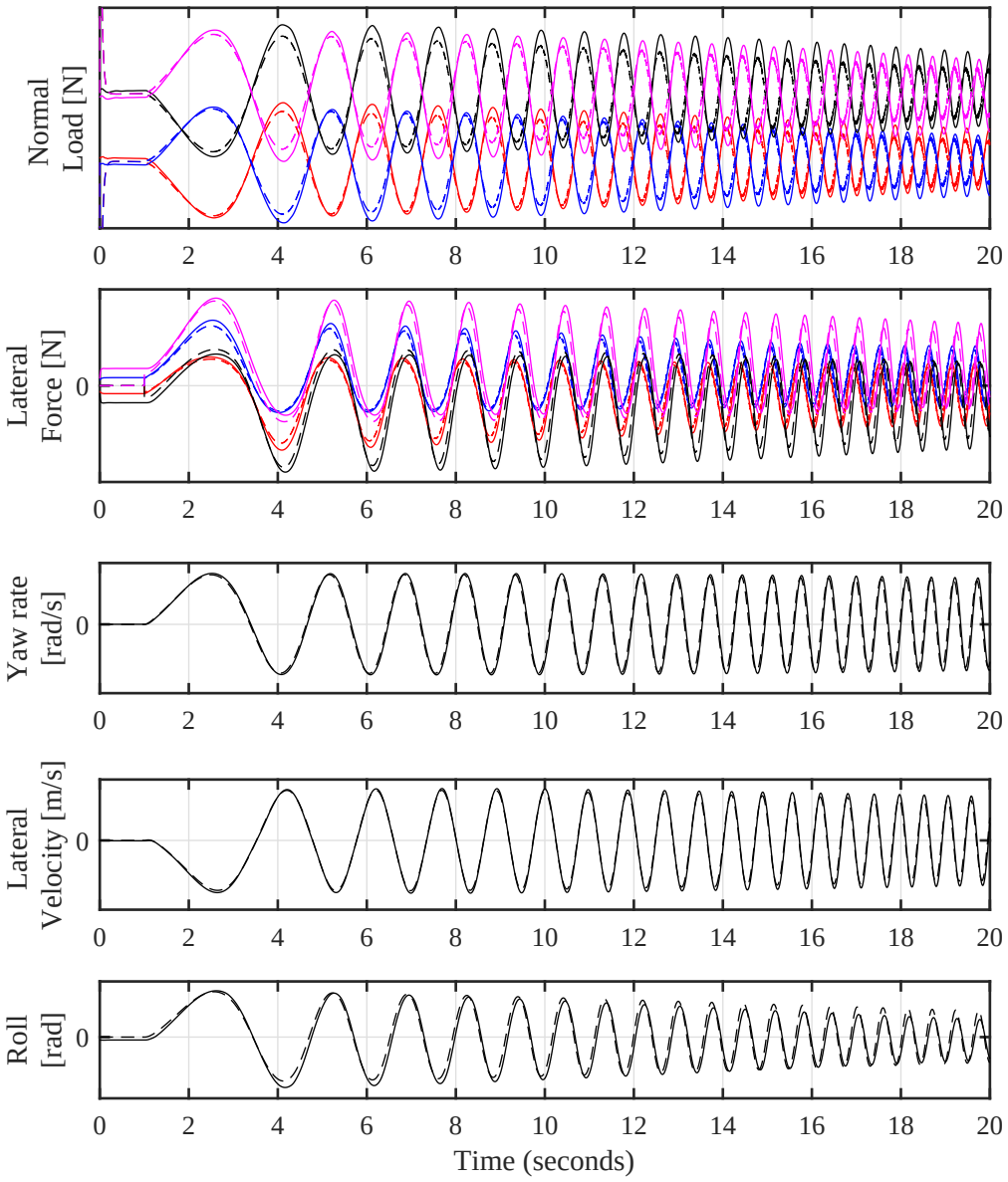

Figure 2.10 Validation of the 4 DOF (dashed lines) vehicle model with a multi-body VI-CarRealTime vehicle model(solid lines) which has been calibrated with the actual vehicle for a sine sweep steer manoeuvre. Blue- FL wheel, red- FR wheel, black- RL wheel, magenta- RR wheel.

the two vehicles is tested by looking at the match in the normal loads to verify the load transfer equations, the lateral forces to check the tire model of the four DOF model, the yaw rate, the lateral velocity and the roll angle to check the match in the vehicle dynamics model parameters.

Figure 2.8 shows the various parameters for a step steer manoeuvre applied to both the models at 100 km/h. It can be seen that the normal loads match quite accurately whereas the lateral forces show some offset errors due to the absence of camber angle modelling and the difference in the number of degrees of freedom of the two models (4 DOF vs 16 DOF). Nevertheless, the sum of the net axle lateral forces is very close for the two models as the error in the left wheel's lateral force is compensated by the error in the right wheel's lateral force. The yaw rate, the lateral velocity and the roll angle seem to match quite accurately, indicating that the 4 DOF model is able to represent the vehicle dynamics to a satisfactory level for its use in the observer.

Similar behaviour is seen in Figure 2.9, which is a test involving a sine steer manoeuvre where the match is quite accurate. To verify the model's performance across a range of input steer frequencies, a sine sweep steer manoeuvre is also simulated for both the models. It can be noticed in Figure 2.10 that both models match quite well in terms of all the parameters, indicating that even within the whole range of the drivable input steering frequency, the reduced order model can represent the vehicle dynamics quite efficiently. Thus, the calibrated vehicle model is suitable to incorporate in the observer design.

2.3 Extended Kalman Filter

An EKF is used to observe the non-linear lateral dynamics of the vehicle. The observer has five states $r, u, v, \phi, \dot{\phi}$. The five sensors mounted on the vehicle as seen

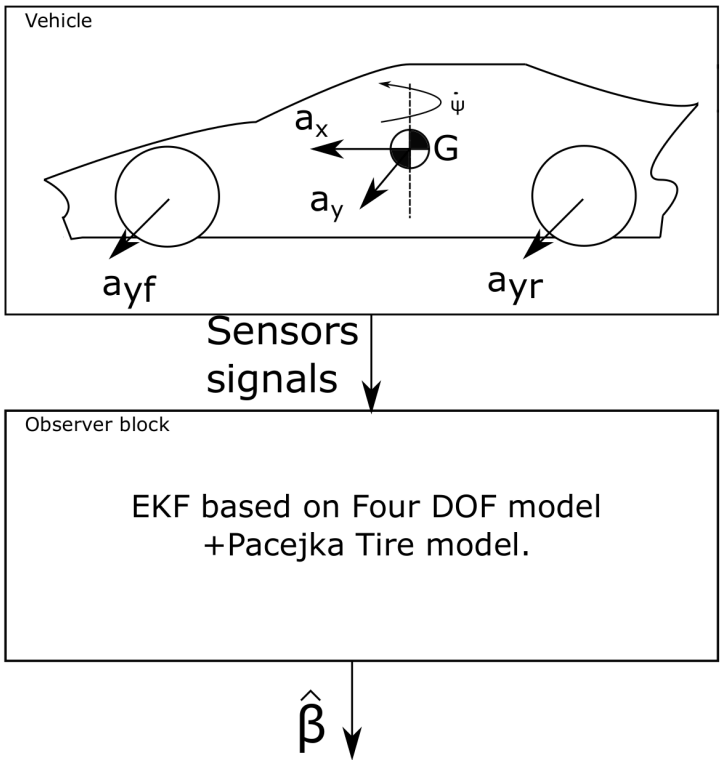

Figure 2.11 Schematic diagram of the estimation algorithm.

in the vehicle block of Figure 2.11 are modelled in the observer as follows:

$$a_x = \dot{u} - r(v + h_{cgrc}\dot{\phi}), \tag{2.19}$$

$$a_y = \dot{v} + h_{cgrc}\ddot{\phi} + ru, \tag{2.20}$$

$$a_{yf} = \dot{v} + a\dot{r} + ru, \tag{2.21}$$

$$a_{yr} = \dot{v} - b\dot{r} + ru, \tag{2.22}$$

$$\dot{\psi} = r. \tag{2.23}$$

From Equations 2.1-2.4, the system can be written as a system with continuous states as

$$\dot{x}(t) = \begin{bmatrix} \dot{r} & \dot{v} & \dot{u} & \ddot{\phi} & \dot{\phi} \end{bmatrix}^T = f_{ekf}(x(t)) + w(t). \tag{2.24}$$

From Equations 2.19-2.23, the output of the system is written in a discrete form as

$$y_k = \begin{bmatrix} a_x & a_y & a_{yf} & a_{yr} & \dot{\psi} \end{bmatrix}^T = h_{ekf}(x_k) + v_k. \tag{2.25}$$

The process noise (in the discrete formulation) w_k and the measurement noise v_k are modelled to be correlated since h_{ekf} and f_{ekf} are correlated. As a result the cross covariance matrices are represented as follows:

$$e_k = \begin{bmatrix} w_k \\ v_k \end{bmatrix}, E(e_k e_k^T) = \begin{bmatrix} Q & S \\ S^T & R \end{bmatrix}, \tag{2.26}$$

where R is the measurement noise covariance matrix, Q is the process noise covariance matrix and S is the measurement-process noise cross covariance matrix.

To model this correlation between process and measurement noise, Lagrange multipliers are used to modify, $\dot{x}(t)$ in equation 2.24 [14] as

$$\dot{x}(t) = f_{ekf}(x(t)) + w(t) + SR^{-1}\left\{y_k - h_{ekf}(x_k) - v_k\right\}. \tag{2.27}$$

Thus the system model Jacobian matrix F(x) and the output model Jacobian matrix H(x) for the formulation of the Kalman filter may be written as follows.

$$F(\hat{x}(t)) = \frac{\partial f_{ekf}(x(t))}{\partial x(t)}\Big|_{x(t)=\hat{x}(t)} - SR^{-1}H(\hat{x}(t)), \tag{2.28}$$

$$H(\hat{x}(t)) = \frac{\partial h_{ekf}(x(t))}{\partial x(t)}\Big|_{x(t)=\hat{x}(t)}. \tag{2.29}$$

Given a sampling time T_s and using Euler's integration method, the Extended Kalman filter can be now written as a series of the following equations:

$$K_k = P_k H^T(\hat{x}_k)[H(\hat{x}_k)P_k H^T(\hat{x}_k) + R]^{-1}, \tag{2.30}$$

$$P_k^* = [I - K_k H(\hat{x}_k)]P_k, \tag{2.31}$$

$$P_{k+1} = P_k^* + T_s[F(\hat{x}_k)P_k^* + P_k^* F^T(\hat{x}_k) + Q - SR^{-1}S^T], \tag{2.32}$$

$$\hat{x}_{k+1} = \hat{x}_k + K_k(y_k - h(\hat{x}_k)) + T_s[f_{ekf}(\hat{x}_k + SR^{-1}(y_k - h_{ekf}(\hat{x}_k))]. \tag{2.33}$$

where K is the optimal Kalman gain matrix, P is the state error covariance matrix.

The sideslip angle estimate is then obtained as

$$\hat{\beta} = atan(\frac{\hat{x}(2)}{\hat{x}(3)}). \tag{2.34}$$

2.4 Results

The EKF observer developed in the previous sections is tested on track using an instrumented prototype vehicle with a lateral and longitudinal accelerometer and a yaw rate sensor placed at the CG, wheel speed sensors, a steering angle sensor and RWS actuator position sensor. All the above sensors are present in the standard vehicle ESP sensor cluster and their signals are read from the vehicle CAN-BUS which is updated at 100 Hz. To have an accurate validation of the sideslip angle observer, an optical sideslip sensor from Kistler is placed in the vehicle. This sensor is very expensive and provides a very accurate estimate of the sideslip angle at 500 Hz update rate. The observer is tested at the Nardo Technical Center (NTC) in the South of Italy. The vehicle is driven by professional test drivers who are able to perform highly dynamic manoeuvres and push the vehicle to its limit. This allows from a extensive testing of the observer. The quality of the estimate of the sideslip angle observed is demonstrated as follows.

Sine Sweep

Sine sweep manoeuvres are carried out from 0.1 Hz to 2 Hz at 125 km/h. This manoeuvre is carried out to test the sideslip angle observer's accuracy across the human operable steering input frequency. As shown in Figure 2.12, the estimate of the observer (red line) is quite accurate as it matches the measured sideslip angle (blue dashed line). At the low frequency part of the sweep manoeuvre, there is a slight phase lag of about 0.1 seconds which vanishes as the frequency of the manoeuvre increases. The magnitude of the estimate is a bit larger than the actual sideslip angle in the high frequency region. However, this error in magnitude is not very large. On the contrary, the phase of the measured and the estimated signals are aligned perfectly. This is desirable and crucial for any control system which relies on the estimate of the sideslip angle for feedback control.

Double Lane Change

Figure 2.13 shows the estimated sideslip angle for a double lane change (DLC) manoeuvre performed at around 150 km/h on a road surface with high friction coefficient. This manoeuvre is used to create the vehicle's dynamic operating range con-

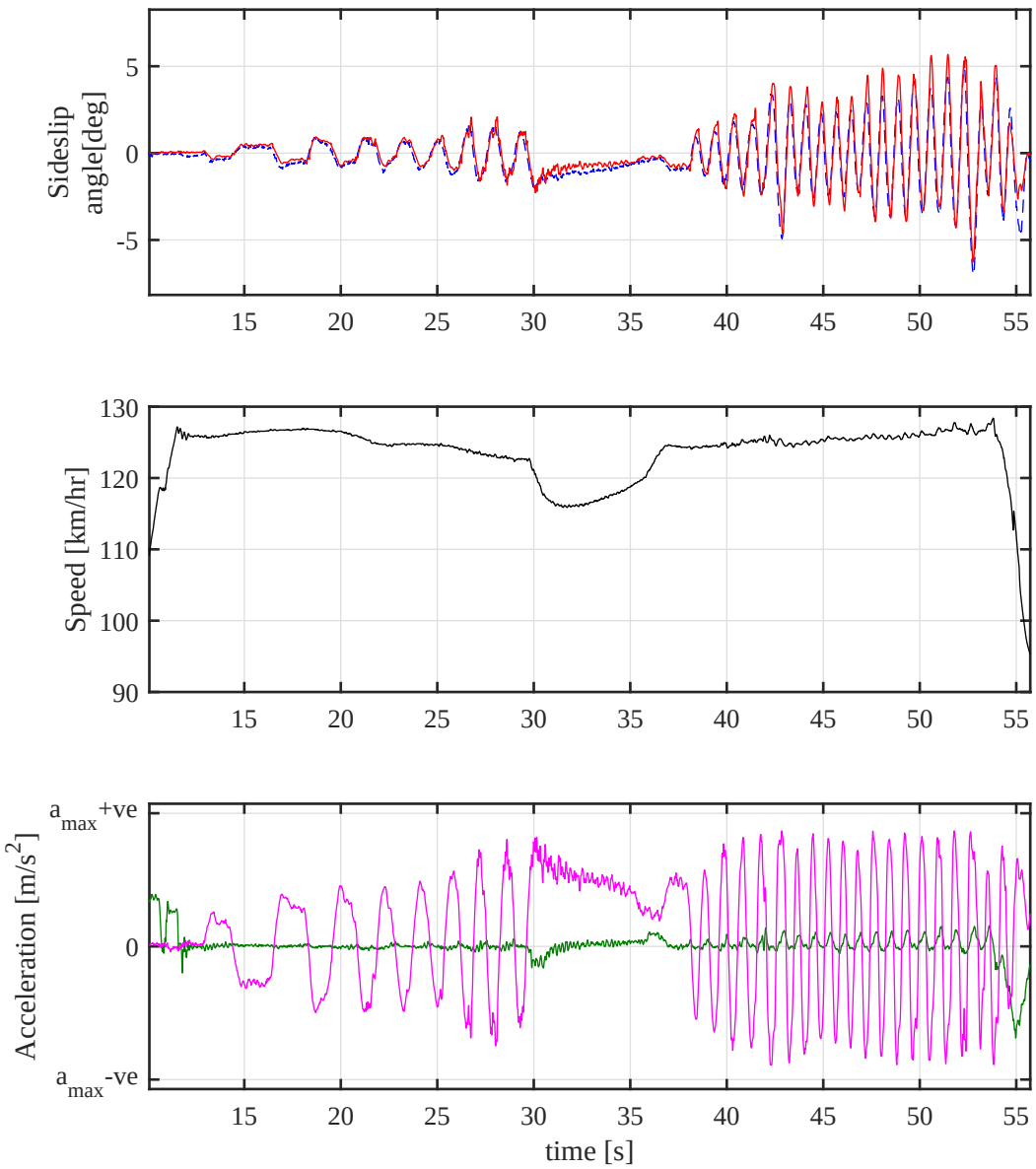

Figure 2.12 Sideslip angle estimation for a sine sweep manoeuvre. The blue curve represents the sideslip angle measured with a Kistler optical sensor, the red curve represents the sideslip angle estimated by the observer, the green curve shows the longitudinal accelerometer reading and the magenta curve is the lateral accelerometer reading. a_{max} refers to the maximum possible acceleration of the vehicle permitted by the tire-road adherence.

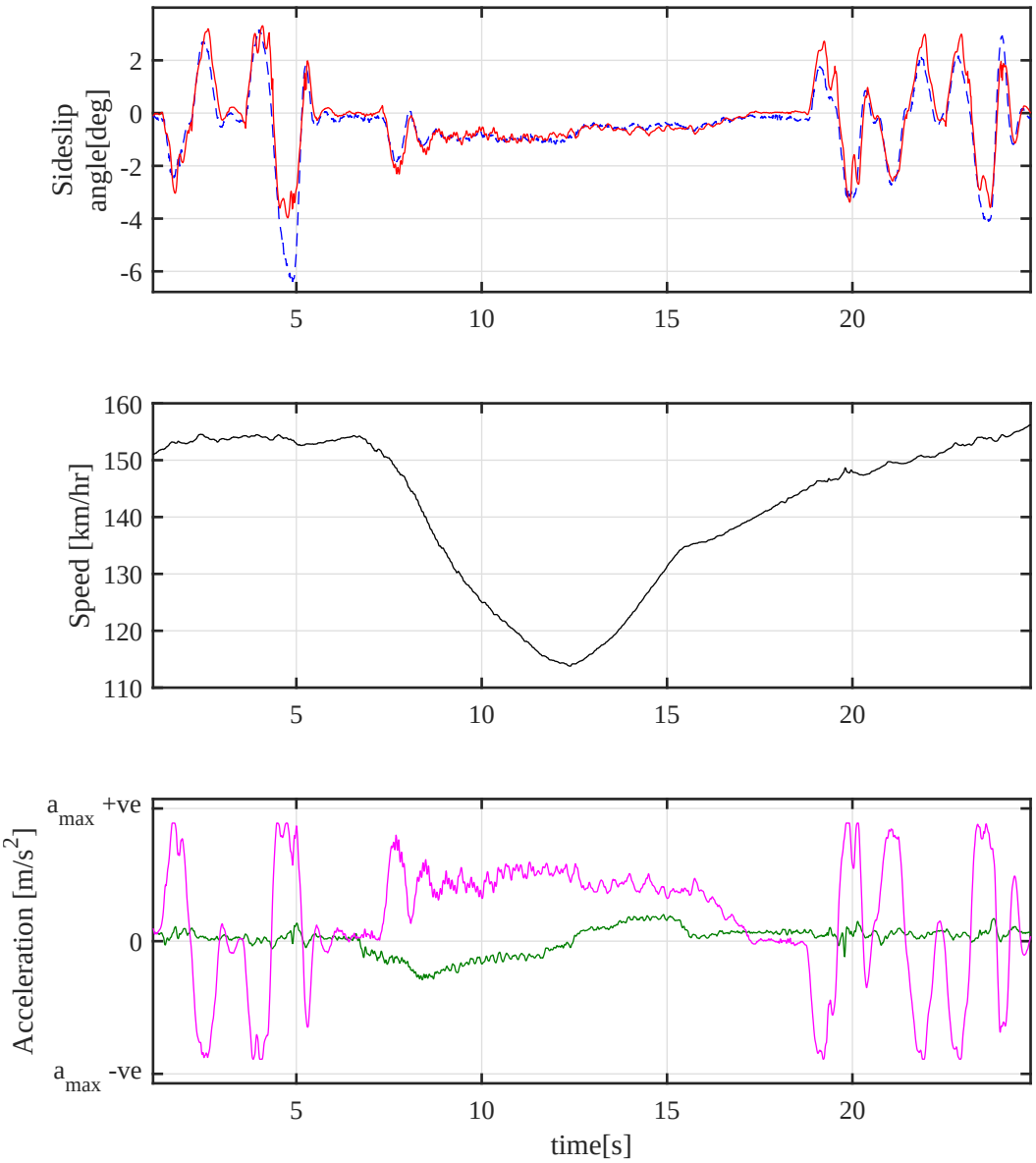

Figure 2.13 Sideslip angle estimation for a double lane change manoeuvre. The blue curve represents the sideslip angle measured with a Kistler optical sensor, the red curve represents the sideslip angle estimated by the observer, the green curve shows the longitudinal accelerometer reading and the magenta curve is the lateral accelerometer reading. a_{max} refers to the maximum possible acceleration of the vehicle permitted by the tire-road adherence.

ditions. The observer estimates the sideslip angle quite accurately. Only at a time instant when the sideslip angle is quite large (about 6 degrees), the estimator fails to have an accurate estimate. It should be noticed that the manoeuvres are extreme in nature as the lateral acceleration reaches up to around 95% of a_{max}, after which its reading saturates due to the limitation in the allocated bytes to the A/D conversion. As the manoeuvre takes the tires to their limits, the observer is expected to perform even better when day to day life manoeuvres involving lower accelerations are carried out.

Handling Circuit

To test the performance of the sideslip observer during combined tire slip conditions, laps of the handling circuit of the NTC were driven by professional test drivers. Figure 2.14 shows the estimation results for a lap of the handling circuit driven with less aggression. It can be seen that the lateral acceleration does not exceed 80% of a_{max}. The estimate is quite accurate with occasional offset errors as seen at times 342 seconds, 410 seconds. Figure 2.15 shows the estimation for a lap driven with an aggressive driving style. It can be seen that the peak lateral accelerations exceeds 95% of a_{max}, indicating that the vehicle is being driven to its limits. The longitudinal acceleration also indicates that the vehicle is being accelerated and decelerated quite hard. Looking at the longitudinal acceleration between times 150 seconds and 170 seconds, it can be seen that the vehicle is being accelerated on full throttle. The quality of the sideslip estimation for this set of laps is also quite good. Occasionally when the sideslip angle becomes large (greater than 5 degrees), the quality of the estimate goes down, as seen at times 70 seconds, 155 seconds and 305 seconds.

Figure 2.16 shows the observer's estimate for a lap of the handling circuit of NTC when the driver is performing large drifts at the corners. This is a very extreme case of driving condition, and the sideslip angles rise up to 30 degrees. It can be seen that the observer is unable to estimate the sideslip angle when the vehicle is drifting. This is evident at times from 65 seconds to 75 seconds and from 157 seconds to 170 seconds. For the rest of the lap, the observer functions quite well. The reason for the poor quality of estimate is that the vehicle and especially the tire model is unable to accurately represent the vehicle dynamics at such large tire sideslip angles. The tire models are empirical models that are fit to operate well only in the standard working region of the vehicle. Thus, they are unable to account for the tire forces in

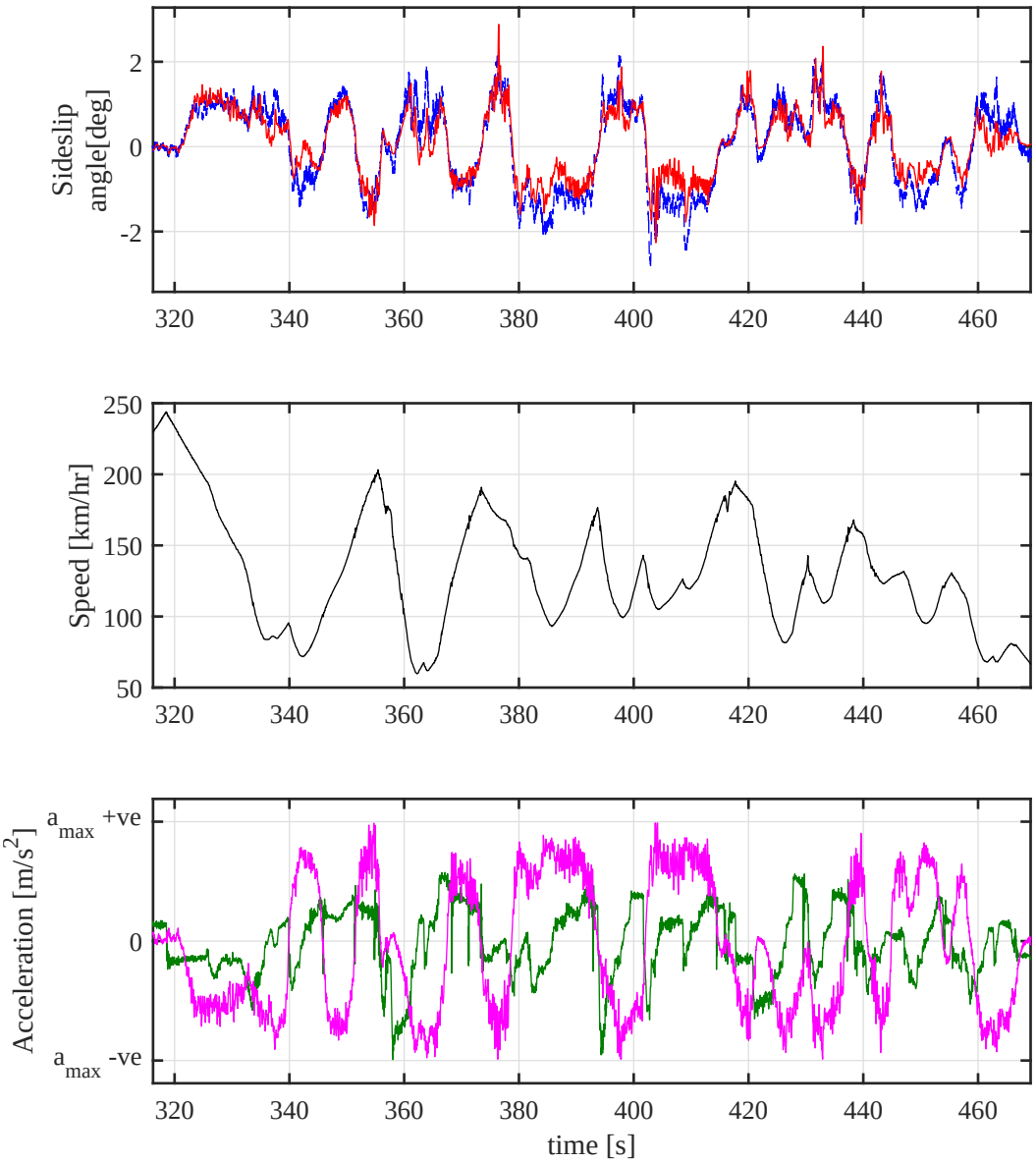

Figure 2.14 Sideslip angle estimation for a lap around the handling circuit of NTC with a less aggressive driving style. The blue curve represents the sideslip angle measured with a Kistler optical sensor, the red curve represents the sideslip angle estimated by the observer, the green curve shows the longitudinal accelerometer reading and the magenta curve is the lateral accelerometer reading. a_{max} refers to the maximum possible acceleration of the vehicle permitted by the tire-road adherence.

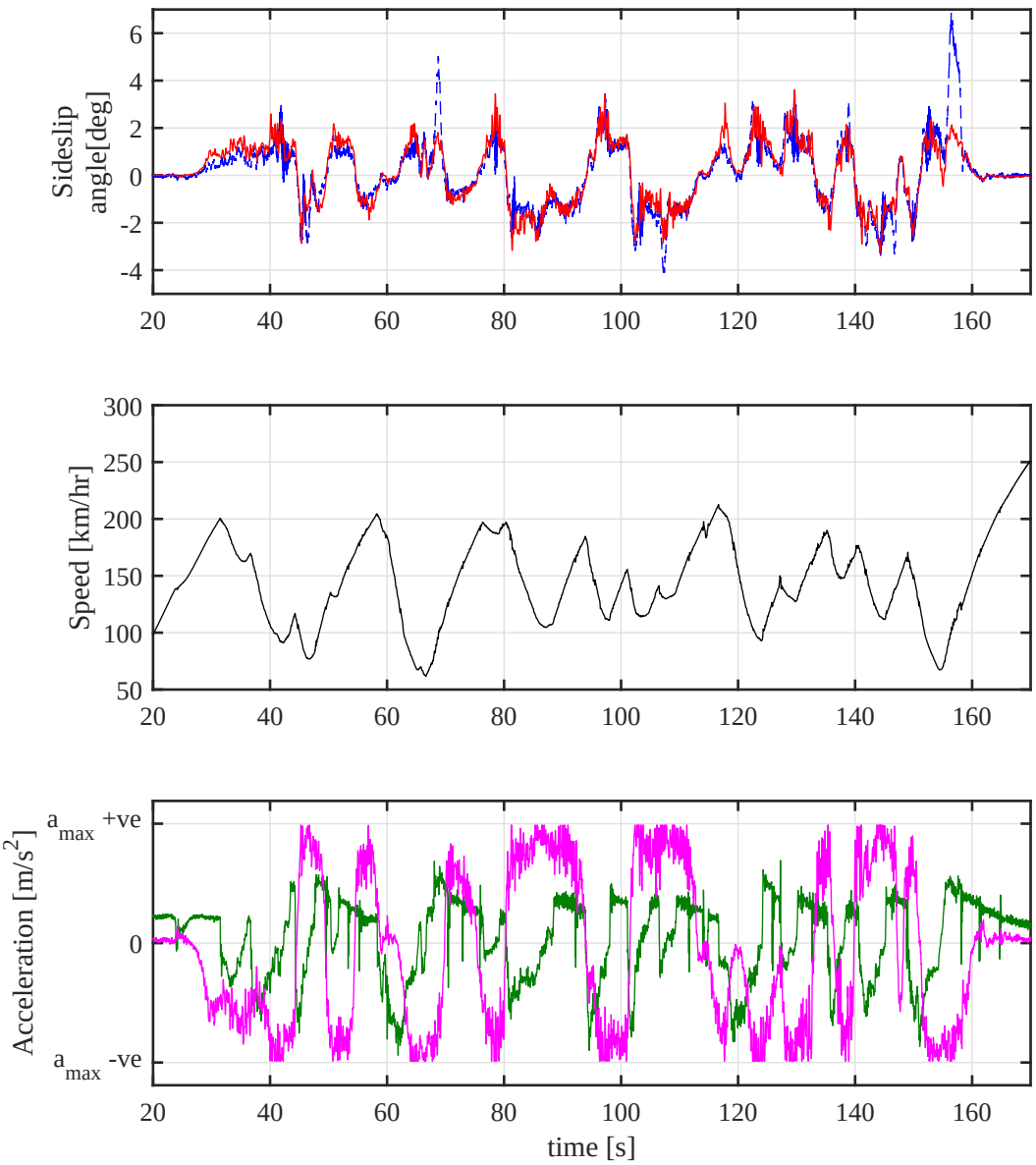

Figure 2.15 Sideslip angle estimation for two laps around the handling circuit of NTC with a very aggressive driving style . The blue curve represents the sideslip angle measured with a Kistler optical sensor, the red curve represents the sideslip angle estimated by the observer, the green curve shows the longitudinal accelerometer reading and the magenta curve is the lateral accelerometer reading. a_{max} refers to the maximum possible acceleration of the vehicle permitted by the tire-road adherence.

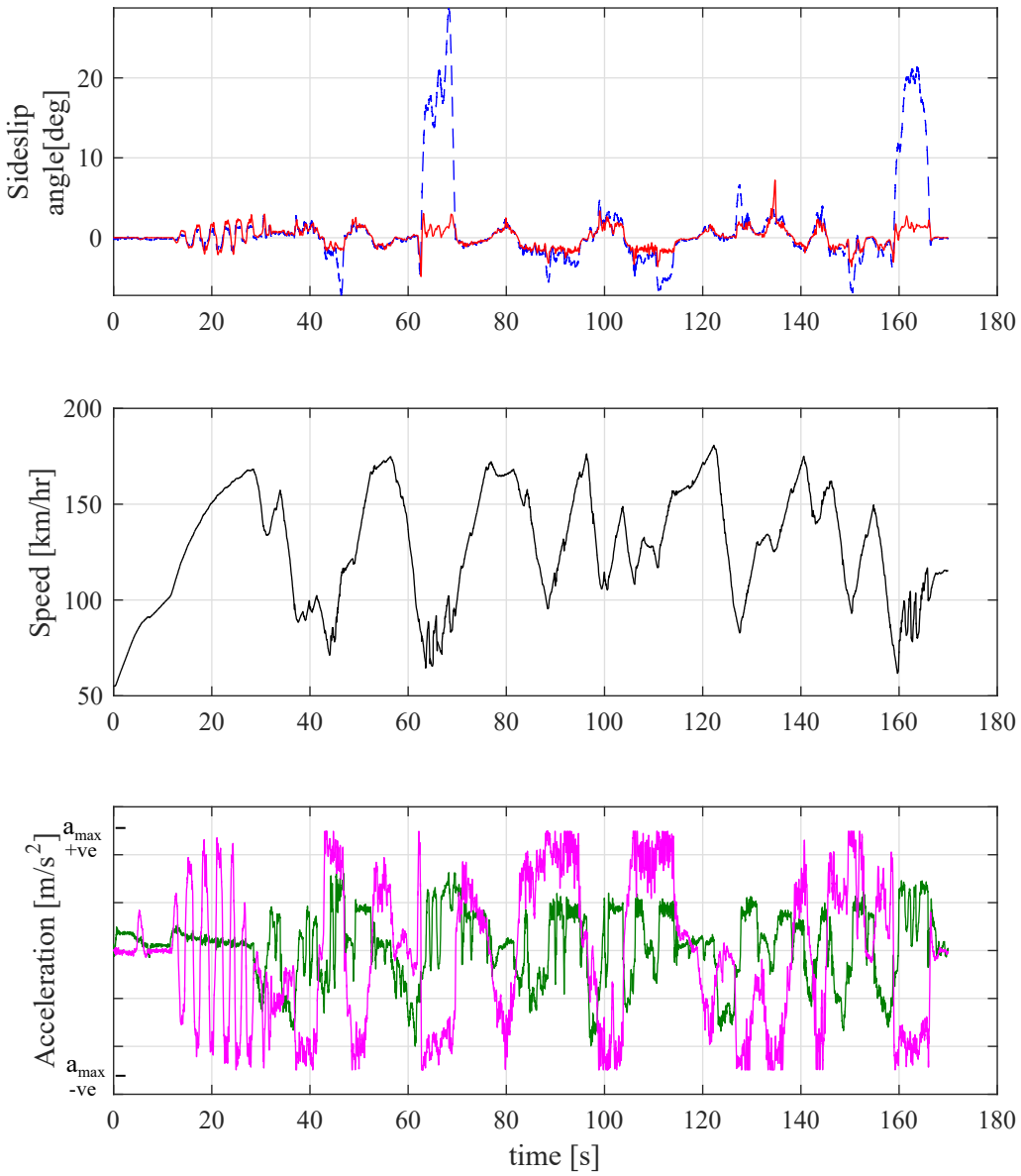

Figure 2.16 Sideslip angle estimation for a laps around the handling circuit of NTC with heavy drifting. The blue curve represents the sideslip angle measured with a Kistler optical sensor, the red curve represents the sideslip angle estimated by the observer, the green curve shows the longitudinal accelerometer reading and the magenta curve is the lateral accelerometer reading. a_{max} refers to the maximum possible acceleration of the vehicle permitted by the tire-road adherence.

such extreme conditions. Secondly, during such drifting, the tire loses rubber very quickly due to the wheel spin and the sideways motion of the vehicle, so much so that a new set of tires can be completely worn out to the point of tire failure within a timespan of three laps. As a result, any tire model, calibrated when the tire is new can never be used to model such conditions with extreme wear and tear.

2.5 Conclusions

A sideslip angle observer based on an EKF was presented in this chapter. The EKF consists of a four degree of freedom vehicle model with the tire behaviour modelled with an experimentally calibrated Pacejka's model. The advantage of the presented observer is the fact that it only requires information from onboard sensors and thus allows a real software implementation onboard any vehicle. The observer's performance is tested with experiments performed at the NTC with the help of a prototype vehicle and seasoned test drivers using a range of manoeuvres for the testing of a vehicle's handling performance. The vehicle is tested rigorously to ensure that it reaches its non-linear operating range. Results indicate the observer performs quite well for standard driving manoeuvres with occasional small offset errors. However, when the sideslip angle increases to large values during drifting, the estimation error becomes quite large. This is due to the incapability of the utilised tire model to represent the tire forces during such extreme and variable conditions. In the following chapter, this problem is resolved by formulating a new kind of observer that does not require a vehicle or a tire model.

Chapter 3

Sideslip Angle Estimation II

In the last chapter, it was evident that an EKF based on a vehicle model works well for the estimation of the sideslip angle under normal driving conditions. However, it was found that such observers based on vehicle models are not so reliable during aggressive manoeuvres, such as drifting. Moreover, the EKF is unable to take into account the change of tires on the vehicle from summer tires to winter tires by itself. This warrants the need for an algorithm that does not rely on a vehicle model or on a tire model. In this domain, black box techniques are much more suitable. Machine learning is one such group of techniques, which is presented in this chapter to solve the problem of robust sideslip angle estimation.

3.1 Racing Driver Brain: A Black Box

Top racing drivers, especially rally drivers, are exceptionally good at controlling a vehicle even when its tires are working in the non-linear region or even when they are going on gravel or a surface with low tire-road friction coefficient. Apart from very good reflexes (high controller bandwidth), this is also possible because they have a very good idea of how the vehicle is going to behave, even with the introduction of disturbances in the system. They are able to predict the vehicle behaviour because their brains have been trained with years of experience of driving to understand and predict the vehicle states (state estimation). Without entering into the details of the biological part of the discussion, the driver's brain neurons are trained to be able to estimate the vehicle states such as the sideslip angle. The inner ear in the human

Figure 3.1 A rally driver controlling a vehicle with a large sideslip angle on a low friction road surface (Source: http://www.revvedmag.com/).

body is able to detect translational and angular accelerations. Together with the steering torque feedback, road vibrations transmitted through the driver's seat and the sensed accelerations by the inner ear, the drivers are able to estimate the vehicle sideslip angle and then control the vehicle with the control inputs and drive the vehicle as desired. In essence, such a modelling should be theoretically possible by the use of black box machine learning techniques. With the help of such techniques, it should be possible to train a learning method to give out the continuous estimate of the vehicle sideslip angle with the standard vehicle sensor cluster signals as inputs. In the following sections, this idea is investigated to understand the capabilities, practicalities and limitations of employing such a machine learning method.

3.2 Introduction to Machine Learning

Machine learning (ML) involves a group of techniques that enable a computer to 'learn' the ability to think and decide just like a biological system. This sub-field of computer science has emerged from the quest for imparting Artificial Intelligence (AI) to machines. While machine learning has its roots from as early as 1943, it has recently gained a lot of attention after its resurgence in the 1990's as one of the best methods for realising AI [79]. Most of the techniques involved in ML are based on theories borrowed from statistics and probability theory [80].

ML can be classified broadly into three categories based on the training methods of the algorithms.

- Supervised learning involves a machine learning the relationship between inputs and outputs from a set of data. This technique is useful in time series prediction where the machine gives out the estimate of a parameter(s) based on the time histories of a group of other different parameters that are known to have an influence on the parameter(s) to be estimated.
- Unsupervised learning is the machine learning performed by the computer on unlabelled data. As a result, the algorithm finds hidden patterns between input and output by itself and evaluates which input has a higher sensitivity to the output. This kind of learning is more useful in the context of predicting a parameters when the input to output sensitivity is not known.
- Reinforced learning involves the absence of a standard input/output structure and the training algorithm rewards the final outcome of an event. Unlike the above two events, it does not reward intermediate results obtained as output by the algorithm. This type of technique has become popular in applications such as the AI controller of video games, control systems and robot control, where the control algorithm learns from trial and error.

3.2.1 Machine Learning in the Automotive Domain

In recent years, machine learning is being utilised more and more in the automotive domain with the passage of time. With the introduction of autonomous vehicle technologies, machine learning is being used in image classification problems for the detection of road signs and symbols [81, 82]. Artificial neural networks have been used in the past to model the non-linearities of various vehicle components [21, 83]. For example, Kang et al. in [84] used an artificial neural network to estimate the state of charge of the batteries of an electric vehicle.

As it can be seen, a lot of the above applications involve the use of a supervisory learning algorithm where the network is trained at first with the correct and expected outputs. Once the training is complete, the algorithm is used in a feedforward manner to give an estimate of the desired output of the system to be modelled/observed.

In the context of our application, the use of a supervised learning technique is applicable as the objective is to estimate the timeseries of the sideslip angle using sensor signals from the vehicle CAN-BUS.

3.2.2 Artificial Neural Networks

An artificial neural network is a machine learning technique that tries to mimic the functioning of a biological neural network, i.e. an interconnection of neurons by the combination of simple computation units called 'neurons'. The neurons are arranged in different topologies and interconnected with each other by the means of weighted connections. The standard layout of a neural network is composed of columns of

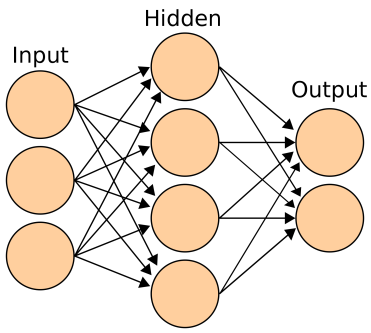

Figure 3.2 Artificial Neural Network architecture. The neurons are indicated by the circles and they are interconnected.

neurons called layers, where the neurons of one layer are connected to the neurons of the following layers. A simple neural network, which is also called a shallow neural network, is composed of an input layer where the neurons are connected to the inputs of the network, a single hidden layer that interacts with inputs and an output layer that combines the outputs of the hidden layers to give out the output(s) of the network. Each neuron within a neural network is generally composed of two components, the propagation function and the activation function. The propagation function is responsible for combining the inputs of all the preceding neurons connected to it with their respective weights. The weight of these connections represent the level of strength between the two neurons [79]. For a given neuron j in the network, the output of the propagation function can be written as

$$net_j = \sum_{i=I} (o_i w_{i,j}), \tag{3.1}$$

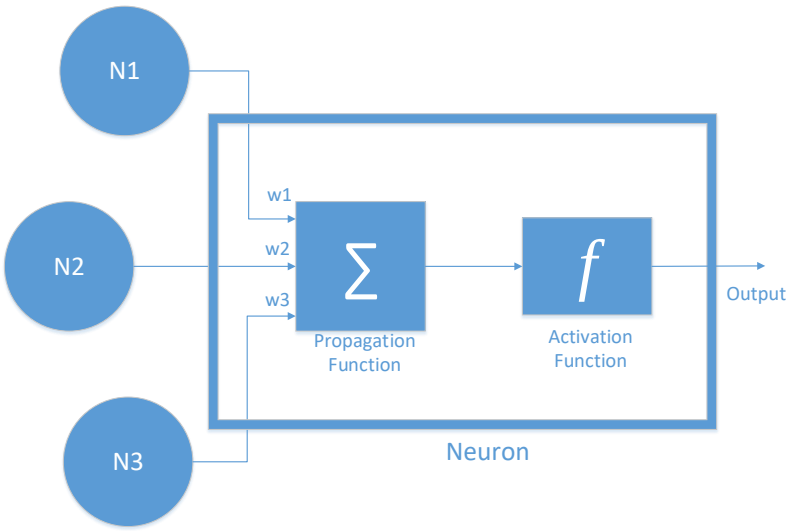

Figure 3.3 The structure of an individual neuron.

where I is the set of all the neurons from the preceding layer connected to the neuron j, o_i is the output of neuron i of the previous layer, $w_{i,j}$ the weight of the connection between neuron i and neuron j.

The activation function is responsible for activating a neuron if the value of the propagation function exceeds a certain threshold. It is an indicator of the extent of the neuron's activity. This function is generally a sigmoidal function, but there are other possible candidate functions as well.

3.2.3 Artificial Neural Network for Sideslip Estimation

Researchers have utilised ANNs to estimate the sideslip angle of a vehicle from low cost sensors mounted on the vehicle. These networks have a relatively simple architecture with a single input layer, a single hidden layer and a single output layer. Abdulrahim presented a neural network with 8 inputs and 16 neurons in the single hidden layer of the network [21]. The above work utilisied an array of 8 accelerometers placed on different positions of the vehicle body. Milanese et. al. utilised a neural network with 5 hidden neurons that take the vehicle accelerometer, gyroscope

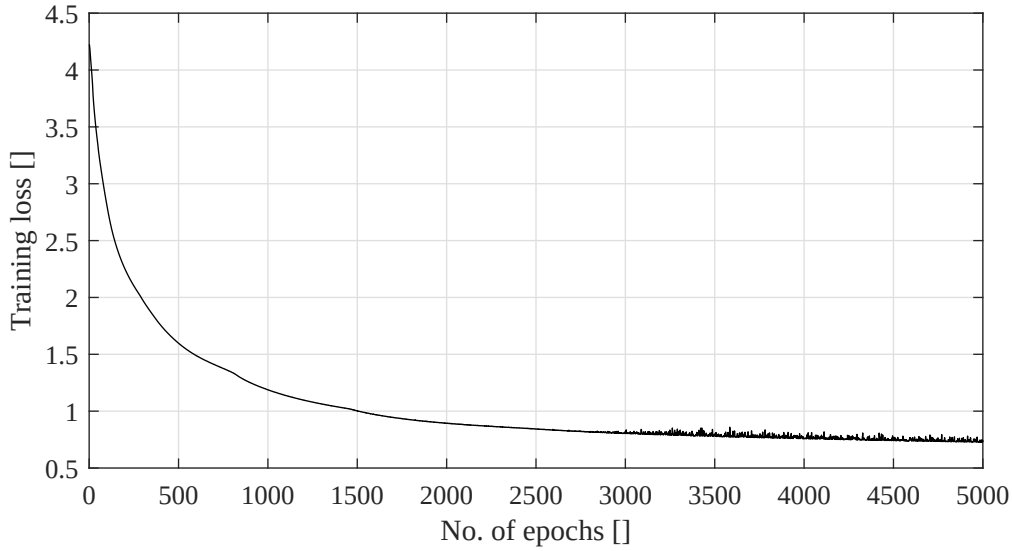

Figure 3.4 Reduction of ANN's training loss versus number of training epochs.

and wheel speed sensors readings as inputs [85]. The same inputs are used by Melzi et.al., however, with a neural network that has a single hidden layer containing 10 hidden neurons [86]. The interesting aspect of the work presented is that the input to the network contains sensor information from the present and past time instants. The works presented in the above articles have been found to be very difficult to replicate across the entire working range of the vehicle. The results of the network presented in [86] are evaluated by repeating the training and validation from experimentally generated data. It has been found that during the training phase of the aforementioned neural network, the training loss hits a plateau, which indicates that the network in its most optimised state is unable to reduce the error between the network output and the training sideslip angle. This is seen in Figure 3.4, where the training loss saturates to a certain value that is not negligible with respect to the required accuracy. The principal reason is that a neural network containing a single hidden layer with around 10-20 neurons is too simple of an architecture to map all the range of the input-output space. Figures 3.5 and 3.6 show the estimation result for the algorithm from [86]. It can be seen that the sideslip estimation is inaccurate when the algorithm is tested for manoeuvres containing large sideslip angles.

Due to the limitations in the selection of manoeuvres of the training dataset, it is also found that the aforementioned algorithms have difficulty in estimating the sideslip angle accurately when they are validated with a dataset having a manoeuvre that is not present in the training data set. This indicates that the training dataset

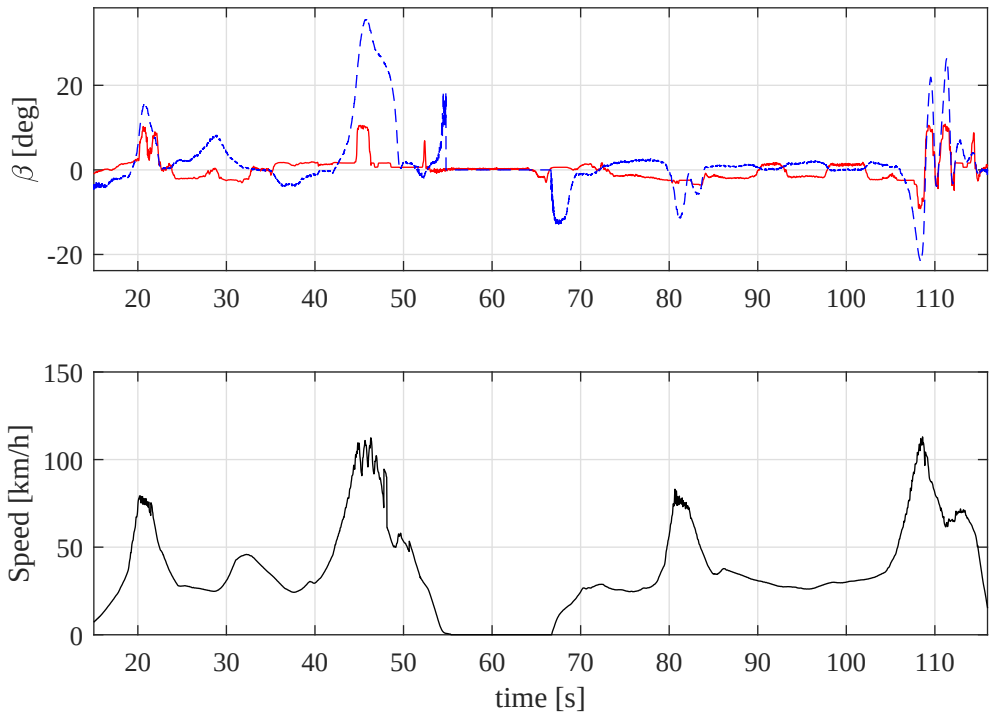

Figure 3.5 Sideslip estimation of a single hidden layer ANN containing 10 neurons for a handling lap with sporty driving behavior on a dry racetrack. Blue dashed line indicates the sideslip angle measured using a Kistler sensor, while the red line shows the ANN's estimate.

must include a larger gamut of all possible manoeuvres that can be executed by the driver. This warrants the need to find a different kind of neural network structure that is more capable of learning different patterns. Along with that, the training dataset needs to be enlarged in a way such that it may contain all the foreseeable driving manoeuvres.

3.3 Sideslip Angle Dynamics and the Choice of the Neural Network Structure

The sensor inputs that are available onboard a standard vehicle are the lateral and longitudinal accelerometer, the yaw rate sensor, the steering angle sensor and the four wheel speed sensors. A neural network used for estimating the sideslip angle should thus be trained based on the time histories of the aforementioned signals. The time plots of the onboard vehicle sensors along with the actual sideslip angle

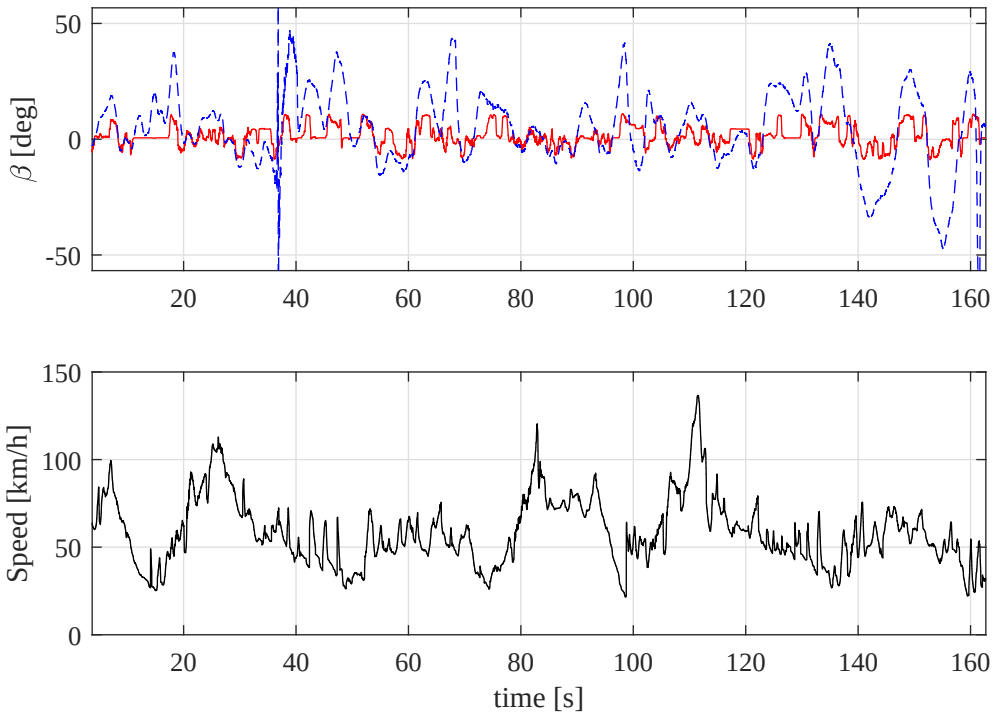

Figure 3.6 Sideslip estimation of a single hidden layer ANN containing 10 neurons for a handling lap with sporty driving behavior on a snowy racetrack. Blue dashed line indicates the sideslip angle measured using a Kistler sensor, while the red line shows the ANN's estimate.

measured with an optical sensor for the vehicle under drifting conditions are shown in Figures 3.7 and 3.8. It can be seen that when the vehicle is drifting, some peculiar patterns within the signals emerge. For example, it can be seen in Figure 3.7 between times 293 seconds and 295 seconds, the longitudinal velocity of the vehicle decreases, but the longitudinal accelerometer still reads out a positive reading instead of reading out a negative value as expected due to braking. If one looks at the signals between 277 and 282 seconds, it can be seen that, as expected, braking leads to a negative longitudinal acceleration and reduction in the vehicle speed. The positive accelerometer reading can be explained by the fact that the longitudinal accelerometer measures the longitudinal acceleration which is made up of two components, the first due to the rate of change of longitudinal velocity and second, the component due to the rotation of the body about its yaw axis as seen in Equation 2.19. When the sideslip velocity/sideslip angle is small, the component due to the rotation of the vehicle about the yaw axis is also small. However, when the vehicle has a large sideslip velocity, it results in a substantial component of the net

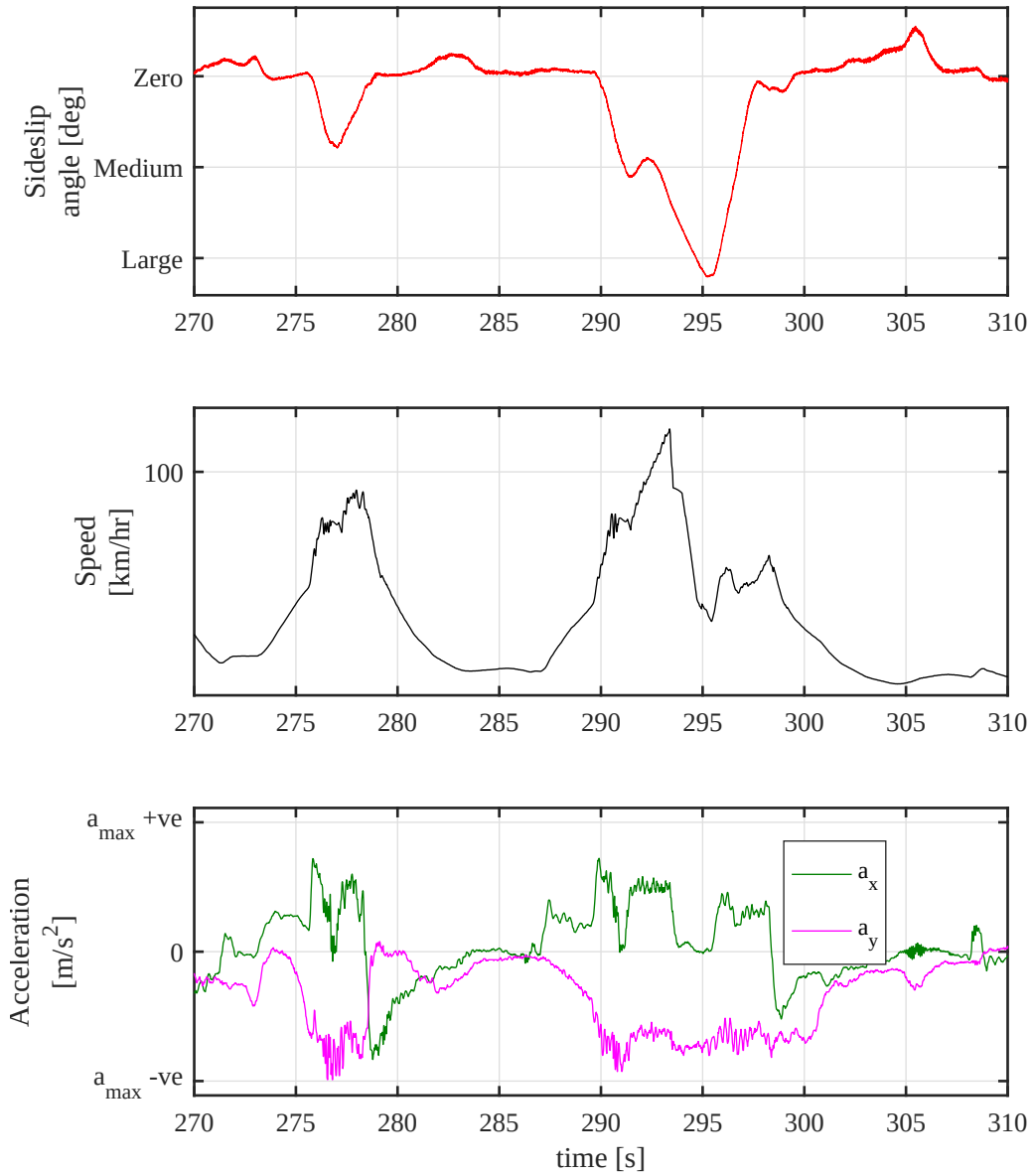

Figure 3.7 Onboard sensor input logs during drifting-I. The sideslip angle is measured using a Kister optical sensor which is a non standard sensor. a_{max} refers to the radius of the g-g plot of the vehicle, small, medium and large sideslip angles refer to ranges 0-10, 5-30 and 20-60 degrees of sideslip angles. The y-axis data has been removed to respect the confidentiality of the data of the industrial partner.

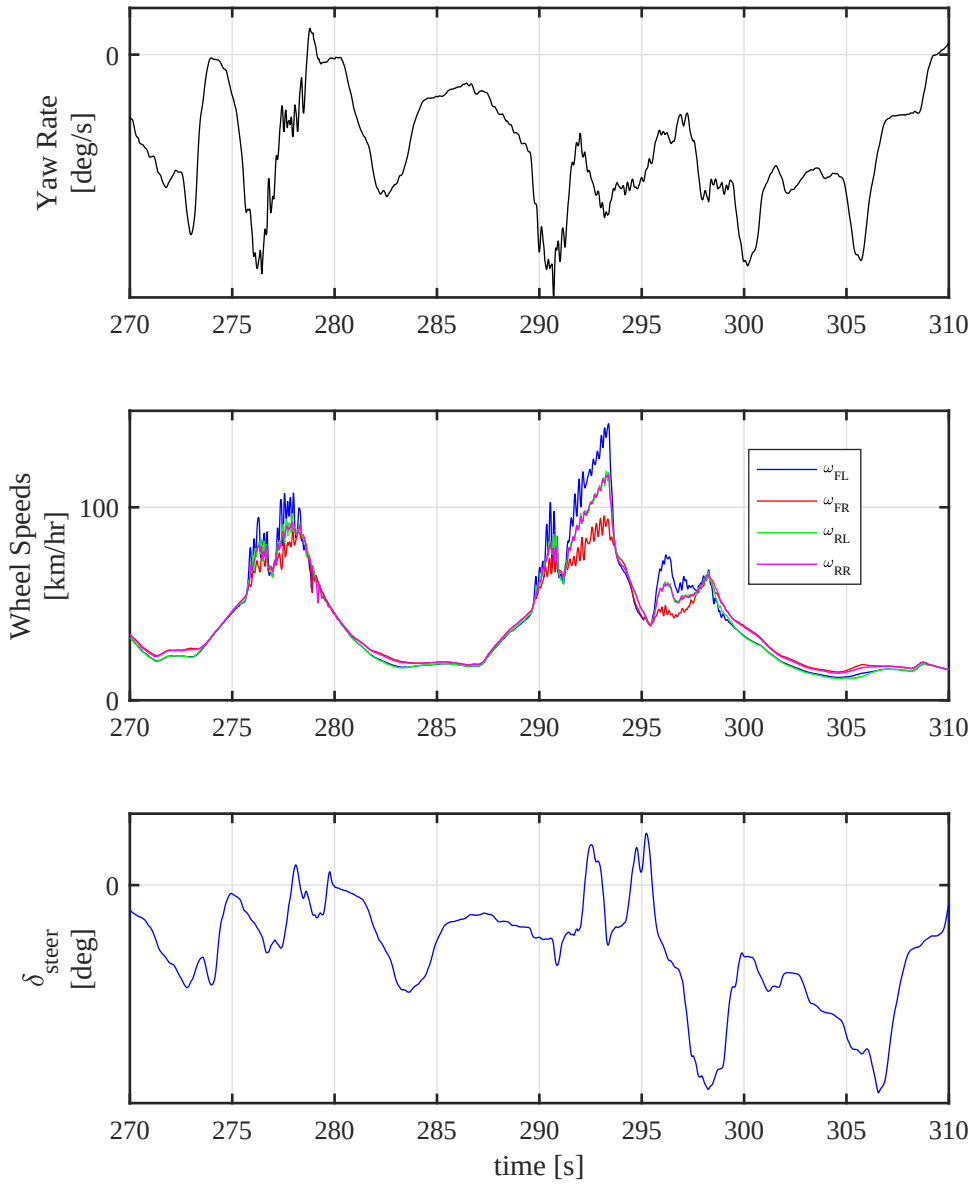

Figure 3.8 Onboard sensor input logs during drifting -II. The y-axis data has been removed to respect the confidentiality of the data of the industrial partner.

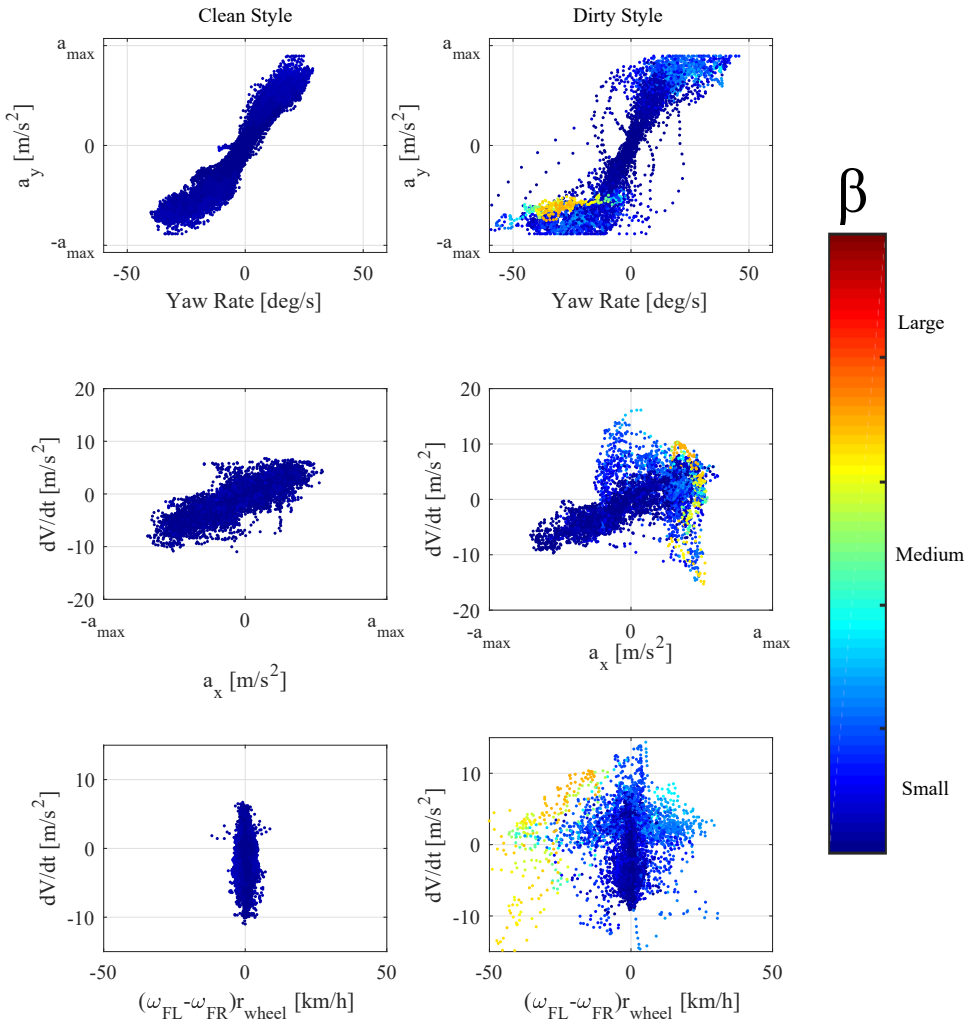

Figure 3.9 Correlations between different sensor inputs. The plots on the left show data from a lap around the NTC's handling circuit with a 'clean' driving style resulting in very small sideslip angles. The plots on the right show the same variables in the case of a lap around the same circuit with a 'dirty' driving style resulting in large drift angles. a_{max} refers to the radius of the g-g plot of the vehicle. Small, medium and large sideslip angles refer to ranges 0-10, 5-30 and 20-60 degrees of sideslip angles respectively. The y-axis data has been removed to respect the confidentiality of the data of the industrial partner

accelerometer reading. This is what causes the non-zero a_x reading between 293 and 295 seconds, as it can be seen that the sideslip angle is very large. Similarly, from Figure 3.8, it can be noticed that the difference between the front left and the front right tire speeds is directly correlated to the sideslip angle. While such simple correlations can be easily noticed by the naked eye with the help of telemetry data analysis, many more of such correlations exist that cannot be noticed visually. Figure 3.9 shows the comparison of two different laps of the same circuit driven with different driving styles. The plots show the correlation of various combinations of two input signals from the onboard sensors. The sideslip angle is shown with the help of a color scheme. The left column shows a lap without drifting ('clean' driving) while the right column shows a lap with heavy drifting ('dirty' driving). It can be seen that when the vehicle is driven with a 'clean' driving style, the sideslip angle remains small and the various parameters are linearly correlated. On the other hand, when the driving style is 'dirty', it causes large sideslip angles and these occur in the non linear region of the input correlation space. While, on paper it is only possible to demonstrate a 2D relationship, such relations also exist in the entire input space, that is a 10 dimensional space in our case. Moreover, the way a driver senses a drift condition is that after the driver turns the steering wheel suddenly, and then presses the throttle to send a large amount of torque to the rear wheels, the driver senses the loss of grip/saturation of the rear tires as the vehicle's back end steps out. This is normally characterised by a sudden rise in yaw rate and lateral acceleration. After this, the vehicle's yaw rate reduces and the vehicle starts moving sideways. As a result, the lateral acceleration still remains high. When the drift ends, the lateral acceleration reduces as well. As a result, it is very important to realise that detecting drifting involves the detection of a sequence of events and not just the input signals at one particular instant.

Since standard feedforward ANNs give an output based on the values of the input signals at that particular time instant, they are not expected to perform very well when it comes to the estimation of the sideslip angle during drifting maneuvers. A special kind of deep learning techinque based neural network called the Recurrent Neural Network (RNN) has become quite popular amongst AI scientists for applications regarding learning of sequences. Amongst the different types of RNNs, a particular type of deep learning RNN known as Long Short-Term Memory (LSTM) has shown the most promise in the field of sequence learning. Unlike feedforward networks, LSTMs have extra internal memory state(s) that make them ideal

for modelling of dynamical processes. LSTMs have been proven to provide exceptional results in applications such as language translation or speech recognition due to their ability to model temporal sequences [87]. As a result, LSTMs have been widely used by reserachers in the field of handwriting recognition, speech and context recogntion and image recognition. The advantage that LSTM networks have over traditional RNNs is that they do not suffer from the vanishing or exploding gradient problem and have been demonstrated to be able to handle problems that require knowlegde from a thousand time steps in the past [88]. Although LSTMs have been widely implemented in the aforementioned applications, their application in vehicle dynamics and state estimation have never been studied or presented in literature. Motivated by the successful utilisation of LSTMs in the field of speech and text learning AI, the idea of using an LSTM network to estimate the time series dynamics of the vehicle sideslip angle is presented and investigated in the following section.

3.4 Deep Learning with LSTM Networks

LSTM networks are composed of basic units called memory cells, which may contain up to four components, namely, an input gate, a neuron with a self-recurrent connection, a forget gate and an output gate [89, 90]. Each memory cell is characterised by its memory state, that is the value stored by the neuron's internal state. The self-recurrent connection has a weight of 1 so that the memory cell can preserve its state during the next iteration. Figure 3.10 shows the structure of a LSTM cell. The input gate is used to control the influence of the input to the memory cell on the state of the memory cell. Similarly, the output gate controls the effect of the state of the memory cell on the output of the memory cell. The forget gate is used to modulate the self-recurrent connection, thereby controlling how the cell forgets its previous values. The equations describing a single LSTM memory cell can be written as following [90].

Let x_t be the input vector to the memory cell at a given time step t. The value of the input gate activation y_{in} is computed as

$$y_{in}(t) = f_{in}(W_i x_t + U_i h_{t-1} + b_i), \tag{3.2}$$

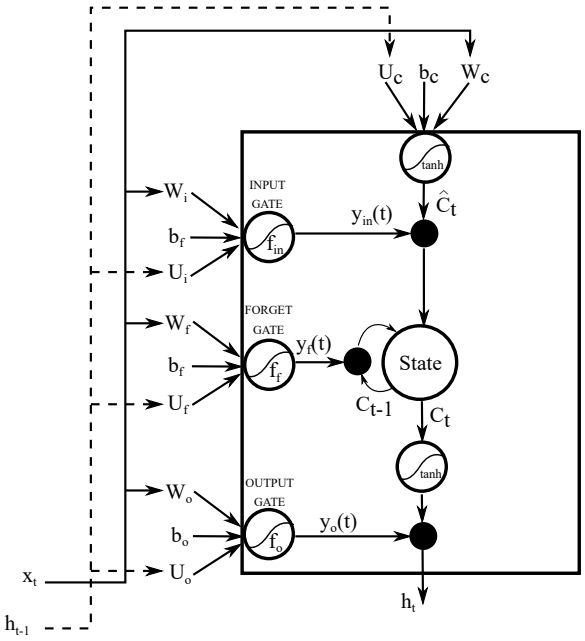

Figure 3.10 LSTM memory cell structure after [90].

where f_{in} represents an activation function of the designer's choice, W_i is the input gate's weighing matrix, U_i is the weighting matrix for the outputs from the other cells in the hidden layers, b_i is the input gate bias matrix.

The candidate value, $\hat{C}_t$ for the states of the memory cells at time t is obtained as

$$\hat{C}_t = tanh(W_c x_t + U_c h_{t-1} + b_c), \tag{3.3}$$

where tanh represented the hyperbolic tangent function, W_c is the candidate memory state's weighing matrix, U_c is the weighting matrix for the outputs from the other cells in the hidden layers to the candidate memory state, b_c is the candidate memory state's bias matrix.

The activation of the forget gate of the memory cell is calculated as

$$y_f(t) = f_f(W_f x_t + U_f h_{t-1} + b_f), \tag{3.4}$$

where f_f is the forget gate's activation function, W_f is the forget gate's weighing matrix, U_f is the weighting matrix for the outputs from the other cells in the hidden layers to the forget gate, b_c is the forget gate's bias matrix.

The update for the memory cell's state at time t is given by

$$C_t = y_{in}(t)\hat{C}_t + y_f(t)C_{t-1}. \tag{3.5}$$

The value of the output gate is computed as

$$y_o(t) = f_o(W_o x_t + U_o h_{t-1} + b_o), \tag{3.6}$$

where f_o is the output gate's activation function, W_o is the output gate's weighing matrix, U_f is the weighting matrix for the outputs from the other cells in the hidden layers to the output gate, b_c is the output gate's bias matrix.

Finally the output of the memory cell is obtained as

$$h_t = y_o(t) * tanh(C_t). \tag{3.7}$$

A deep network architecture is chosen for the estimation of the sideslip angle. The network has 10 inputs each connected to one of the 10 measured sensor signals. The number of hidden layers is chosen to be 7, each having 200 LSTM units. The network is chosen in such a manner so that it accepts input samples worth the last 2 seconds in order to process the estimated sideslip angle. Figure 3.11 shows the network topology and architecture.

3.4.1 Training Data

Experimental data logs from various track tests are collected for the training and the validation of the DLO. An instrumented prototype super-sport vehicle is used to carry out the experiments. The data is collected from various proving grounds across Europe in order to have data from both high and low friction roads. The logged data includes all the onboard sensors information which includes the lateral and the longitudinal accelerometers, the yaw rate sensor, the steering angle sensors, the vehicle speed estimated by the ESP and the wheel speed sensors for the four wheels. In addition, the actual sideslip angle required for the supervised learning is measured using an optical sensor as seen in Figure 3.12. The utilised optical

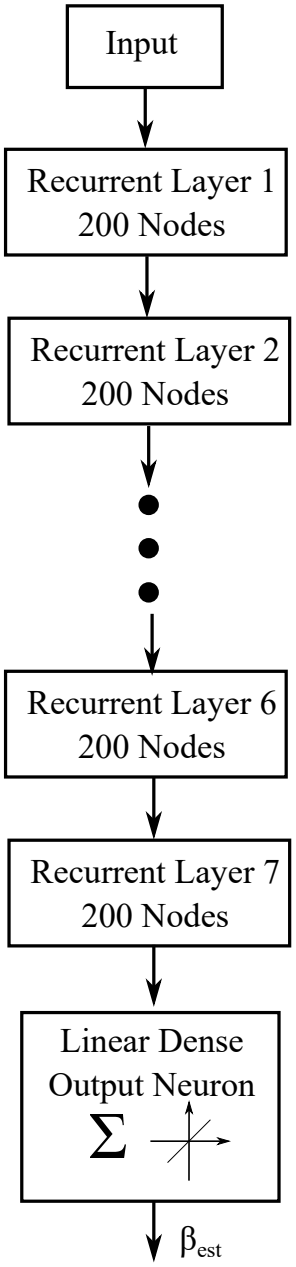

Figure 3.11 Deep learning network structure.

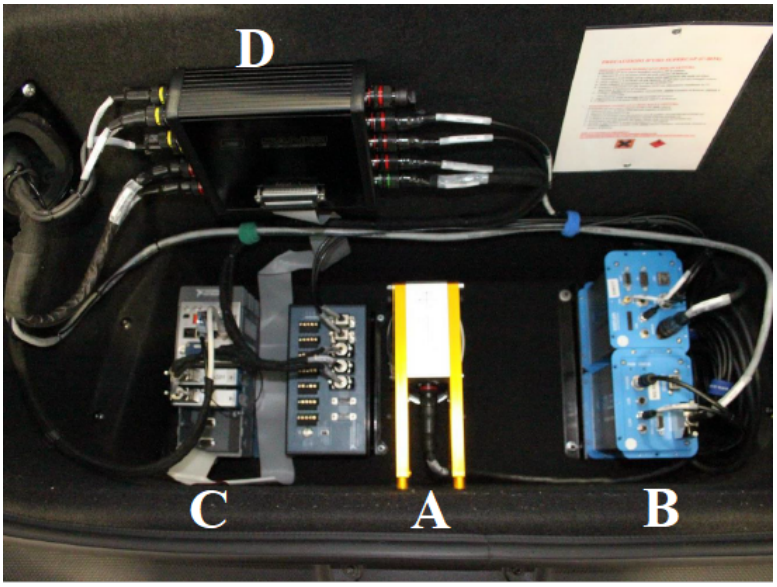

Figure 3.12 The setup of the optical sideslip sensor used for measuring the sideslip angle for the neural network training and validation. A- Optical sensor and lamp, B- Image correlation processor, C- Rapid prototyping ECU, D- CAN signal connector box.

sideslip sensor is the Correvit® S-Motion sensor from Kistler [1] which measures the sideslip angle with a sampling rate of 500 Hz and an accuracy of less than 0.2 degrees. The actual sideslip angle used for the supervised learning is logged at 100 Hz. The manoeuvres used for training are mentioned below:

1. Laps of the various handling circuits of the different proving grounds in all the different calibration modes the control systems of the vehicle with 'clean' and 'dirty' driving style.
2. Laps of the above handling circuits with heavy drifting while cornering.
3. Sine sweep manoeuvres at constant longitudinal velocities (varying from 50km/h to 150 km/h).
4. Double lane change manoeuvres at different constant longitudinal velocities.
5. Acceleration and braking while cornering.
6. Steering ramp.

[1] https://www.kistler.com/?type=669&fid=63383&model=document&callee=frontend

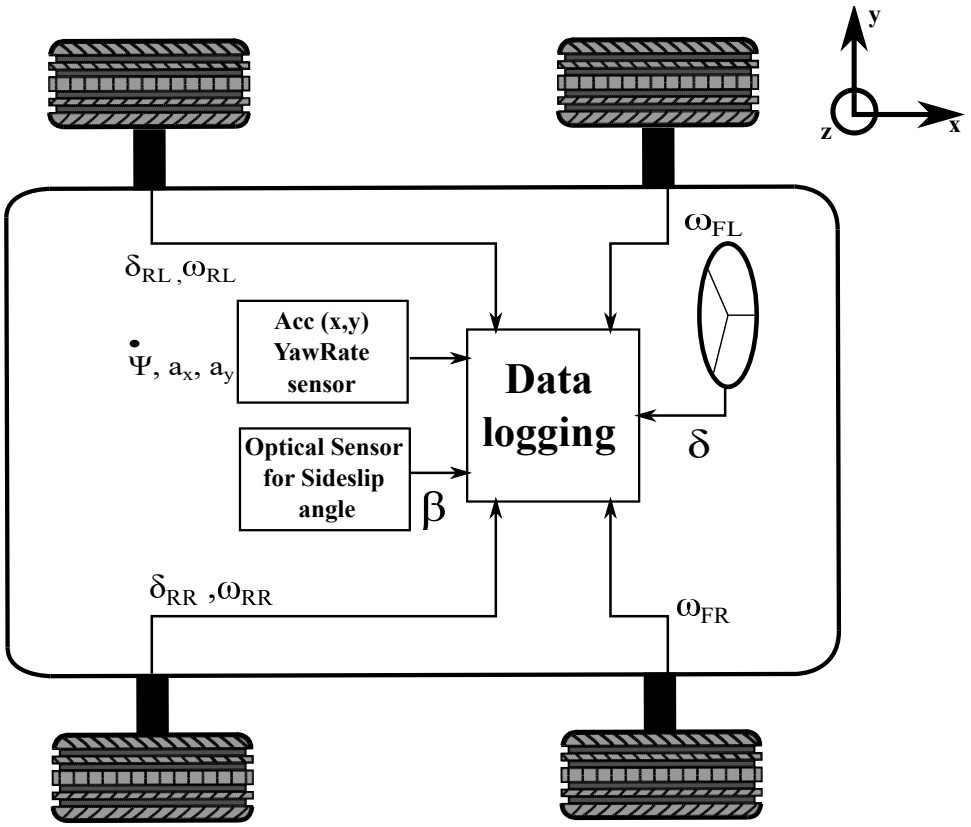

Figure 3.13 Training data acquisition phase schematics.

7. Miscellaneous handling manoeuvres such as power on and power off while turning.

All the manoeuvres are carried out in dry, wet and icy road conditions to account for the vehicle sensitivity to changing tire road friction coefficients and they are repeated with the active safety systems on and off. The dry and wet tests are performed with summer tires while the icy road tests are performed with winter tires. The vehicle is driven by drivers with varying vehicle controllability in order to generate driving conditions that cover the maximum possible range of foreseeable conditions. This range of variable controllability includes a novice driver at the bottom of the range, a vehicle engineer/calibration engineer in the middle and a professional test driver at the top.

3.4.2 Training Process

All the selected test manoeuvres are combined together one after another to form an input matrix of the training data, which contains the measured sideslip angle as the training network output, used for tuning of the network hyper parameters. The inputs to the neural network are the logged sensor signals as seen in Figure 3.13 and include the time histories of the last 2 seconds of the following logged sensor signals which are available on the vehicle CAN-BUS.

1. Longitudinal accelerometer at CG from ESP
2. Lateral accelerometer at CG from ESP
3. Yaw speed sensor at CG from ESP
4. Vehicle speed from ESP
5. Wheel speed sensors of all four wheels
6. Front and rear steering angle sensors

The length of this moving window of 2 seconds has been found to be the long enough to give a smooth sideslip estimation as reducing the length leads to a noisy sideslip angle estimate. A longer window length could be chosen but that will lead to an increase in computation burden without a substantial improvement in the quality of the estimated signal.

The network is trained on the High Performance Computer (HPC) of Politecnico di Torino named 'Hactar'. The HPC has two Intel Xeon E5-2680 v3 2.50 GHz processors (turbo 3.3 GHz) containing 12 cores and two NVIDIA Tesla K40 GPU with 12 GB of ram and 2880 cuda cores. The training is carried out on the GPU. The NVIDIA CUDA® Deep Neural Network library (cuDNN) is used to accelerate the training process on the cuda cores of the GPU as it allows one to exploit the parallel architecture of the GPU. This helps to drasctically reduce the training time of the DLO by approximately two orders of magnitude. The RMSprop learning algorithm is used for training the network [91]. The learning rate is set to 0.00001. The training data is split into 70% for training and 15 % for cross validation while training and the remaining 15% for testing while training. The training algorithm is stopped when the network's training and validation loss become smaller than a certain number. The

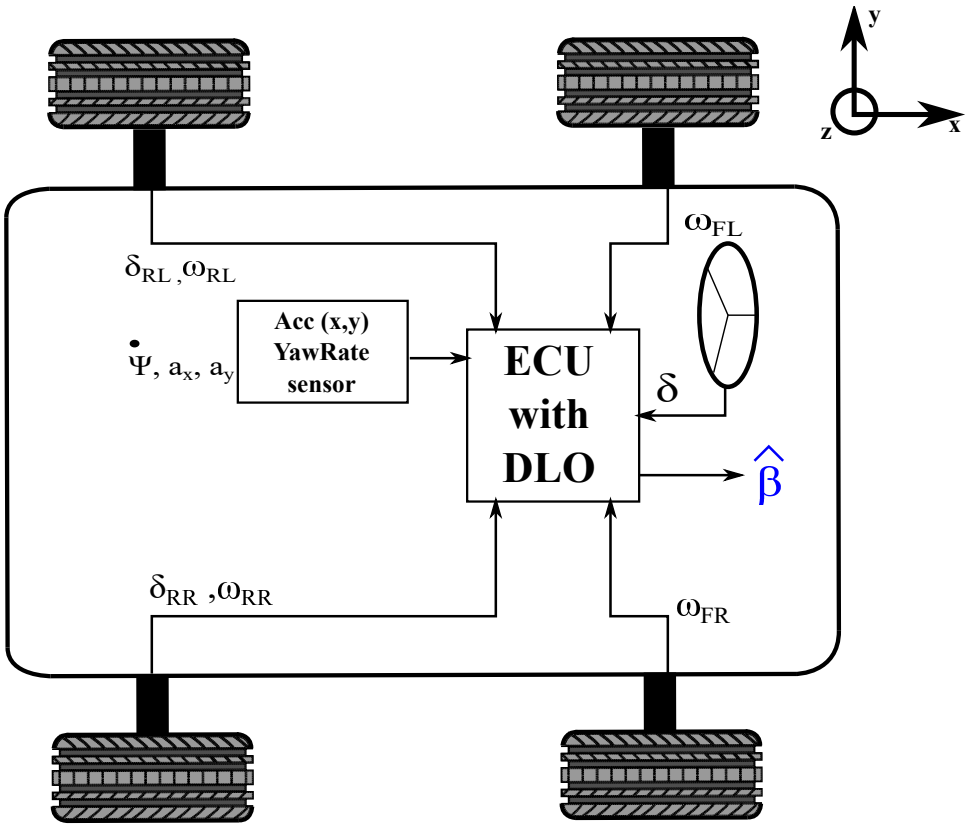

Figure 3.14 DLO usage schematics after the completion of training phase.

choice of this number is critical from the point of having a good network accuracy and at the same time avoiding issues of over fitting. Once the trained network is obtained, the same network can be implemented in an ECU and made to provide the estimate of the sideslip angle using the standard sensor suite of the vehicle.

For the operation configuration of the DLO, its ECU collects the sensor information and provides the estimate of the sideslip angle as shown in Figure 3.14. It is to be noted, that once the training phase in the HPC is over, the tuned hyper parameters are plugged into the neural network architecture to obtain the trained neural network.

3.5 Results

The sideslip angle estimated by the deep learning observer (DLO) is evaluated for a series of manoeuvres. For the purpose of validation, separate data is used from the

training data. The validation is also carried out with data from tests performed on different dates so as to study the effect of the variability of the training conditions and vehicle drivers.

The estimation results for a lap around the handling circuit of Nardo with a 'clean' driving style is presented in Figure 3.15. It can be seen that the sideslip angle mostly remains within the linear working range of the vehicle. The DLO estimates the sideslip angle quite accurately with some errors in the first part of the manoeuvre. It is worth noticing that the observer seems to be quite effective in modelling the sideslip angle dynamics even in the conditions of combined slip as seen at around 482 seconds when the vehicle brakes in to a turn while cornering and then accelerates out of the corner.

The estimation result for a lap around the same circuit but with a different driving style is presented in Figure 3.16. The style is referred to as a 'dirty' driving style, which includes rough acceleration and braking profiles and more oversteer while cornering. The sideslip angles for this manoeuvre go up to 10 degrees at times, indicating that the tires are working in their non-linear domain. It can be noticed that the DLO estimates the sideslip angle quite accurately. It does not show any phase lags. From 2050 to 2080 seconds it shows some error in the magnitude of the sideslip angle.

In Figure 3.17, the sideslip angle estimation is performed by the DLO for a vehicle fitted with used tires. It can be noted that used tires have different cornering stiffness properties than the same tires when they are new. Where a model based method such as an EKF presented in the previous chapter will definitely show offset errors, the DLO is able to estimate the sideslip angle correctly. This demonstrates the robustness of the method.

Figure 3.18 shows the performance of the DLO for a sine sweep manoeuvre at 80 km/h. The accuracy of the DLO is reasonable for the high frequency manoeuvre with slight phase lags at certain instants such as at around 1130 seconds.

Next, the DLO is tested for a handling lap of the NTC which large drifting manoeuvres. It can be seen in Figure 3.19 that the DLO is very accurate in estimating the sideslip angle even when it goes up to 30 degrees. It should be noted that the observer has not been trained on the data from the same day of the aforementioned manoeuvre and yet it is capable of estimating the sideslip angle with minor errors at around 30 seconds in to the manoeuvre. It is interesting to notice that the largest

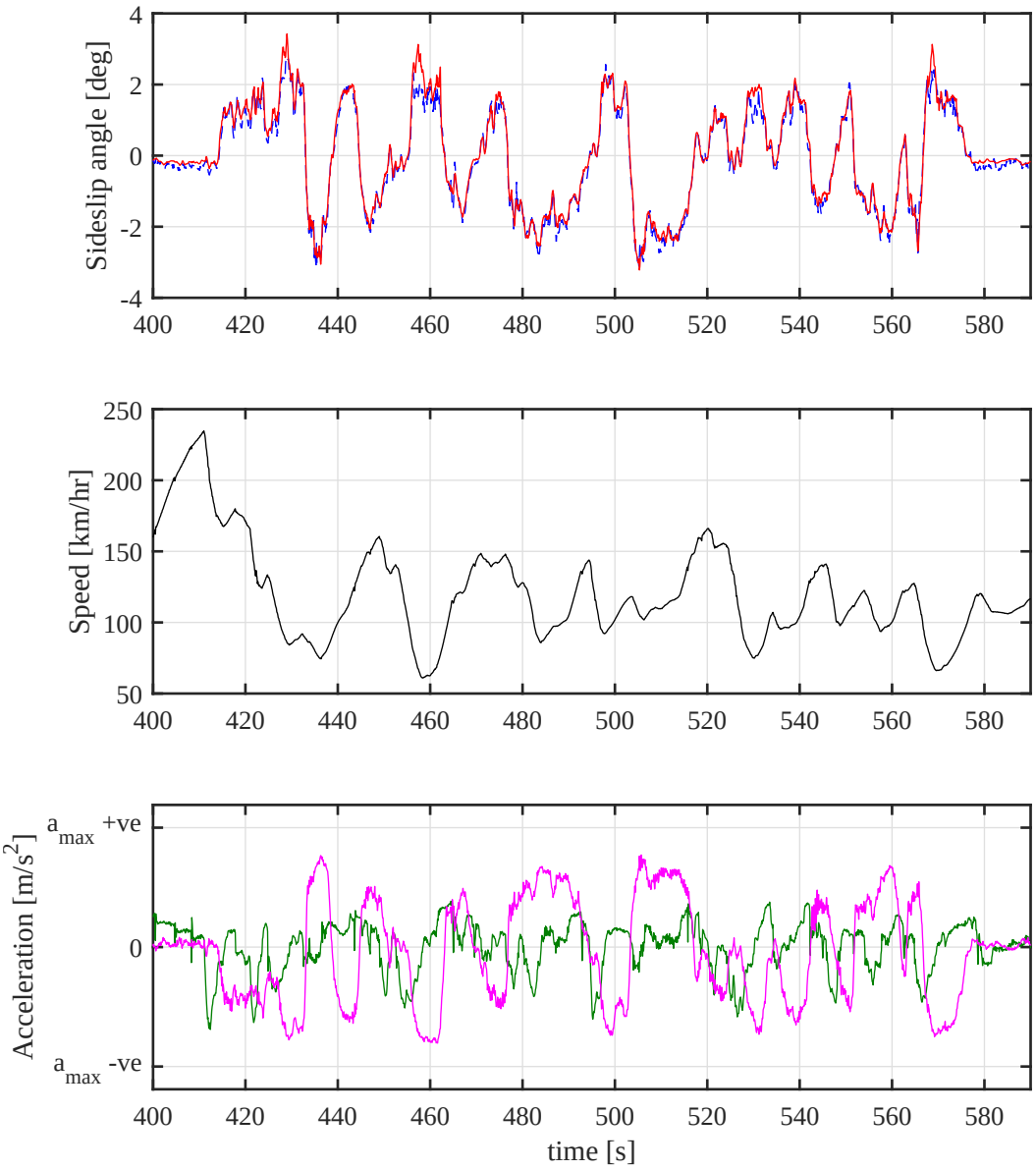

Figure 3.15 Sideslip angle estimation using the DLO for a lap around the handling circuit of Nardo with 'clean' driving style. The blue curve represents the sideslip angle measured with a Kistler optical sensor, the red curve represents the sideslip angle estimated by the observer, the green curve shows the longitudinal accelerometer reading and the magenta curve is the lateral accelerometer reading. a_{max} refers to the maximum possible acceleration of the vehicle permitted by the tire-road adherence.

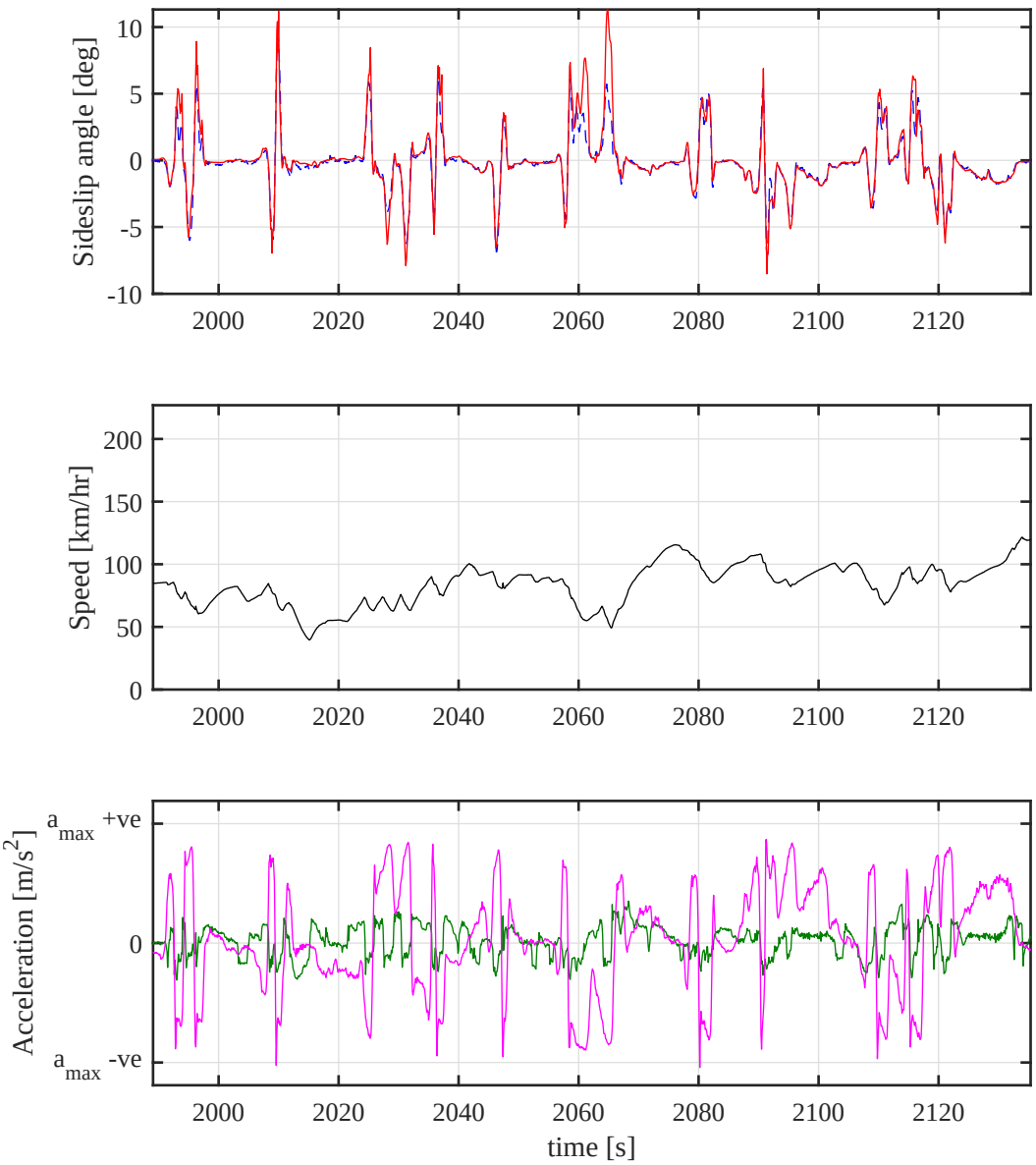

Figure 3.16 Sideslip angle estimation using the DLO for laps around the handling circuit of Nardo with 'dirty' driving style. The blue curve represents the sideslip angle measured with a Kistler optical sensor, the red curve represents the sideslip angle estimated by the observer, the green curve shows the longitudinal accelerometer reading and the magenta curve is the lateral accelerometer reading. a_{max} refers to the maximum possible acceleration of the vehicle permitted by the tire-road adherence.

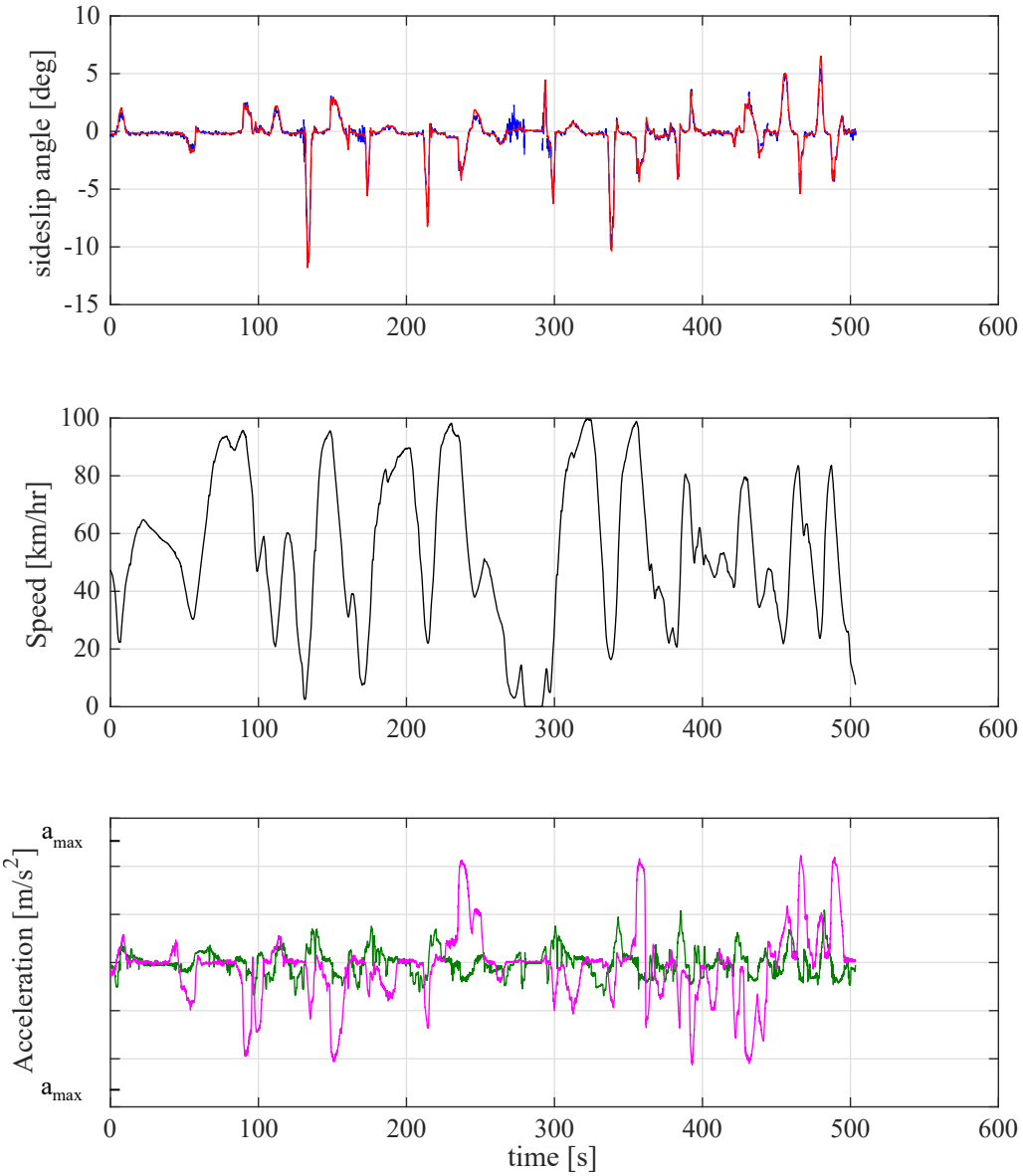

Figure 3.17 Sideslip angle estimation using the DLO for laps around the handling circuit of Nardo with used tires. The blue curve represents the sideslip angle measured with a Kistler optical sensor, the red curve represents the sideslip angle estimated by the observer, the green curve shows the longitudinal accelerometer reading and the magenta curve is the lateral accelerometer reading. a_{max} refers to the maximum possible acceleration of the vehicle permitted by the tire-road adherence.

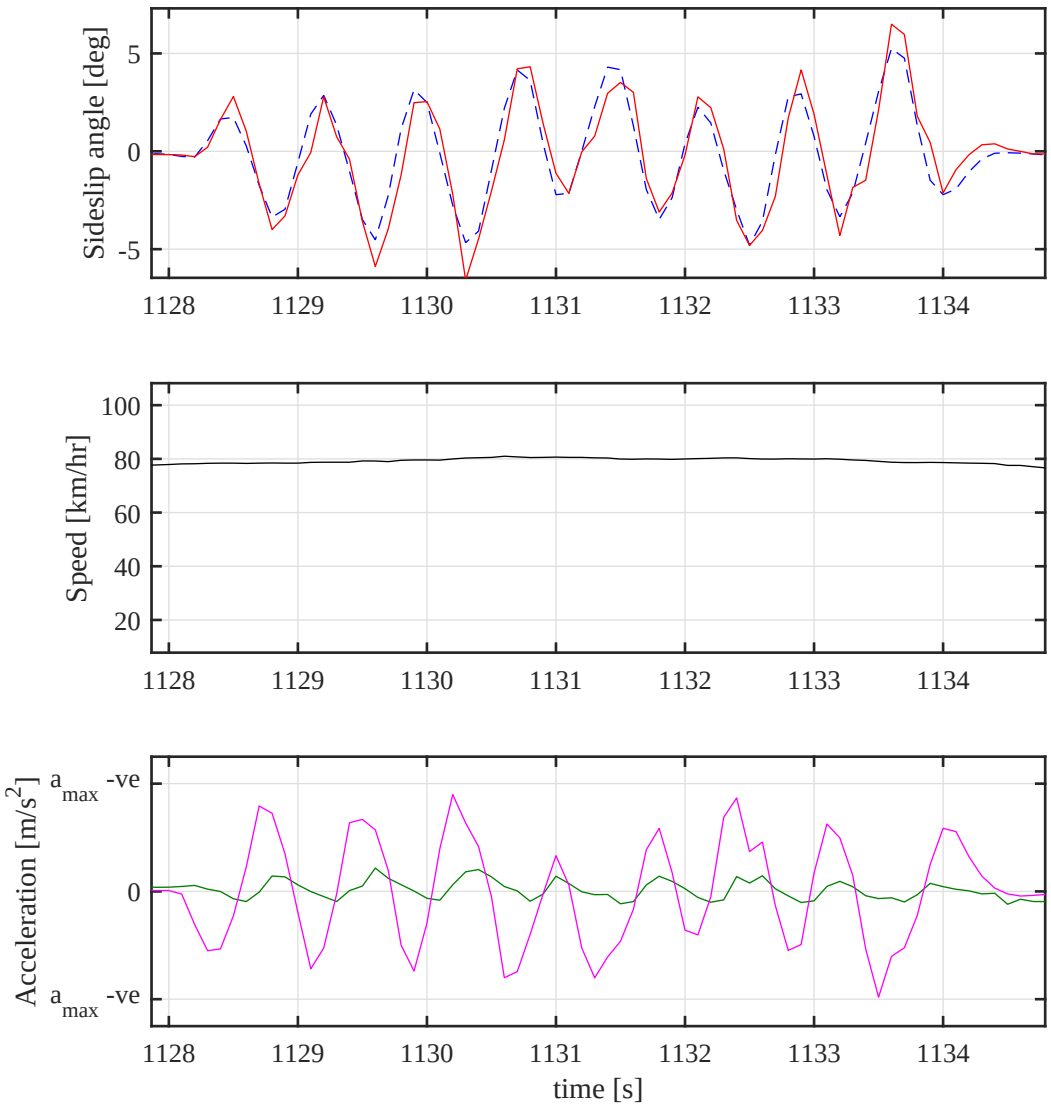

Figure 3.18 Sideslip angle estimation using the DLO for a sine sweep manoeuvre. The blue curve represents the sideslip angle measured with a Kistler optical sensor, the red curve represents the sideslip angle estimated by the observer, the green curve shows the longitudinal accelerometer reading and the magenta curve is the lateral accelerometer reading. a_{max} refers to the maximum possible acceleration of the vehicle permitted by the tire-road adherence.

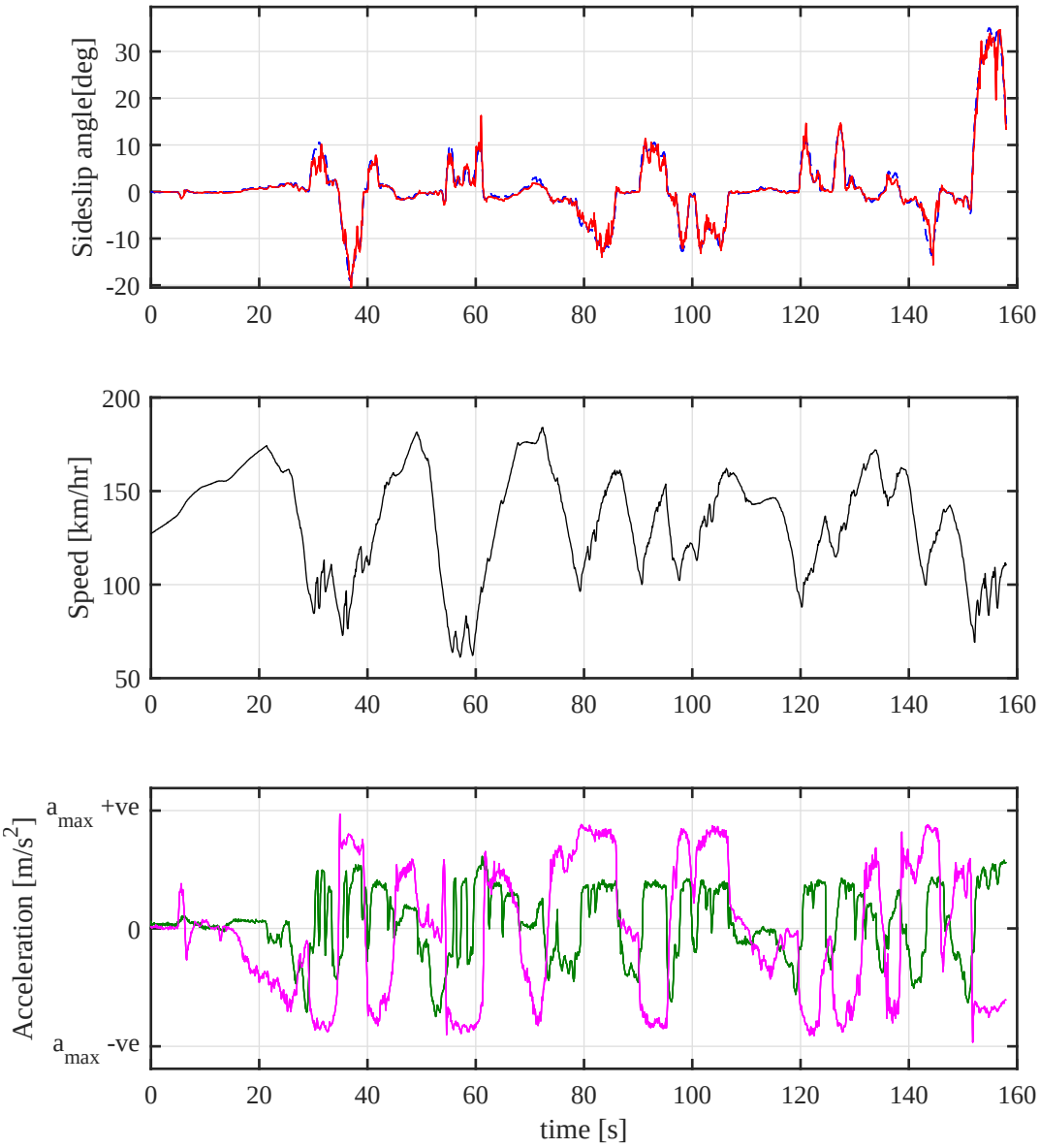

Figure 3.19 Sideslip angle estimation using the DLO while drifting. The blue curve represents the sideslip angle measured with a Kistler optical sensor, the red curve represents the sideslip angle estimated by the observer, the green curve shows the longitudinal accelerometer reading and the magenta curve is the lateral accelerometer reading.a_{max} refers to the maximum possible acceleration of the vehicle permitted by the tire-road adherence.

sideslip angles are obtained while the vehicle enters and exits a turn of the circuit. These turns can be denoted by the local minima of the speed versus time plots. Figure 3.20 shows the performance of the DLO during manoeuvres with hard acceleration and hard braking while cornering. The DLO is quite accurate in estimating

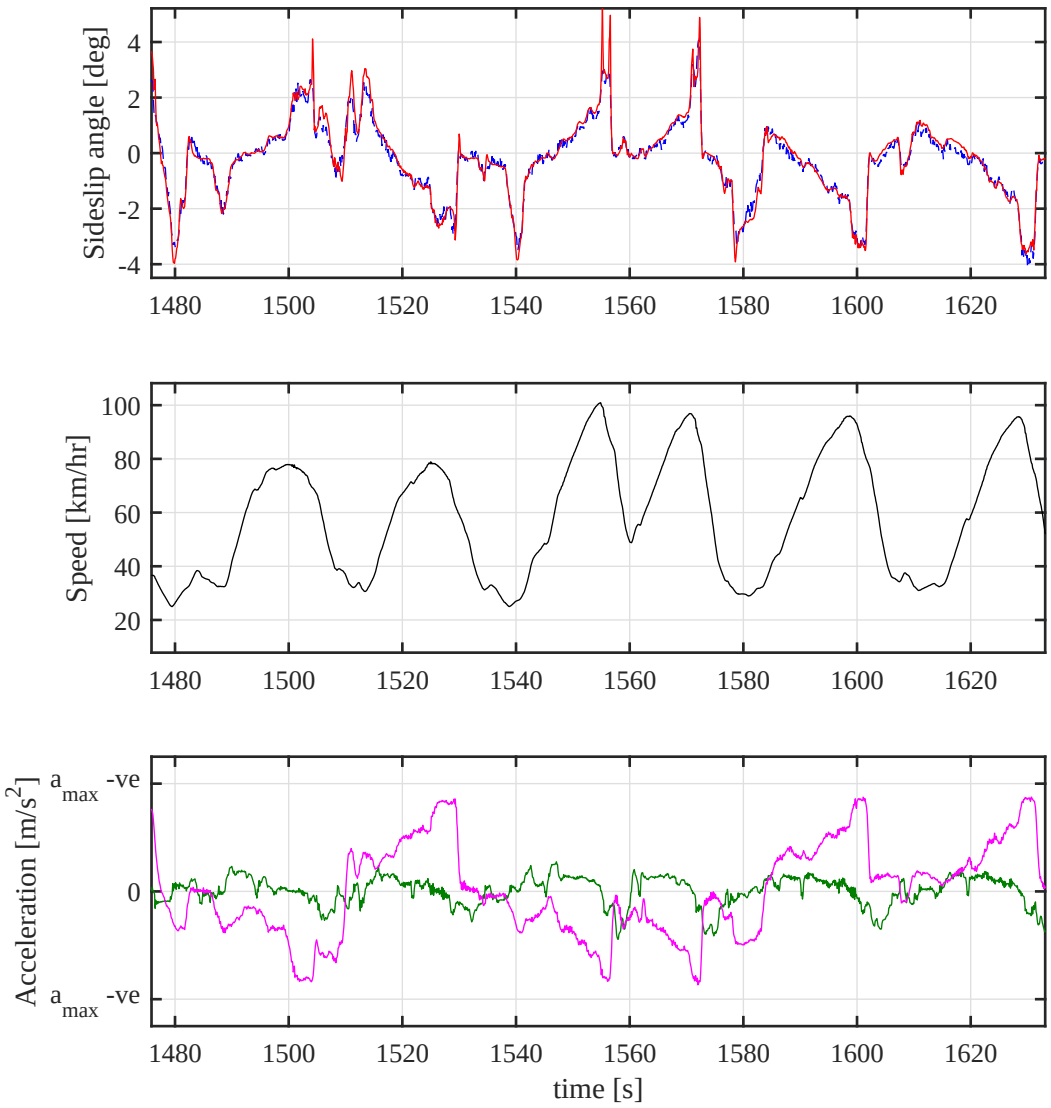

Figure 3.20 Sideslip angle estimation using the DLO for cornering while accelerating and braking. The blue curve represents the sideslip angle measured with a Kistler optical sensor, the red curve represents the sideslip angle estimated by the observer, the green curve shows the longitudinal accelerometer reading and the magenta curve is the lateral accelerometer reading. a_{max} refers to the maximum possible acceleration of the vehicle permitted by the tire-road adherence.

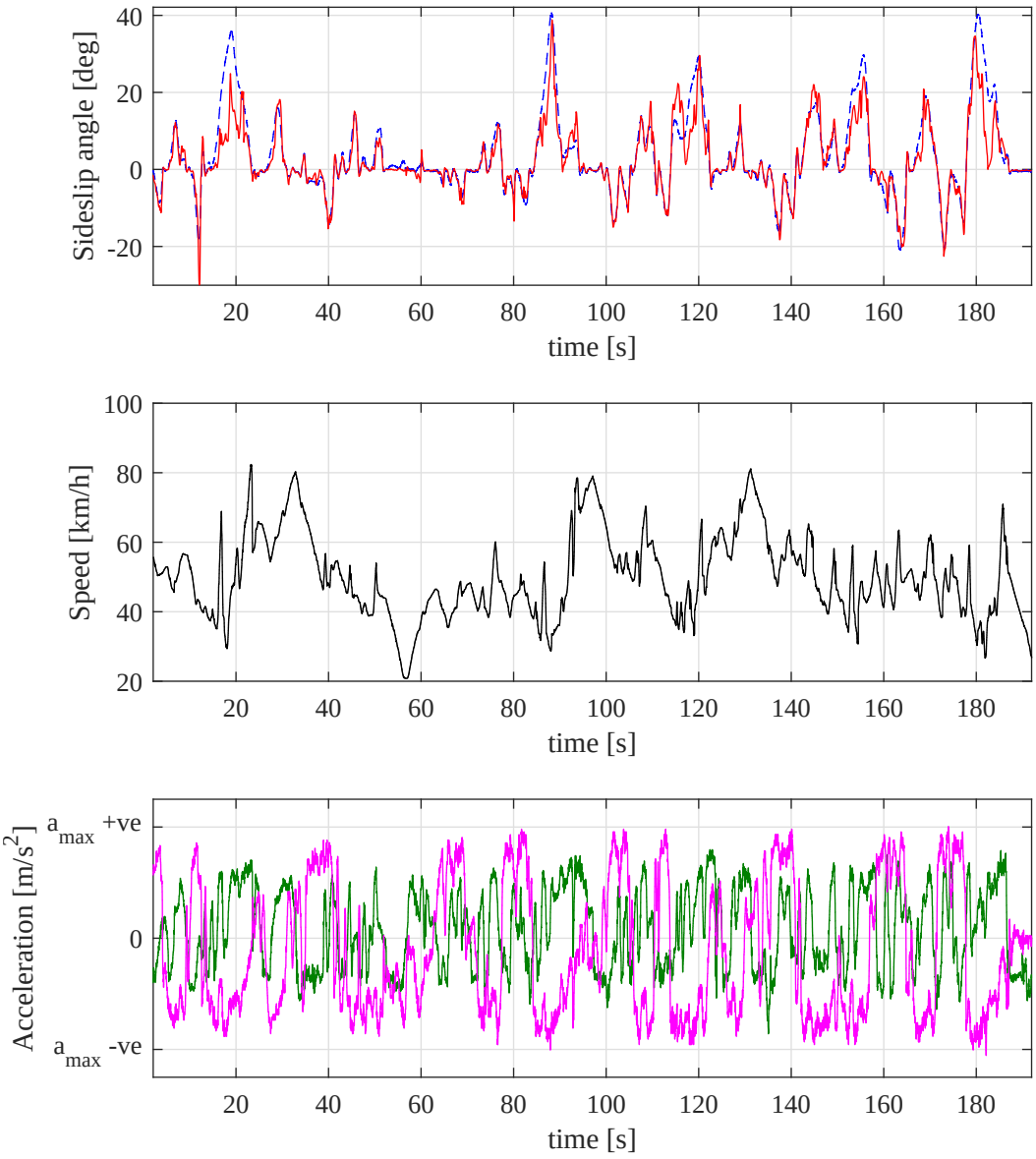

Figure 3.21 Sideslip angle estimation using the DLO for a handling circuit in snow with drifting. The blue curve represents the sideslip angle measured with a Kistler optical sensor, the red curve represents the sideslip angle estimated by the observer, the green curve shows the longitudinal accelerometer reading and the magenta curve is the lateral accelerometer reading. a_{max} refers to the maximum possible acceleration of the vehicle permitted by the tire-road adherence.

the sideslip angle. While model based methods rely on an accurate tire model for combined slip conditions, such tire models are not so accurate in most cases. As a result, EKF fails to achieve an accurate result. The DLO on the other hand is not susceptible to conditions with combined slip.

Figure 3.21 shows the performance of the DLO when tested in low grip conditions on a snowy racetrack with winter tires. The vehicle is programmed with a different set of calibration for the torque vectoring control system with respect to the calibration used for generating the training dataset. In addition, the vehicle is being driven by a different driver with respect to the set of drivers utilised for the training dataset generation. It can be noticed that the DLO performs quite well with occasional errors in the estimated sideslip angle at around 20 seconds. This plot demonstrates that the DLO is quite robust to a varying set of external factors that may include a slightly different control system calibration, different driving styles and so on.

3.6 Conclusions

The biggest strength of the DLO is that it is a model-less method, as it does not require a vehicle model. Doing so, the errors due to inaccurate vehicle modelling can be avoided. The method instead depends on learning patterns and sequences from training data and the method to a certain extent does become sensitive to the training data. As a result, the choice of training data becomes fundamental in order to achieve a good design from an engineering point of view. Although the DLO is a very potent tool for the estimation of the sideslip angle, it also suffers from some technical limitations. If any changes are made to the vehicle that alter its behaviour, and this change has not been taken into account in the training data, it could lead to minor estimation errors. Although this is not a fundamental flaw of the method itself, it might pose challenges to R&D engineers for using this tool during the development of a vehicle. A hybrid observer structure could be utilised to overcome this issue where traditional model based methods work in conjunction with the DLO. Any changes in the vehicle can be accounted easily by the model based methods and this could in turn be used to correct the output of the DLO. Another issue that is faced by this method is the long amount of computation time it requires to train a DLO for the whole training data set. To reduce the training times, an optimisation should be

performed on the training data set to eliminate any data that does not introduce any new learning pattern or sequence to the DLO.

Weighing in the advantages and the limitations of the DLO, it can be concluded that the advantages still heavily outweigh the limitations. The DLO shows robust performance both in pure lateral slip conditions as well as combined slip conditions. Moreover, it is able to adapt and correct itself to tire invariabilities such as tire temperature, tire consumption and wear, even to the extent when the tire is about to be shredded while drifting.

Chapter 4

Vehicle Mass Estimation

4.1 Introduction

Along with the vehicle sideslip angle, another crucial yet unmeasurable parameter is the vehicle mass. For model based control, vehicle models have a high sensitivity to vehicle mass. Thus, it is very important to have knowledge of the vehicle mass, which can vary during the course of the operation of the vehicle due to change in fuel level in the fuel tank or change in the number of passengers. The algorithm presented in this chapter utilises the principle of Newton's second law of motion to calculate the mass, given knowledge of the force and the acceleration acting upon the body. The longitudinal vehicle motion is chosen for the mass estimation algorithm as it is possible to compute the vehicle longitudinal forces and the longitudinal acceleration with relative ease given the current state of the vehicle sensor cluster.

4.2 Driving Resistances of a Vehicle

The forces acting on a vehicle during longitudinal motion are the driving resistances due to air drag, the tire rolling resistance, the inertial forces and the gravitational forces due to the presence of road grade [92] as seen in Figure 4.1. The equation of motion in the longitudinal direction can be written as follows:

$$ma_x = F_{traction} - F_{brake} - F_{aerodrag} - F_{rollingresist} - F_{roadgrade}. \tag{4.1}$$

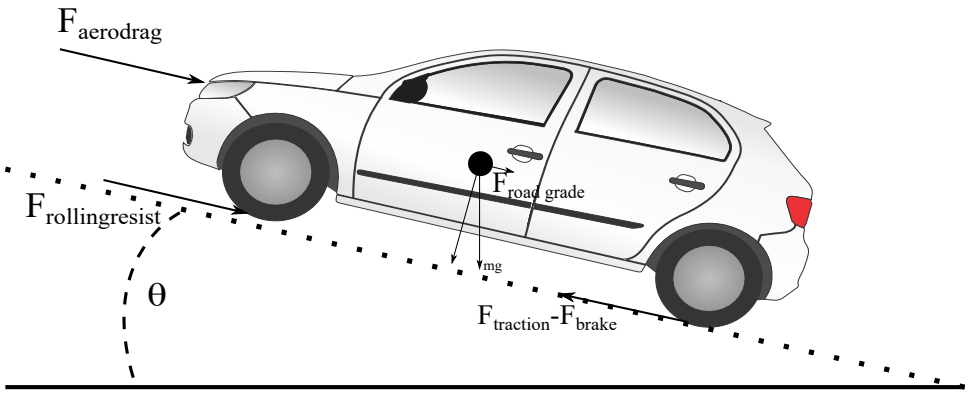

Figure 4.1 Various longitudinal forces acting on the vehicle.

The traction force $F_{traction}$ depends on the engine torque and the transmission dynamics. The engine torque information is available on the CAN-BUS as an estimated parameter by the engine ECU. The braking force F_{brake} is a function of the brake pressure and unless the wheels are locked, this force is linear with the brake pressure.

The aerodynamic drag force acting on the vehicle, $F_{aerodrag}$ is a function of the square of the longitudinal vehicle speed, u, the vehicle effective frontal surface area S_x, the aerodynamic drag coefficient C_x and the air density ρ.

$$F_{aerodrag} = \frac{1}{2}\rho S_x C_x u^2. \tag{4.2}$$

The rolling resistance force is modelled as the product of the normal load of the vehicle and a rolling resistance coefficient.

$$F_{rollingresist} = mgC_r cos(\theta). \tag{4.3}$$

The resistance force due to road grade is a component of the gravitational force acting on the vehicle, with θ being the road grade angle.

$$F_{roadgrade} = mgsin(\theta). \tag{4.4}$$

Looking at the individual equations of the forces, it is clear that the various forces are functions of constant parameters and time varying parameters. Looking at the time varying parameters, they are namely the vehicle speed, the road grade angle and the tractive torque. It is interesting to note that out of the above three parameters, the road grade and the vehicle velocity do not change with a high frequency

components. This is due to a simple reason that the vehicle velocity cannot change at a very high frequency as the vehicle mass introduces a large inertia in the longitudinal dynamics. The same is valid for the road grade which is often constant or changes very gradually. To objectively study this effect, a power spectral density (PSD) of the various longitudinal forces acting on the vehicle is studied by simulating one lap of the test track at Griesheim, Germany. The PSD is presented for a variety of manoeuvres including acceleration, braking, cornering and coasting in Figure 4.2. It can be observed that after a certain frequency, the majority of the con-

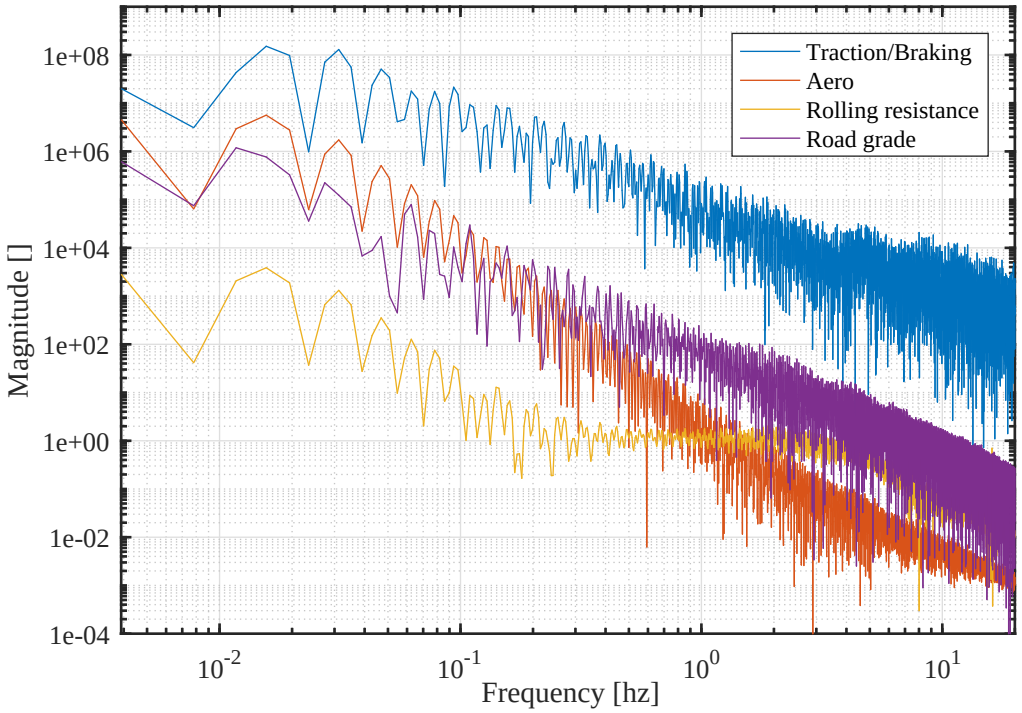

Figure 4.2 Power Spectral Density of the various longitudinal forces acting on the vehicle. Above around 5 Hz, the majority of the contribution is due to traction and braking forces.

tribution to the longitudinal dynamics is only due to inertial forces of traction and braking [32]. As a result, for high frequency excitations in the region of 0.5 Hz to 5 Hz, the effect of the aero dynamic drag, road grade and rolling resistance can be neglected owing to their negligible contribution. This is because aerodynamic drag changes as a function of the longitudinal velocity, the rolling resistance as a function of road grade angle and normal load and the road grade resistance as a function of road grade angle. As mentioned before, under normal driving conditions, it is evident that these three parameters/states do not change with a very high frequency. As a result, if the vehicle longitudinal acceleration is filtered with a band-pass filter,

the longitudinal acceleration captured would be the one only due to wheel traction and braking forces. Thus, it can be said that in the band-pass frequency range of the acquired signals, the force balance can be written as

$$ma_x \approx F_{traction} - F_{brake}. \tag{4.5}$$

This relation can used to compute the vehicle mass, given the knowledge of the traction and the braking forces.

4.3 Estimation Algorithm

An accurate estimate of the a_x and the traction and braking forces can be used to estimate the mass of the vehicle using a recursive least squares estimation. Longitudinal acceleration, a_x is measured in all vehicles by the onboard ESP sensor cluster. Regarding the estimation of the longitudinal forces as presented by Fathy et al. in [32], the engine torque information was utilised by the estimation algorithm to estimate the torque at wheel. This created issues as the transmission dynamics remained unmodelled, which led to a slow convergence of the estimation algorithm when complex transmissions such as the dual-clutch transmission were used.

For computing the traction and braking forces, wheel torque estimate from a torque observer and brake pressure signal are used. The mass estimation uses information available on the vehicle CAN-BUS to estimate the mass of the vehicle in real time. The required information includes the raw longitudinal accelerometer reading and information about the vehicle powertrain as mentioned in the section on the torque observer. As the theory of the mass estimation is based on events having only longitudinal motion, a longitudinal motion detector is required, that switches on the mass estimation algorithm when it detects conditions with only longitudinal motion. The estimated wheel torque and the measured longitudinal acceleration are then filtered using band pass filters, which filter out the low frequency components of the signals coming from the aerodynamic drag, rolling resistance and road grade resistance and very high frequency components coming from noise. The filtered signals are input to a recursive least squares filter which gives out the estimate of the vehicle mass. The algorithm can be visualized in the Figure 4.3.

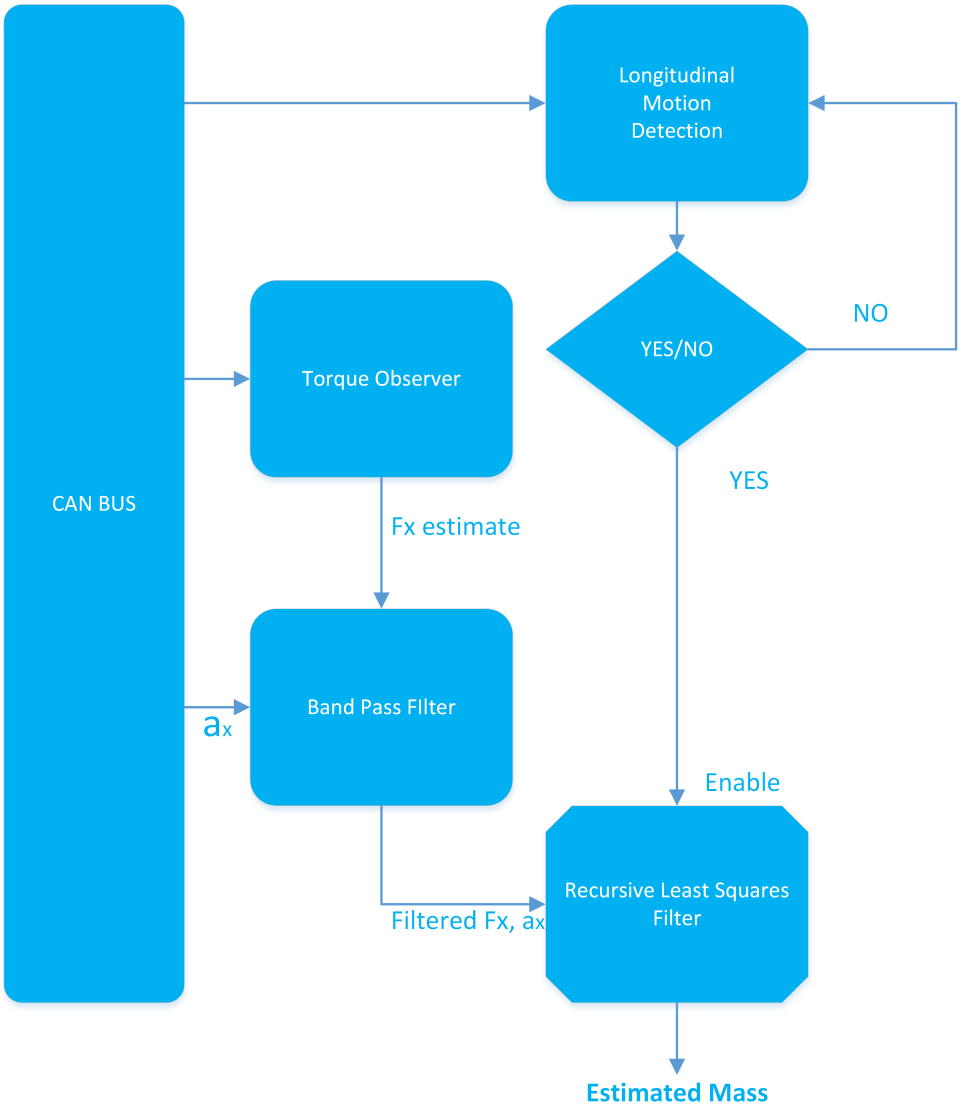

Figure 4.3 Overview of the mass estimation algorithm.

4.3.1 Longitudinal Motion Detector

The main task of the longitudinal motion detector is to activate the mass estimation algorithm in conditions when a pure longitudinal motion is being made by the vehicle. The motion detection is based on heuristics. For the detection of pure longitudinal motion, certain detection conditions are implemented. The conditions are as follows:

- The ESP lateral accelerometer reading should be less than 0.5 m/s^2.

- The ESP longitudinal accelerometer reading should be larger than 0.3 m/s^2.
- The wheel slips should be less than 0.05 in order to avoid conditions when the tractive wheels of the vehicle are spinning. This is because under such conditions, some of the wheel longitudinal force gets used up in accelerating the wheel rotation. As a result, this might introduce errors in the mass estimation algorithm. The detection is done from the ABS/ESP system flags, which indicates the high slip levels of the individual wheels.
- The speed of the vehicle should be more than 15 km/h. This is used to refine the quality of the result as it is noted that the estimation works well when the speed is not very close to 0 km/h.

All the above conditions are implemented as fuzzy maps which vary from 0 to 1 in a certain range. The final detection of the longitudinal motion is obtained by multiplying the outputs of all the individual conditions detection. The product is then assumed to be zero for any value lower than 1. Thus, the output of the longitudinal motion detection block is either 0 or 1, where 1 represents the occurrence of a pure longitudinal motion. This signal is thus used as the enable switch for the RLS estimator block. The estimation takes place only when it receives a 1 as the enable signal. This way the algorithm does not perform the RLS estimation when Equation 4.5 is not valid.

4.3.2 Torque Observer

The torque observer is based on a Kalman Filter, which exclusively involves signals already available on the vehicle CAN-BUS. The torque observer is derived from Foulard in [93, 94] and it is directly used for the estimation of the torque signal. As the goal of the current work is to evaluate the effect of the use of a torque observer in order to estimate the vehicle mass, the torque observer development is not a part of the work done in this thesis. It is however presented in this chapter to provide a concise idea about the functioning of the torque observer.

The observer design relies on the simplified powertrain model depicted in Figure 4.4, which aims at representing the first drivetrain eigenfrequency as well as start-up sequences and gear shifts through the modelling of the clutch dynamics with regard to stick/slip effects. In the proposed figure, J_e, J_{out} and J_v are the mass of inertia of

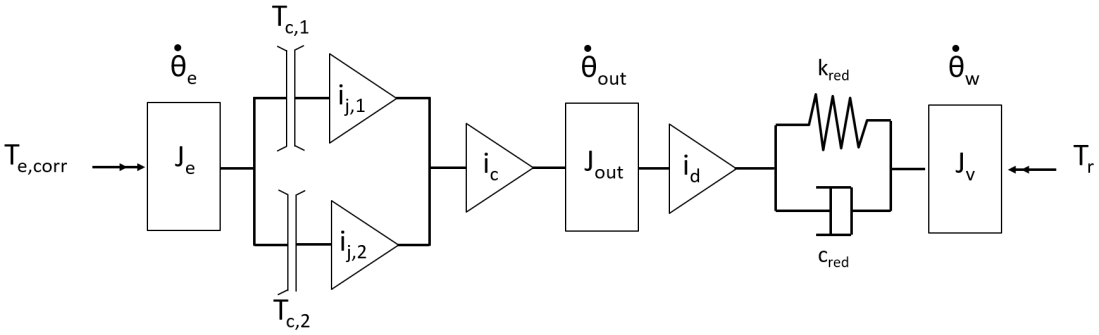

Figure 4.4 Simplified drivetrain model adopted for the observer design.

the engine, of the gearbox reduced on the transmission output and of the rest of the vehicle reduced on the wheels respectively. The engine speed, the transmission output speed and the average wheel speed are represented by θ_e, θ_{out} and θ_w while k_{red} and c_{red} are the reduced drivetrain stiffness and damping ratio. $T_{e,corr}$ is a corrected engine torque taking the drivetrain losses into consideration:

$$T_{e,corr} = \eta T_e \tag{4.6}$$

where T_e is the engine torque information available on the vehicle CAN-BUS and η is the drivetrain efficiency, which is calculated as a function of engine speed, engine torque and current engaged gear [94]. $T_{c,1/2}$ is the clutch torque of half-transmission 1 and 2 respectively and T_r represents the driving resistances. Finally, $i_{j,1/2}$ is the transmission ratio of half-transmission 1 and 2 respectively, i_c the constant transmission ratio and i_d the differential ratio. From these considerations, the transmission dynamics can be represented with the following set of equations as,

$$J_e \ddot{\theta}_e = T_{e,corr} - T_{c,1} - T_{c,2}, \tag{4.7}$$

$$J_{out} \ddot{\theta}_{out} = i_c (i_{j,1} T_{c,1} + i_{j,2} T_{c,2}) - k_{red} \frac{\triangle \theta_{red}}{i_d}, \tag{4.8}$$

$$J_v \ddot{\theta}_w = k_{red} \triangle \theta + c_{red} \triangle \dot{\theta}_{red} - T_r, \tag{4.9}$$

$$\triangle \theta_{red} = \frac{\dot{\theta}_{out}}{i_d} - \dot{\theta}_w. \tag{4.10}$$

T_r is considered as a process noise with high dynamics, so that no exact modelling of the driving resistances is achieved [93]. In this framework, the observer design

relies on a discrete linear stochastic system:

$$x_{k+1} = A_d x_k + B_d u_k + w_k, \tag{4.11}$$

$$y_k = C_d x_k + v_k, \tag{4.12}$$

where k is a subscript representing the actual sampling. x_k is the state vector, y_k the measurement vector and u_k the input vector. w_k is the discrete process noise vector and v_k the discrete measurement noise. A_d is the discrete system matrix in the absence of process noise, which can be easily deduced by discretising the previously proposed system equations. B_d and C_d are respectively the discrete input matrix and the discrete output matrix. Thus, the Kalman filter is formulated using the following states denoted by $x(k)$, the following measurements $y(k)$ and the following inputs $u(k)$.

$$x_k = [\theta_{e,k}\theta_{out,k}\theta_{w,k} \bigtriangleup \theta_{red,k}T_{c,1,k}T_{c,2,k}T_{r,k}]^T, \tag{4.13}$$

$$y_k = [\theta_{e,k}\theta_{out,k}\theta_{w,k}T_{c,1,k}T_{c,2,k}]^T, \tag{4.14}$$

$$u_k = T_{e,corr,k}. \tag{4.15}$$

The engine torque correction is done outside of the observer, so that the corrected engine torque is the observer input. All the signals contained in the measurement vector are available on the vehicle CAN-BUS. Concerning the clutch torques, the information is estimated by a model on the Transmission Control Unit through the consideration of the clutch pressures or engine torque according to the actual clutch state. Figure 4.5 shows a representative torque observer result. In this figure, a comparison is done between measurement and torque observer. In order to also show the advantage of the torque observer in contrast to a simple calculation of the driving torque based on the CAN-BUS engine torque information, the product of engine torque by the total drivetrain ratio is depicted too. It can be noticed that the drivetrain dynamics is well reconstructed by the observer, especially with regard to the jerking frequencies. Moreover, the absolute torque level is better estimated with the torque observer than through the simple multiplication of the engine torque information by the total drivetrain ratio. This can be particularly noticed in case of negative torque between 0 and 2 s as well as during the acceleration phase between 3 and 7 s. The better estimation of the absolute driving torque level is explained by two aspects. First, the modelling of the drivetrain efficiency enables the consider-

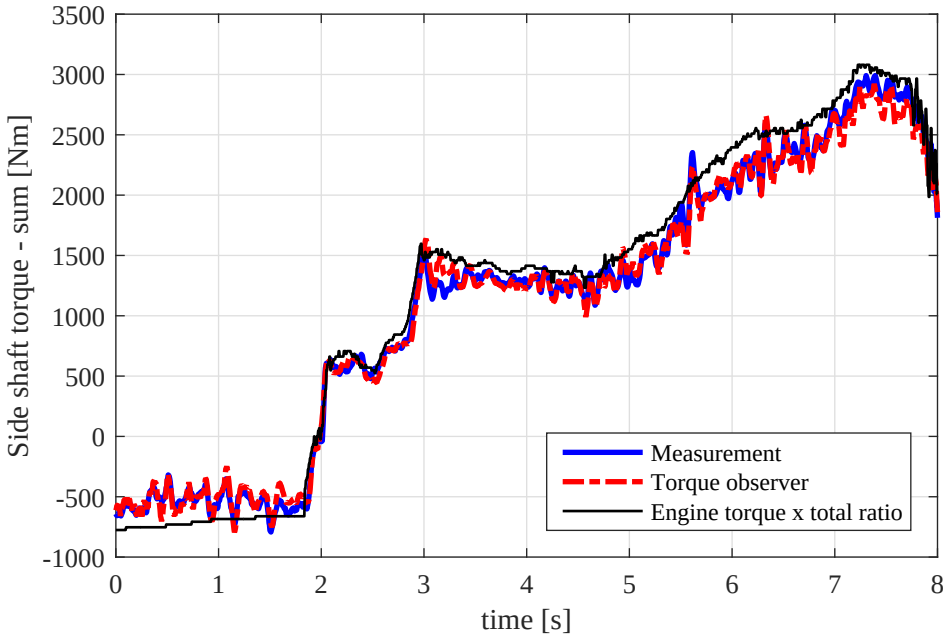

Figure 4.5 Comparison between torque measurement (blue), torque observer (red) and CAN-BUS engine torque multiplied by total drivetrain ratio (black).

ation of the torque losses, which can reach in some situations to almost 20 % [94]. Secondly, during transient phases (i.e. during acceleration or deceleration phases), a non-negligible part of the drivetrain torque serves to accelerate or decelerate the drivetrain's rotating parts. In other words, this means that a part of the torque is absorbed by the inertial masses and does not contribute to the effective wheel driving torque. This is of special relevance for vehicles with big engines, like the one investigated here (BMW M3 E92).

In the end, an accurate CAN-BUS based torque information is delivered to the mass estimation algorithm and better estimation results can be expected. The wheel longitudinal force can be computed from the estimated drivetrain torque and the brake pressure, P_{brake} from the CAN-BUS as follows:

$$F_{x,wheel} = \frac{T_r}{r_w} - P_{brake} K_{brake}, \tag{4.16}$$

where K_{brake} is a constant that is a product of the brake piston surface area on which the brake fluid acts with pressure and the friction coefficient between the brake pads and the brake disk.

4.3.3 Recursive Least Squares Estimator

A recursive least square algorithm with a forgetting factor is used to estimate the vehicle mass [95]. Recursive least squares filter is used to fit a linear model to a data such that the model's parameters are computed in order to reduce the sum of the squares of the error between the measured output and the output of the identified model computed with the measured input. In our case, the measured input is the filtered longitudinal accelerometer reading whereas the measured output is the estimated longitudinal force on the wheels calculated from the torque observer and the brake pressure signals. At the n^{th} sample, starting from the filtered longitudinal accelerometer sensor reading the $a_{f,x}$ and the filtered torque estimator output which gives an estimate of the filtered wheel longitudinal force $F_{f,x,wheel}$, Equation 4.5 can be written as a linear equation with one unknown

$$F_{f,x,wheel}(n) = m(n)a_{f,x}(n) + e(n), \tag{4.17}$$

where $e(n)$ is the measurement error and noise. Then a RLS estimator for the above linear system can be written as,

At each time instant the estimated vehicle mass, $\hat{m}(t)$ is updated as,

$$\hat{m}(n) = \hat{m}(n-1) + K_{rls}(n)(F_{f,x,wheel}(n) - \hat{F}_{f,x,wheel}(n)). \tag{4.18}$$

The estimated longitudinal wheel force, $\hat{F}_{f,x,wheel}$ is computed from the filtered longitudinal accelerometer signals and the mass estimated at the previous time step as

$$\hat{F}_{f,x,wheel}(n) = \hat{m}(n-1)a_{f,x}(n). \tag{4.19}$$

The RLS correction gain factor $K_{rls}(n)$ is obtained as

$$K_{rls}(n) = a_{f,x}(n)\frac{P_{rls}(n-1)}{(\lambda + a^2_{f,x}(n)P_{rls}(n-1)}, \tag{4.20}$$

where $P_{rls}(n)$ is obtained as

$$P_{rls}(n) = \frac{1}{\lambda}(P_{rls}(n-1) - \frac{a^2_{f_x}(n)P^2_{rls}(n-1)}{(\lambda + a^2_{f_x}(n)P_{rls}(n-1)}), \tag{4.21}$$

where λ is the forgetting factor.

4.4 Results and Discussion

To test the quality of the estimation algorithm, it is tested for a variety of manoeuvres including longitudinal acceleration, braking, coasting, constant radius circle on skidpad, lane change and slalom manoeuvres. The algorithm is first tested in simulation to test the validity of the method. Using simulation, the vehicle parameters are changed and a sensitivity analysis is presented based on the various parameters which may vary to show the robustness of the method. The experimental results are then presented. For all the tests, the forgetting factor in the RLS filter is set to 0.995.

4.4.1 Simulation Results

Simulations of the vehicle are carried out in a VI-CarRealTime–Simulink co-simulation environment. The choice is motivated by the fact that this CAE tool replicates the behaviour of the vehicle very accurately over a reasonable frequency band. Moreover, it is also used widely in the automotive industry by OEMs to have accurate simulation of the vehicle without the need to go on a track. The chassis is modelled considering both sprung and unsprung masses. The suspension characteristics include non-linear models of the springs, dampers and anti-roll bars. Effects of roll steer, roll camber, toe angle variation and camber angle variation are taken into account with the help of suspension and steering geometry modelling. Combined slip effects of the tires are modelled with the help of Pacejka's formula, which also takes effects due to the tire relaxation length into account. The powertrain dynamics is modelled, including the engine inertia. Modelling of the clutch and gear shifts is also included.

The results of the estimation algorithm are presented in Figure 4.6. The algorithm is tested for two different working conditions in terms of vehicle mass. The first case (blue curves) is the case when only the driver is driving the vehicle and the mass of the vehicle is imposed at 1938 kg in the simulation model. The second case is the vehicle with full load and its weight is imposed at 2250 kg. The estimation algorithm is initialized at 2000 kg. In the first case the mass estimation is very accurate while in the second case the algorithm is able to estimate the vehicle mass with

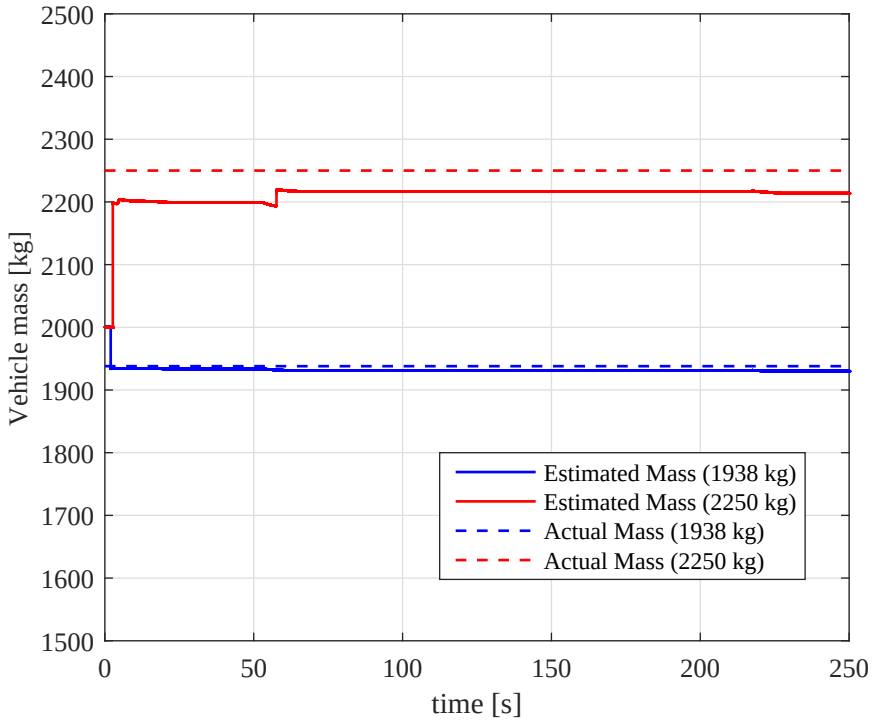

Figure 4.6 Estimation of vehicle mass with one driver (blue) and with one driver and three passengers (red).

an error of 2%. This demonstrates that the algorithm is quite accurate. Moreover, the algorithm converges to the accurate mass value within the first few seconds of the manoeuvres.

Robustness Analysis

The sensitivity of various parameters such as the rolling resistance and aerodynamic drag coefficient is studied on the accuracy of the estimation algorithm. This is carried out by simulating the same tests done in the section above and varying the parameters in the simulation model. Since in real life, it is very difficult to objectively change the parameters such as rolling resistance and aerodynamic resistance of the same vehicle without drastically changing the test vehicle itself, simulation is chosen to perform this analysis. The sensitivity of the estimation algorithm with respect to variation in the rolling resistance of the tires is presented in Figure 4.7, while the sensitivity with respect to the aerodynamic drag coefficient is presented in Figure 4.8. It can be noted that the algorithm presents the almost the same amount

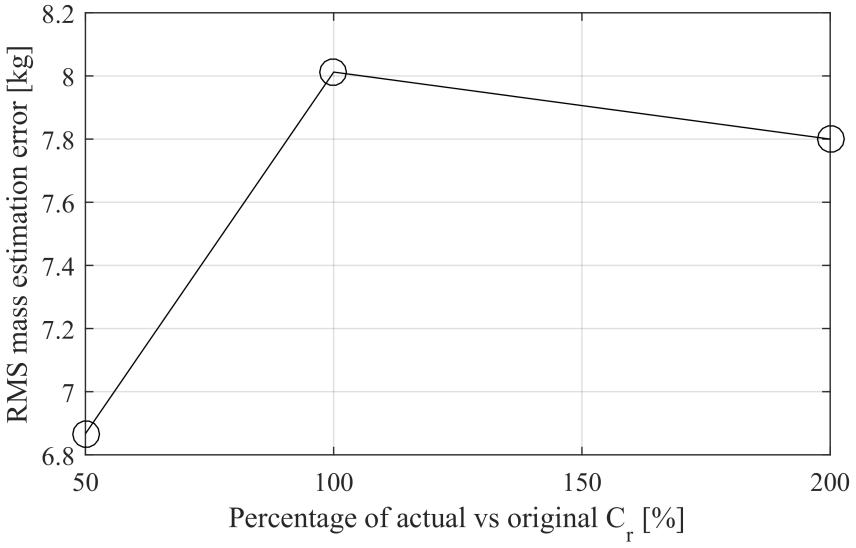

Figure 4.7 Sensitivity of wheel rolling resistance to the results of the mass estimation algorithm. The test vehicle's mass is 1938 kg.

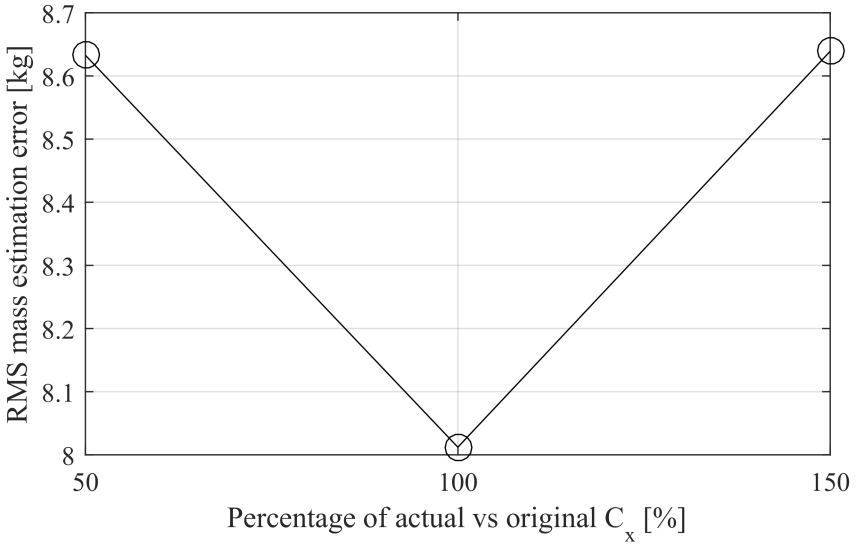

Figure 4.8 Sensitivity of aerodynamics longitudinal drag coefficient to the results of the mass estimation algorithm. The test vehicle's mass is 1938 kg.

of error for different values of both parameters. This indicates that the algorithm is not sensitive to parameters influencing rolling resistance and aerodynamic drag. This can be understood from the fact that the estimation algorithm filters out the

Figure 4.9 Aerial view of the test track Griesheim. The manoeuvre paths are shown in magenta(Source: maps.google.de).

contribution due to these effects and thus is unaffected by any deviations in such parameters.

4.4.2 Experimental Results

The validation of the mass estimation algorithm is further tested experimentally by carrying out tests at the TU Darmstadt's vehicle test track at Griesheim. Acceleration, braking, coasting, slalom and lane change manoeuvres are performed on the long straight sections while constant radius circle manoeuvres are done on the skidpad. The long straight has a road grade angle of around 1 degree. The tests are carried out on an instrumented prototype BMW M3 E92. The CAN-BUS data is logged using an ETAS ES1000 and INCA software. Additional altitude and position signals are also measured by a code based GPS sensor and an active antenna and they are also published on the CAN-BUS. As the vehicle has a dual clutch transmission, the engine torque is no longer able to correctly represent the longitudinal dynamics at high frequencies. Thus, the method with and without the torque observers are compared in the results to demonstrate the efficacy of the presented estimation method.

The mass estimation results for a test with a single driver and an additional passenger and near empty tank is shown in Figure 4.11. It can be seen that the vehicle starts moving from rest at around 130 seconds. The estimation algorithm's mass es-

Figure 4.10 Test vehicle (BMW M3 E92) for the validation of the mass estimation algorithm.

timate is initialized at 5000 kg. It can be seen that as soon as the algorithm gets the first excitation at around 155 seconds, it starts to converge to the actual mass of the vehicle's value. All throughout the test, the estimate hovers around the actual value with an error of less than 5%. The algorithm presented in [32] is also compared to demonstrate the contribution of the work done in this thesis. It can be seen that although the algorithm based on the CAN engine torque signal tends to converge to the actual mass value, the convergence is very slow, and until the convergence, the errors presented are too large. This is attributed to the fact that the algorithm presented in Fathy et al. does not take the transmission dynamics into consideration. As a dual clutch transmission introduces its own dynamic behaviour, this causes large discrepancies. The test is again repeated with four people on board and a full tank of fuel to verify the algorithm in the maximum loaded use case scenario. It can be seen in Figure 4.12 that the presented algorithm converges again to the actual vehicle mass whereas the compared algorithm has a very slow convergence rate and is unable to satisfactorily converge to the actual vehicle mass even after 350 seconds. Figure 4.13 shows the output of the torque observer. It can be seen that the filtered longitudinal force obtained from the torque observer matches has an average value very close to the force obtained by multiplying the filtered measured longitudinal acceleration by the known vehicle mass. This acts an indication to test the accuracy of the torque observer. Although, it is evident that the two signals do not overlap at all times, it is perhaps interesting to notice that the average values of the two signals are equal most of the time. This is desirable as this permits the RLS algorithm with a forgetting factor tuned to be non-impulsive (less than 1) to estimate the vehicle mass as a slowly time-varying signal.

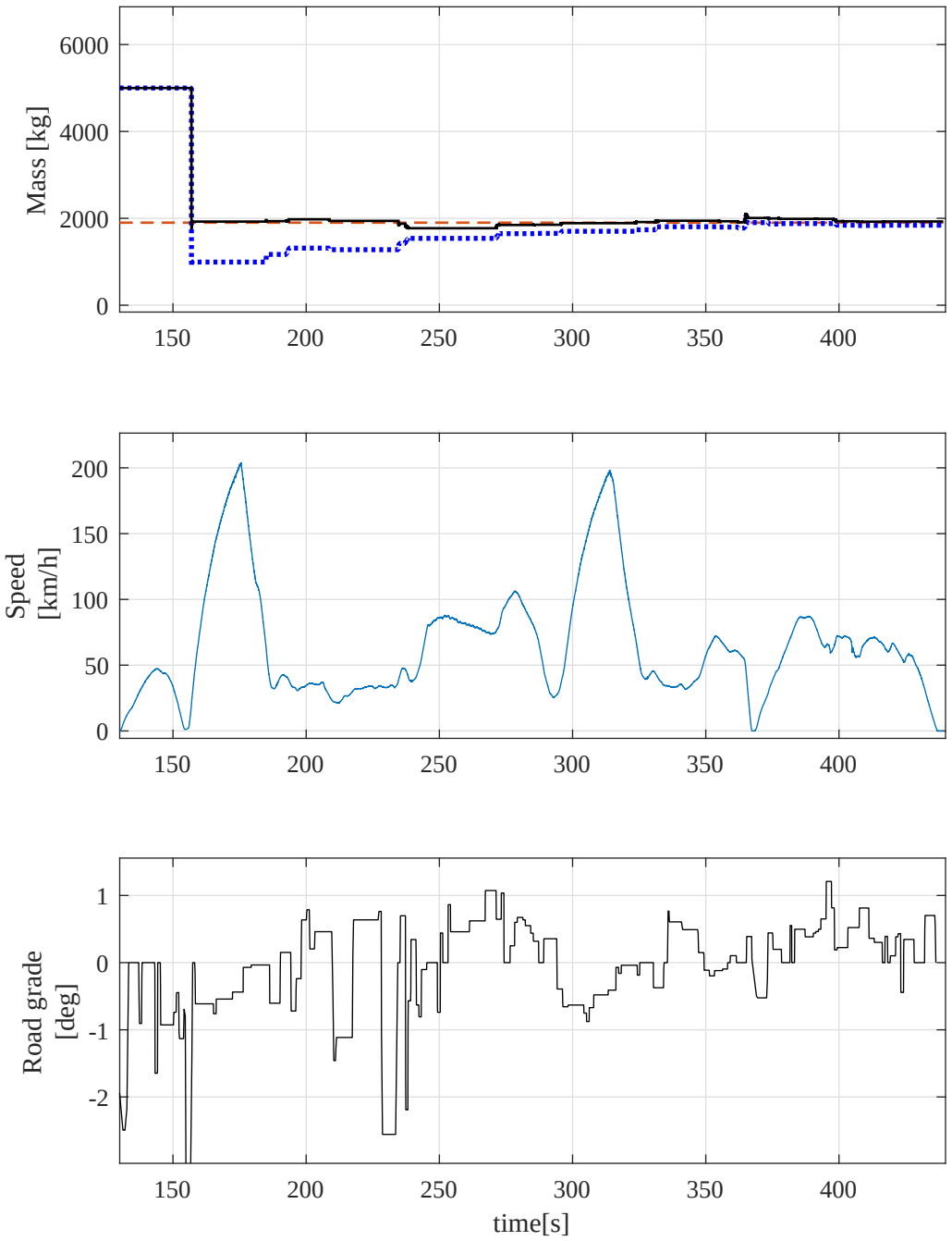

Figure 4.11 Mass estimation with one driver, one passenger and empty fuel tank. Black line indicates the mass estimation with torque estimation whereas the blue dotted line is the mass estimation without torque estimation.

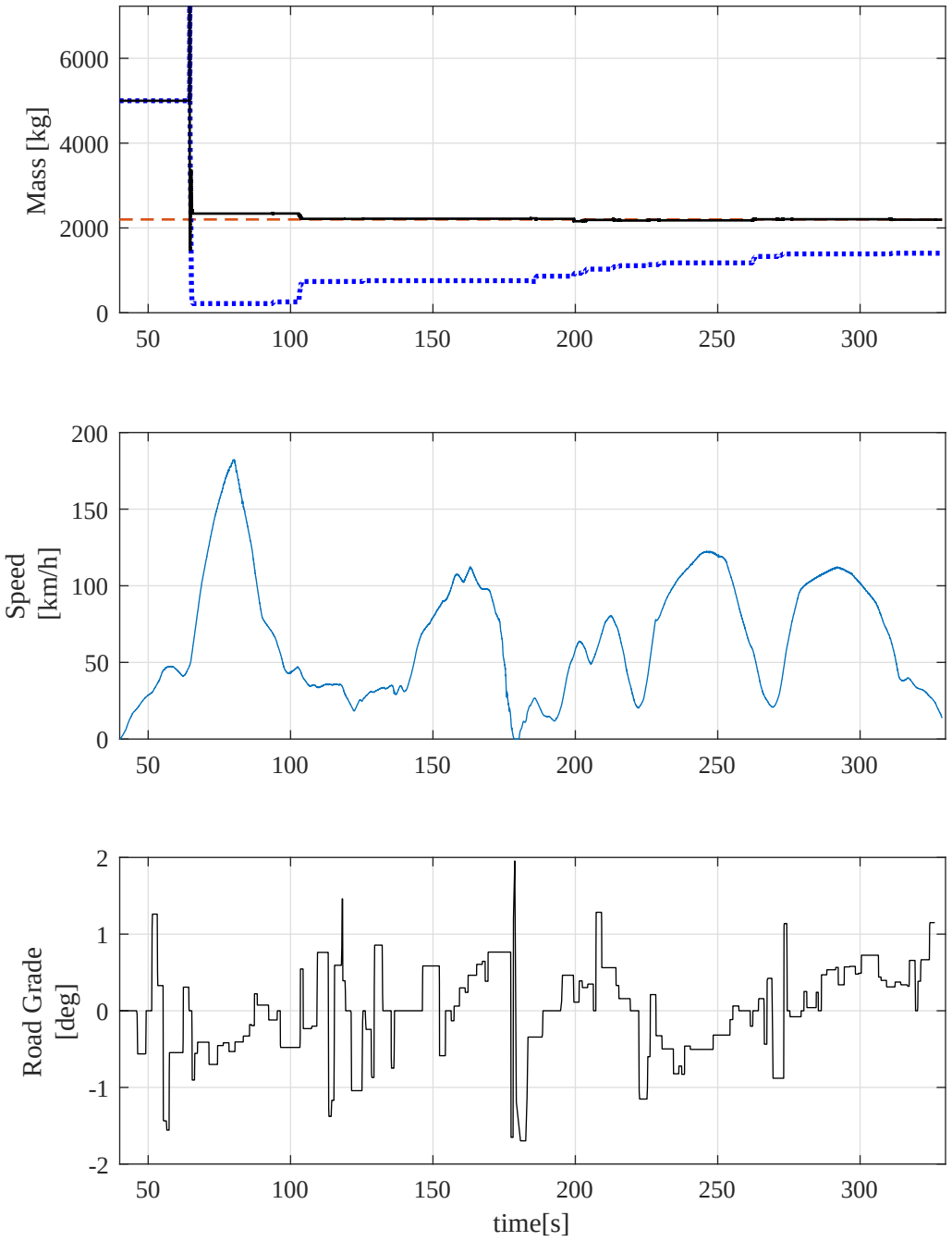

Figure 4.12 Mass estimation with one driver, three passengers and a full tank of fuel. Black line indicates the mass estimation with torque estimation whereas the blue dotted line is the mass estimation without torque estimation.

4.5 Conclusions

The presented mass estimation algorithm for passenger cars, based on vehicle longitudinal dynamics excitations, works on information derived only from the vehicle

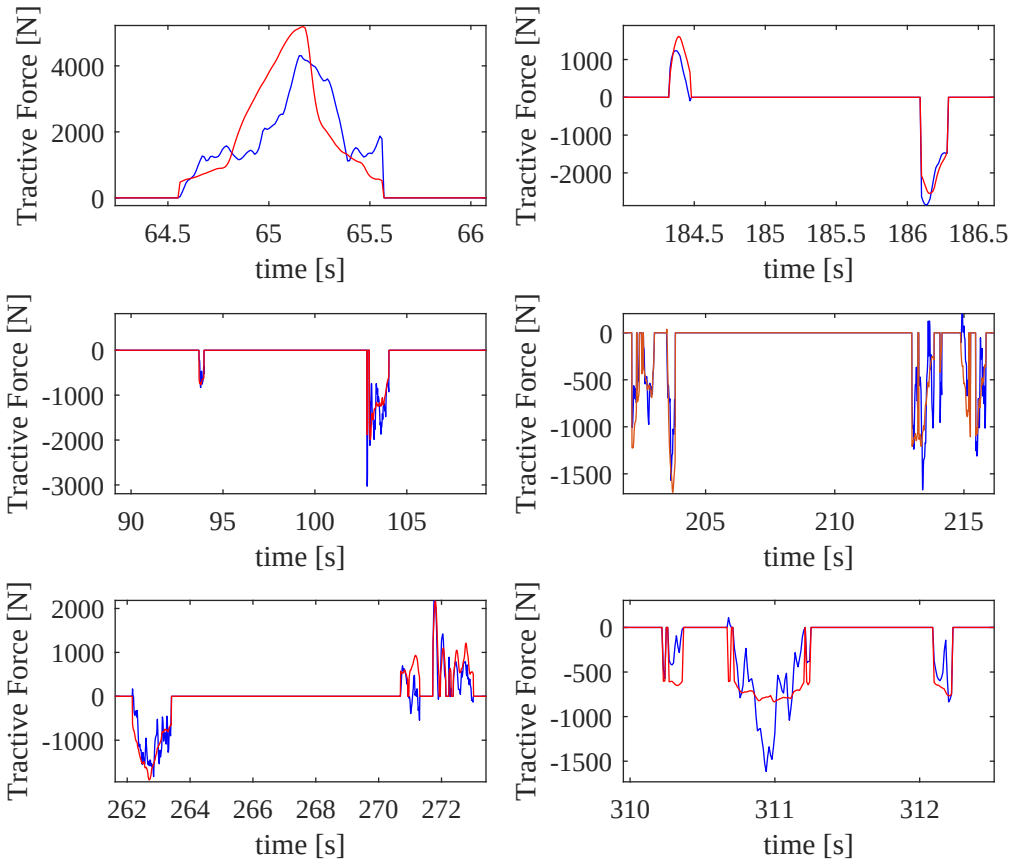

Figure 4.13 Comparison of the filtered estimated longitudinal force obtained from the torque observer(red line) and the filtered longitudinal accelerometer reading multiplied by the known vehicle mass (blue line). A match indicates a good torque estimate by the torque observer. The signals are only shown when the longitudinal motion detector output is 1.

CAN-BUS and it does not require any non-production sensors on board. The algorithm models the effect of the vehicle transmission and observes the longitudinal wheel forces with a torque observer. The algorithm does not require the modelling of the vehicle as it filters out the effects introduced due to road grade, aerodynamics drag and rolling resistance by using a band pass filter. The filtered longitudinal force and the filtered longitudinal acceleration are input into a RLS filter which provides the estimated of the vehicle mass. The algorithm is validated in simulation and with experiments performed on a test track. Results indicate that the torque observer allows a much faster convergence of the estimation algorithm to the actual mass of the vehicle as compared to a traditional method involving only the engine torque signal. Robustness studies done in simulation indicate that the estimation process is not very sensitive to the change in vehicle aerodynamics drag behaviour or tire rolling

resistance. The algorithm is able to accurately estimate the mass of the vehicle with around 5 % error.

Part II

Control Systems Design

Chapter 5

Rear Wheel Steering

5.1 Introduction

Electromechanical rear wheel steering systems offer independent active control of the toe angles of the rear wheels. The advantage this offers with respect to the conventional front wheel steered vehicles is that the control of the rear wheel cornering forces can be achieved. In a passive vehicle, the cornering forces in the rear wheels are generated due to the rear wheel sideslip angles generated as a consequence of the vehicle motion. This causes some inherent delays in the generation of the cornering force due to the vehicle yaw and sideslip dynamics. As a result, the vehicle responsiveness is presumed to be much lower.

In high performance vehicles, for setting fast-lap times, stiffer suspension springs are used to avoid the vehicle body roll and improve the aerodynamic efficiency. But when it comes to the vehicle lateral dynamics, there are mainly two issues that need to be resolved in order to improve the driver's confidence. The first issue is that these vehicles suffer from yaw oscillations during the transient phase of cornering. The second issue is that there is a phase lag between the lateral acceleration and the yaw rate which makes the vehicle more difficult to control.

5.2 Desired Control Action

For high performance vehicles, RWS systems can introduce the following benefits:

- Reduction in the phase lag between the yaw rate and the lateral acceleration.
- Yaw damping.
- Reduction in the turning radius at low speeds.
- Imposing a fixed understeering gradient for steady state manoeuvres.

These benefits can be objectively studied by looking at the mathematical representation of the vehicle. For a simple RWS control law with

$$\delta_r = k\delta_f, \tag{5.1}$$

and a bicycle model representation of the lateral vehicle dynamics, the state space representation of the system is written as:

$$\begin{bmatrix} \dot{\beta} \\ \ddot{\psi} \end{bmatrix} = \begin{bmatrix} \frac{-(C_{af}+C_{ar})}{mu} & \frac{-aC_{af}+bC_{ar}}{mu^2-1} \\ \frac{-aC_{af}+bC_{ar}}{I_{zz}} & \frac{-a^2C_{af}-b^2C_{ar}}{I_{zz}u} \end{bmatrix} \begin{bmatrix} \beta \\ \dot{\psi} \end{bmatrix} + \begin{bmatrix} \frac{C_{af}}{mu} + k\frac{C_{ar}}{mu} \\ \frac{aC_{af}}{I_{zz}} + k\frac{-bC_{ar}}{I_{zz}} \end{bmatrix} \delta_f.$$

The lateral acceleration can be written as

$$a_y = (\dot{\beta} + \dot{\psi})u. \tag{5.2}$$

From the above state space representation, the transfer function between the lateral acceleration and the yaw rate can be written as

$$G_{\frac{a_y}{\dot{\psi}}}(s) = G_{\frac{a_y}{\dot{\psi}}}(0)\frac{N_2 s^2 + N_1 s + 1}{D_1 s + 1}, \tag{5.3}$$

where

$$\begin{aligned} D_1 &= -(mu(C_{af}a - C_{ar}bk))/(C_{af}C_{ar}(a+b)(k-1)), \\ N_1 &= -(b+ak)/(u(k-1)), \\ N_2 &= -(I_{zz}(C_{af} + C_{ar}k))/(C_{af}C_{ar}(a+b)(k-1)), \\ G_{\frac{a_y}{\dot{\psi}}}(0) &= u. \end{aligned}$$

The lag of the lateral acceleration to the vehicle yaw rate can be understood by looking at the denominator of their transfer function given in Equation 5.3. The higher

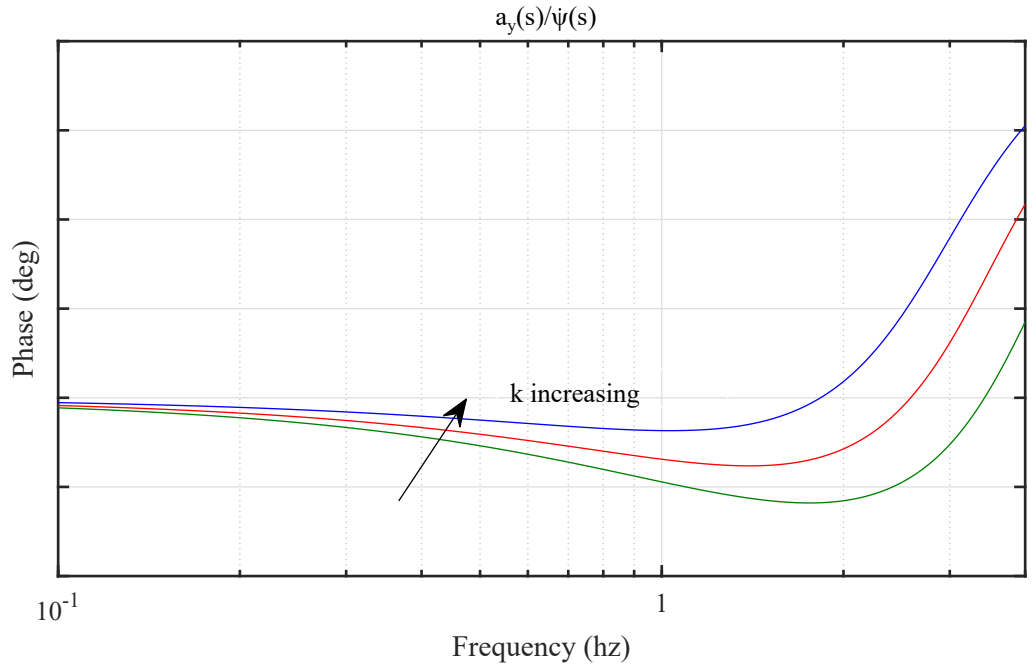

Figure 5.1 Frequency response of the phase of the lateral acceleration to the yaw rate. The vehicle is running at 30 m/s. The blue, red and the green curves represent different gains of k at 0.1,0 and -0.1 respectively.

the value of the steering gain k, the lower the value of D_1. The lower the value of D_1, the more negative the real part of the pole becomes. This leads to lower phase lag. It can be seen in Figure 5.1 that with an in-phase rear steer (positive k), the phase lag seems to reduce while with opposite steer (negative k), the phase lag increases. Moreover, in Figure 5.2 it can be noticed that the phase lag worsens with an increase in velocity of the vehicle, which indicates that more RWS correction is needed at higher velocities. With the reduction of this lag, an improvement in the transient response of the vehicle will be perceived by the driver. This will lead to improved driving dynamics and a reduction in the lap times. Thus, the desired vehicle should have a low phase lag between the yaw rate and the lateral acceleration. The frequency response of the yaw dynamics of vehicle can be understood by looking at the transfer function of the vehicle yaw rate to the front steering angle,

$$G_{\frac{\dot{\psi}}{\delta_f}}(s) = G_{\frac{\dot{\psi}}{\delta_f}}(0)\frac{N_{\dot{\psi}1}s + 1}{D_{\dot{\psi}1}s^2 + D_{\dot{\psi}1}s + 1}, \tag{5.4}$$

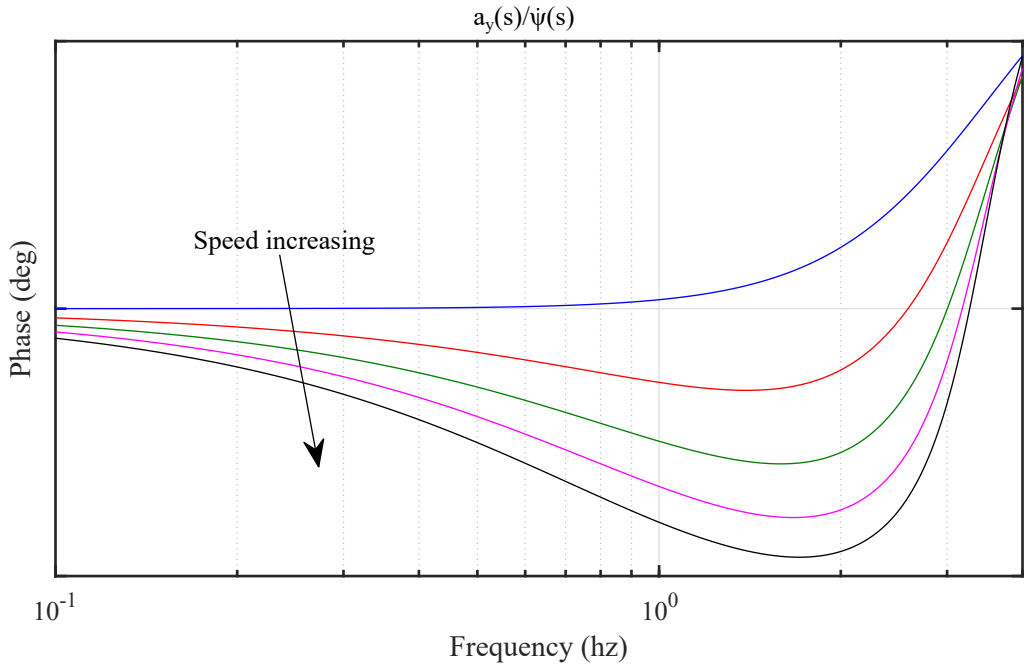

Figure 5.2 Frequency response of the phase of the lateral acceleration to the yaw rate for a passive vehicle at different speeds. The blue, red, green, magenta and black curves represent speeds of 20 m/s, 30 m/s, 40 m/s, 50 m/s and 60 m/s respectively.

where

$$N_{\dot{\psi}1} = \frac{-mu(C_{af}a - C_{ar}bk)}{(C_{af}C_{ar}(a+b)(k-1)},$$

$$D_{\dot{\psi}1} = \frac{u(C_{af}ma^2 + C_{ar}mb^2 + C_{af}I_{zz} + C_{ar}I_{zz})}{(C_{af}C_{ar}a^2 + 2C_{af}C_{ar}ab - C_{af}mau^2 + C_{af}C_{ar}b^2 + C_{ar}mbu^2},$$

$$D_{\dot{\psi}2} = \frac{I_{zz}mu^2}{C_{af}C_{ar}a^2 + 2C_{af}C_{ar}ab - C_{af}mau^2 + C_{af}C_{ar}b^2 + C_{ar}mbu^2},$$

$$G_{\frac{\dot{\psi}}{\delta_f}}(0) = \frac{-C_{af}C_{ar}u(a+b)(k-1)}{C_{af}C_{ar}a^2 + 2C_{af}C_{ar}ab - C_{af}mau^2 + C_{af}C_{ar}b^2 + C_{ar}mbu^2}.$$

Figure 5.3 shows the magnitude of the frequency response of the passive vehicle at different speeds. It is worth noting that the yaw magnitude tends to show a resonance like peak at around 1.4 Hz. This behaviour becomes stronger as the vehicle speed increases. It is therefore imperative to have a sort of yaw damping in this frequency region.

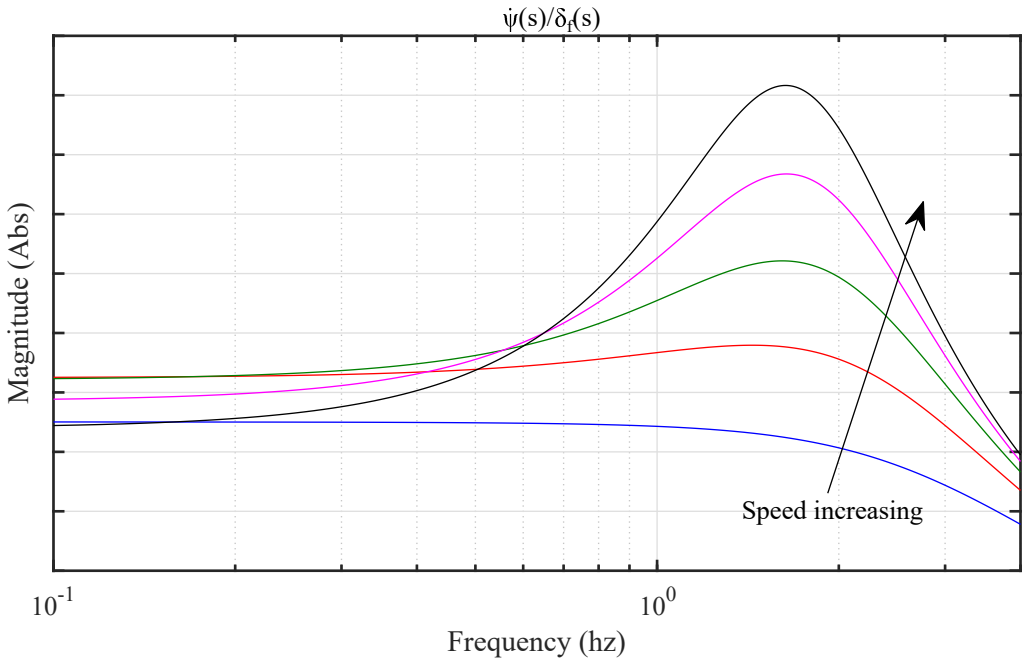

Figure 5.3 Frequency response of the magnitude of the yaw rate to the front steering angle at different speeds for a front wheel steering vehicle. The blue, red, green, magenta and black curves represent speeds of 20 m/s, 30 m/s, 40 m/s, 50 m/s and 60 m/s respectively.

The transient behaviour of the yaw rate response of a front wheel steering vehicle can be studied by looking at the poles and the zeros of $G_{\frac{\dot{\psi}}{\delta_f}}(s)$ at various speeds. It can be noticed in Figure 5.4 that the complex conjugate pair of the poles become closer to the positive real domain and have lower damping as the vehicle speed increases. This effect is undesirable as the yaw response of the vehicle should be fast in order to give a reactive feeling to the driver. Moreover, as the velocity increases, the response to a yaw perturbation would be increasingly oscillatory as the complex component of the poles increases with velocity. This is also undesirable as the driver will have to give more corrective steering inputs to correct the vehicle yaw. This will increase driver workload and would also lead to an unstable feeling in the vehicle. Thus, it is desirable to have poles to be placed such that the response is reasonably fast and the yaw motion is optimally damped. The ideal yaw response would be that of a low pass filter with the yaw gain rolling off at a certain frequency like 2 Hz. In other words the poles of the yaw dynamics should have a very high damping at all velocities. This will lead to a more natural and secure feeling of the car as the yaw rate would not suddenly increase when the driver gives a transient input around the

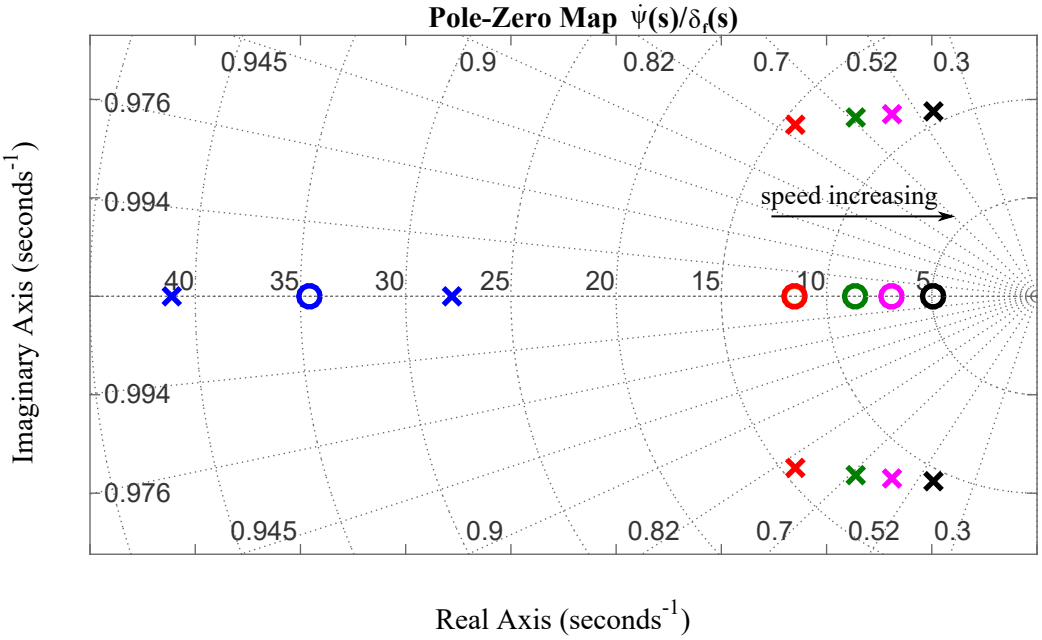

Figure 5.4 Pole (x) zero (o) map of the second order transfer function of the yaw rate to the front steering angle at different speeds for a front wheel steering vehicle. The blue, red, green, magenta and black markers represent speeds of 20 m/s, 30 m/s, 40 m/s, 50 m/s and 60 m/s respectively.

frequency range of the resonance peak region from the yaw response of the passive vehicle.

Figure 5.5 shows the pole zero map of the yaw rate to the front wheel steer angle for a vehicle with a proportional RWS action with k as the proportionality constant. It can be seen that as k becomes smaller, the zero of the transfer function moves towards the RHP. This indicates that to reduce the overshoot behaviour of the vehicle during a step input or a lane change, an in-phase steer (i.e. positive k) is useful. This reduces the overshoot in the yaw response and makes the vehicle feel more secure to drive. In addition, at low speeds the RWS system can improve the vehicle manoeuvrability. Figure 5.6 shows the effect of turning the rear wheels in the opposite direction to the front wheels. The opposite steer leads to reduction in the vehicle turning radius.

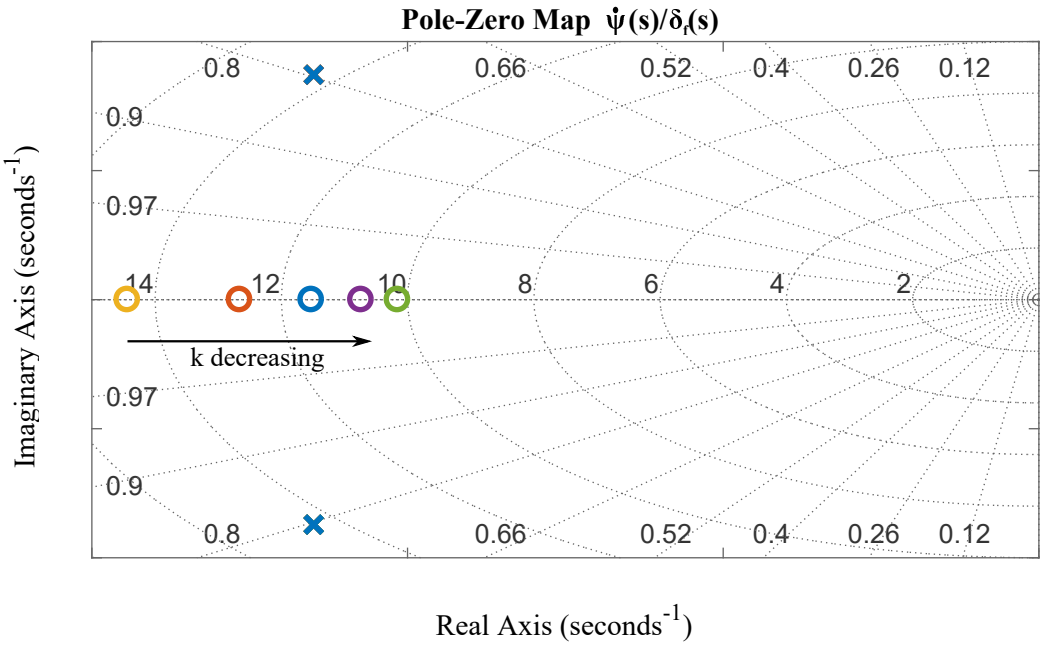

Figure 5.5 Pole (x) zero (o) map of the second order transfer function of the yaw rate to the front steering angle at 100 km/h for different values of k for a prportional front to rear steering vehicle. The green, purple, blue, red and yellow markers represent k equals to -0.2, -0.1, 0, 0.1 and 0.2 respectively.

5.2.1 Objective Evaluation of Subjective Driver Feeling

Subjective evaluation of a vehicle is one of the most important tasks that need to be done during the design and calibration phase of the vehicle. This evaluation involves driving the vehicle in various scenarios and obtaining the feedback of the test drivers. This feedback is primarily composed of responses involving the test driver's opinion of the vehicle's handling characteristics. Often drivers use the level of understeer/oversteer as an indicator. However, this too is subjective in the sense that the drivers are only able to tell the designer whether they want more understeer or more oversteer in a certain situation.

For a control systems designer, the challenge is to understand this subjective jargon and convert it into terms, explainable by standard control system design metrics used in time domain and frequency domain analysis. In the following paragraphs, a set of subjective terms used by the test drivers (OEM) are presented, that have been deciphered, and their objective meanings are presented.

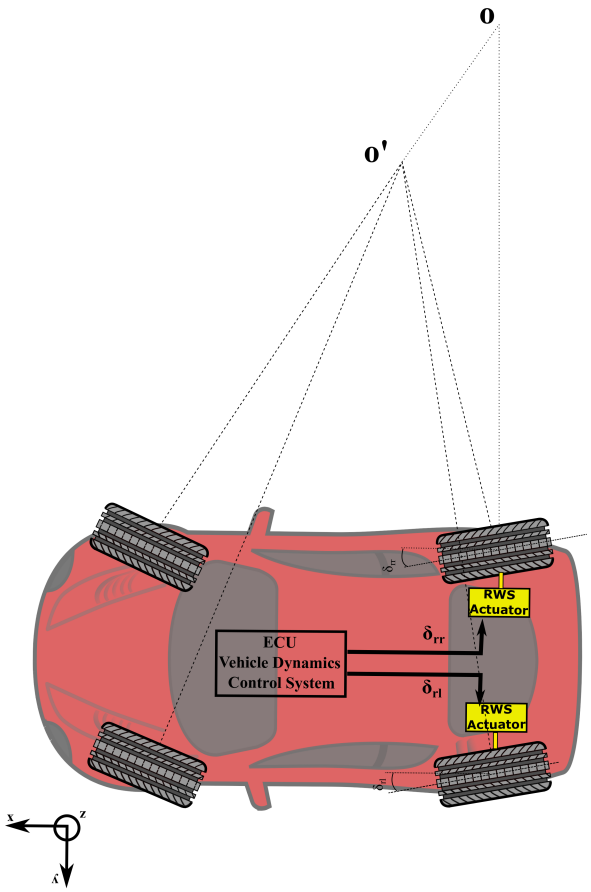

Figure 5.6 Reduction in turning radius of a vehicle due to opposite front and rear wheels steer.

Reactivity

The term ‘reactivity’ is used by the drivers to indicate the rise time of the vehicle yaw rate to a step steer input. For example, at 150 km/h for a step steer of 90 degrees, low reactivity can be classified by a rise time of more than 0.3-0.4 seconds and this is undesirable as the sporty feeling of the vehicle gets lost. On the other hand, a rise time less than 0.1 seconds can be considered as very reactive and this too is also to be avoided as the vehicle becomes too responsive for an average driver. The various driving modes should thus have a calibration that allows the vehicle to have a rise time between 0.1 and 0.3 seconds for the stated manoeuvre. Thus, to adjust the ‘reactivity’ of the vehicle as per the liking of the test driver, a control engineer

should try to move the poles of the effective transfer function of the yaw response to the front steering angle of the vehicle's desired behaviour model along the negative real axis. Moving the poles left would increase reactivity while moving them right would reduce reactivity.

Stability

The term 'stability' is perceived by the drivers as the absence of a large yaw overshoot and the presence of adequate yaw damping to avoid the effect of fishtailing. The higher the presence of the two effects mentioned above, the better the vehicle is subjectively perceived to be. The overshoot in the uncontrolled vehicle can be attributed to the LHP zero that is present in the vehicle's representative yaw rate to the front steering transfer function. As seen in Figure 5.5, the LHP zero moves towards the imaginary plane (more overshoot) when a counter-phase rear wheel steering (negative k) is given whereas the LHP zero moves away from the imaginary axis (less overshoot) when an in-phase rear wheel steering (positive k) is given. Thus, to improve the perception of vehicle stability to the drivers, a control engineer should increase the in-phase rear wheel steering. This may be achieved by a feedback controller or a dynamic feedforward controller since a static feedforward controller cannot change the damping of the poles as seen in Figure 5.5. Thus, the subjective desired behaviour translates to desired vehicle behaviour whose yaw rate to steering angle transfer function has no (or away from the imaginary axis) i) LHP zero(s) ii) imaginary component of the LHP poles iii) No RHP zeros to avoid non-minimum phase behaviour.

5.3 Controller Design

To realise the desired control action, a control structure with both feedforward and feedback control blocks are used. While the feedforward component can be used to control the transient response of the vehicle, the feedback will act as fail-safe in conditions when the behaviour of the vehicle is different from that expected. As the vehicle dynamics is non-linear with respect to speed, a series of scheduled controllers at different velocities are used to realise the entire control system.

5.3.1 Feedforward Controller

The feedforward controller is obtained by inverting the plant model of the vehicle yaw dynamics. The vehicle yaw rate, $\dot{\psi}(s)$ can be written as a function of the front and rear steering angles, denoted by $\delta_f(s)$ and $\delta_r(s)$ as

$$\dot{\psi}(s) = G_{\frac{\dot{\psi}}{\delta_f}}(s)\delta_f(s) + G_{\frac{\dot{\psi}}{\delta_r}}(s)\delta_r(s), \tag{5.5}$$

where $G_{\frac{\dot{\psi}}{\delta_f}}(s)$ and $G_{\frac{\dot{\psi}}{\delta_r}}(s)$ are the transfer functions of yaw rate to the front and the rear steering angles respectively.

The desired vehicle response can be obtained from the bicycle model of a front only steering vehicle with the same properties mentioned in section 5.2. The transfer function of the desired vehicle yaw rate response, $\dot{\psi}_{des}(s)$ can be written as

$$\dot{\psi}_{des}(s) = G_{\frac{\dot{\psi}}{\delta_f}des}(s)\delta_f(s), \tag{5.6}$$

where $G_{\frac{\dot{\psi}}{\delta_f}des}(s)$ is the yaw dynamics transfer function of the desired vehicle. To achieve the desired vehicle response, the controlled vehicle's response should be similar to the desired vehicle. This can be written as

$$G_{\frac{\dot{\psi}}{\delta_f}des}(s)\delta_f(s) = G_{\frac{\dot{\psi}}{\delta_f}}(s)\delta_f(s) + G_{\frac{\dot{\psi}}{\delta_r}}(s)\delta_r(s), \tag{5.7}$$

$$G_{\frac{\dot{\psi}}{\delta_r}}(s)\delta_r(s) = (G_{\frac{\dot{\psi}}{\delta_f}des}(s) - G_{\frac{\dot{\psi}}{\delta_f}}(s))\delta_f(s), \tag{5.8}$$

$$\frac{\delta_r(s)}{\delta_f(s)} = \frac{G_{\frac{\dot{\psi}}{\delta_f}des}(s) - G_{\frac{\dot{\psi}}{\delta_f}}(s)}{G_{\frac{\dot{\psi}}{\delta_r}}(s)}. \tag{5.9}$$

From Equation 5.9, a feedforward control rule comes out that uses the inverted vehicle plant dynamics to obtain the desired rear wheel steering angle from the desired yaw rate. The feedforward control rule is applied on the input steering angle, which is converted to the desired yaw rate using the desired vehicle yaw dynamics plant. As the vehicle's plant is non-linear with respect to the changes in the longitudinal velocity, a scheduling based on the vehicle's longitudinal velocity is done to guarantee optimal results throughout the working range of the vehicle.

The resulting feedforward controller is implemented as a series of digital filters. From Equation 5.9 and a linear bicycle model representation of the vehicle, the series of the feedforward filters are obtained. Then, the order of the feedforward filters is reduced to a second order system with one zero in such a way that the frequency response of the systems before and after the model order reduction are the same up to the frequency range of the driver's steering input. From experimental studies, it has been found out that even with the help of a power steering system, the maximum frequency at which the drivers are able to steer is about 4 Hz. Thus, reducing the model order to have a similar frequency response up to 4 Hz will provide the same performance with a simpler dynamic system for the feedforward controller. This is desirable from the code implementation point of view.

Once the basic filters are obtained, they are further calibrated in order to remove discrepancies emerging from the difference between the actual vehicle's yaw response and the yaw response of the vehicle's linear bicycle model. For this, the inputs from the expert test drivers are taken into account. After a series of iterations with the positioning of the zeros and the poles of the feedforward filters, the calibration is finalised based on the subjective evaluation of the test drivers. As it is the case with luxury and high performance vehicles, these test drivers have the final say when it comes to determining the desired vehicle response as they are able to distinguish what the final client of the vehicle would or would not like to have in the vehicle. The filters after the calibration can be seen in Figure 5.7.

5.3.2 Feedback Controller

A yaw rate feedback controller is designed to achieve the desired yaw dynamic characteristics in the controlled vehicle. The block diagram of the system can be seen in Figure 5.8. The yaw response of the whole vehicle can be written as the superimposition of two components as represented in Equation 5.5. Since the rear wheel steering angle is the only controlled input and the steering input to the front wheels is just managed by the driver, the yaw rate contribution due to the front steering angle is considered as the disturbance to the feedback control system. The yaw rate feedback controller tries to follow a reference yaw rate at each moment by controlling the rear wheel steering angles. The design of this reference yaw rate is crucial as it determines the effective yaw response of the whole vehicle and as a consequence, the feeling that the driver gets while driving the car. For luxury and high perfor-

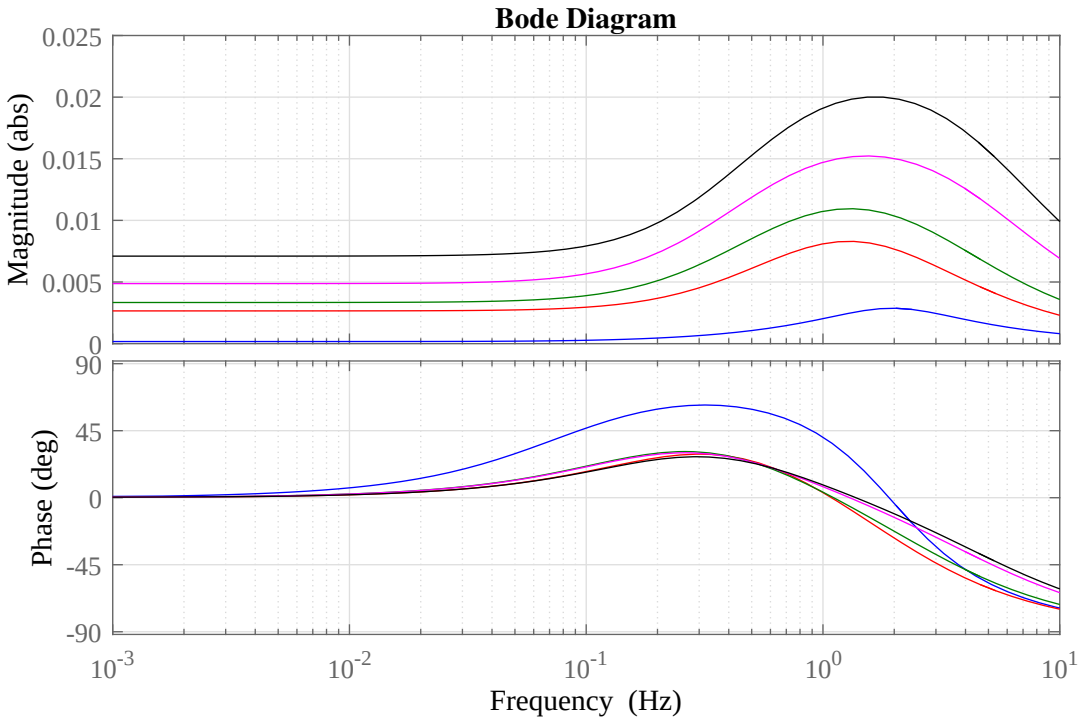

Figure 5.7 The feedforward controller filters. The different colors show the filters for different longitudinal velocities. Blue- 72 km/h, red- 100 km/h, green- 150 km/h, magenta- 200 km/h, black- 250 km/h

mance vehicles, this is a very important factor as it determines the 'soul' of the car.

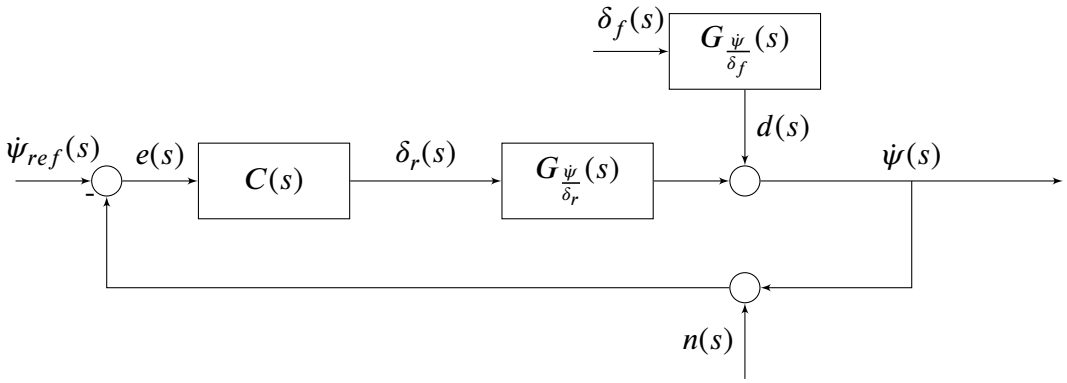

Figure 5.8 Closed loop feedback controller architecture for vehicle yaw rate control.

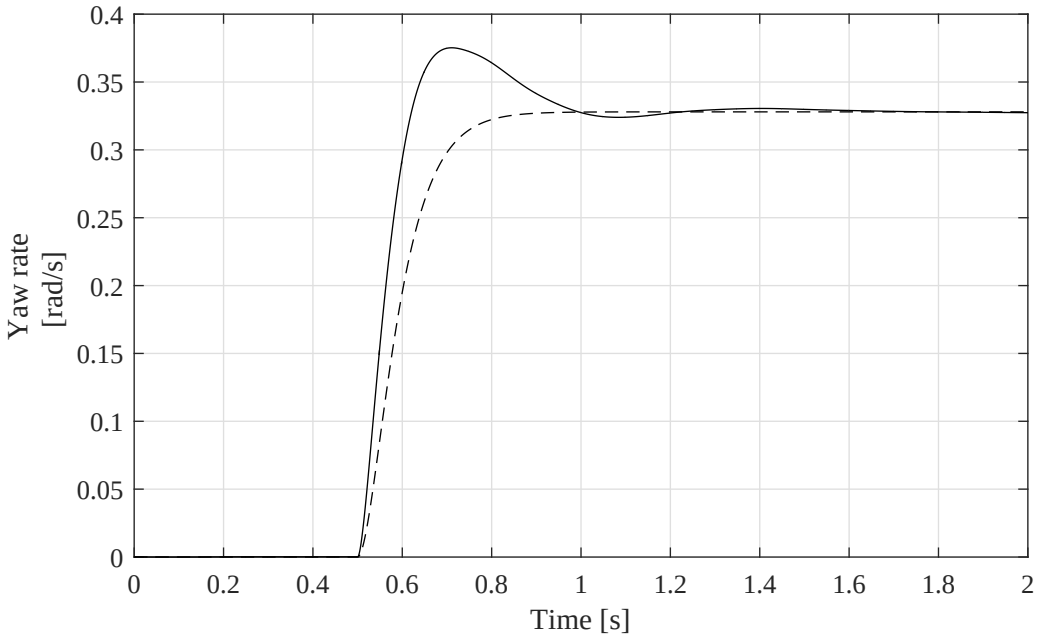

Figure 5.9 Step response of the vehicle yaw to a front steering angle step input at 100 km/h. The actual passive vehicle is denoted by the solid line while the desired vehicle response is denoted by the dashed line.

Reference Signal to Feedback Controller

The reference signal to the yaw rate feedback control is obtained by simulating a desired vehicle behaviour. Looking at the passive vehicle's yaw rate response to the front steering angle in Figure 5.3 and the locations of the zeros and poles in Figure 5.4, it can be inferred that the yaw dynamics is oscillatory due to the presence of a pair of complex conjugate poles in the passive vehicle's yaw dynamics transfer function. Moreover, the presence of a zero leads to an overshoot in the yaw response, which can cause undesirable fishtailing behaviour. To achieve the required yaw damping characteristics, the desired vehicle behaviour is obtained by taking a first order system which takes the driver's demand for front steering angle as input and gives the yaw rate as output. The first order system is chosen to behave as a low pass filter, where the yaw rate gain rolls off after a frequency between 1 Hz to 4 Hz. A reasonable first order system could be a system with the same steady state yaw rate gain as the passive vehicle with no zeros and a single pole that is slightly slower that the poles of the passive system and has no imaginary component. Keeping in mind the vehicle non-linearity due to the saturation of the tire forces, the yaw rate is saturated to a value that corresponds to a lateral acceleration of 1 g for any

given speed. Figure 5.9 shows the step response of the passive vehicle's multibody model versus the desired vehicle response. It can be noticed that the rise time of the desired vehicle is slightly slower compared to the passive vehicle, which also has an overshoot behaviour. A slightly slower rise time makes the vehicle handling feel less intimidating to a normal driver.

Feedback Control Design

A loopshaping technique is used to design the feedback filter. The design of the feedback filter is carried out such that the system has small tracking errors and is also immune to measurement noises and process disturbances introduced by the driver's front steering action. For this, it is desirable to have a feedback controller which renders both the sensitivity and the complementary sensitivity function small using loop-shaping techniques [96].

Referring to the feedback control system as shown in Figure 5.8, given that the open loop transfer function of the controlled system is $L(s) = G_{\frac{\dot{\psi}}{\delta_r}}(s)C(s)$, the error in the reference tracking signal can be written as

$$e(s) = -(1+L(s))^{-1}\dot{\psi}_{ref}(s)+(1+L(s))^{-1}G_{\frac{\dot{\psi}}{\delta_f}}(s)\delta_f(s)-(1+L(s))L(s)n(s), \quad (5.10)$$

where

$$S(s) = (1 + L(s))^{-1}, \quad (5.11)$$

$$T(s) = (1 + L(s))^{-1}L(s). \quad (5.12)$$

To have disturbance rejection and reference yaw rate tracking, the error has to be small, which indicates that the sensitivity function S(s)$\approx$ 0. However, for noise rejection, the complementary sensitivity function should be zero. But the sum of S and T is always 1. So the loop-shaping technique takes advantage of keeping S close to zero up to a certain frequency and then keeps T close to zero beyond that frequency. The controller design which involves designing the shape of the open loop transfer function L is thus a design to balance this trade-off of conflicting requirements.

Since the actual vehicle is non-linear with respect to speed and with respect to tire saturation, the feedback controller is obtained by linearising the vehicle at

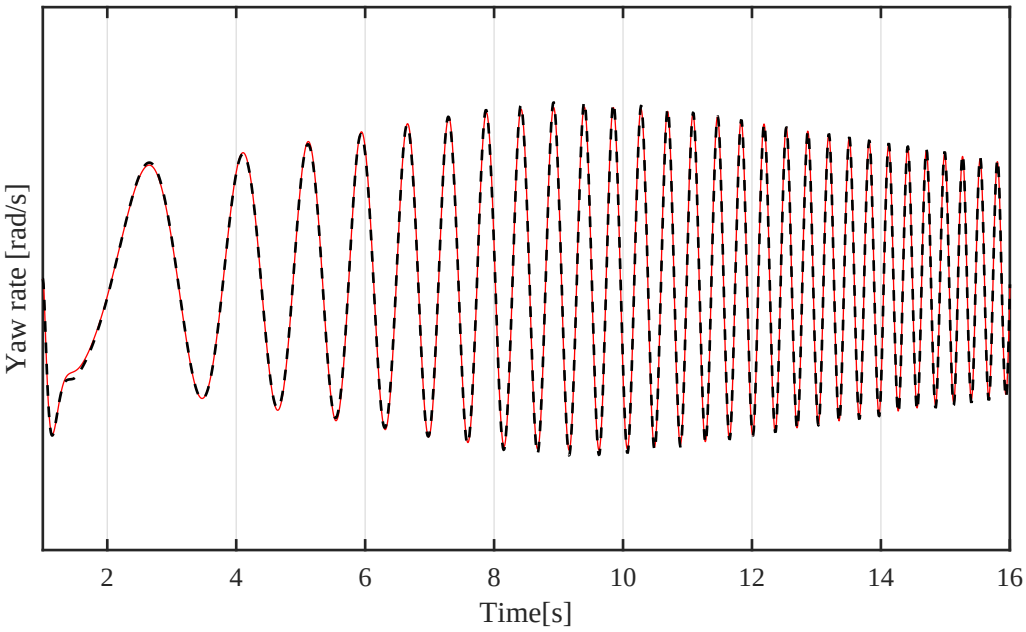

Figure 5.10 Identified model (red) vs actual measurement (black dash) for the yaw response of the rear wheel steering sine sweep input. The y-axis data is removed to respect the confidentiality of the industrial partner.

different operating points and then using scheduling to ensure a good performance over the entire working range. The control design for vehicle speed of 100 km/h is shown in this chapter. A similar procedure is followed for obtaining a series of filters scheduled at different vehicle longitudinal speeds.

The vehicle's multibody model developed in VI-CarRealTime is used to obtain the linearised models. At various speeds, sine sweep inputs are given to the front and then the rear wheel steering in separate manoeuvres to obtain the yaw response of the vehicle with respect to the front steering and the rear steering input. System identification methods are then used on the simulated data to extract the linearised vehicle plant model for the yaw contribution of the front wheel steering and the rear wheel steering. As seen in Figure 5.10, a model with two zeros and three poles is able to represent the vehicle RWS yaw response quite accurately. The identified transfer function is obtained as

$$G_{\frac{\dot{\psi}}{\delta_r}}(s) = K_{\frac{\dot{\psi}}{\delta_r}} \frac{(s - Z_1)(s + Z_2)}{(s + P_1)(b_{s2}s^2 + b_{s1}s + b_{s0})}, \tag{5.13}$$

where $K_{\frac{\psi}{\delta_r}}$ is a constant, Z_1 is a RHP zero of the system, Z_2 is a LHP zero, P_1 is on of the LHP poles of the system, b_{s2}, b_{s1}, b_{s0} are the coefficients of the polynomial in the denominator due to a pair the complex conjugate poles.

To guarantee stability of the feedback controller, the following control design objectives need to be met.

1. The Gain Margin of the open loop system L, should be more than 2.
2. The Phase Margin of L should be more than 30 degrees.
3. The crossover frequency, ω_c should be smaller than $Z_1/2$ to ensure stability.
4. The maximum value of the sensitivity function, S_{max} should be less than 6 dB.

Keeping in mind the above control design objectives, the following open loop shape is proposed.

$$L(s) = K_L \frac{s - Z_1}{s(s + Z_1)(s + P_{l2})}. \tag{5.14}$$

The open loop contains the RHP zero, Z_1 of the plant as cancelling RHP zeros with RHP poles in the controller will render the system internally unstable. This RHP zero poses an inherent limitation in the feedback control design as it cannot be removed from L(s). An integrator is added to ensure good low frequency tracking performance. To ensure the slope of L = -1 at low frequencies, a LHP pole at Z_1 rad/s is added to L. A pole at P_{l2} rad/s is added to roll off L with a higher slope after Z_1 rad/s. K_L is a constant used to tune the loopshape. The frequency response of L(s) is shown in Figure 5.11. The resulting open loop L has a gain margin of 2.4 and a phase margin of 45.5 degrees which ensures stability. Figure 5.12 shows the sensitivity function, S and the complementary sensitivity function, T of L. It can be seen that with the current choice of the loop shape, the value of S_{max} is 6.15 dB which is slightly higher than the design threshold of 6 dB. The controller bandwidth comes to be around 8.7 Hz. This results in a controller C(s) as

$$C(s) = \frac{K_L}{K_{\frac{\psi}{\delta_r}}} \frac{(s + P_1)(b_{s2}s^2 + b_{s1}s + b_{s0})}{(s(s + Z_2)(s + Z_1)(s + P_{l2})}. \tag{5.15}$$

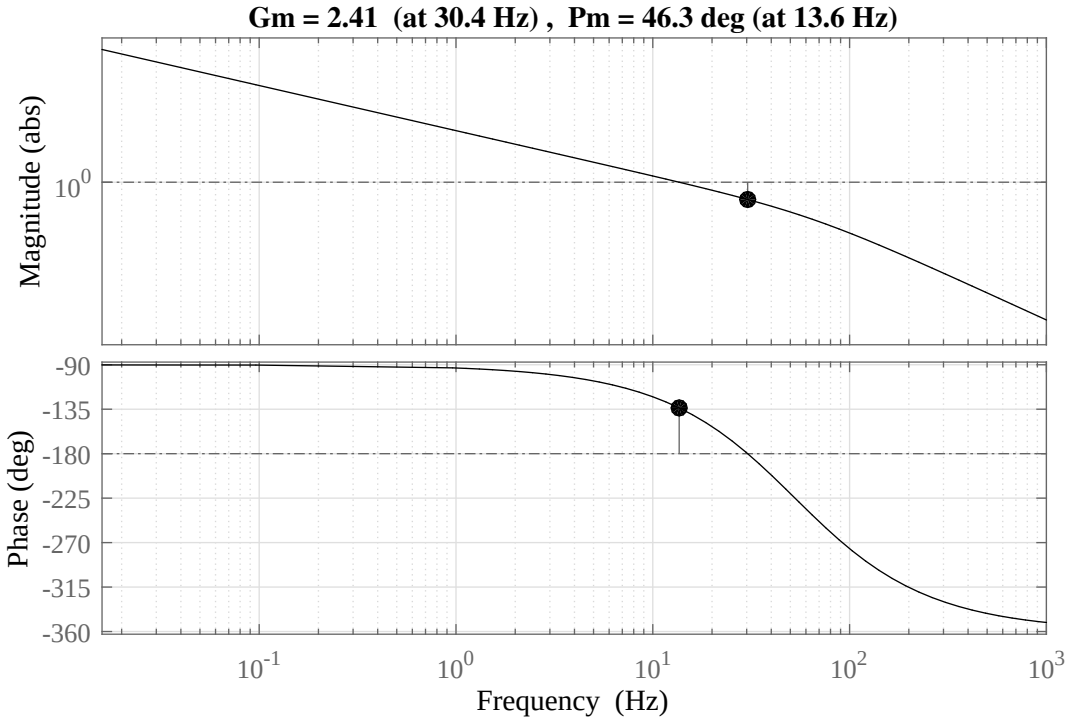

Figure 5.11 Frequency response of L(s) for the plant $G_{\frac{\psi}{\delta_r}}(s)$ and the controller $C(s)$.

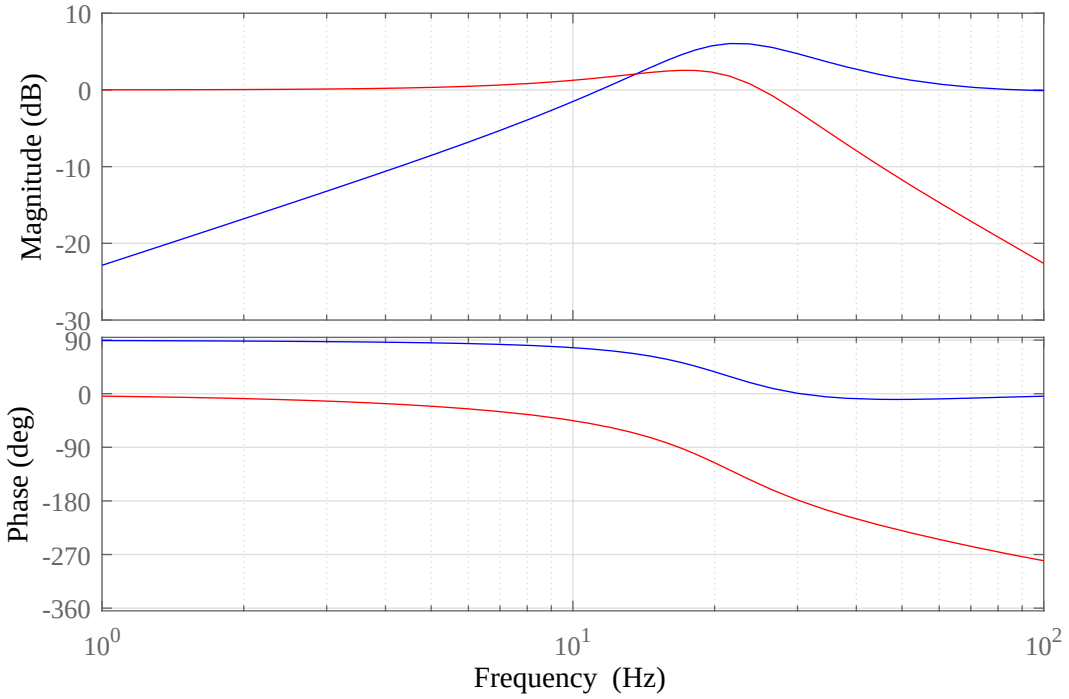

Figure 5.12 Sensitivity function, S(s) (blue) and the complementary sensitivity function, T(s) (red).

5.3.3 Feedback Controller with Actuator Dynamics

The control design in the preceding section accounted only for the vehicle dynamics. However, due to physical constraints with the actuator, which is also a mechanical system, it is important to include the actuator dynamics within the control system design. For this, it is first important to model the actuator dynamics from experimental data.

RWS Actuator and its Dynamics

The RWS actuator consists of an electric motor, a trapezoidal spindle drive and a pinion, which are driven by a belt. The trapezoidal spindle drive converts the rotational motion from the electric motor to translational motion of the actuator's arm, which acts as the tie rods for steering the rear wheels of the vehicle. The advantage of using a trapezoidal spindle drive is that it has a self-locking characteristic. This ensures that at non zero steady state toe angle operations, no extra energy is required by the actuator to maintain its position. The actuator also consists of its own ECU, which has an internal position control loop. This control acts as a low level controller and takes in as input the desired actuator position commanded by the vehicle dynamics controller. Since the actuator has a position sensor, the low level position controller has a feedback loop to track a reference signal. The RWS ECU receives the reference position signal via the CAN-BUS.

To study the dynamic behaviour of the actuator, tests are first carried out under unloaded conditions on a HIL test-bench. The response of the actuator in the frequency domain for a sine sweep test is shown in Figure 5.13. It can be seen that the actuator has good response up to a certain frequency, after which it starts to roll off. Looking at the time domain response for the same sine sweep test, one can notice in Figure 5.14 that the actuator has a fixed time lag of τ_{delay} seconds irrespective of the system dynamics. This time lag is attributed to the property of the lower level position control loop that is present within the ECU of the actuator. A pulse response test was carried out and the response of the system to a pulse input from one end of the actuator travel limit to the other end is presented in Figure 5.15. It can be noticed that the actuator also has a limitation on the maximum velocity that it can move about. As a result, the resulting actuator dynamics can be represented by a time delay and a low pass filter. The transfer function representing the actuator

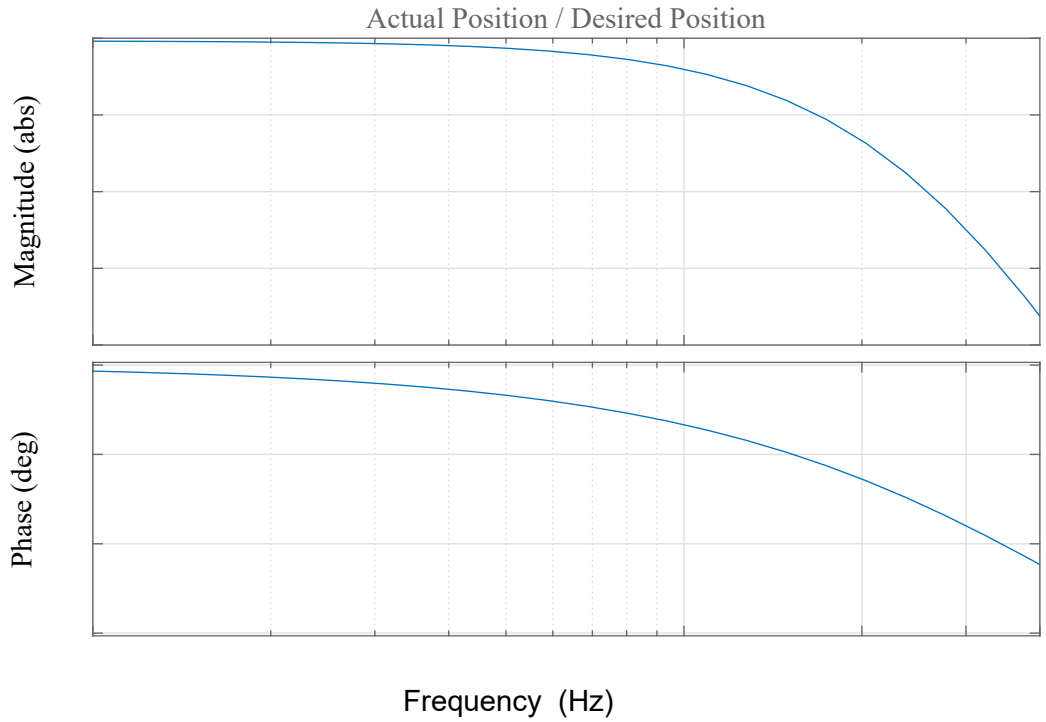

Figure 5.13 Frequency response of the actuator obatined by sine sweep tests.

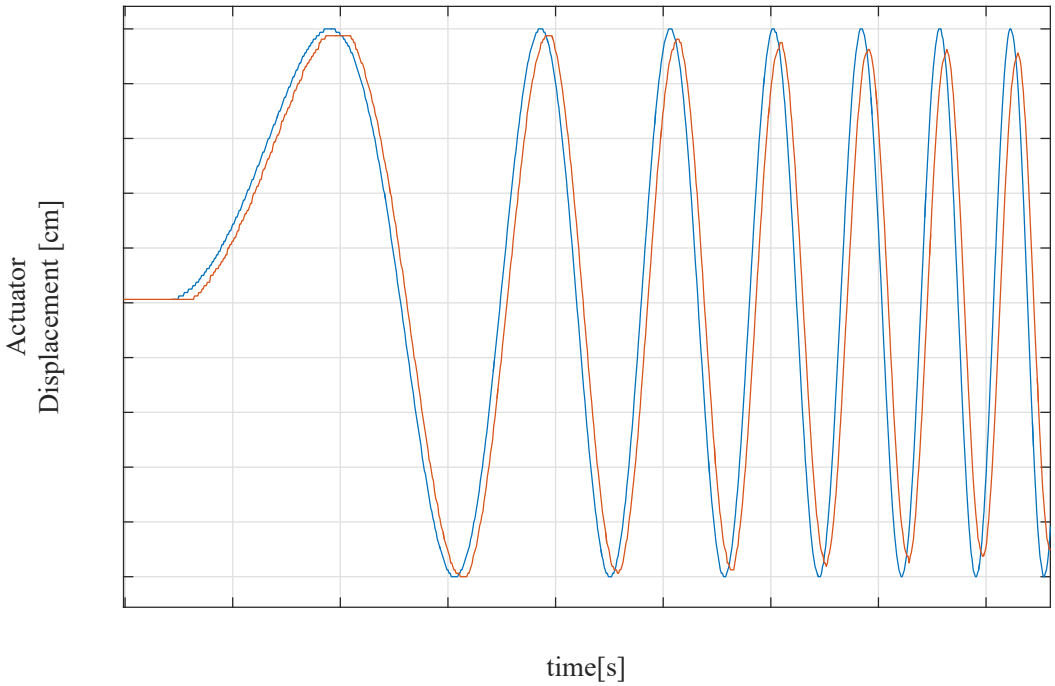

Figure 5.14 Time domain response of the actuator obatined by sine sweep tracking. Blue- reference RWS actuator position, red- actual actuator position.

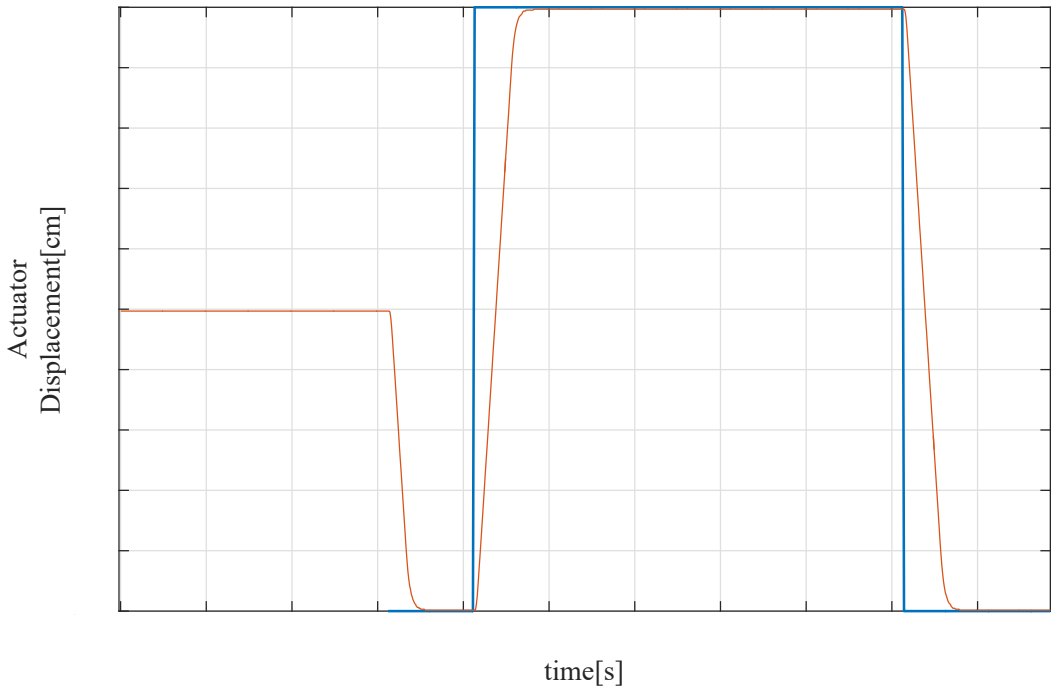

Figure 5.15 Time domain response of the actuator obatined by pulse reference tracking. Blue- reference RWS actuator position, red- actual actuator position.

dynamics is identified as

$$G_{act}(s) = e^{-\tau_{delay}s} K_{act} \frac{s + Z_{a1}}{s + P_{a1}}, \tag{5.16}$$

where K_{act}, $Z_{a1} and P_{a1}$ are the constant gain, the zero and the pole of the identified linear system. However, since the low level position control is based on heuristics, it is found out that the system identification is unable to fit a linear model on to the experimental data. As a result, the actuator dynamics is just simply modelled as a delay of τ_{delay} seconds.

Loopshaping with Actuator Dynamics

Since the actuator has a delay of τ_{delay} seconds, this will lead to limitations in the design of the loop shaping controller. As the time delay introduces an additional phase contribution of -$\tau_{delay}\omega$, to ensure stability, the cross-over frequency ω_c should be smaller than $1/\tau_{delay}$ rad/s. Thus, the combined plant model which includes both actuator and vehicle dynamics can be written as product of the two separate transfer

function as

$$G_{\frac{\dot{\psi}}{\delta_r}tot}(s) = G_{\frac{\dot{\psi}}{\delta_r}}(s)G_{act}(s). \tag{5.17}$$

An acceptable loopshape function, $L_{act}(s)$ which satisfies the control design constraints is obtained as

$$L_{act}(s) = K_{Lact}e^{-\tau_{delay}s}\frac{s - Z_1}{s(s + Z_1)(s + P_{l2})}. \tag{5.18}$$

It can be noticed that the above loopshape is obtained by reducing the constant K_{Lact} in the transfer function to account for the delay. The reduced DC gain leads to a very small control action as increasing it will lead to an unstable controller. The frequency response of the open loop function, L_{act} is shown in Figure 5.16. It can be seen L_{act} has a gain margin of 2.13 (at 4.23 Hz) and a phase margin of 47.7 deg (at 1.99 Hz). Due to the presence of the time delay, the crossover frequency is reduced from 13.6 Hz to 1.99 Hz. The resulting controller bandwidth can be understood by looking at the magnitude of the sensitivity transfer function of L_{act}. It is noticed from Figure 5.17 that the controller bandwidth drops from 8.7 Hz to 1.3 Hz. With respect to active lateral yaw vibration control, the presence of the time delay thus poses a limitation, as the controller is now unable to actively damp frequencies over 1.3 Hz. Thus, the action of the feedback controller will be only in the low frequency domain, while the transient response will be mostly affected by the feedforward controller.

5.4 Controller Performance Evaluation

The performance of the controllers developed in the above section are studied in detail to understand the level of performance improvement that each introduces. The controllers are first tested in simulation using a calibrated VI-CarRealTime vehicle multibody model that represents the vehicle dynamics very accurately up to a reasonable frequency range for the study of vehicle lateral dynamics. Hardware in the loop tests are then carried out to have an exact idea of the effect of the actuator dynamics on the controller's performance. Finally, the controllers are tested on the track onboard the actual prototype vehicle to have subjective feedback from the test drivers in addition to the verification and validation of the results obtained in simulation studies.

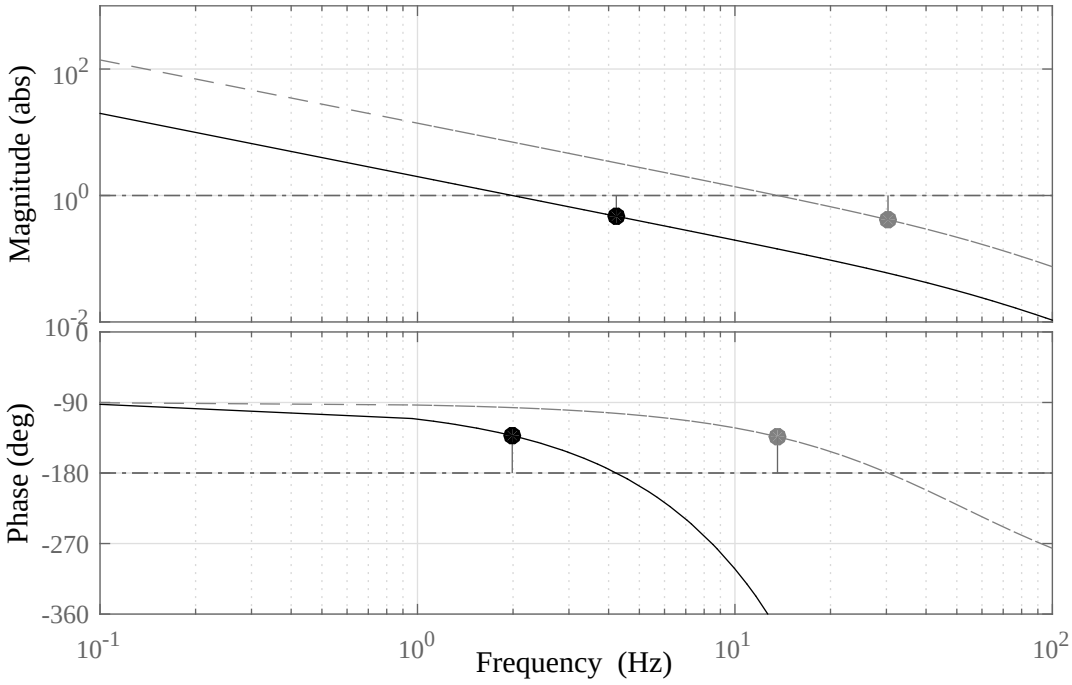

Figure 5.16 Frequency response of $L_{act}(s)$ (black) compared to the frequency response of L(s) (gray).

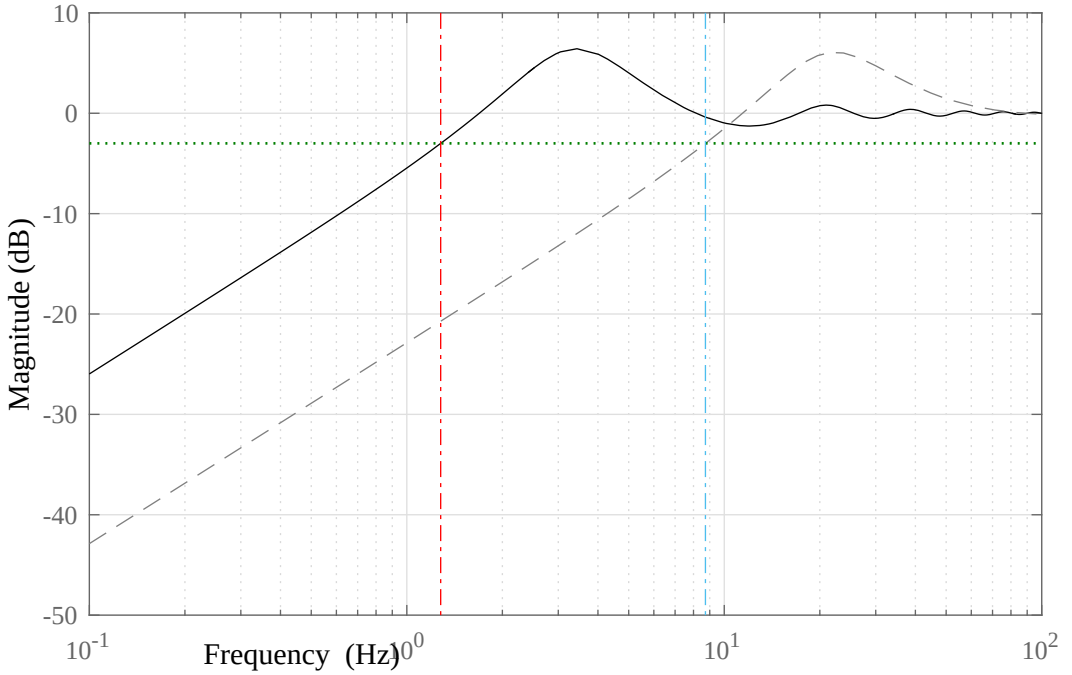

Figure 5.17 Sensitivity function, S(s) for the control system design without (gray dashed) and with the actuator model (black). The controller bandwidth reduces due to the presence of the delay in the actuator.

5.4.1 Multibody Simulation

Co-simulation tests are carried out with the help of VI-CarRealTime running in tandem with Simulink to test the performance of the controllers in various manoeuvres. While the vehicle model runs in VI-CarRealTime environment, the control system runs in Simulink. As the vehicle model is obtained directly from the vehicle manufacturer, it is calibrated to a point where it is very close to the actual vehicle. Rather than using a simple bicycle or 4-DOF four wheel vehicle model to test the controller performance, the multibody model permits one to arrive very close to the final control design while staying at the desk. The list of standard tests that are carried out are as follows:

- **Sine sweep**: The purpose of this test is to extract the frequency response of the vehicle.
- **Step steer**: To study the transient behaviour of the controlled and uncontrolled behaviour vehicle.
- **Ramp steer**: To study the quasi steady state behaviour of the vehicle.
- **Double lane change**: To study the stability of the vehicle under sudden changes of direction.

To simulate the actuator behaviour, a fixed time delay of τ_{delay} second is added between the controller output and the rear toe angle input to the vehicle model. The maximum rear toe angle is also saturated to its maximum physically possible value. While the simulation sampling time is 1 ms, the controller is updated once in every 10 ms. This is to replicate the behaviour of the digital electronics within the actuator, which is a discrete system.

Step Steer

Figure 5.18 shows the time domain response of the vehicle yaw rate for a step input of 30 degrees at the steering wheel while the vehicle is running at 100 km/h. The step response of the passive vehicle is shown in black, the desired response with the black dashed line, the controlled vehicle with just the FF controller in blue, the controlled vehicle with FF and FB in red and the controlled vehicle with FF and FB and no

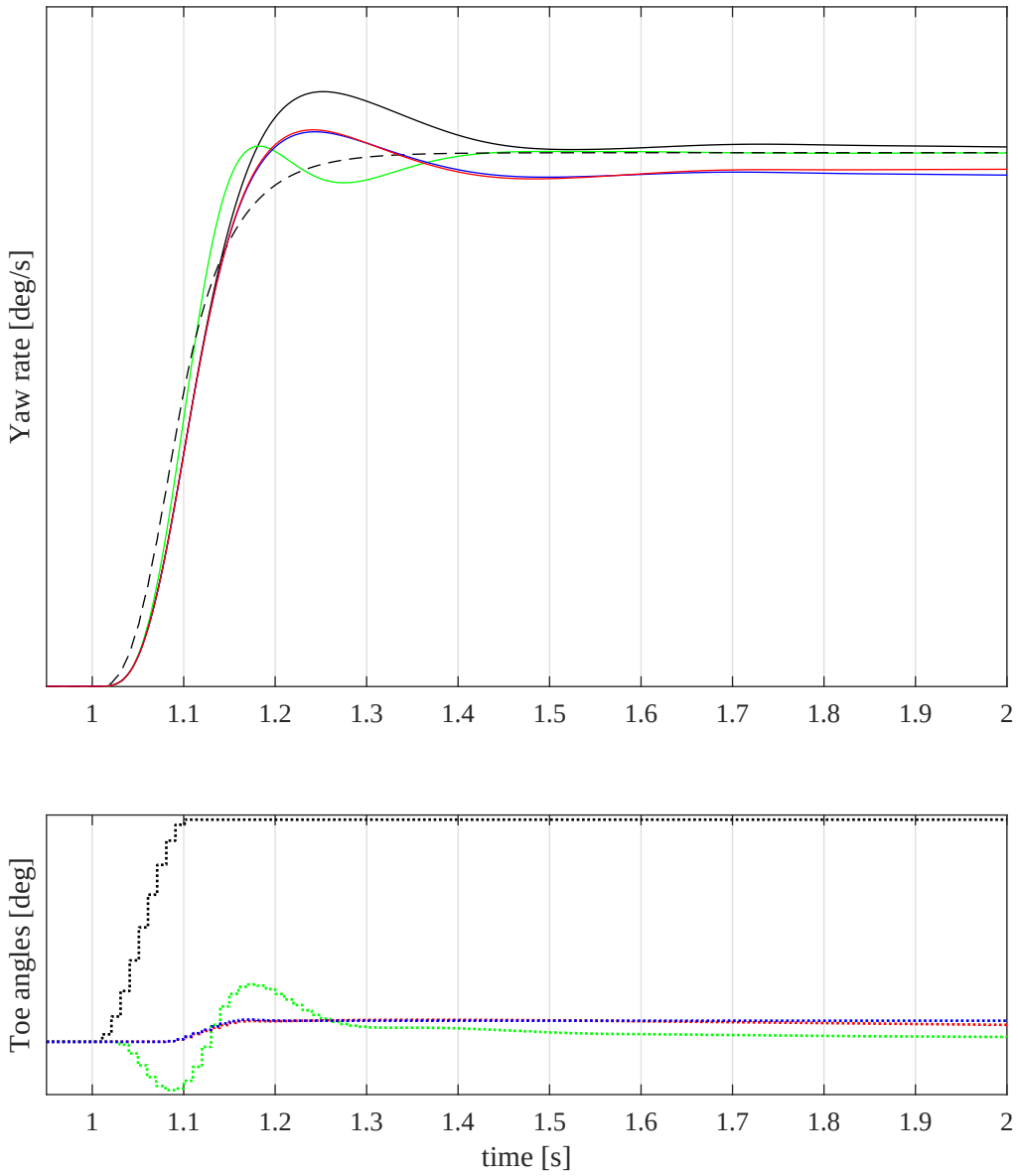

Figure 5.18 Step response of the controlled and the uncontrolled vehicles. A step of 30 degrees at the steering wheel is applied within 0.1 second. Black- uncontrolled, blue- FF only, red- FF+FB, green- FF+FB without delay, black dashed- desired vehicle.

actuator delay in green (maximum performance of the controller without actuator limitations). It can be noticed that the passive vehicle has a fast rise time which is desirable from the agility point of view. The passive vehicle has a large overshoot of around 1.117 and settling time of around 0.5 seconds. The controlled vehicles with FF and with both FF and FB have very similar responses because the FB's contribution or fast dynamics is negligible. It can be seen that for the controlled vehicles (red and blue), the rise time is the same as the passive vehicle while the yaw rate peak is much lower. This corresponds to a much more secure feeling for the driver. The overshoot is slightly smaller than the passive vehicle which is a desired attribute and the settling time is around 0.45 seconds which is a fraction faster. As there is yaw damping in the system due to the RWS action, the response reaches steady state faster. For the controller with FB (red), it can be seen that the integral part of the controller corrects the yaw response as it follows the reference yaw rate with a relatively slow rate of convergence. Finally, the green curve shows the control system's performance assuming an actuator with zero dead time. This may be a possibility in the future, to have the same actuator without the time lag between the desired actuator position command and actual actuator position due to a firmware update of the low level controller of the actuator. It can be seen that the yaw response is very close to the desired yaw rate which has a similar rise time, a much faster settling time of around 0.2 seconds and a negligible overshoot. As as result, the elimination of the actuator dead time can bring about a drastic improvement in the yaw damping of the yaw dynamics of the vehicle.

Sine Sweep Steer

To study the frequency response of the yaw rate of the controlled and the passive vehicles, sine sweep manoeuvres with a steering amplitude of 30 degrees at 100 km/h are simulated. It is worth noticing in Figure 5.19 that the yaw rate to steering angle gain for the passive vehicle, which is shown with a black line, has a peak. This is an undesirable behaviour as ideally it is desirable to have a constant gain up to a certain frequency, followed by a roll-off as denoted by the black dashed line. The yaw response of the vehicle simulated with controllers only FF and FF+FB, shown in blue and red respectively, have slightly better yaw damping as compared to the passive vehicle. The FB contribution is again negligible due to the limitation coming due to the actuator delay. The green line shows that if the delay is removed,

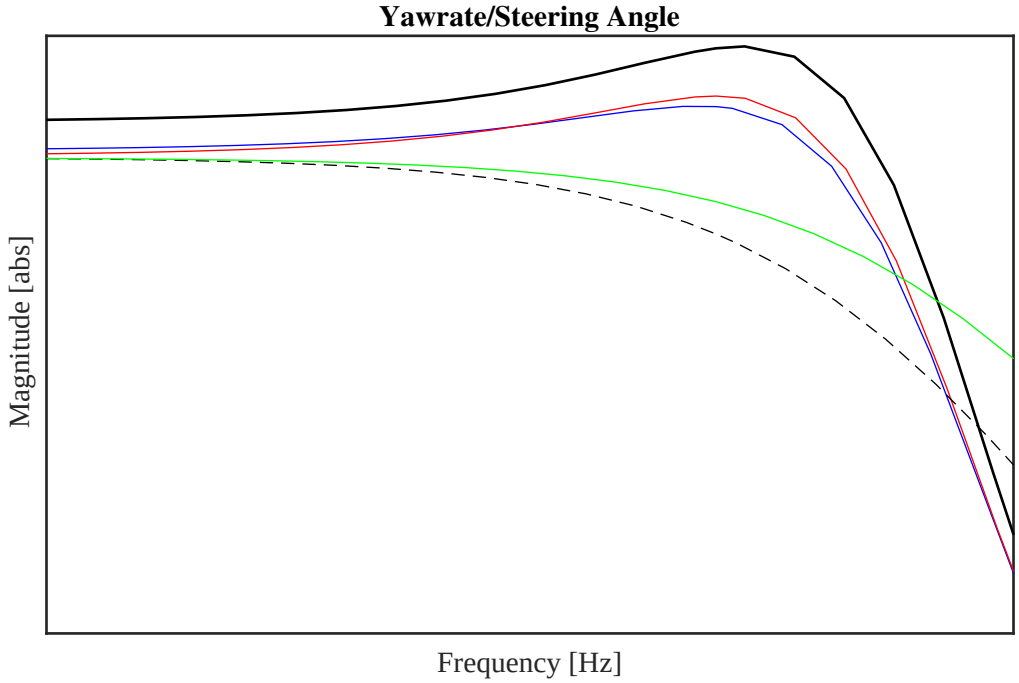

Figure 5.19 Sine sweep response of the controlled and the uncontrolled vehicles at 100 km/h. A sine steering of 30 degrees amplitude and a sweep is applied with a sweep rate of 0.1 Hz per second. Black- uncontrolled, blue- FF only, red- FF+FB, green- FF+FB without delay, black dashed- desired vehicle.

then a yaw response close to the desired response can be obtained. The vehicle with perfect actuators has no peak in the yaw response, which results in a very good driver feeling. This results in improved driver confidence in the vehicle.

Figure 5.20 shows the frequency response plot for the same sweep manoeuvre at 150 km/h. As the velocity of the vehicle increases, the resonance peak in the yaw frequency response of the passive vehicle becomes more prominent as seen in the black curve. It can be seen that the controlled vehicle with FF has a lower peak (blue curve) and relatively higher yaw damping. The controlled vehicle with FF + FB has a more linear response (red curve) as the feedback contribution slightly improves the controller performance. The controller with the lag free actuator shows a very well damped yaw rate frequency response (green curve) with is almost constant within the operating frequency range.

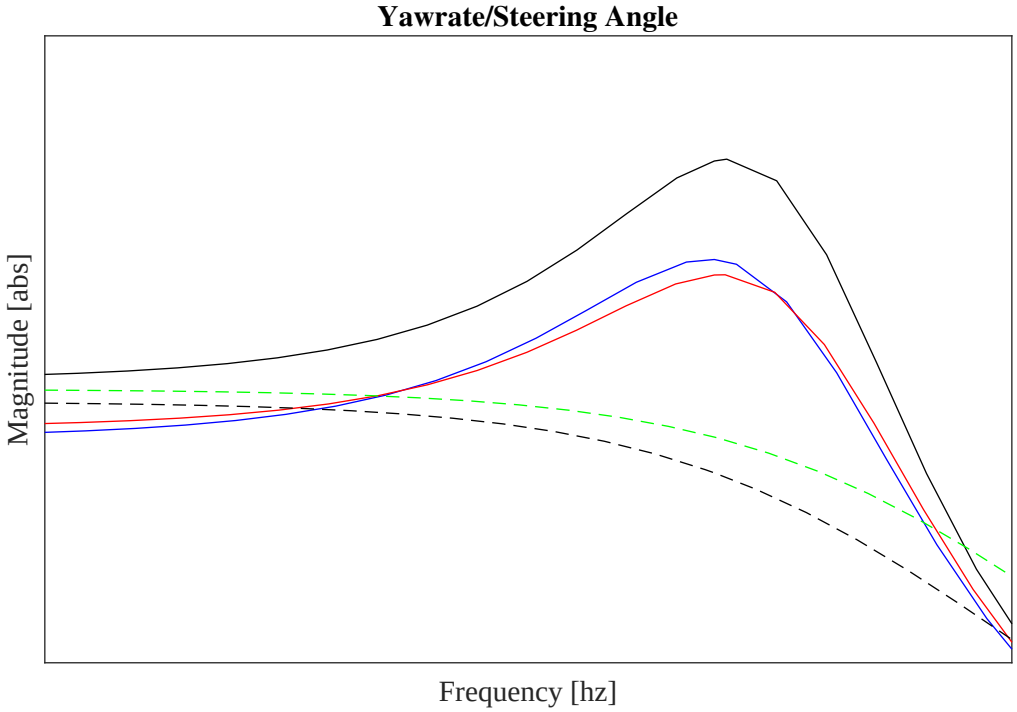

Figure 5.20 Sine sweep response of the controlled and the uncontrolled vehicles at 150 km/h. A sine sweep steering of 30 degrees amplitude is applied with a sweep rate of 0.1 Hz per second. Black- uncontrolled, blue- FF only, red- FF+FB, green- FF+FB without delay, black dashed- desired vehicle.

Ramp steer

A ramp steering manoeuvre is simulated to study the steady state response of the vehicle. The parameter of interest is the vehicle's understeering gradient, which is the slope of the curve between the steering angle and the lateral acceleration. A lower understeering gradient can introduce driving comfort as the driver can reach higher lateral accelerations with a lower input of the steering. It can be noticed that the feedforward controller (blue) is unable to introduce large changes in the understeering gradient. The feedback controller with the delay-prone actuator is able to lower the understeering gradient (red) whereas as the feedback controller with delay free actuator can lower the understeering gradient by the maximum amount. This is owing to the larger DC gain of the delay free controller as compared to the controller designed for the system with delay.

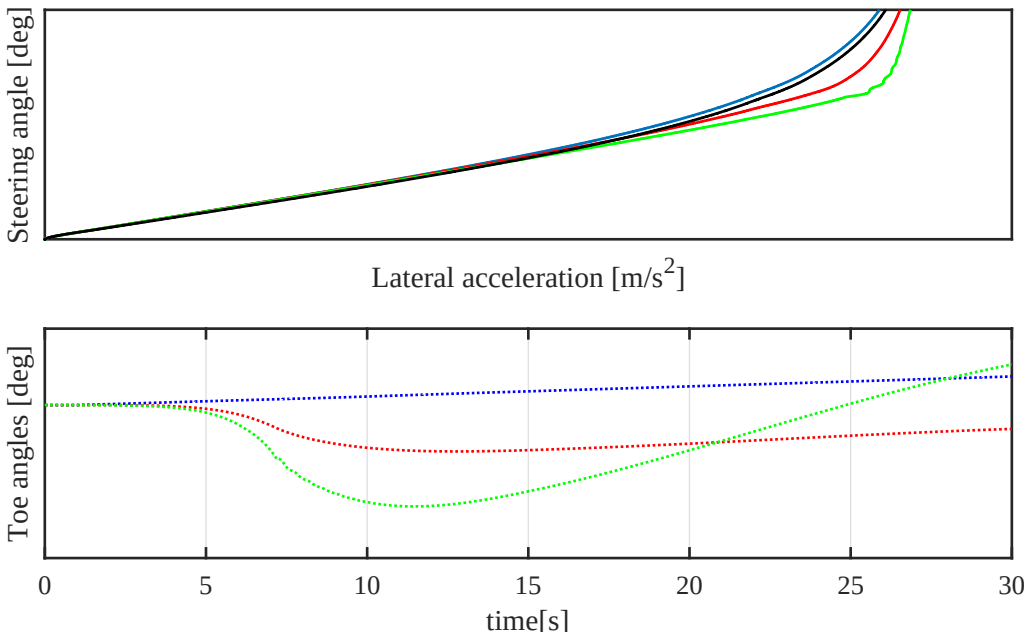

Figure 5.21 Response to a ramp steering of the controlled and the uncontrolled vehicles at 100 km/h. Black- uncontrolled, blue- FF only, red- FF+FB, green- FB without delay, black dashed- desired vehicle.

Double Lane Change

The double lane change test is simulated to test the controllers' transient performance when sudden changes in directions are involved. The DLC test is carried out at 100 km/h and the results are shown in Figure 5.22. The passive vehicle's response is shown with the black curve. It can be seen that the passive vehicle's response has a very high yaw rate peak value at around 1.5 seconds with respect to the steady state part of the manoeuvre at around 1.8 seconds. The controlled vehicle with the lag prone actuator with FF (blue) and both FF+FB (red) controllers has a slightly lower yaw rate peak for the same steering input which indicates the controlled vehicle feels much more secure. The controller with the perfect actuator (green) has a response that is very close to the desired vehicle response (dashed).

5.4.2 HIL Simulation

Hardware in the loop (HIL) tests are carried out to study the effect of the real actuator dynamics with the designed control system. Due to the delay introduced by the low

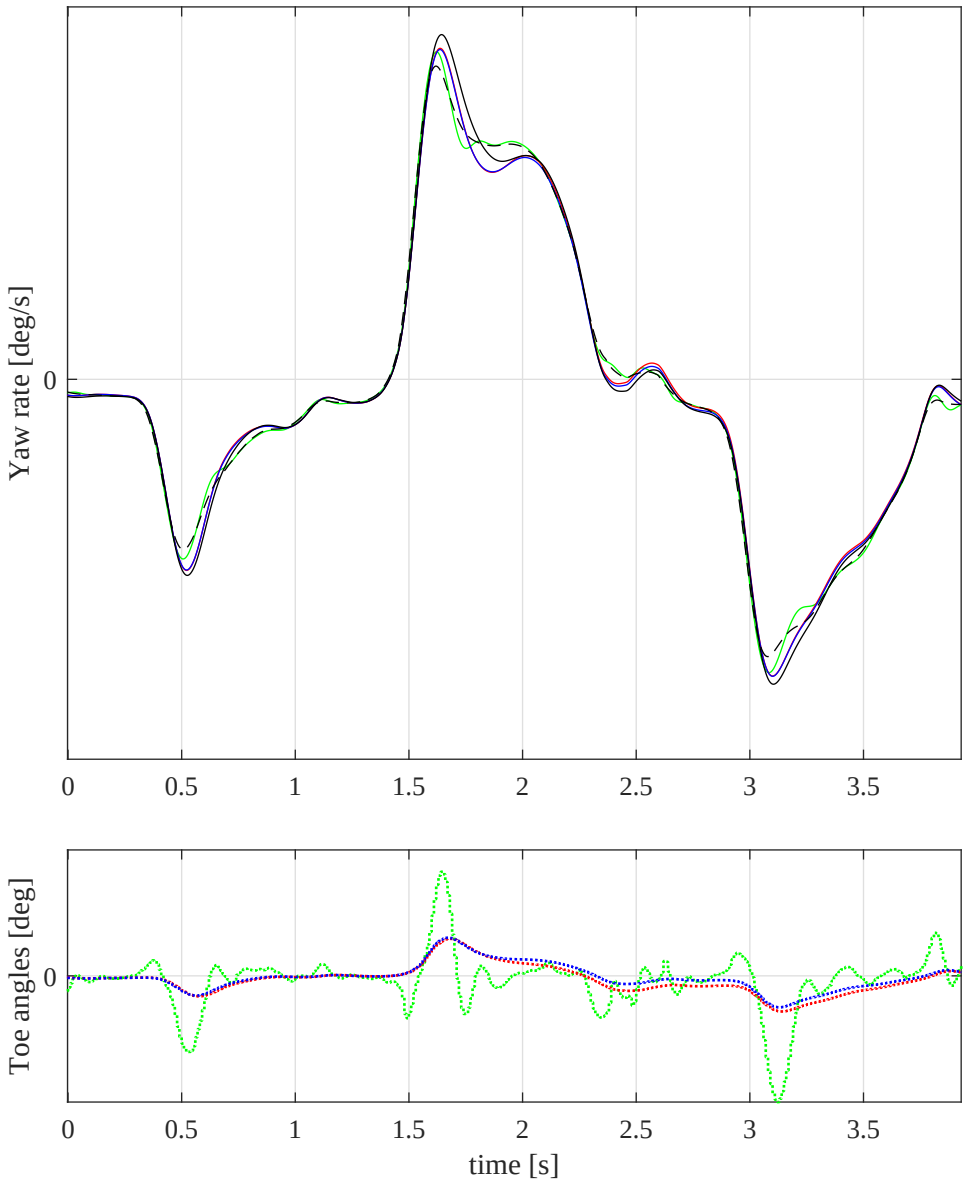

Figure 5.22 Response to a double lane change manoever for the controlled and the uncontrolled vehicles at 100 km/h. Black- uncontrolled, blue- FF only, red- FF+FB, green- FF+FB without delay, black dashed- desired vehicle.

level control logic of the actuator, during the multibody simulation, the actuator was modelled with a time delay. However, this low-level control system logic is unknown and the delay is not always a fixed delay. From test bench experiments, it has been noticed that the low-level logic includes heuristics based algorithms. As a result, it is important to first test the controller with a virtual vehicle model and the real actuators on a test bench with HIL simulations. Secondly, as human drivers are not very precise in replicating the same steering inputs for two different tests, it is difficult to objectively test the controller with track tests. Thus, HIL tests allow the execution of objective testing while being ever closer to the track test conditions, due to the inclusion of the real actuator dynamics.

The HIL setup used for the testing is shown in Figure 5.23. The vehicle model is the calibrated vehicle model in the VI-CarRealTime environment, which is run on a real time computer. The computer has a real time operating system based on Linux and has a CAN-BUS I/O for communication with the control unit. The controller is embedded in a National Instruments rapid prototyping ECU called cRIO-9033. The cRIO has CAN-BUS I/O modules through which it receives the input signals of the controller. The controller sends out the desired RWS actuator position to the the RWS actuator's low level controller via CAN. The RWS actuators send the actual RWS actuator positions to the real time computer, which receives it through its CAN- BUS I/O and sends it to the vehicle model to replicate the vehicle dynamics including the actual actuator dynamics. The vehicle model is run at 1 kHz while the CAN-BUS is run at 100 Hz to simulate the vehicle CAN-BUS communication. The controller is also run at 100 Hz. Various tests are carried out with the HIL test rig and their results are presented in the following paragraphs. For dynamics tests, only the FF part of the controller is implemented as FB has a negligible contribution in the control action owing to the very small DC gain. For the steady state manoeuvres, the FB controller is tested.

Double Lane Change

Double lane change manoeuvres are simulated in real time simulation to study the efficacy of the designed controlled system. The steering input profile is taken from an experimental log of an actual DLC manoeuvre executed by a test driver on a proving ground, to investigate the effects introduced by a steering input profile that is more realistic, which cannot be generated by the in-built driver models of VI-

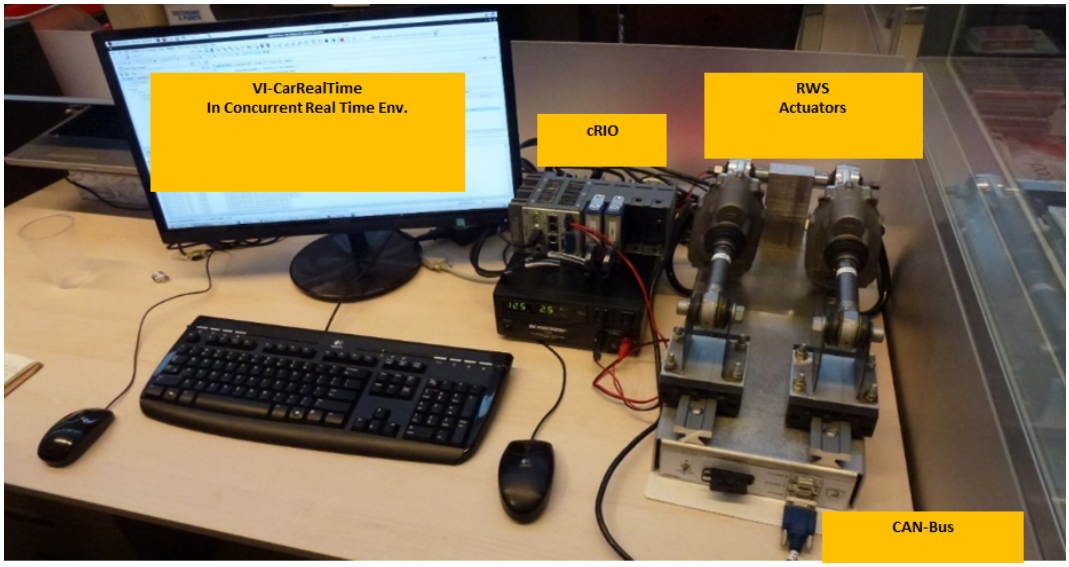

Figure 5.23 The Hardware in the Loop setup for the virtual validation of the control system including the actuator dynamics.

CarRealTime. The responses of the controlled and the uncontrolled vehicles for the DLC manoeuvre simulation are shown in Figure 5.24. The controlled vehicle is denoted by blue curves while the uncontrolled vehicle is shown with black lines. From the yaw rate time response, it can be noticed that the uncontrolled vehicle has a larger overshoot for the same steering input as compared to the controlled vehicle. This can be seen at times 33.3 seconds and 34.7 seconds. This indicates that the controlled vehicle has higher yaw damping, which is desirable as it enhances the driver's confidence in the vehicle. Secondly, due to the RWS action, a secondary effect is also noticed in the yaw response, where after the initial overshoot, there is a second peak in the yaw rate response. This is seen at times 33.3 seconds, where after the initial overshoot, the passive vehicle settles quickly to the steady state value where as the controlled vehicle exhibits a second and more prominent yaw rate peak. This oscillation is an undesirable effect and is produced as a result of the dead time of the actuator.

To resolve this issue in the controlled vehicle, a correction function is introduced in the controller that reduces the RWS action when the driver turns the steering wheel to return to the zero steering angle position from the maximum steering angle for a cornering manoeuvre. In mathematical terms, this is the case when the derivative of the steering wheel signals has an opposite sign to the steering angle itself. In such conditions, the correction function reduces the gain of the RWS with respect

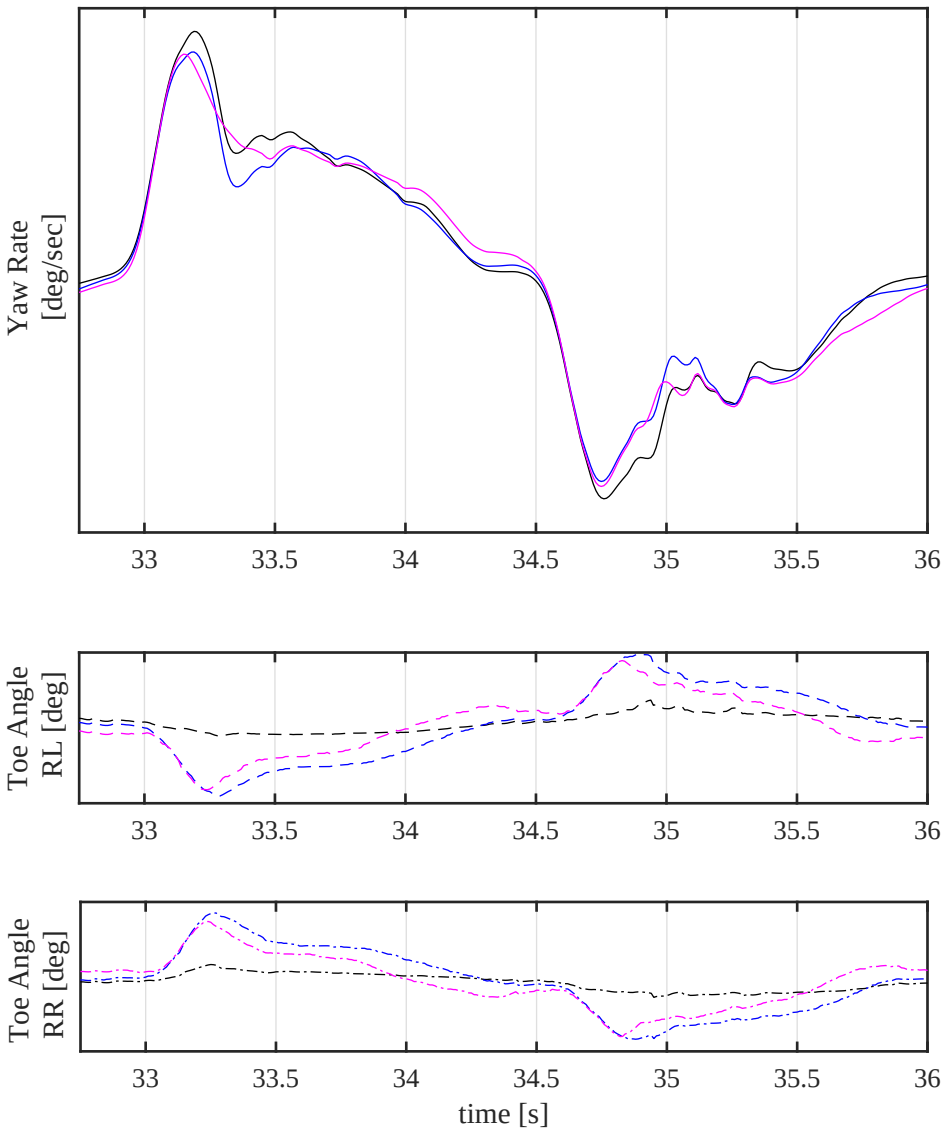

Figure 5.24 Response to a double lane change manoever for the controlled and the uncontrolled vehicles at 150 km/h using Hardware in the Loop simulation. Black- uncontrolled, blue- FF only, magneta- FF+correction function.

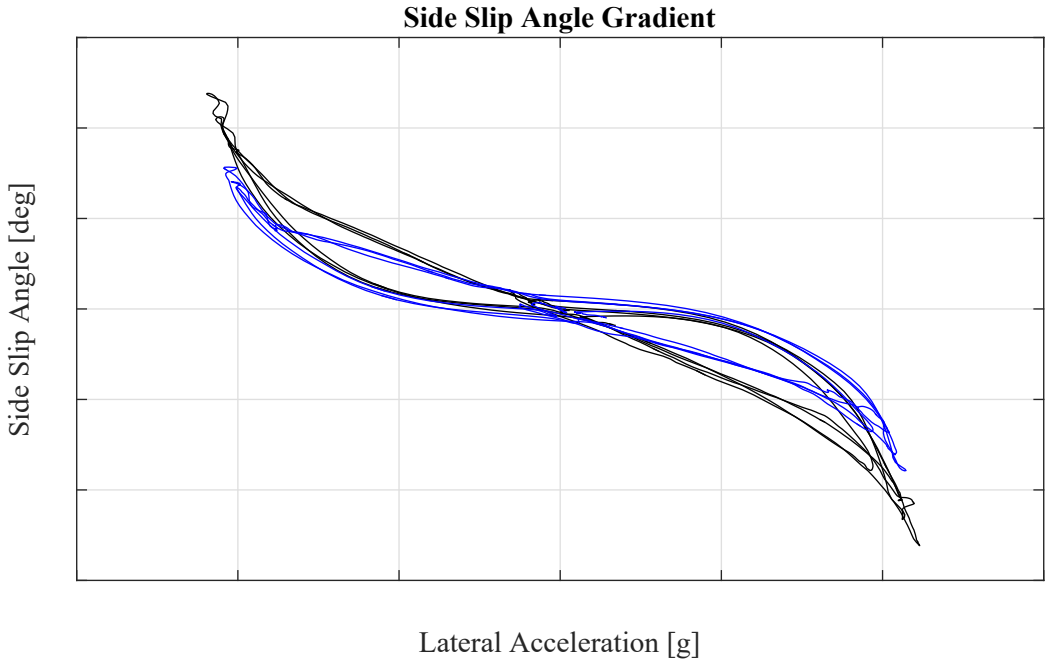

Figure 5.25 Slope of the plot between sideslip angle and lateral acceleration which indicates the lateral stiffness of the vehicle increases in the controlled vehicle (blue) with respect to the passive vehicle (black).

to the front steering wheel by a certain percentage. As a result, the response of the controller with the new correction function can be seen in magenta. With the introduction of the correction function, the controlled vehicle has a damped response and it also does not suffer from the presence of a second peak as seen at 33.3 seconds and at 35 seconds where the yaw response is smoother than the controlled vehicle without the correction function. Looking at the rear toe angles, it can be seen that the controller with the correction function has a lower value of toe angle magnitude when the steering wheel angle is returning back to the center position from the maximum steering angle.

The lateral stiffness of the controlled and the uncontrolled vehicles are compared by looking at the plot of the vehicle sideslip angle versus the lateral acceleration. A lower gradient of the plot indicates a laterally stiff vehicle. This is desirable as the vehicle is able to produce larger lateral accelerations at lower values of vehicle sideslip. This not only improves the vehicle stability but also indicates an improvement in the lag between lateral acceleration and yaw rate. Figure 5.25 shows the plot of sideslip versus lateral acceleration for the DLC manoeuvre shown above. It can be noticed that the slope of the curve for the controlled vehicle is lower than the uncontrolled

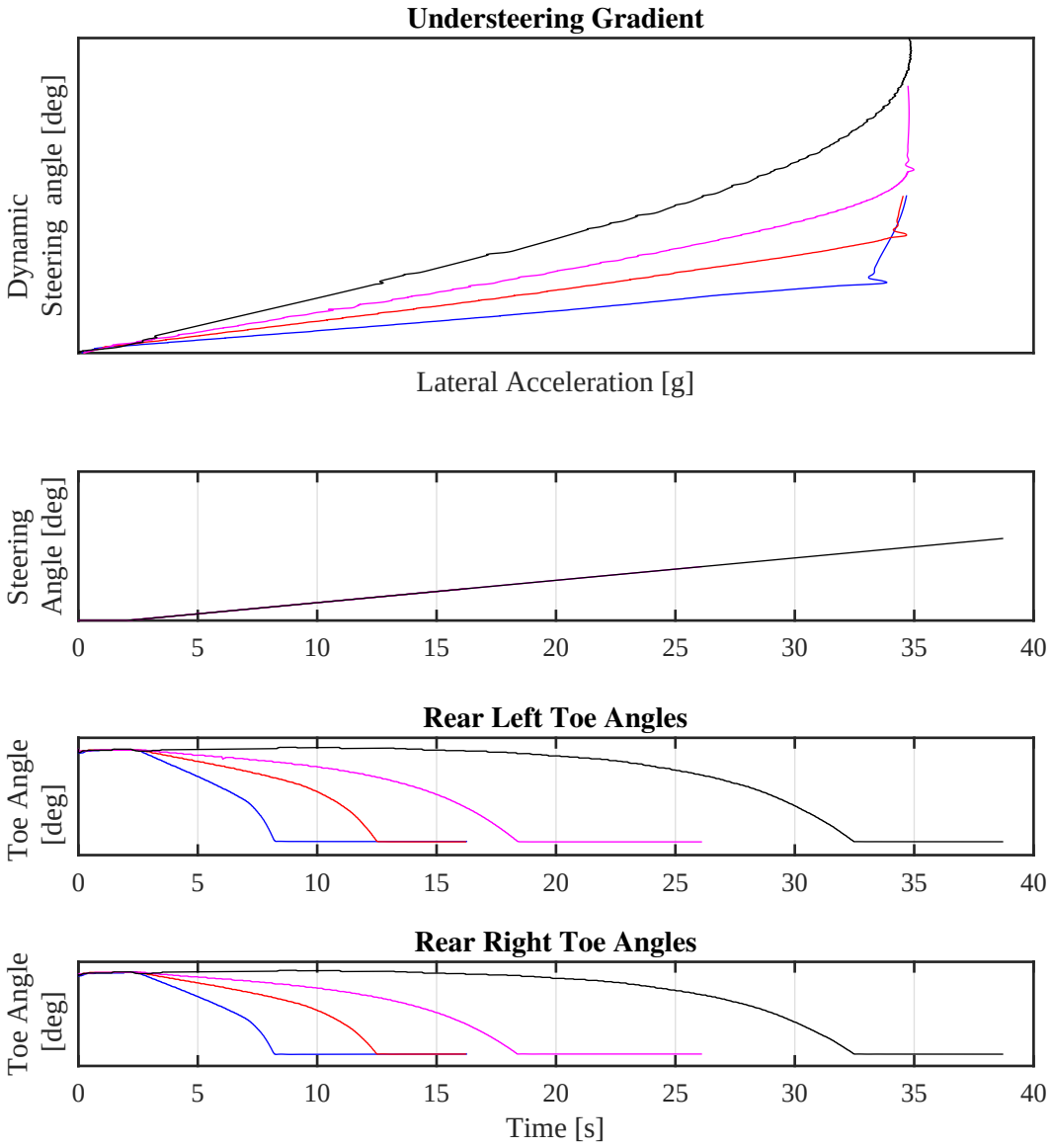

Figure 5.26 Understeering gradients imposed by the feedback controller. The vehicle understeering characterstics can be controlled from a highly understeering behaviour (black) to an almost neutral steering vehicle (blue) with intermediate behaviour shown by the red and the magenta curves.

vehicle. As a result of RWS action, due to in-phase steering, the sideslip angle of the controlled vehicle remains smaller than that of the uncontrolled vehicle.

Ramp Steer

The feedback controller, which is useful for the control of the vehicle during steady state manoeuvres, is tested by executing ramp steer manoeuvres. The manoeuvre involves giving a ramp steering input to the vehicle while driving at constant speed. Various desired understeering gradients are chosen as the target vehicle handling characteristics. While the passive vehicle has slightly understeering steady state behaviour, a slightly more understeering behaviour could be desirable while driving in urban scenarios. On the other hand, a more oversteering behaviour could also be chosen as the target vehicle characteristics to give the vehicle a more sporty feeling. Nevertheless, this would depend on the calibration choice of the engineer. In the simulation, a range of understeering gradients are imposed to demonstrate the capability of the feedback controller. The vehicle's response for the various controller settings can be seen in Figure 5.26. The vehicle is running a 100 km/h. It can be seen that the RWS actuators steer out of phase to the front steering angle. This reduces the vehicle understeer. Four different understeer gradients are implemented with the black curve having the calibration with the highest understeer and the blue curve having the lowest understeer. As it can be noticed, the larger is the magnitude of the out of phase RWS steering with respect to the input steer, the lower is the understeer.

5.4.3 Experimental Tests

To validate the controller performance in a real life environment, the controller is tested with the help of a prototype vehicle. The controller is embedded on a National Instruments cRIO control unit and run at 100 Hz. Various dynamic tests are carried out at the Nardo Technical Centre (NTC), in the south of Italy. The dynamic manoeuvres such as sine sweep and DLC are executed on the dynamic platform of the NTC. The vehicle handling is tested on the handling circuit of NTC. The prototype vehicle is driven by expert test drivers. These drivers have a very high sensitivity to the vehicle's dynamic behaviour and their subjective inputs are utilised to calibrate and fine tune the final controllers. Objective evaluation of the controller performance with a traditional performance metric, however, is difficult due to the inclusion of noise and other variable factors, such as track temperature, limitations of the human drivers in manoeuvre reproducibility, etc. As a result, time domain comparisons are

Figure 5.27 The dynamic platform at the Nardo Technical Center
The dynamic platform at the NTC. This area was used for the sine sweep, the double lane change and the ramp steer tests.

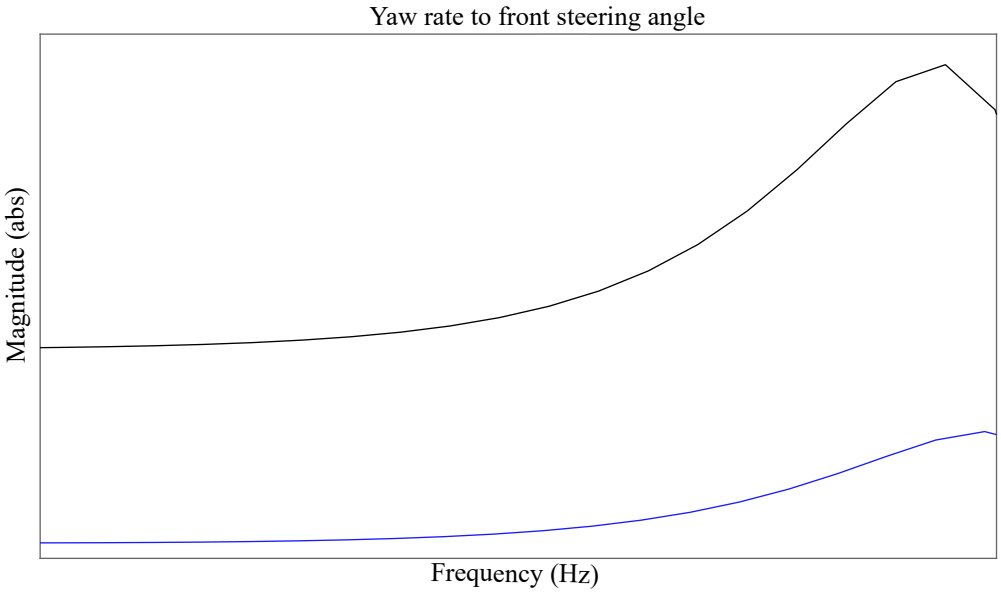

Figure 5.28 Magnitude of the yaw rate response to the front steering wheel angle input for the vehicle with (blue) and without (black) RWS control.

not utilised to perform an objective evaluation. In general, the drivers reported the controlled vehicle to be responsive yet stable, which are the desired characteristics, whereas the passive vehicle was found to be responsive but not as stable. A few objective results are presented as follows:

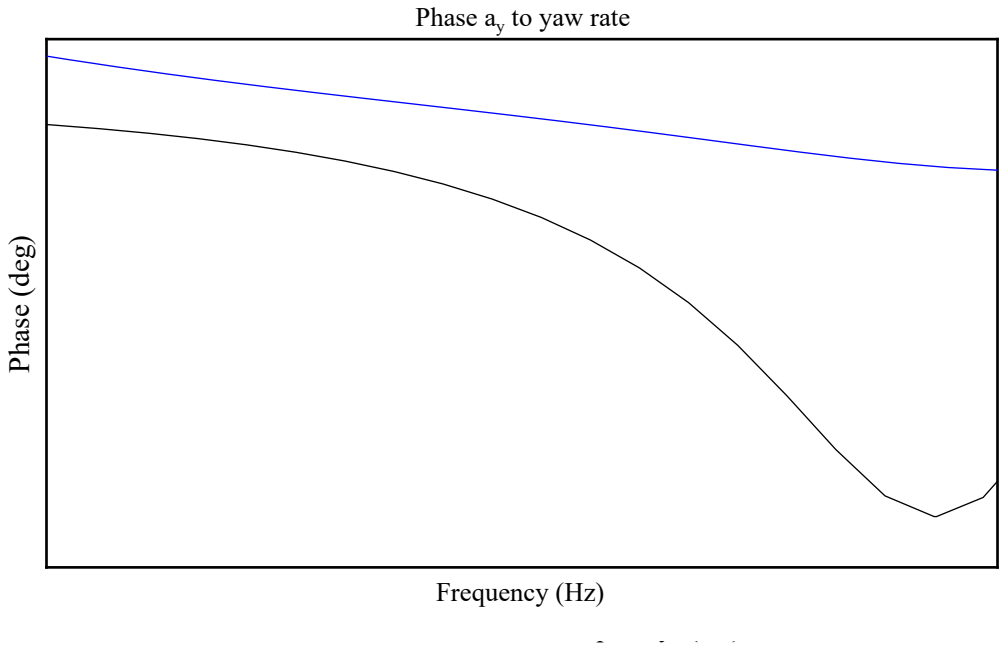

Figure 5.29 Phase between lateral acceleration and yaw rate for the controlled (blue) and the uncontrolled vehicle (black).

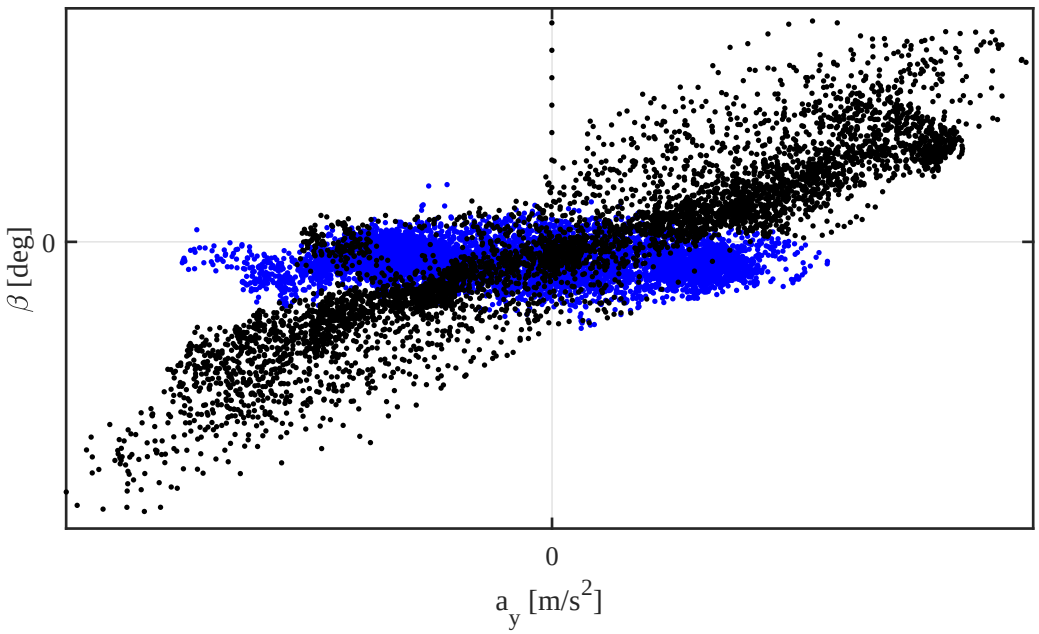

Figure 5.30 Plot of sideslip angle to the lateral acceleration for the controlled (blue) and the uncontrolled vehicle (black).

Sine Sweep

Sine sweep manoeuvres are executed at 100 km/h with the control system turned on and off. The human drivers are able to steer up to a frequency after which they are limited by their bio-mechanical capabilities. As a result the sweep manoeuvres include results plotted up to a frequency that is physically possible to be realised by the drivers. The transfer function of the yaw rate to the steering wheel input is identified by looking at the data log and then utilising system identification techniques. After the system identification, the Bode plot of the two identified transfer functions are plotted. Figure 5.28 shows the two transfer functions' Bode plot. It can be seen that the controlled vehicle has a lower yaw rate gain all through out the frequency range. Moreover, the uncontrolled vehicle shows a stronger resonance behaviour , while the resonance peak in the controlled vehicle is much smaller. As the resonance behaviour is undesirable, this undesirable behaviour is successfully eliminated by the use of the RWS system. Figure 5.29 shows the improvement in the lag between lateral acceleration and yaw rate due to the use of RWS. The blue curve shows the active vehicle while the black curve represents the passive vehicle. Again, the phase part of the Bode diagram is plotted by identifying the transfer functions from experimental data. It can be seen that all throughout the input frequency range, the active vehicle has very small phase lag. In the passive vehicle, the phase lag first increases with frequency after which it starts to reduce again. This demonstrates that the vehicle appears more responsive to the driver now due to the reduction of this phase lag. Furthermore, in Figure 5.30 it can be seen that the slope of the plot between sideslip angle and lateral acceleration is much more lower in the case of the controlled vehicle. This indicates that the controlled vehicle appears to be laterally more stiff to the driver, which is a desired effect.

Handling Circuit

The vehicle is driven around the handling circuit of NTC, once with the controller turned on and once with the controller turned off. Special care was taken to keep the conditions of both tests very similar to each other. This includes track temperature, tire pressures and the condition of the tires. Subjective feedback from the drivers indicated that the vehicle is more desirable to drive in terms of stability while entering and exiting a corner. For an objective evaluation, the sideslip angle of the

Figure 5.31 The handling circuit of the NTC. This area was used for the handling tests.

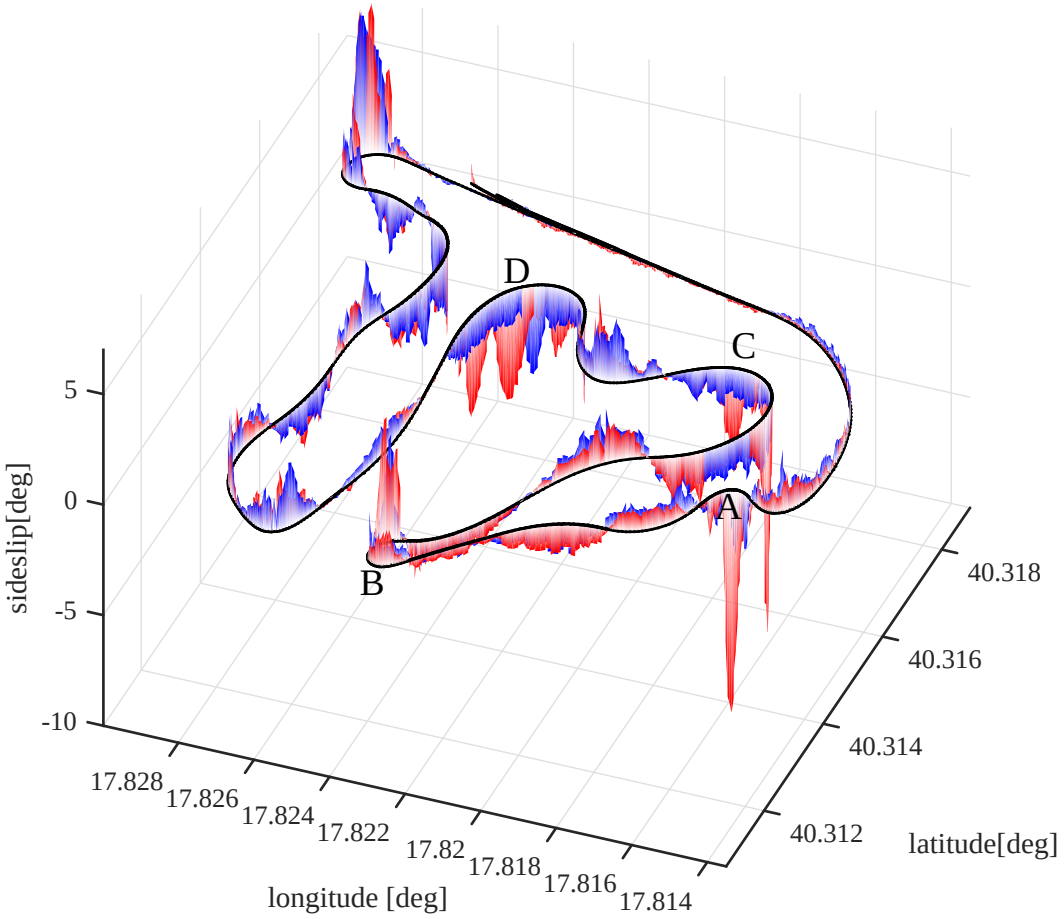

Figure 5.32 Spatial plot of the sideslip angle for the controlled (blue) and the uncontrolled vehicle (red).

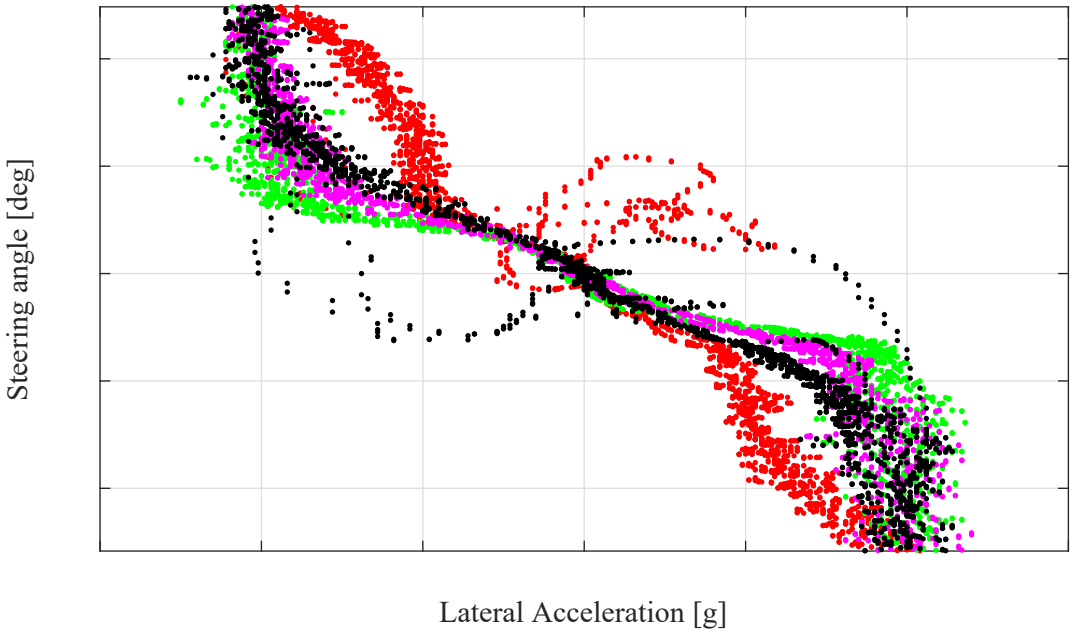

Figure 5.33 Different understeering curves obtained for the same vehicle using different RWS controller calibrations for a ramp steer manoeuvre.

vehicle is plotted for each section of the handling circuit of NTC. It can be noticed from Figure 5.32 that at turns of the circuit denoted by the letters 'A', 'B', 'C', 'D', the sideslip angle of the uncontrolled vehicle is larger than the sideslip angle of the controlled vehicle. This indicates that the controlled vehicle is more stable than the uncontrolled vehicle.

Ramp Steer

The designed feedback controller is tested in real life conditions on the prototype vehicle to repeat the same ramp steering test done in the HIL test. Three different understeering levels are chosen for the reference vehicle for the generation of the reference yaw rate signal to the feedback tracking controller. The plots of the steering angle versus the lateral acceleration for the different controller calibrations can be seen in Figure 5.33. The passive vehicle is shown in black, whereas the magenta curve shows a sporty calibration with lower understeer. The green curve shows a highly reactive vehicle, while the red curve shows a highly understeering vehicle. Subjective opinion of the test drivers for the three different calibrations indicate that the magenta curve is a desirable behaviour where the vehicle is slightly less under-

steering than the passive vehicle. The green calibration is too reactive and might not be suitable as normal drivers might get afraid due to the high reactivity of the vehicle. The red calibration on the other hand is too much understeering which is also very undesirable as the vehicle refuses to turn even after a very large input of the steering wheel.

Looking at the plot, it can be noticed that all the four scatter plots for the four different cases are the same for small values of lateral acceleration in both right and left directions. This is due to the fact that delay of the actuator causes no RWS action for the first τ_{delay} seconds and after that, the low gain of the feedback controller (due to stability concerns) gives a very slow feedback correction. As a result, for the initial part of the ramp manoeuvre, all the four cases have no or negligible RWS action. This discrepancy also introduces a strange subjective feeling as the understeering gradient of the vehicle changes after the initial part of a ramp manoeuvre.

5.5 Conclusions

A control algorithm for the RWS system is developed with the target of introducing yaw damping and reducing the lag between lateral acceleration and yaw rate. The passive vehicle's behaviour was studied with the help of simple linearised models that indicated the presence of a resonance peak in the vehicle's yaw rate frequency response, as well as the presence of zeros, which caused overshoot. The designed control algorithm comprised of feedforward and feedback controllers that work in tandem. The design of the FF controller has been carried out by inverting the dynamics of the passive vehicle and multiplying it with the desired vehicle response to obtain the RWS steer angle from the desired yaw rate of the vehicle. The feedback controller has been developed by the means of a loopshaping technique, which is designed by linearising the vehicle and the actuator dynamics model. It has been found that the presence of a time delay in the actuator dynamics and a RHP zero in the vehicle dynamics are the limiting factors of the feedback controller's performance.

The designed control scheme is tested in multibody simulation, HIL simulation and on a prototype vehicle. Multibody simulations indicate that the FF controller alone is quite capable to achieve the desired performance, while the contribution of the FB controller is minimal due to the presence of time delays. Hypothetical

scenarios where the actuators do not suffer from time delays are also simulated to demonstrate the performance benefits of the FB controller designed for a system without the delay. The outcome strongly motivates the development of a lag free actuator. HIL simulations are used to objectively study the benefits introduced by the control system while simulating a more realistic plant including the actual actuator dynamics. Tests demonstrate that the controller is able to improve the response of the vehicle by eliminating secondary oscillation peaks while the vehicle is executing DLC manoeuvres. Finally, the controller is extensively tested on track with the prototype vehicle for having the subjective feedback of the test drivers which in turn leads to a fine tuning of the controller calibration. Subjective evaluation indicates that the control system introduces a feeling of improved stability in the vehicle while it executes dynamic manoeuvres.

Chapter 6

Torque Vectoring

6.1 Introduction

Figure 6.1 Politecnico di Torino's electric racing vehicle, the SCXV, is an AWD vehicle. It is capable of full torque vectoring due the presence of independently actuated in-wheel electric motors

Torque vectoring involves the transfer of uneven driving torque across different wheels of the vehicle. For FWD/RWD vehicles, it involves uneven driving torques on the left and the right wheels. For AWD vehicles, it can include just variable torque distribution across the front and rear axles [56] or variable front-rear axle distribution followed by variable left right torque distribution across the front and the rear axles [74]. The uneven distribution of torque across the left and the right wheels causes a yaw moment across the vehicle's vertical axis. When controlled, this yaw moment can be used to control the vehicle's dynamic response, which can be

then used to obtain a desired vehicle handling performance. The following sections in this chapter will develop a torque vectoring algorithm that is aimed to improve the lap-time of an electric racing vehicle.

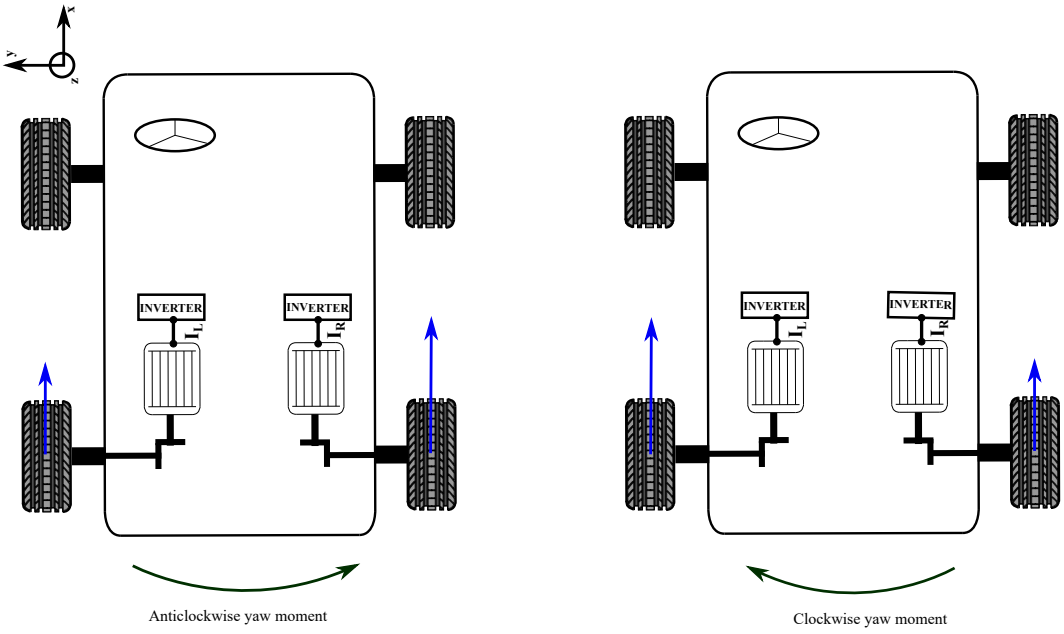

Figure 6.2 Yaw moment generation by uneven driving torque distribution across an axle.

6.2 Vehicle and Driver Modelling

The baseline vehicle under study is a rear wheel drive electric vehicle with two permanent magnet electric motors each driven by a separate inverter module. The vehicle model for numerical simulations is realized using a VI-CarRealTime-Simulink co-simulation based model. The reason for this choice is that VI-CarRealTime is a software that replicates the behaviour of the vehicle very accurately in terms of a reasonable frequency band. Moreover, it is also used widely in the automotive industry by OEMs to have accurate simulation of vehicles without the need to go on the track. The layout of the powertrain can be seen in Figure 6.3. The chassis is modelled considering both sprung and unsprung masses. The suspension characteristics includes non-linear models of the springs, dampers and anti-roll bars. Effects of roll steer, roll camber, toe angle variation and camber angle variation are taken into account with the help of suspension and steering geometry modelling. The kinematics of the

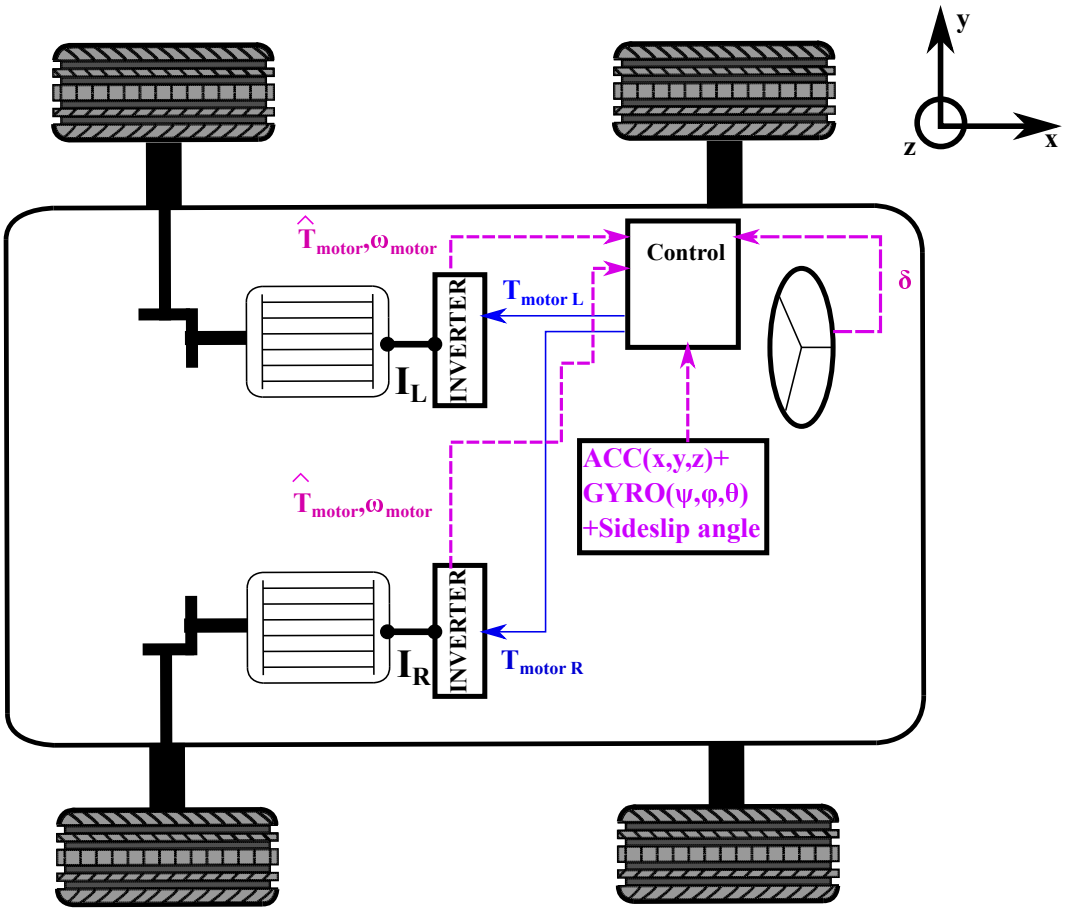

Figure 6.3 Vehicle powertrain layout.

steering and suspension are modelled with the help of lookup tables, which eliminate the need of a complex multibody subcomponent modelling. Combined slip effects of the tires are modelled with the help of Pacejka's formula, which also takes effects due to the tire relaxation length in account. The electric motors are modelled with the help of experimentally validated and scaled torque speed maps. The torque speed maps consider the effect of de-fluxing within the electric motors after a certain motor speed. The electric motors' moment of inertia is considered in the modelling along with the transmission ratio. This is necessary as when the wheels start slipping or locking under braking, the effects of the motor inertia on the wheel rotational dynamics is no longer negligible. Regenerative braking is enabled on the rear wheels using the electric motors, while the front wheels use conventional hydraulic powered friction brakes. However, if the braking demand on the rear wheels exceed the electric motor's torque capabilities, the friction brakes are then engaged

to fill in the excess braking torque demand. This is assumed to be possible due to the presence of the ABS system in most vehicles, which allows individual wheel braking using an electro-hydraulic braking system. The typical characteristics of the vehicle is mentioned in Table 6.1.

Table 6.1 Vehicle Parameters

Property	Symbol	Value	Unit
Mass	m	1300	kg
CG from front axle	a	1500	mm
CG from rear axle	b	1000	mm
CG height from ground	h_{cg}	415	mm
Front track width	t_f	1760	mm
Rear track width	t_r	1740	mm
Yaw moment of inertia	I_{zz}	850	kgm^2
Maximum Torque of Electric motor	T_{max}	290	Nm
Maximum speed of Electric motor	ω_{max}	16000	rpm
Motor to wheel transmission ratio	τ_d	6	-

Various driver models for racetrack lap time optimization are presented in [97–100]. The above methods use preview based and/or model predictive control(MPC) techniques. The inbuilt VI-CarRealTime driver model is widely accepted in the automotive industry for CAE testing and it has been also utilised in [100] as benchmark for testing the author's algorithm performance. Thus, the VI-CarRealTime driver model, which has a preview based MPC controller, is chosen for running the fastest lap time manoeuvres and testing the performance of the motor torque control strategy. The driver model consists of steering, throttle and brake controllers. The steering controller's objective is to follow a desired vehicle path that is available as a predetermined trajectory. The steering controller calculates the amount of required steering angle input based on a preview time which allows it to 'look' ahead in time to compute the connecting contour from the initial trajectory to the final trajectory of the vehicle at the end of the preview time. Using the differential flatness principle, the connecting contour is inverted to obtain the appropriate steering angle [101]. The longitudinal vehicle dynamics is controlled by a throttle and braking controller that calculates the traction or braking torque demand as a function of the reference speed profile. Using a FF and FB control structure, the torque demand reduces the error between the actual vehicle speed and the target vehicle speed. Finally, once the torque demand is known, the throttle is computed as a percentage of the maxi-

mum powertrain available torque, which is a function of the vehicle speed and the transmission ratio, while the braking torque is computed as a percentage of the maximum braking torque available, which is a function of the braking circuit's physical properties [101]. The driver is set to the 'Professional' setting which allows it to replicate the behaviour of a racing driver. The driver model also takes into account the tire limits and thus it is able to replicate the performance of an expert racing driver and take the vehicle very close to its physical handling limits. For simulating the fastest laptime, the driver model uses an algorithm called the 'MaxPerformance'. This algorithm works by first generating a speed profile for a given trajectory of the racetrack circuit. This speed profile is generated by approximating the vehicle's lateral and longitudinal acceleration capabilities. Then, the algorithm runs the vehicle simulation while trying to follow the speed profile. While cornering, when the initial cornering speed is set too high, the vehicle might go off the track. In such cases, the speed profile is modified by reducing the cornering speed and the simulation is reiterated. After a series of iterations, the fastest laptime is obtained.

6.2.1 Passive Vehicle Characterisation

The steady state handling behavior of a vehicle is determined qualitatively by looking at the slope of the steering angle to the lateral acceleration during a constant radius circle (CRC) manoeuvre [76]. In this manoeuvre, the vehicle is made to follow a circular path with a fixed radius and the speed of the vehicle is altered. Since the lateral acceleration changes as function of the square of the longitudinal velocity of the vehicle, the steer input needed to maintain the circular path with changing lateral acceleration can be plotted. CRC plot manoeuvres with a radius of 100 meters and different acceleration levels are shown in Figure 6.4. The vehicle is driven along a circle at a fixed initial speed until the steering angle and the lateral acceleration reach steady state level. Then the vehicle is accelerated or decelerated while maintaining the same circular path. For the acceleration manoeuvres, the initial speed is 10 m/s while for the deceleration manoeuvres, the speed is 40 m/s. It can be noticed that the vehicle exhibits understeering nature while accelerating during cornering as the slope of the steering angle to lateral acceleration is positive. On the contrary, oversteering tendency is seen when the vehicle brakes during cornering. It is interesting to see that the understeering nature increases with the increase in acceleration and the oversteering nature increases with the increase in deceleration. This

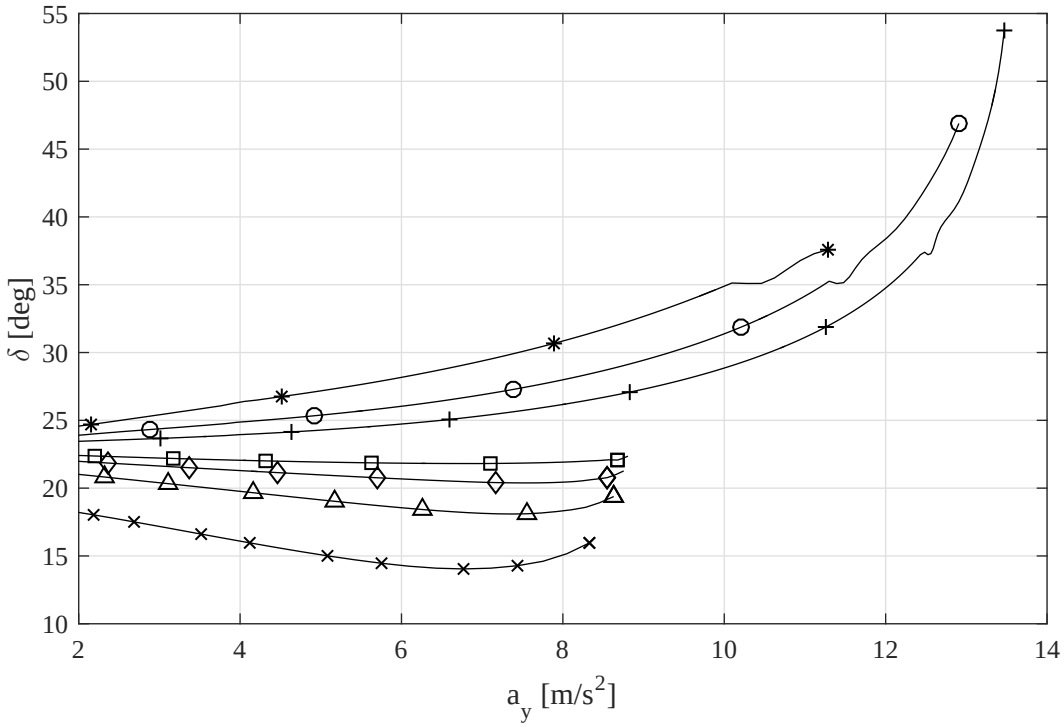

Figure 6.4 Baseline vehicle understeering gradient variation with different longitudinal acceleration during constant radius circle manoeuvres. The different markers namely asterisk, circle, plus, square, diamond, triangle and cross represent a_x equal to 4 m/s^2, 2 m/s^2, 1 m/s^2, -1 m/s^2, -2 m/s^2, -4 m/s^2 and -8 m/s^2 respectively.

behaviour can be explained by the 40 - 60 static weight distribution and the effect of longitudinal load transfer due to longitudinal acceleration or deceleration. When the vehicle accelerates, the load is transferred from the front to the rear wheels. As a result the front wheels are able to generate less cornering forces as compared to the rear wheels and thus go into saturation earlier. This causes understeer. The reverse happens during braking. Due to load transfer to the front, the rear wheels saturate earlier and this leads to an oversteering behaviour.

6.2.2 Desired Vehicle Response

While left right torque transfer will increase the axle lateral force, the effect of tire sideslip should also be considered. Increasing the tire sideslip up to the saturation limit of the tire also leads to an increase in the tire lateral force. It is common knowledge that a vehicle with a neutral handling characteristics is most suited for setting

laptimes. This is because during understeer, the front sideslip angles are larger than the rear sideslip angles. The reverse happens when the vehicle is oversteering. In either case, at limit conditions, only the front or the rear tires are able to reach saturation, while there is still some grip left in the unsaturated tire. The objective of setting a fast laptime boils down to maximising the maximum grip available from the tires which is possible with a neutral handling behaviour.

As demonstrated in [102], it is possible to use TV to increase the sideslip angles of the unsaturated tires and increase the maximum possible lateral force from the tires. This leads to higher lateral accelerations and in turn faster lap times. Thus, the TV control strategy should work to bring the sideslip angles of both the tires close to each other. In this case, the response of the controlled vehicle becomes closer to a neutral steering vehicle. As a result, the driver also needs to work less with the steering inputs as the understeer/oversteer correction is done by TV and not by the driver's steering. This leads to a less nervous driver action and the manoeuvrability of the vehicle also increases. Since the vehicle is understeering during cornering with acceleration and oversteering during cornering with deceleration, torque transfer to the outer wheel will lead to an oversteering moment during acceleration and understeering moment during deceleration. This helps to counter the natural tendency of the vehicle as shown in Figure 6.4 and helps it to achieve neutral steer characteristics.

6.3 Control System Design

Supervisory control schemes have proven to be a popular choice in chassis control systems [61, 78]. In the domain of torque vectoring, such control schemes are generally composed of a two level nested control architecture. The outer level is responsible for computing the desired value of yaw moment for achieving the desired vehicle response. The desired vehicle response is generally obtained from simple models such as a first order system as shown in Nagai et al. [43, 48], where the gain and the time constant are tuned to obtain a desired response or a two degree of freedom bicycle model with a fixed understeering gradient as demonstrated by Chung et al. in [52] or an offline optimized function with customized understeer characteristic as used by DeNovellis et al. [59, 61, 62]. The inner level controller is responsible for the generation of the desired yaw moment provided by the outer

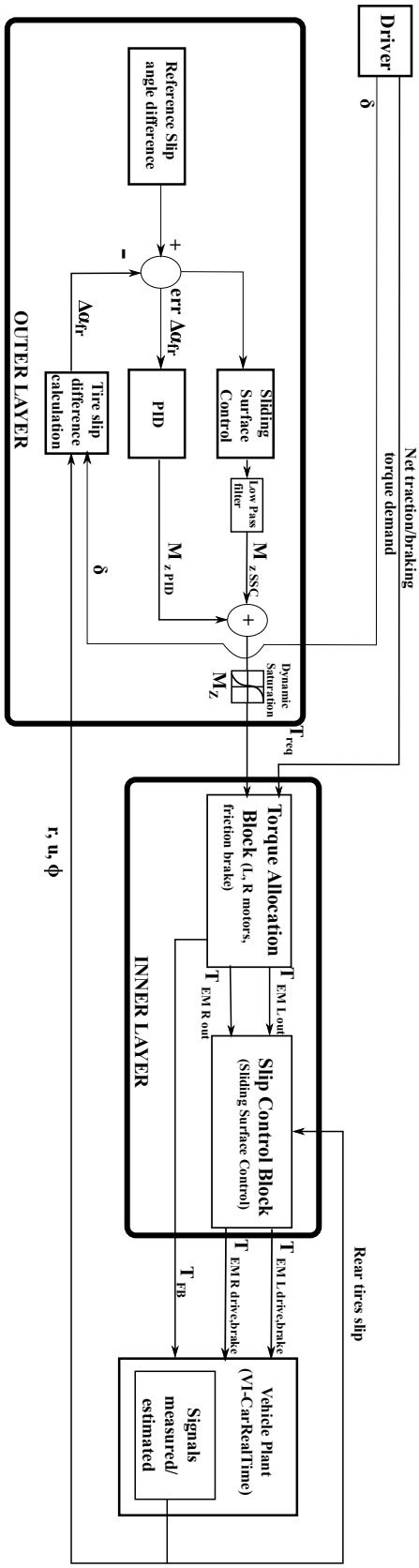

Figure 6.5 Control system architecture.

control layer. It controls the actuators such as brakes, motor torque etc., keeping in mind the actuators' saturation levels and actuator dynamics.

The implemented control architecture, which is composed of an outer and an inner level controller, is shown in Figure 6.5. The outer layer control is responsible for generating a desired TV yaw moment, which acts as a reference to the lower layer control. The objective of this TV yaw moment is to give the vehicle a desired behaviour in terms of its handling characteristics. The lower layer control is responsible for generating the desired TV yaw moment by controlling the individual motor torques while regulating the drive quality and the rear wheel longitudinal slips. The individual blocks are explained in detail in the following sections.

6.3.1 Outer Control Layer

The outer control layer is composed of two feedback control blocks, a tire slip angle difference calculation block and a reference slip angle difference block. While in literature, one always finds the vehicle yaw rate or the sideslip angle as the control parameter, in this work, a new control parameter is introduced, that is the difference between the front and the rear tire sideslip angles. The advantage that this new control parameter introduces is the lack of a vehicle reference model. Often reference yaw rate models need to be saturated as a function of the maximum lateral acceleration, which causes issues near the grip limit. This method instead allows a more direct control of vehicle understeer/oversteer. This difference is computed using the tire slip angle difference block, and the error in this parameter is computed by taking the difference between the desired and the actual tire sideslip angle difference. The error is then reduced using feedback blocks. The feedback controller ensures a neutral steer behaviour by controlling the difference of the sideslip angles of the front and rear axle.

Tire Slip Angle Difference

For the slip angle computation, the vehicle can be represented by a bicycle model as seen in Figure 6.6. Using kinematics, the slip angles of the front and rear tires

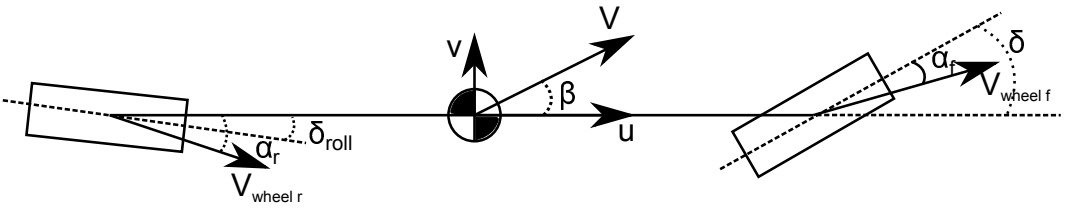

Figure 6.6 Bicycle model representation of the vehicle.

denoted by α_f, α_r can be written as

$$\alpha_f = \beta + \frac{ar}{u} - \delta, \tag{6.1}$$

$$\alpha_r = \beta - \frac{br}{u} - \delta_{roll}, \tag{6.2}$$

where β is the sideslip angle, r is the yaw rate, u is the vehicle velocity along the longitudinal axis, δ is the input steer at the front tire due to driver input and roll steer and δ_{roll} is the steer at the rear tire due to roll. From Equation 6.1 and Equation 6.2, the difference between the front and rear tire slip angles can be written as

$$\alpha_f - \alpha_r = \frac{(a+b)r}{u} - \delta + \delta_{roll}. \tag{6.3}$$

The desired sideslip angle difference is set to zero so that the vehicle achieves a neutral steer characteristics.

It is interesting to notice that the vehicle sideslip angle gets eliminated from the computation of the difference of the tire slip angles in Equation 6.3. A simplified model for obtaining the roll steer is implemented as

$$\delta_{roll} = \mathrm{K}_{\mathrm{rollsteer}}\phi, \tag{6.4}$$

where $\mathrm{K}_{\mathrm{rollsteer}}$ is the roll steer constant and ϕ is the roll angle [103, 12].

Feedback Controllers

The feedback control loop is composed of two components, a PID controller and a sliding surface controller (SSC). Both the PID and the SSC controllers control the difference between the front and rear tire sideslip angles. The reason for utilising an integrated stucture with both PID and SSC instead of just SSC or just PID is

to have the advantages of both these kinds of controllers. It has been noticed that while a continuous controller such as PID ensures a smooth tracking response, it may not be robust enough. On the other hand sliding surface controllers have been demonstrated to be robust on modeling uncertainties, but they suffer from issues like chattering and un-smooth reponse. Using them together ensures a robustness along with a smoother response as demonstrated in the work of Sorniotti et al. [61, 62]. Thus, the total corrective yaw moment to be generated by torque vectoring can be written as

$$M_z = M_{zPID} + M_{zSSC}. \tag{6.5}$$

The input to the PID controller is the error in the desired value of the difference between the front and rear axle sideslip angles. The output of the controller is the TV torque contribution, which is represented by M_{zPID} and it can be written as

$$M_{zPID} = \mathrm{K_p}(\alpha_f - \alpha_r) + \mathrm{K_d}\frac{d(\alpha_f - \alpha_r)}{dt}, \tag{6.6}$$

where $\mathrm{K_p}$ are $\mathrm{K_d}$ are the proportional and derivative feedback constants respectively. The integral part of the PID controller is not used.

The SSC controller is based on the yaw dynamics of a bicycle model representation of the vehicle. The equation of motion which represents the yaw dynamics of the vehicle is given by

$$\dot{r} = \frac{aF_{yf} - bF_{yr} + M_{zSSC}}{I_{zz}}. \tag{6.7}$$

Since the objective of the controller is to reduce the difference between the front and the rear tire sideslip angles, the desired sliding surface to be controlled is written as a scalar s_{ss} where

$$s_{ss} = \alpha_f - \alpha_r. \tag{6.8}$$

Thus for the vehicle to have the front and rear tire sideslip angles to be the same, the scalar s_{ss} is kept to zero. This is achieved by using the following control law,

$$\frac{1}{2}\frac{d}{dt}s_{ss}^2 = s_{ss}\dot{s}_{ss} \leq -\eta_{ssc}s_{ss}^2, \tag{6.9}$$

where η_{ssc} is a positive constant.

Using Equation 6.3, the derivative of the scalar variable s_{ss} can be written as

$$\begin{aligned}\dot{s}_{ss} &= \frac{d(\alpha_f - \alpha_r)}{dt} \\ &= \frac{d(\frac{(a+b)r}{u} - \delta + \delta_{roll})}{dt}.\end{aligned} \tag{6.10}$$

The control law in Equation 6.9 can be written as

$$\dot{s}_{ss} = -K_{M_{z,ssc}} s_{ss}. \tag{6.11}$$

Using Equation 6.10 in 6.11,

$$\begin{aligned}&\frac{d(\frac{(a+b)r}{u} - \delta + \delta_{roll})}{dt} = -K_{M_{z,ssc}}(\alpha_f - \alpha_r), \\ &(a+b)[\frac{\dot{r}u - r\dot{u}}{u^2}] - \dot{\delta} + \dot{\delta}_{roll} = -K_{M_{z,ssc}}(\alpha_f - \alpha_r),\end{aligned} \tag{6.12}$$

Ignoring $\dot{\delta}$ and $\dot{\delta}_{roll}$ from the above equation as they are small numbers,

$$\dot{r} = \frac{\dot{u}r}{u} - \frac{K_{M_{z,ssc}} u(\alpha_f - \alpha_r)}{(a+b)}. \tag{6.13}$$

From Equations 6.7 and 6.13,

$$\begin{aligned}&\frac{aF_{yf} - bF_{yr} + M_{zSSC}}{I_{zz}} = \frac{\dot{u}r}{u} - \frac{K_{M_{z,ssc}} u(\alpha_f - \alpha_r)}{(a+b)}, \\ &M_{zSSC} = \frac{I_{zz}\dot{u}r}{u} - \frac{I_{zz}K_{M_{z,ssc}} u(\alpha_f - \alpha_r)}{(a+b)} - aF_{yf} + bF_{yr},\end{aligned} \tag{6.14}$$

where $K_{M_{z,ssc}}$ is a positive constant greater than η_{SSC} and large enough to guarantee stability of the controller [78]. A low pass filter is added to the output of the controller so as to avoid chattering [62, 104]. The sliding surface controller requires the information about the lateral forces. However for the sake of brevity, it is assumed that the knowledge of the lateral forces is available as the topic of study is not to find a method for estimating the lateral forces. The literature provides numerous methods to estimate the lateral forces [6, 8, 12, 15, 16, 18, 23, 105, 106].

The force generating capability of a tire is limited by its friction circle, which is the boundary of maximum force a tire can produce in the lateral and longitudinal directions, given all possible operating points [75, 77]. The larger the friction circle is, the larger the g-g diagram of a vehicle would be [92]. The maximum performance can be extracted from a vehicle when all four tires are working on the boundary of this friction ellipse and thus, they are generating the maximum amount of available force. For cornering at maximum speeds, racing drivers try to always make all the tires work along the boundary of the friction circle [92]. However, with conventional differentials which have 50-50 torque distribution between the left and right wheels, it is not always possible to fully exploit each tire. Such effects occur during cornering due to the effect of lateral load transfer, where the inner wheel has lower vertical load than the outer wheel. As a result, the maximum transmissible traction/braking torque by the wheels is limited by the inner wheel. Assuming that in a limiting condition, the inner wheel produces longitudinal force whose magnitude is equal to the radius of the friction circle, the maximum lateral force that could be produced by that tire is equal to zero. While cornering, if some of the traction torque is transmitted to the outer wheel, the maximum lateral force that the outer wheel can produce will decrease a bit due to the increase in its longitudinal force, but the inner wheel at the same time will be able to generate some lateral force and the net sum of lateral forces generated by the inner and the outer wheel can be larger than the sum of the lateral forces generated by both wheels in the case without TV. However, if amount of transferred torque is beyond a certain threshold, this might lead to a reduction of the net lateral force produced by the axle.

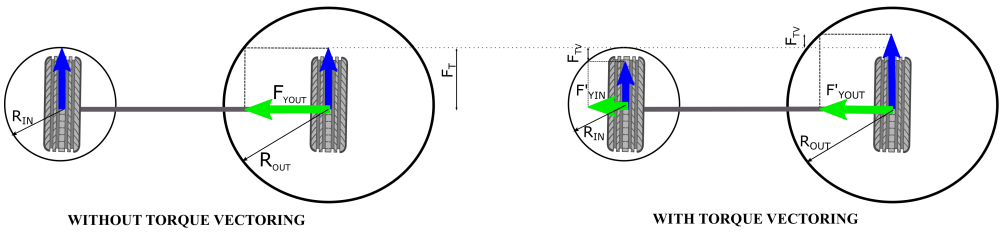

Figure 6.7 Increase in the net axle lateral force by torque vectoring.

A simplified analysis on this effect has been described by Sawase et al. in [70]. This can be seen in Figure 6.7. The figure shows left and right tires of a given axle. The vehicle is assumed to be cornering in the left direction, which introduces higher load on the right wheel. For a given rear axle tire sideslip angle and assuming that the lateral load transfer in the case with and without torque vectoring is close to each

other, the increase in the net axle lateral force, ΔF_y can be computed as follows,

$$\begin{aligned}\Delta F_y &= F'_{Yin} + F'_{Yout} - F_{Yout} \\ &= (R_{in}^2 - (F_T - F_{TV})^2))^{\frac{1}{2}} + (R_{out}^2 - (F_T + F_{TV})^2))^{\frac{1}{2}} - (R_{out}^2 - F_T^2)^{\frac{1}{2}},\end{aligned} \tag{6.15}$$

where F'_{Yin}, F'_{Yout} are the lateral forces on the inner and outer tires of the vehicle with TV, F_{Yout} is the lateral force on the outer tire of the vehicle without TV, F_{Yin} is zero due to tire saturation, R_{in}, R_{out} are the radii of the left and right tire friction circles, F_T is the traction force on demanded by the driver on each wheel, F_{TV} is the increase/decrease in traction force due to TV. Sawase et al. in [70] analytically calculated that the maximum increase in lateral force is obtained when

$$F_{TVmax} = \frac{F_T(R_{out} - F_T)}{(F_T + R_{out})}. \tag{6.16}$$

Figure 6.8 shows the variation of the increase in the net axle lateral force due to

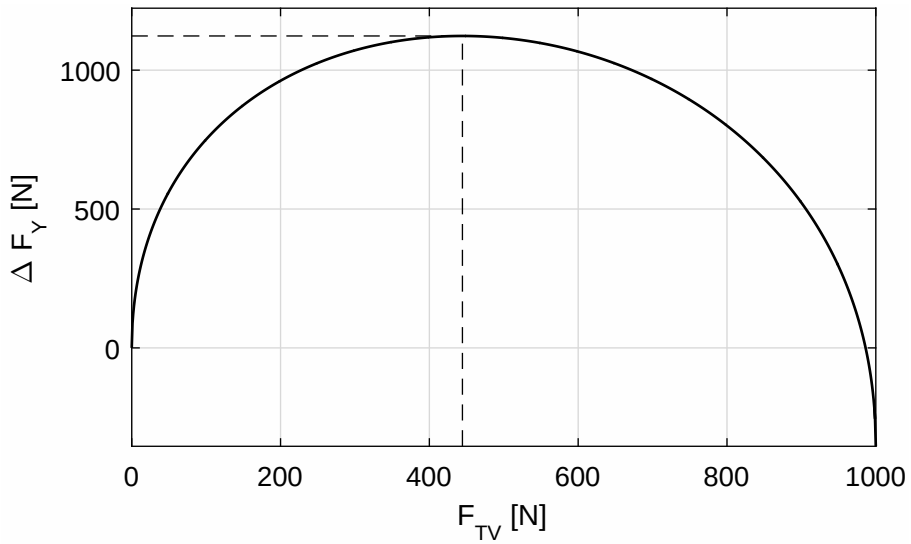

Figure 6.8 Variation of increase in axle lateral force (ΔF_Y) due to torque vectoring with increasing value of force on wheel due to torque vectoring (F_{TV}). The dashed line indicates the value of F_{TV} which gives the maximum ΔF_Y

.

torque vectoring as a function of F_{TV}. It can be observed that the ΔF_y has a maxima whose abscissa value is given by Equation 6.16. Using the lateral and longitudinal load transfer equations and assuming that the road surface friction, μ is known, R_{out}

can be written as

$$R_{out} = \mu F_{z,out} \\ = \mu \left(mg(\frac{a}{2L} + \frac{a_x h_{cg}}{2gL}) + \frac{abs(a_y)}{gt_r}(\frac{K_{\phi r} mg h_{cgrc}}{K_{\phi f} + K_{\phi r} - mg h_{cgrc}} + \frac{mg h_{rc} a}{L}) \right), \tag{6.17}$$

where m is the mass of the vehicle, a, b are the distances of the front and rear axles from the CG, l is the wheelbase length, h_{cg} is the CG height from the ground, h_{cgrc} is the CG height from the roll axis, g is acceleration due to gravity, a_y is the lateral acceleration, $K_{\phi f,r}$ are the front and rear axle roll stiffness, t_r is the rear axle trackwidth. $F_{z,out}$ is the normal load on the outer wheel of the axle while a vehicle is cornering [76]. The expression is obtained by considering the load transfer due to lateral acceleration and considering the roll of the vehicle body across the roll center. Thus the maximum amount of TV moment which allows increase in the net rear axle lateral force is given by

$$M_{z,TVmax} = F_{TVmax} t_r. \tag{6.18}$$

A saturation block is added to the output of the feedback controller such that the torque vectoring moment is saturated dynamically at M_{TVmax}.

6.3.2 Inner Level Controller

The inner level controller is responsible for the generation of the requested corrective yaw moment by the outer level controller by controlling the two rear motor torques. It is composed of two main components. The first component is responsible for the allocation of individual motor torques to generate the torque vectoring moment from the given throttle demand by the driver and torque vectoring demand by the outer level controller. The second component is responsible for controlling the wheel's longitudinal slip such that the wheel slip always stays within the linear behaviour working zone.

Torque Allocation Block

This block is responsible for the allocation of torque to the individual rear electric motors and to also activate the rear wheel friction brakes when necessary. The torque allocation block divides the requested motor drive/braking torque T_{req} equally between the left and right motors. If the braking torque demand is higher than the braking capability of the electric motors, the low level controller activates the rear wheel friction brakes to fill in the extra braking torque demand on each wheel.

$$T_{EML,R} = \begin{cases} \frac{T_{req}}{2} & \text{if } T_{req} > -2T_{max}(\omega) \quad (6.19) \\ -T_{max(\omega)} & \text{if } T_{req} \leq -2T_{max}(\omega) \quad (6.20) \end{cases}$$

$$T_{FB} = \begin{cases} 0 & \text{if } T_{req} > -2T_{max}(\omega) \quad (6.21) \\ (\frac{T_{req}}{2} + T_{max(\omega)})\tau_d & \text{if } T_{req} \leq -2T_{max}(\omega), \quad (6.22) \end{cases}$$

where T_{FB} denotes the rear wheel friction brake demand. Since an active hydraulic braking circuit is absent in the baseline passive vehicle, the braking torque due to the friction brakes is the same on the the left and the right wheels. The torque required for generating the requested TV moment, M_z, is then added to the wheel torques. The sum of the torques acting on the left and the right wheel is always kept equal to the traction/braking torque demand. When the sum of the torque contributions due to driver torque demand and outer level controller demand on a motor is larger than the maximum motor torque, the torque contribution due to torque vectoring is reduced on both wheels equally so that the net torque request on each motor is always within the maximum torque limit of the motor. The motor torque computation for this block is expressed as follows:

$$T_{lim} = min(T_{max(\omega)} - |T_{EML}|, T_{max(\omega)} - |T_{EMR}|), \quad (6.23)$$

$$\Delta T = min(T_{lim}, |\frac{M_z R_w}{t\tau_d}|)sign(M_z), \quad (6.24)$$

$$T_{EMLout} = T_{EML} - \Delta T, \quad (6.25)$$

$$T_{EMRout} = T_{EMR} + \Delta T, \quad (6.26)$$

where T_{lim} defines the maximum limit of torque available for TV, ΔT represents the torque added due to TV, T_{EMLout}, T_{EMRout} represent the actual amount of torque

output to the slip control block, t is the average of the track width of the front and rear axles.

Slip Control Block

This block is important for operation conditions such as high longitudinal accelerations at low longitudinal speed or during combined cornering with traction/braking. When the motor traction torques on the wheels exceed the grip limit of the tire, the wheels tend to slip and this causes a loss in the longitudinal acceleration performance. This behaviour can be regulated with a traction control system that limits the motor torque to a limit such that it does not exceed the tire grip. Researchers have presented various control strategies on threshold slip control [107–111]. In [112], fuzzy logic was used for individual wheel slip assignment for achieving a yaw rate control of the vehicle. Additionally, the continuous sub-limit slip control has been demonstrated to offer benefits in terms of longitudinal vehicle dynamics control by Wang et al. in [73, 113]. The authors used quadratic programming optimization to computed the desired reference slip values to be allocated to the individual wheel slip controllers. However, quadratic programming introduces elevated computation expenses which might pose an issue in implementation in production vehicles. Another issue might be the lack of robustness in such methods as for the optimisation, the above method requires a very accurate model of the vehicle and the tire. Tire physics are very non-linear and tire behaviour changes with temperature, road conditions and tire pressure, so it is in general quite difficult to have a complete modelling of tires. This was also one of the reasons that motivated the use of a black box technique for the estimation of the sideslip angle in Chapter 3. Thus, a simplified logic for the sub-limit control of the tire slip angles is presented in this section. The idea is to use a feedback controller for the tire slip values where the reference slip values for the individual tires are computed from a 3-dimensional map that keeps the slip values of the tire within the linear working region of the tires. The slip control loop needs to be an order of magnitude faster than the high level yaw moment controller in order to avoid interference between the high level and the low level control loops. In addition, the wheel slip dynamics is very fast with respect to the chassis yaw dynamics. Thus, it is desirable to operate the slip control loop at around 500 Hz to 1 kHz. This in turn requires the knowledge of the current wheel slip at a similar update sampling rate. While it is expected that slip observers would be unable to

operate at such a high update rate, fortunately optical sensors currently available in the market are able to give a very accurate measurement of the vehicle's longitudinal wheel slips at such frequencies. These sensors work by correlating two subsequent images of the ground below the car and processing the direction in which the two images have been translated to obtain the velocity vector in the x and y directions. For simulation, the slip values are obtained from the multibody vehicle model, but it is safe to assume that the same information could be available for a real life racing vehicle. Figure 6.9 shows the force-slip characteristics of the utilised tire. It

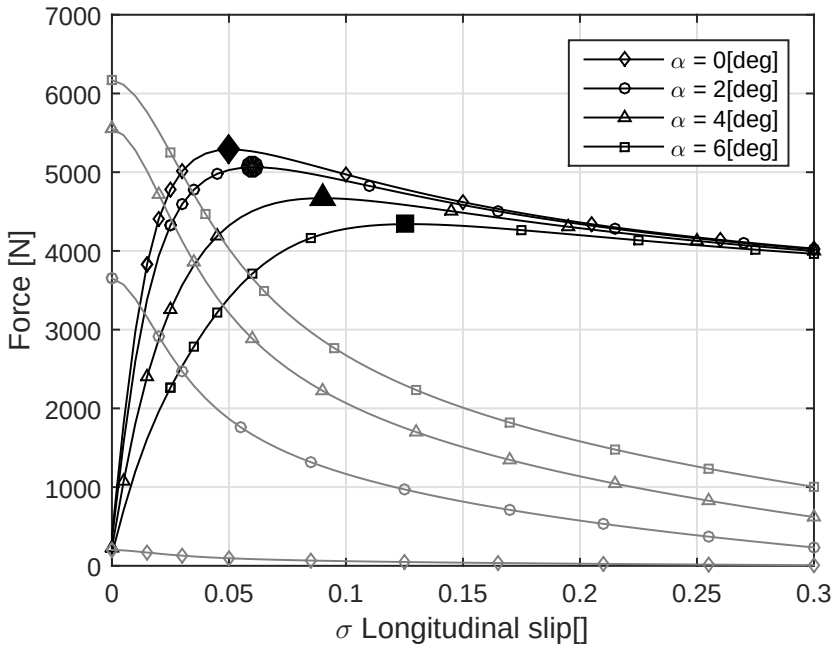

Figure 6.9 Longitudinal (black line) and lateral (grey line) tire forces as a function of longitudinal slips (σ) for various tire lateral slip angles (α).

can be seen that the tire longitudinal force, denoted by black lines, first increases with longitudinal slip, σ then saturates at a certain slip level, and finally decreases with increase in tire slip. The lateral force, denoted by grey lines, on the other hand decreases with increase in the tire longitudinal slip for a given value of lateral slip. Thus, it is highly desirable to operate within the threshold value of σ depicted by solid black markers in Figure 6.9. In the presented work, an offline optimized three-dimensional map is used to obtained the desired reference slip values, σ_{des} for the control of the wheel longitudinal slip. This introduces lower computation load and the behaviour of the controller can be easily calibrated at the same time. Thus σ_{des}

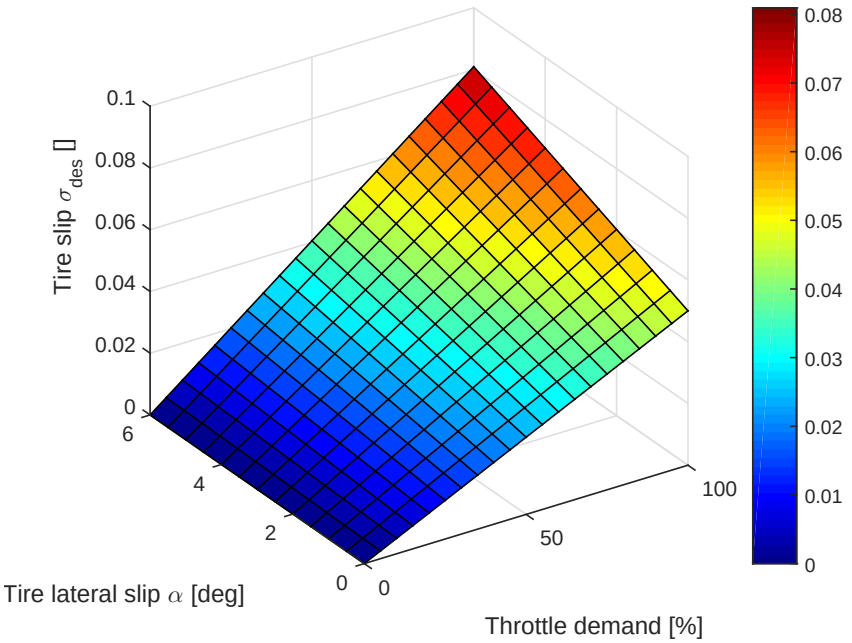

Figure 6.10 Desired longitudinal slip values as function of throttle demand and tire lateral sideslip angle.

is obtained as a function of the driver throttle input and the tire sideslip angle as seen in Figure 6.10. As a result, pressing a certain amount of throttle ensures that the tire slip doesn't rise above a certain threshold value. This ensures smoother acceleration and better drive quality along with increase in the lateral grip.

A sliding mode slip tracking controller has been used to control the wheel slips and set them equal to the desired wheel slip values. The feedback sliding surface controller design has been adapted from [73]. A sliding surface that defines the error between the desired and actual values of tire slip is chosen as

$$S_{slip} = \sigma - \sigma_{des}. \tag{6.27}$$

The wheel rotational dynamics can be written as

$$I_w \dot{\omega} = T_{wi} - F_{xi} r_w, \tag{6.28}$$

where r_w is the wheel radius, I_w is the rotational mass moment inertia of the wheel and T_{wi} is the traction torque applied on the i^{th} wheel.

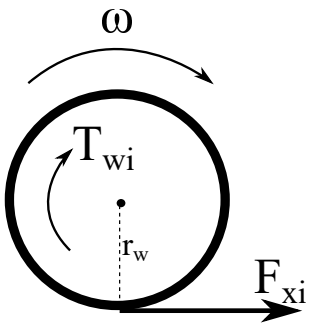

Figure 6.11 The forces and moments acting on an individual wheel with in-wheel electric motor traction.

The transient slip equation can be written as

$$r_w\omega_i - v_i = v_i\sigma_i + l_r\dot{\sigma}_i, \tag{6.29}$$

where l_r is the tire relaxation length and v_i is the wheel's velocity across its plane.

Taking the derivative of Equation 6.29 and equating the $\dot{\omega}_i$ from Equation 6.29 to Equation 6.28 and neglecting the transient slip, the slip dynamics equation for the i^{th} wheel is obtained as:

$$\dot{\sigma}_i = -\frac{r_w^2 F_{xi}}{I_w v_i} - \frac{\dot{v}_i}{v_i}(\sigma_i + 1) + \frac{r_w}{I_w v_i}T_{wi}. \tag{6.30}$$

The Lyapunov function, V_{lyp} of the sliding surface S_{slip} can be written as

$$V_{lyp} = \frac{1}{2}S_{slip}^2, \tag{6.31}$$

$$\begin{aligned}\dot{V}_{lyp} &= S_{slip}\dot{S}_{slip},\\ &= S_{slip}\Big(-\frac{r_w^2 F_{xi}}{I_w v_i} - \frac{\dot{v}_i}{v_i}(\sigma_i + 1) + \frac{r_w}{I_w v_i}T_{wi} - \dot{\sigma}_{i\,des}\Big).\end{aligned} \tag{6.32}$$

Choosing the control law

$$T_{w\,i} = -\frac{I_w K_{ssc\sigma}}{r_w} sgn(S_{slip}), \tag{6.33}$$

yields

$$\dot{V}_{lyp} = S_{slip}\Big(- \frac{r_w^2 F_{x\,i}}{I_w v_i} - \frac{\dot{v}_i(\sigma_i + 1)}{v_i} - \frac{K_{ssc\sigma}}{v_i} sgn(S_{slip}) - \dot{\sigma}_{i\,des}\Big),$$
$$= S_{slip} sgn(S_{slip})\Big(- \frac{r_w^2 F_x}{I_w v_i} sgn(S_{slip}) - \frac{\dot{v}_i(\sigma_i + 1)}{v_i} sgn(S_{slip})$$
$$- \frac{K_{ssc\sigma}}{v_i} - \dot{\sigma}_{i\,des} sgn(S_{slip})\Big), \tag{6.34}$$

which implies that

$$\dot{V}_{lyp} \leq |S_{slip}|\Big(\frac{r_w^2}{I_w v_i}|F_{xi}| + \frac{(\sigma_i + 1)}{v_i}|\dot{v}_i| - \frac{K_{ssc\sigma}}{v_i} + |\dot{\sigma}_{i\,des}|\Big). \tag{6.35}$$

The condition of the sliding surface is given by

$$\dot{V}_{lyp} \leq -k_{st}|S_{slip}|, \tag{6.36}$$

where k_{st} is a positive constant which guarantees the stability. Comparing equations 6.35 and 6.36, we get

$$\Big(\frac{r_w^2}{I_w v_i}|F_{xi}| + \frac{(\sigma_i + 1)}{v_i}|\dot{v}_i| - \frac{K_{ssc\sigma}}{v_i} + |\dot{\sigma}_{i\,des}|\Big) \leq -k_{st}, \tag{6.37}$$

or

$$K_{ssc\sigma} \geq \frac{r_w^2}{I_w}|F_{xi}| + (\sigma_i + 1)|\dot{v}_i| + k_{st} v_i + v_i|\dot{\sigma}_{i\,des}|. \tag{6.38}$$

The condition of attractivity is then satisfied if K is chosen as

$$K_{ssc\sigma} = \frac{r_w^2}{I_w} F_{ximax} + 2g + v_{i\,max}(k_{st} + \dot{\sigma}_{max}). \tag{6.39}$$

where F_{xmax} is the maximum longitudinal force the tire can generate, $v_{i\,max}$ is the maximum velocity of the wheel across its plane, 2g is assumed as the maximum possible longitudinal acceleration, $\dot{\sigma}_{max}$ the maximum rate of change in desired slip [73]. In order to avoid chattering, the sign function in 6.33 is replaced by a saturation function [104].

The torque to the wheels is saturated by the slip controller when the torque from the electric motors computed by the torque allocation block is larger than the torque demand given by the slip controller. The electric motor drive torque to the wheels can be given by the following expression

$$T_{EM\,L,R\,drive} = \begin{cases} T_{EM\,L,R} & \text{if } T_w/\tau_d > T_{EM\,L,R} \quad (6.40) \\ T_w/\tau_d & \text{if } T_w/\tau_d \leq T_{EM\,L,R}, \quad (6.41) \end{cases}$$

$$T_{EM\,L,R\,brake} = \begin{cases} T_{EM\,L,R} & \text{if } T_w/\tau_d < T_{EM\,L,R} \quad (6.42) \\ T_w/\tau_d & \text{if } T_w/\tau_d \geq T_{EM\,L,R}. \quad (6.43) \end{cases}$$

6.4 Results and Discussion

For testing the performance of the controller under study, the advantage of using a high fidelity simulation environment over experimental vehicle testing is that it allows the evaluation of the effect introduced by the controller in a much more objective manner. With such simulations, it is possible to eliminate many of the variable effects such as track temperature, tire conditions and driver bias on the vehicle behaviour. As a result, the assessment of the overall control structure is made by simulating a variety of tests in the VI-CarRealTime-Simulink cosimulation environment. All the test are done on a high friction road surface. The control loop is executed in Simulink while the chassis dynamics are executed in the VI-CarRealTime environment. The control loop and the vehicle block are connected with a communication bus that transfers information between the two blocks. Both open loop and closed loop tests are executed. The driver model used for the closed loop tests is set to the 'Professional' setting. This allows the driver controller to have a fast response time and thus simulates the behaviour of a racing driver. Limitations are imposed on the rate of actuation of the various control inputs such as the throttle and brake pedal, steering wheel angle to filter out infeasible solutions and simulate a more realistic control behaviour by the driver.

6.4.1 Acceleration Tests

The vehicle is made to accelerate from 20 km/h at full throttle along a straight line on a high adherence road surface to understand effectiveness of the slip control system.

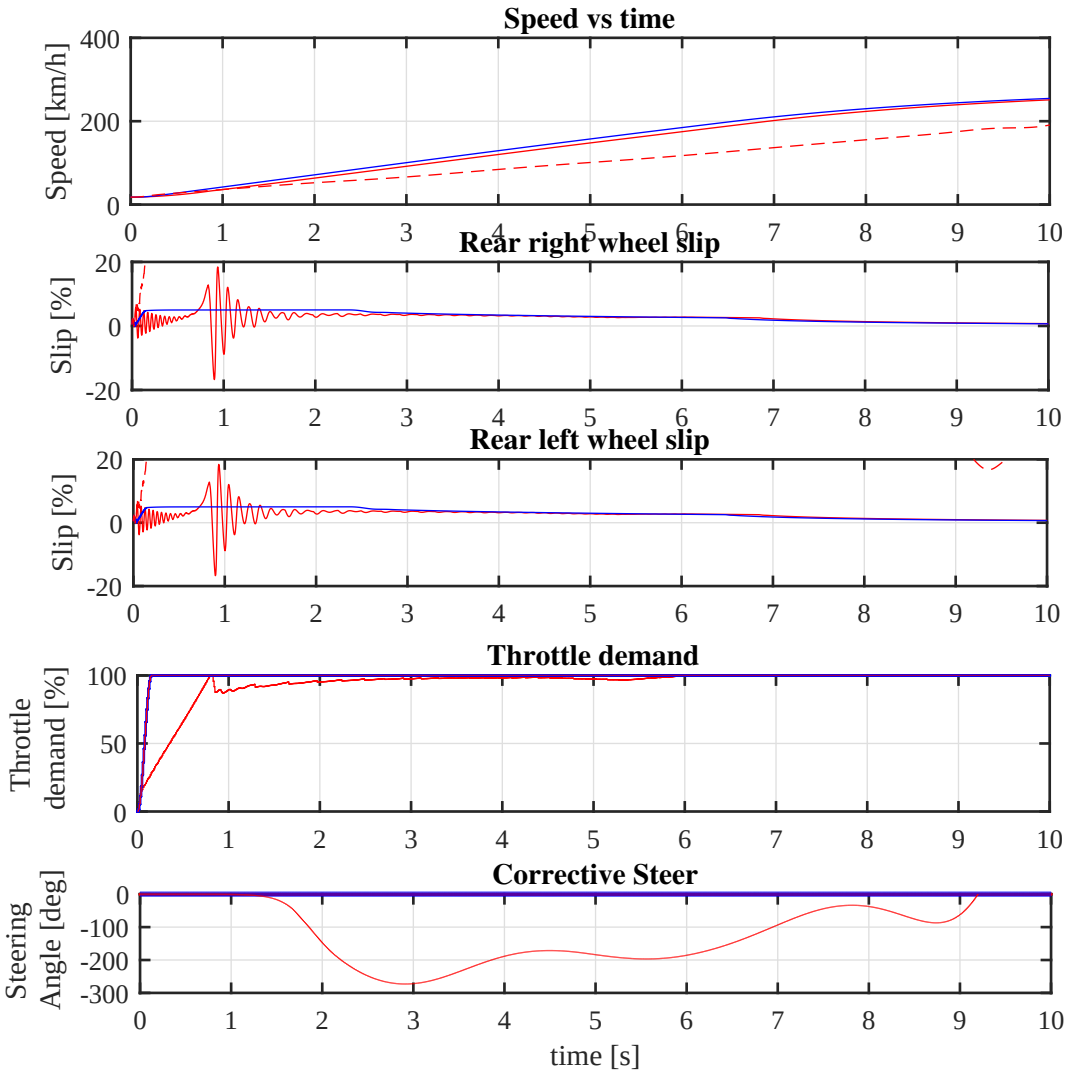

Figure 6.12 Improvement in acceleration performance due to longitudinal slip control during full throttle acceleration test. Blue lines indicate the controlled vehicle, the red dashed lines denote the uncontrolled vehicle with open loop throttle and closed loop steering control and the red solid lines denote the uncontrolled vehicle with closed loop throttle and closed loop steering control.

The choice of the starting speed is due to the fact that the dynamic vehicle model is unstable below 5 m/s. At low velocities when the electric motors are working in their constant maximum motor torque region, there is a possibility of wheel slip due to sudden increase in motor torque. As a result of wheel slip, the vehicle normally tends to yaw towards the direction of the slipping wheel. In order to stay on a straight line, drivers correct the vehicle yaw with the help of counter steering. As result, the vehicle longitudinal acceleration is lower than the case without wheel slip. Figure

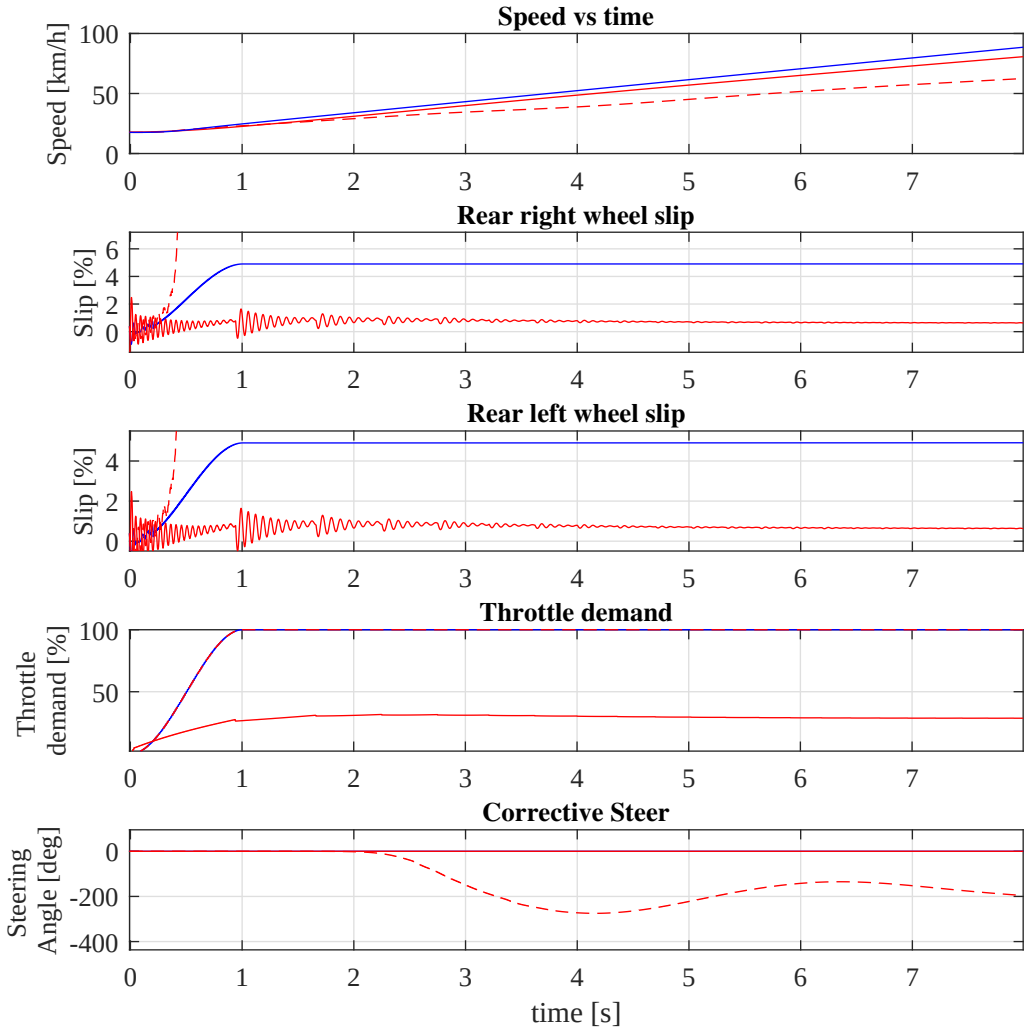

Figure 6.13 Improvement in acceleration performance due to longitudinal slip control during full throttle acceleration test with the tire road friction coefficient 0.4. Blue lines indicate the controlled vehicle, the red dashed lines denote the uncontrolled vehicle with open loop throttle and closed loop steering control and the red solid lines denote the uncontrolled vehicle with closed loop throttle and closed loop steering control.

6.12 shows a comparison between three different cases. In case 1, the vehicle is accelerated with an open loop throttle with the motor torque control turned on as represented by the blue solid lines. In case 2, the vehicle is accelerated with an open loop throttle with the motor torque control turned off as represented by the red dashed lines. In cases 1 and 2, only the steering wheel is controlled in closed loop by the standard driver. Finally, in case 3, the vehicle is accelerated with the motor torque control system turned off with a closed loop throttle with a standard driver at the controls of the both the throttle and the steering wheel. This case is used to demonstrate the best possible performance of the uncontrolled vehicle since case 2 does not represent the maximum potential of the uncontrolled vehicle. For the open loop manoeuvres, i.e. cases 1 and 2, it can be clearly seen that the vehicle can reach higher accelerations when the slip control is turned on. Moreover, the driver does not need to counter steer when the slip control is switched on. Heavy steering corrections are needed by the driver when the slip control is switched off. For the controlled vehicle, it can be seen that the slip follows the reference slip values of 5% up to 2.5 seconds after which the wheel slip reduced as a function of the torque speed characteristics of the electric motor. This is due to the inability of the electric motor to supply the wheels with the required torque due to motor torque limitation. In the case without slip control, the wheel slip goes up in to the non-linear region (up to 100%-not shown in plot to preserve scaling for the other two cases) after which it reduces due to increase in vehicle longitudinal velocity and at the same time reduction in the available motor torque with increase in motor rpm. For case 3, the driver modulates the throttle up to the first 6 seconds in the manoeuvre. Thus, the slip of the vehicle's rear tires stay close to the linear region. However, between 1 sec and 3 sec, the tire slip exhibits oscillatory behaviour due to the lifting of the throttle from 100% to around 90% at around 1 second. It can be noticed that the open loop controlled vehicle is faster than the best possible performance of the passive vehicle. The gain of time to accelerate up to 100 km/h from 20 km/h is around 0.3 seconds due to the introduction of the motor torque control system as the controlled vehicle reaches 100 km/h in 3 seconds, while the uncontrolled vehicle in 3.3 seconds. Thus, during acceleration, the control system can reduce the driver's effort to control the longitudinal slip with throttle modulation and improve the acceleration at the same time.

The same acceleration test is repeated for a tire-road friction coefficient 0.4, which represents a snowy road. The results are quite similar for the three cases

as it is with the dry road. It can be seen in Figure 6.13 that the controlled vehicle accelerates much faster than the passive vehicle when an open loop throttle step input is given. The passive vehicle with closed loop throttle control simulating an expert driver is able to accelerate much better than the passive vehicle with open loop. However, it can be seen that controlled vehicle still outperforms the closed loop throttle controlled vehicle. The slip of the controlled vehicle remains fixed at 5 % which is the desired slip. The passive vehicle's wheel slip increases to 100 % whereas the closed loop driver keeps the wheel slip equal to around 1 %. Similar to the test on the dry road, the passive vehicle needs large correction steer to keep the vehicle straight. The controlled vehicle and the passive vehicle with throttle control do not require any correction steering to keep the vehicle straight.

6.4.2 Braking Test

An open loop full braking test is done to compare the braking performances of both the controlled and the uncontrolled vehicle on high and low adherence road surfaces. The vehicle is running at 200 km/h initially. The brake pedal is pressed fully up to 100% pedal position from 0 seconds onward. The test on the high μ road surface is shown in Figure 6.14. From the speed vs. time curve, it can be seen that the controlled vehicle has a higher deceleration from 200 km/h to 100 km/h. After 2 seconds, the uncontrolled vehicle becomes unstable and it spins out. This can be understood by looking at the exponential growth of the yaw rate of the vehicle after 2 seconds. The controlled vehicle on the other hand remains stable. It can be also noticed that the rear wheels of the uncontrolled vehicle get locked (σ = -100%) under braking at around 0.4 seconds whereas the controlled vehicle maintains its slip within the threshold region which is around -5%. The controlled vehicle takes about 3.8 seconds to decelerate from 200 km/h to 20 km/h.

A very similar trend is noticed in the test with the low μ road surface where the controlled vehicle performs better than the passive vehicle as seen in Figure 6.15. Up to 2.5 seconds, when both the vehicles are stable, the controlled vehicle has a slightly larger deceleration. This is due to the fact that the slip of the controlled vehicle's wheel slips are close to the maximum of the force vs. slip curve, whereas the passive vehicle has a slip of -100% which is the region where the force reduces again due to tire saturation and non-linearity. After 2.5 seconds, the passive vehicle locks its wheels while braking and ultimately it spins out as indicated by the rise in its

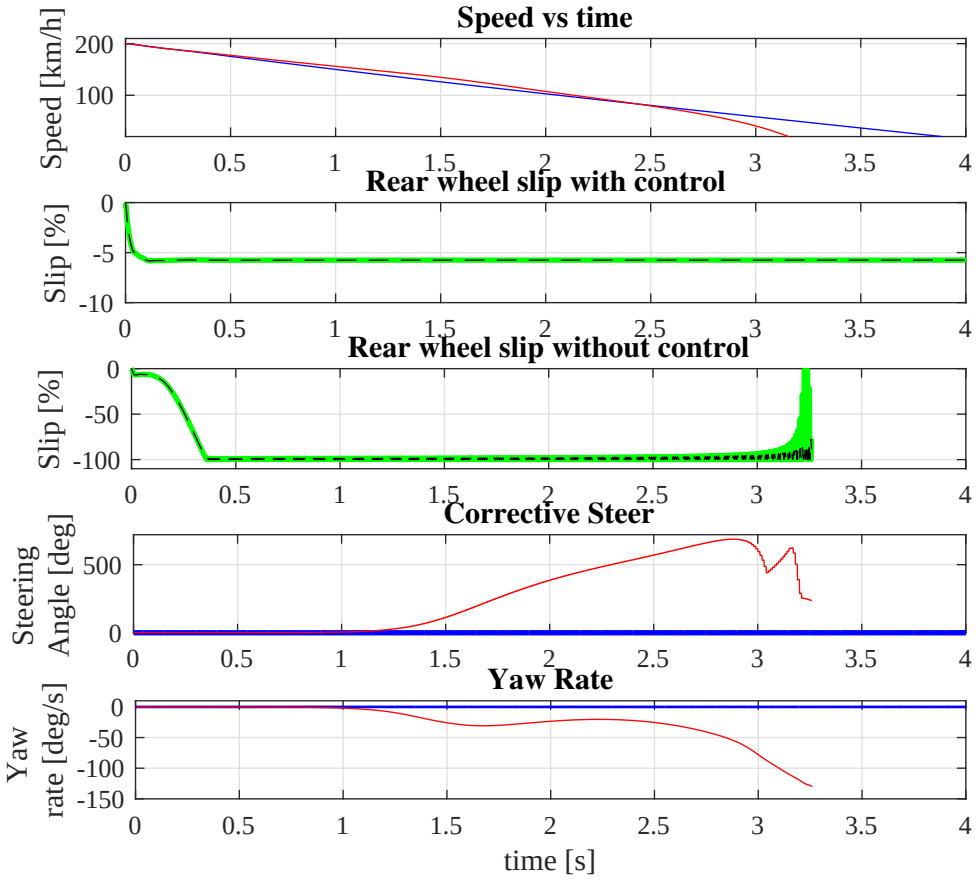

Figure 6.14 Comparison of vehicle performance during a full braking test at 200 km/h on a high adherence road surface with $\mu = 1$. The red curves denoted the uncontrolled vehicle while the blue curves denote the controlled vehicle. Green lines represent the rear right wheel slip while black dashed lines represent rear left wheel slip.

yaw rate. The controlled vehicle remains stable and maintains its deceleration. This indicates that slip control is able to improve the braking performance in both high and low adherence surfaces as well as maintain the vehicle stability when during braking.

6.4.3 Frequency Analysis with Sweep Steer

Open loop sine sweep manoeuvres are executed on the vehicle at two different speeds in order to understand the responsiveness of the vehicle. The frequency response of both vehicles are shown in Figure 6.16. Ideally it is desirable to have similar responsiveness along the whole frequency range of 0.1-4 Hz. It can be seen that the

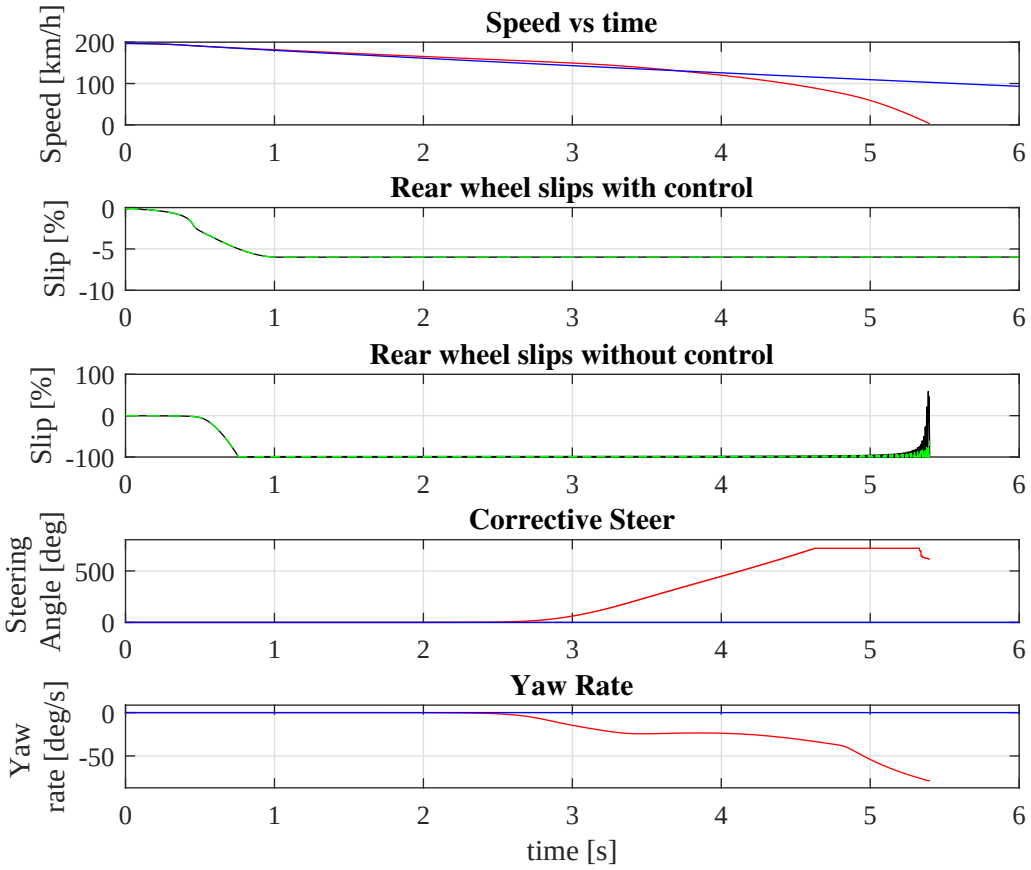

Figure 6.15 Comparison of vehicle performance during a full braking test at 200 km/h on a low adherence road surface with $\mu = 0.4$. The red curves denoted the uncontrolled vehicle while the blue curves denote the controlled vehicle. Green lines represent the rear right wheel slip while black dashed lines represent rear left wheel slip.

yaw gain in the uncontrolled vehicle is larger than the controlled vehicle. This is due to the fact that the uncontrolled vehicle is oversteering, whereas the controlled vehicle's behaviour is closer to a neutral steering vehicle. Although the uncontrolled vehicle is more sporty to drive, it can be clearly seen that the controlled vehicle has a lower yaw rate to steering angle gain which makes the vehicle easier to drive. This makes the vehicle much more controllable for a driver and gives the driver more confidence to push towards the limits. A more significant although minor improvement can be seen in the phase lag between the steering input and the yaw response. Due to lower phase lag in the controlled vehicle, the responsiveness of the vehicle will appear much higher to the driver.

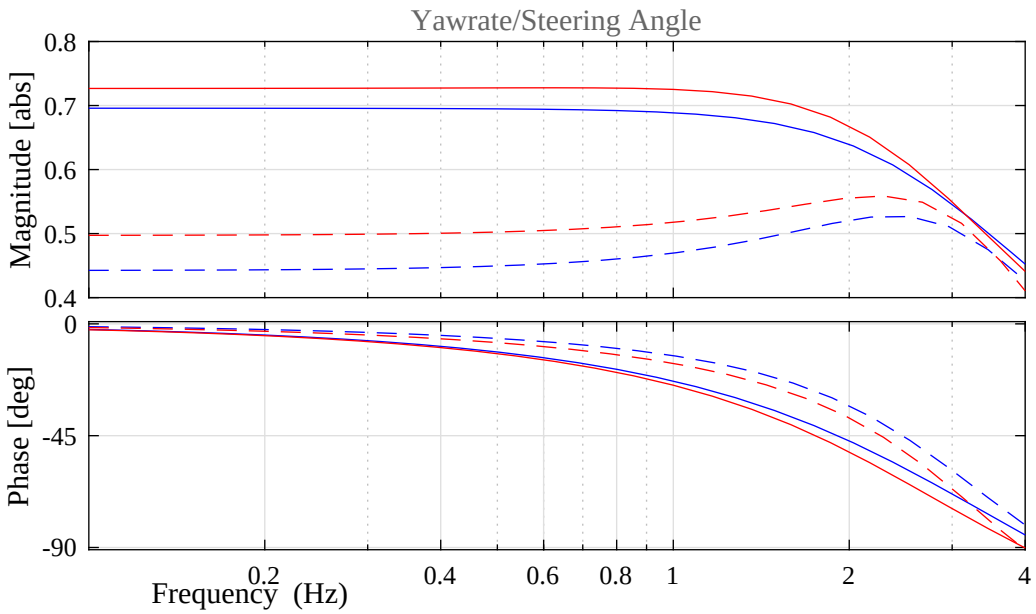

Figure 6.16 Frequency response of the yaw rate of the vehicle computed using sine sweep steer manoeuvres at 72 km/h (dashed lines) and 100 km/h (solid lines). The red curves denoted the uncontrolled vehicle while the blue curves denote the controlled vehicle.

6.4.4 Racetrack Lap

Fastest lap time simulations are carried out on the Hockenheim circuit to study the influence of the control algorithm on the lap times. The driver is made to follow a predetermined fastest racing line. The g-g plot resulting from a single lap for the uncontrolled and the controlled vehicle is shown in Figure 6.17. As per the choice of frame of reference, positive a_x refers to acceleration while negative values indicate braking. Similarly, positive a_y indicate left turns while negative values indicate right turns. It can be seen that there is an enlargement in the g-g plot when the control logic is switched on. Enlargement in g-g plot can be seen in the part that represents acceleration with non-zero a_y. This indicates that the vehicle is able to generate higher lateral force due to torque vectoring when it is exiting a corner.

The local minima of the speed vs. distance curve shown in Figure 6.18 represent the speed at which a vehicle goes around the different corners of the track. The controlled vehicle is able to lap the track about 3.5 seconds faster than the uncontrolled vehicle. Due to its capability of being able to generate higher lateral forces and due to control of the vehicle oversteering behaviour while braking, the controlled vehicle is able to corner at higher speeds. Such improvement can be seen at lap distances

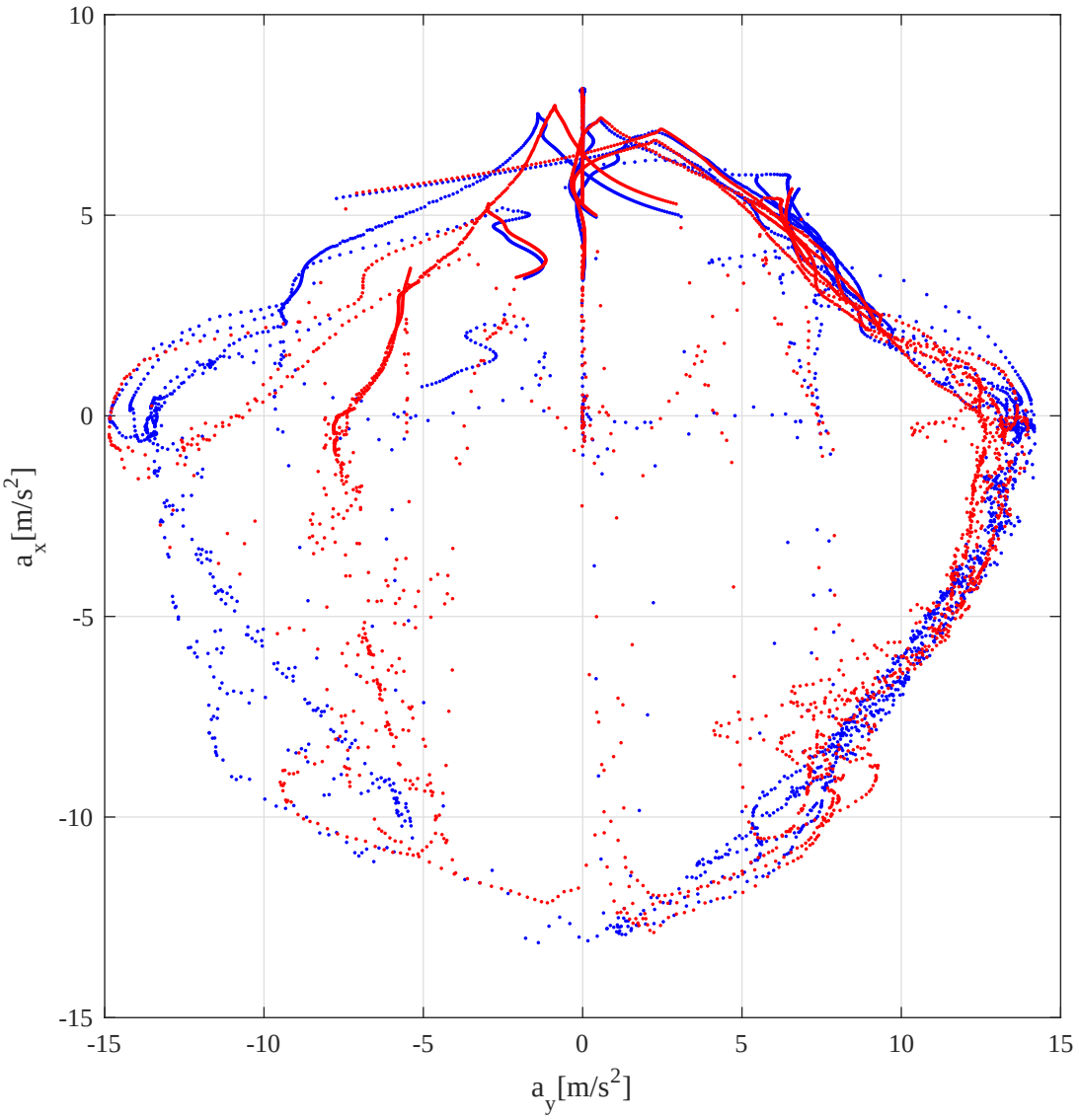

Figure 6.17 Enlargement of the G-G diagram in the controlled vehicle(blue) as compared to the uncontrolled vehicle(red).

equal to 650 m, 790 m, 1120 m and so on in Figure 6.18. There is also a marginal increase in the outline of the g-g plot in the braking part of the plot. The maximum braking deceleration is also increased due to the presence of the wheel slip controller. A major increase in the braking part of the g-g plot is seen in the region with negative a_y (right turns). This is because the control system limits the vehicle oversteer during the corner at 790 m. As the preceding corners at 480 m and 590 m are left turns and the corner at 790 m is a right turn, this involves changes in direc-

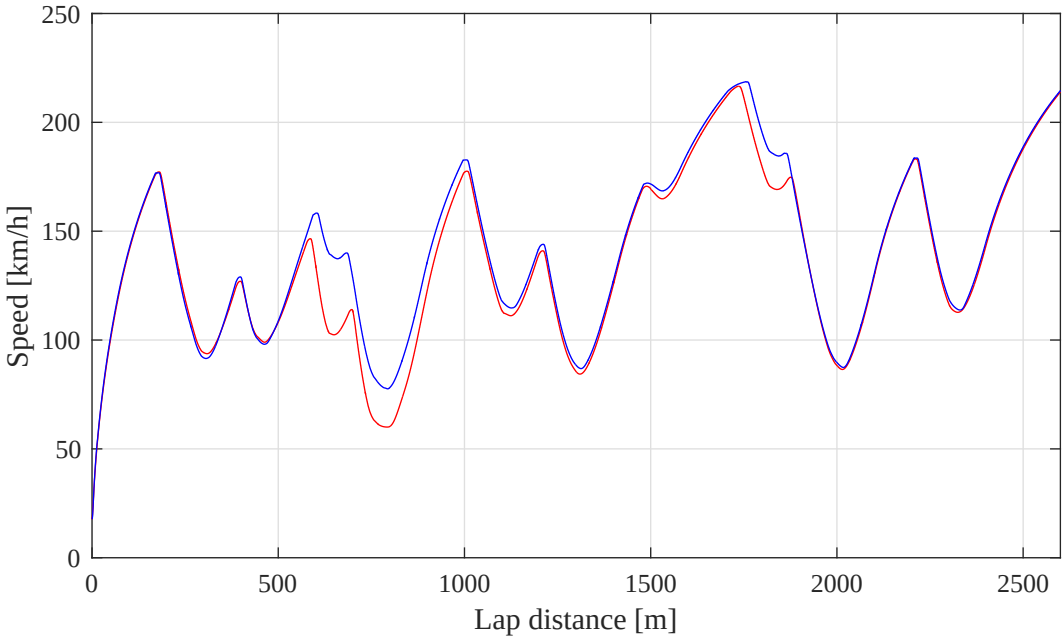

Figure 6.18 Velocity profiles for the controlled (blue line) and the uncontrolled (red line) vehicles. The gap between the two vehicles increases with time. Dashed lines represents the velocity target set for the driver.

tions that pushes the vehicle closer to loss of grip and control. From Figure 6.19, it can be seen that the driver of the uncontrolled vehicle tries to control this instability by heavy counter steer at around 730 m, which is the entry point to the corner. The driver of the controlled vehicle counter steers about a third of the uncontrolled driver's counter-steering as the controlled vehicle is much more stable.

It is also interesting to notice that all throughout the lap, the driver needs to give more frequent steering inputs to control the vehicle in the uncontrolled case. This can be seen in Figure 6.19 and it can be understood that it is much easier to drive the controlled vehicle. In physical terms, it can be realized as counter-steering manoeuvres done by the driver to keep the uncontrolled vehicle stable. The driver steering input also seems to be much less 'nervous' as the inputs look smoother and less oscillatory in the case with the control. This also indicates a reduction in the driver's effort to control the vehicle around the track in a desired way.

The utilization of the four individual tires can be understood by studying the μ_x vs. μ_y plots of each tire. A larger envelop area means higher utilization. The parameters μ_x and μ_y are obtained by dividing the longitudinal force F_x and the lateral force F_y respectively at each instant by F_z, the normal force. The μ_x vs μ_y

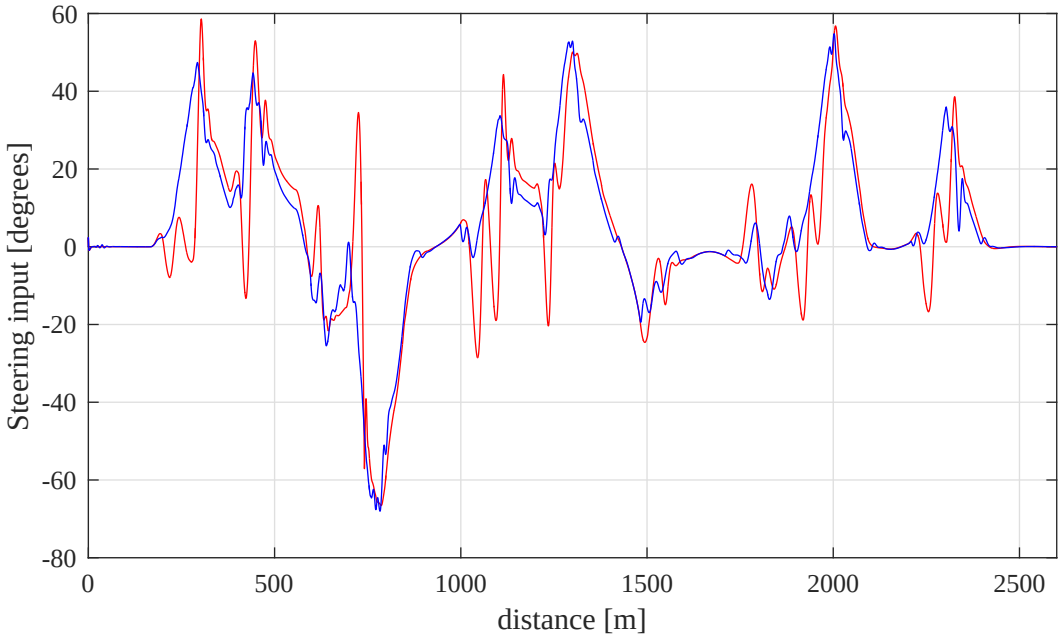

Figure 6.19 Steering input by driver for the controlled (blue line) and the uncontrolled (red line) vehicles.

plots of the tires for the racing lap manoeuvre are shown in Figure 6.20. Looking at the front left and front right tires, it can be seen that the utilization of the front tires are increased during the braking in turn situations in the controlled vehicle. Such situations are shown in the region with non-zero μ_y and negative μ_x. This indicates the fact that the uncontrolled vehicle has more oversteering behaviour in general as it utilizes the front tires much less than the controlled vehicle. This trend also shows the advantage of the control algorithm since during braking, there is a load transfer to the front wheels and thus, the front wheels are much more loaded than the rear wheels. Higher utilization of front tires during braking will lead to generation of overall higher forces. For the rear tires, it can be seen from Figure 6.20 that in the zone with positive μ_x and non-zero μ_y, that is during acceleration while cornering, the controlled vehicle makes higher utilization of the outer rear wheels (right wheel when positive μ_y, left wheel when negative μ_y) while the uncontrolled vehicle utilizes more the inner wheel. Due to the effect of lateral load transfer to the outer rear of the vehicle during acceleration while cornering, the controlled vehicle is able to generate of higher forces than the uncontrolled vehicle. Similarly, during braking while cornering, it can be seen that in the controlled vehicle, the outer rear wheel (right wheel when positive μ_y, left wheel when negative μ_y) is better utilised

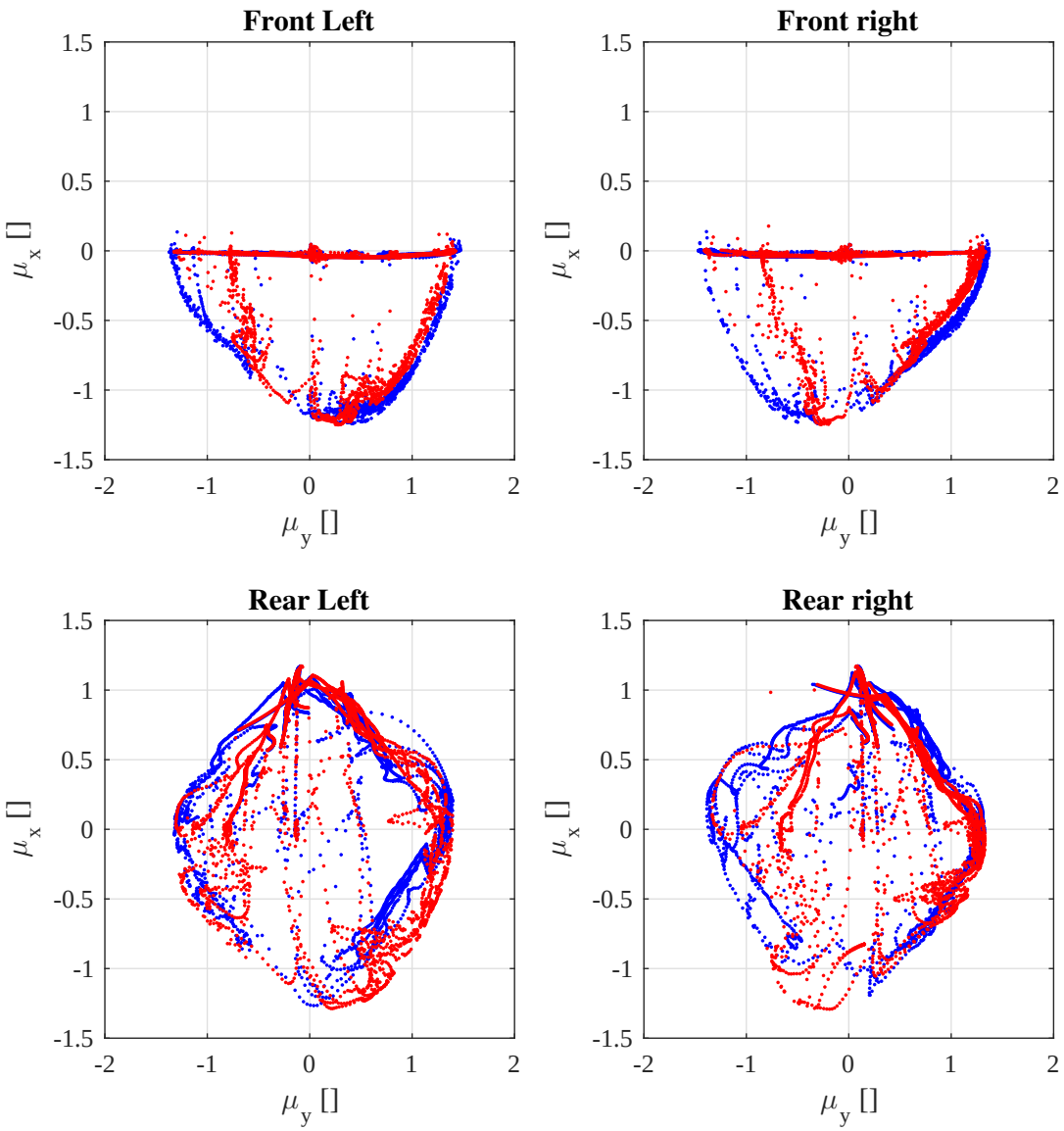

Figure 6.20 Individual utilisation of four tires during a lap. Red markers represent the uncontrolled vehicle while the blue markers represent the controlled vehicle.

while in the uncontrolled vehicle the inner rear wheel is more utilised. This makes it clear to understand that the controlled vehicle also utilizes the rear tires better during cornering while braking. The uncontrolled vehicle on the other hand pushes the inner rear wheel close to the unstable limits.

The acceleration profile of the vehicle is shown with respect to its position on the track Figure 6.21. The track is laid out in an anticlockwise manner. It can be seen that the vehicle starts the lap from the position (0,0) and accelerates (green) in

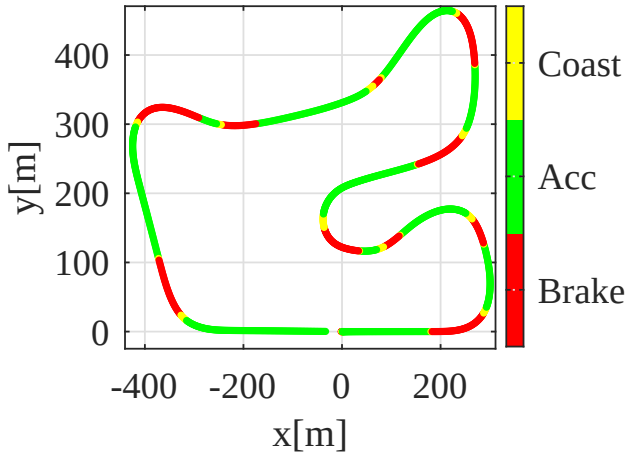

Figure 6.21 Spatial representation of the acceleration profile during one lap. The circuit shown is anticlockwise.

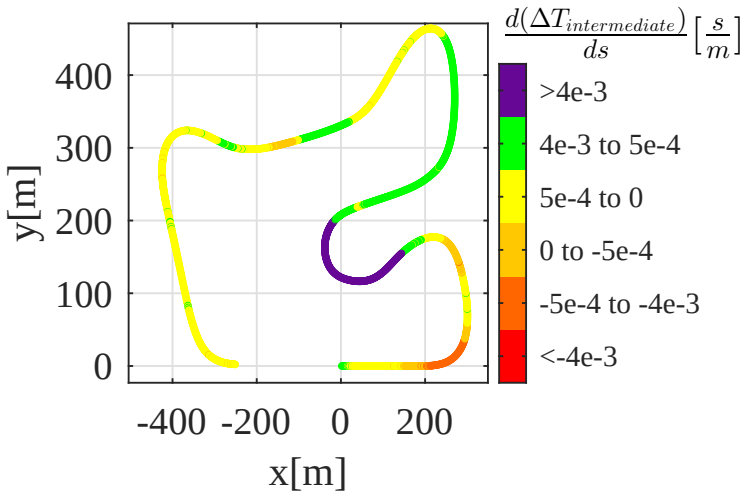

Figure 6.22 Spatial representation of the gain/loss of improvement in lap time during one lap. The circuit shown is anticlockwise. Maximum lap time gain is observed in the tight corner represented by the purple color.

the straight section in the left direction, followed by a braking (red) before entering a curve. It then maintains a coasting velocity (yellow) at the middle of the curve, and then it accelerates out of the corner. It repeats this strategy all throughout the track. The gain and the loss of lap time difference between the controlled and the uncontrolled vehicle can be also understood by studying Figure 6.22. The derivative of the difference between the intermediate lap times of the uncontrolled and controlled vehicles with respect to unit displacement is plotted all throughout the track. It can be seen from the figure that the controlled vehicle gains on the uncontrolled vehicle

in terms of intermediate lap time during almost the entire lap (lower laptime is better). It is especially faster during the tight hairpin corner represented by the color purple. The controlled vehicle is able to go faster since the preceding set of turns to the hairpin involves a pair of left and right turns. When the uncontrolled vehicle passes through this section, the sudden change in direction at higher speeds leads to high oversteering yawing moments. As a result, the uncontrolled vehicle needs to reduce its speed to be able to go around the set of corners without spinning out. The controlled vehicle on the other hand can go faster around the set of corners as the oversteering yaw moment is countered by the stabilizing torque vectoring yaw moment. It can be also seen that the controlled vehicle is almost always faster while getting out of a corner. While during braking in the first two corners, the controlled vehicle is slower by a very small margin.

6.5 Conclusions

The lap time of the vehicle under study around a single lap of the Hockenheim track is improved by 3.5 seconds using a novel motor control strategy. The control algorithm aimed at increasing the g-g diagram of the vehicle by torque transfer between the left-right wheels so that the vehicle achieved a neutral steer characteristics. The control algorithm controls the difference between the sideslip angles of the front and rear tires by the use of an integrated feedback control structure. A lower level tire longitudinal slip control allows the vehicle to accelerate and brake faster. Straight line acceleration and braking tests indicate the improvement in acceleration and braking due to tire longitudinal slip control. Lap time simulations indicate that the controlled vehicle can lap the track faster than the uncontrolled vehicle due to better utilization of the four tires and thus the ability to go at faster speeds around the corners. Driver input analysis shows that the controlled vehicle is much easier to drive as compared to the uncontrolled vehicle.

Chapter 7

Conclusions

Active systems, which have been introduced in production vehicles for many years, have demonstrated the ability to improve vehicle safety and performance by intelligently controlling the various forces acting on a vehicle as a function of the driver inputs. For the control of active systems in vehicles, there are various states (sideslip angle and mass) that need to be estimated because of the lack of onboard sensor(s) that can measure them. For the practical implementation of these algorithm onboard a vehicle, it is necessary that the state observers , that are used to estimate these states, work just with CAN-BUS data and low-cost onboard sensors only. Secondly, it is also necessary that the state estimation algorithms are robust to changing operating conditions of the vehicle, which may include changing tire-road friction coefficient, change of tires etc. Motivated by the above issues, sideslip angle and vehicle mass estimation algorithms are developed in the first part of this thesis.

The presented estimation algorithms have the advantage that they do not need any external sensors to work and just require onboard sensor information. The sideslip estimation is first carried out using an EKF that is based on a vehicle model. The observer works well under operating conditions including combined slip conditions such as a lap of a racetrack. However, the observer fails to estimate the sideslip angle when large wheel-spin and drifting are involved. Due to lack of knowledge of wheel slips, the observer uses a modified Pacejka tire model. This model uses lookup tables to compensate for the effect of combined slip. As a result, the tire cornering stiffness modelling is incorrect whenever large longitudinal slips were involved. Although it has not been demonstrated in this thesis, it is found that using

the measured longitudinal slip values from the Kistler optical sensor and plugging them into a Pacejka tire model with combined slip equations, also does not improve the quality of the sideslip angle estimate. This is due to the lack of reliability of the tire model validation, which are done on tire test rigs. These rigs are incapable of generating extreme conditions such as 'drifting' and thus the tire model is fitted on the Pacejka model for simple pure slip or normal combined slip conditions.

This motivated the idea to look for a sideslip angle estimation method that does not rely on tire models. The solution is the development of a deep learning based observer, that tries to emulate the functioning of a racing driver's brain. Theoretically, deep learning observers are capable of modelling any kind of non-linear input-output relationship, and thus, this observer is developed for the estimation of the sideslip angle from the onboard sensors' signals. By acquiring data for a variety of manoeuvres, the observer is trained to predict the sideslip angle for almost the entire working range of the vehicle. This allows the observer to learn the input-output relationship from the training data. During the extensive experimental validation phase, it is found that the DLO able to estimate the sideslip angle quite accurately for manoeuvres including large drifting on high as well as low adherence road surfaces, which proves its robustness.

The vehicle mass estimation algorithm extended the idea presented by Fathy in [32] by the inclusion of a torque observer, which improves the quality of the estimation of the tire longitudinal forces due to the inclusion of the modelling of a complex transmission. This leads to an improvement in the mass estimation algorithm as the convergence time of the algorithm is reduced.

While active systems have been studied exhaustively in literature and widely implemented for improving vehicle stability, there are still some open points with regard to improvement of vehicle performance with the use of active system. Often, objective criteria is utilised in literature to achieve the design of chassis control systems. However, from a practicality point of view, most OEMs rely on the test drivers' subjective feedback to achieve the control system tuning. This creates a need for an objective metric to quantify the subjective feeling and find a common ground for control system engineers and test drivers to facilitate the controller development. In the second part of this thesis, two performance oriented control algorithms were developed and tested in simulation and in real life (only RWS), always keeping driver feedback in the controller development cycle.

A rear wheel steering control system, which includes a FF and a FB controller, is developed for the vehicle yaw rate control. The controller design process, which considers both the plant and the actuator dynamics, demonstrates that feedback control action is limited by the delay present in the actuator system. The dynamic feedforward controller reduces the phase lag between the yaw rate and the lateral acceleration, which improves the driver's confidence in the vehicle and improved the lap times. Moreover, at high velocity the controller introduces yaw damping that also improves the drivers' subjective feedback of the vehicle handling. While these performance objectives have also been realised by commercial RWS control software (which work on similar logic), the developed controller is also able to reduce the second yaw rate peak during DLC manoeuvres. On the other hand, the commercial control systems are incapable of reducing the double yaw peak, which leads to a poor subjective feeling of the vehicle comfort.

TV control is found to be effective in controlling the difference between the front and the rear sideslip angles of the vehicle, thereby introducing a neutral handling characteristic. This is a novel approach for a controller objective definition as traditional controllers from the state of the art are based on yaw rate or sidelslip control. The use of this control algorithm on a rear wheel drive electric vehicle leads to an improvement in its laptime and also leads to a reduction in the driving effort of the vehicle by the driver. In the controlled vehicle, it is found that the torque transfer between the rear wheels generates a yaw moment, that reduces the driver's steering effort, as the controller intervenes to generate a steering yaw moment, whenever the vehicle deviates from the desired behaviour. This phenomena has a two point benefit. The first benefit is that the driver workload to control the vehicle reduces by a big margin as the TV controller does this job. The second benefit is that by transferring torque to the outer wheel during cornering, it is possible exploit the grip on both wheels of the tractive axle equally. This leads to improved vehicle stability as the inner wheel remains away from the longitudinal grip limit. On the other hand, the passive vehicle requires a large number of countersteering manoeuvres to keep the vehicle stable. This increases the driver workload, that reduces the driver's confidence on the vehicle. Moreover, it is noticed that the inner wheel of the passive vehicle is always fully exploited during cornering, whereas there is a lot of unexploited grip left on the outer wheel which is not utilised. The inner wheel is thus always close to the grip limit, and thus, the vehicle needs more countersteering inputs. Additionally, the introduction of a low level wheel slip control leads to an

improvement of the acceleration and braking times of the controlled vehicle, which also contributes to the improvement in the laptime.

7.1 Future Scope of Work

Although, many algorithms are developed in the thesis, there is certainly a margin for improvement in the work presented in the thesis. The suggested improvements and scope of future work are listed below:

- The DLO's network structure can be optimised to balance the trade-off between training time required and the accuracy of the network. This can be introduced by making a sensitivity analysis of the network topology on the accuracy of the network. In addition, dropout may be introduced in the various network layers. Furthermore, another optimisation can be carried out in the selection of the training data to eliminate unnecessary manoeuvres.
- A LSTM based DLO could be used to estimate other vehicle parameters such as the vehicle longitudinal velocity and the state of charge of battery packs.
- It is demonstrated in simulation that a FB controller for a RWS system without any actuator lag can improve the performance of the system drastically. Therefore, the next step forward in the design and development of the RWS controller could be to find out a way to improve the actuator's response and to eliminate the dead time that is present in the actuator.
- The torque vectoring controller could be extended for an all wheel drive configuration such as the one present in the Politecnico di Torino's racing vehicle SCXV. The high level controller would essentially remain the same but the torque allocation block would have to be modified to obtain four motor reference torques for the four in-wheel motors. This could be formulated as an optimisation problem and solved using a quadratic programming, in which the various objectives are represented by cost functions, which optimise energy consumption or lateral grip etc.

A final overall scope for future work could be to integrate all the above components to have a coordinated estimation and control structure where the full state

feedback control of the vehicle can be achieved due to the availability of two or more actuators such as TV and RWS. The state observer for the sideslip angle along with the yaw rate sensor will make the possibility of full state feedback possible.

Bibliography

[1] 1971 Lincoln Continental brochure, 2014.

[2] A. T. van Zanten. Bosch esp systems: 5 years of experience. In SAE Technical Paper, number 2000-01-1633. SAE International, 05 2000.

[3] Wikipedia. Anti-lock braking system.

[4] National Highway Trafic Safety Administration. Electronic stability control systems, controls and displays. Technical report, Federal Motor Vehicle Safety Standards:, 2012.

[5] WJ Manning and DA Crolla. A review of yaw rate and sideslip controllers for passenger vehicles. Transactions of the Institute of Measurement and Control, 29(2):117–135, 2007.

[6] Yung-Hsiang Judy Hsu, Shad M Laws, and J Christian Gerdes. Estimation of tire slip angle and friction limits using steering torque. IEEE Transactions on Control Systems Technology, 18(4):896–907, 2010.

[7] Rajesh Rajamani, Gridsada Phanomchoeng, Damrongrit Piyabongkarn, and Jae Y Lew. Algorithms for real-time estimation of individual wheel tire-road friction coefficients. IEEE/ASME Transactions on Mechatronics, 17(6):1183–1195, 2012.

[8] David M Bevly, Jihan Ryu, and J Christian Gerdes. Integrating INS sensors with GPS measurements for continuous estimation of vehicle sideslip, roll, and tire cornering stiffness. IEEE Transactions on Intelligent Transportation Systems, 7(4):483–493, 2006.

[9] Jihan Ryu and J Christian Gerdes. Integrating inertial sensors with global positioning system (GPS) for vehicle dynamics control. Journal of Dynamic Systems, Measurement, and Control, 126(2):243–254, 2004.

[10] Jonathan How, Nicholas Pohlman, and Chan-Woo Park. GPS estimation algorithms for precise velocity, slip and race–track position measurements. Technical Report 2002-01-3336, SAE Technical Paper, 2002.

[11] Jong-Hwa Yoon and Huei Peng. Robust vehicle sideslip angle estimation through a disturbance rejection filter that integrates a magnetometer with GPS. IEEE Transactions on Intelligent Transportation Systems, 15(1):191–204, 2014.

[12] Laura R Ray. Nonlinear tire force estimation and road friction identification: simulation and experiments. Automatica, 33(10):1819–1833, 1997.

[13] J Kim. Identification of lateral tyre force dynamics using an extended Kalman filter from experimental road test data. Control Engineering Practice, 17(3):357–367, 2009.

[14] Matt C Best, TJ Gordon, and PJ Dixon. An extended adaptive Kalman filter for real-time state estimation of vehicle handling dynamics. Vehicle System Dynamics, 34(1):57–75, 2000.

[15] Guillaume Baffet, Ali Charara, and Daniel Lechner. Estimation of vehicle sideslip, tire force and wheel cornering stiffness. Control Engineering Practice, 17(11):1255–1264, 2009.

[16] Moustapha Doumiati, Alessandro Correa Victorino, Ali Charara, and Daniel Lechner. Onboard real-time estimation of vehicle lateral tire-road forces and sideslip angle. IEEE/ASME Transactions on Mechatronics, 16(4):601–614, 2011.

[17] HH Kim and J Ryu. Sideslip angle estimation considering short-duration longitudinal velocity variation. International Journal of Automotive Technology, 12(4):545–553, 2011.

[18] Jamil Dakhlallah, Sébastien Glaser, Said Mammar, and Yazid Sebsadji. Tire-road forces estimation using extended Kalman filter and sideslip angle evaluation. In 2008 American control conference, pages 4597–4602. IEEE, 2008.

[19] Håvard Fjær Grip, Lars Imsland, Tor A Johansen, Thor I Fossen, Jens C Kalkkuhl, and Avshalom Suissa. Nonlinear vehicle sideslip estimation with friction adaptation. Automatica, 44(3):611–622, 2008.

[20] Xiaojie Gao, Zhuoping Yu, Jens Neubeck, and Jochen Wiedemann. Sideslip angle estimation based on input–output linearisation with tire–road friction adaptation. Vehicle System Dynamics, 48(2):217–234, 2010.

[21] Mujahid Abdulrahim. On the dynamics of automobile drifting. Technical report, SAE Technical Paper, 2006.

[22] Nenggen Ding and Saied Taheri. Application of recursive least square algorithm on estimation of vehicle sideslip angle and road friction. Mathematical problems in engineering, 2010.

[23] Jyotishman Ghosh, Andrea Tonoli, Nicola Amati, and Weitao Chen. Sideslip angle estimation of a Formula SAE racing vehicle. SAE International Journal of Passenger Cars-Mechanical Systems, 9(2016-01-1662):944–951, 2016.

[24] Rajesh Rajamani and J Karl Hedrick. Adaptive observers for active automotive suspensions: theory and experiment. IEEE Transactions on Control Systems Technology, 3(1):86–93, 1995.

[25] M Doumiati, A Victorino, Ali Charara, and Daniel Lechner. Lateral load transfer and normal forces estimation for vehicle safety: Experimental test. Vehicle System Dynamics, 47(12):1511–1533, 2009.

[26] Moustapha Doumiati, Alessandro Victorino, Ali Charara, Guillaume Baffet, and Daniel Lechner. An estimation process for vehicle wheel-ground contact normal forces. IFAC Proceedings Volumes, 41(2):7110–7115, 2008.

[27] Narayanan Kidambi, RL Harne, Yuji Fujii, Gregory M Pietron, and KW Wang. Methods in vehicle mass and road grade estimation. SAE International Journal of Passenger Cars-Mechanical Systems, 7(2014-01-0111):981–991, 2014.

[28] Robert Wragge-Morley, Guido Herrmann, Phil Barber, and Stuart Burgess. Gradient and mass estimation from CAN based data for a light passenger car. SAE International Journal of Passenger Cars-Electronic and Electrical Systems, 8(2015-01-0201):137–145, 2015.

[29] Michael L McIntyre, Tejas J Ghotikar, Ardalan Vahidi, Xubin Song, and Darren M Dawson. A two-stage Lyapunov-based estimator for estimation of vehicle mass and road grade. IEEE Transactions on Vehicular Technology, 58(7):3177–3185, 2009.

[30] Sanghyun Hong, Chankyu Lee, Francesco Borrelli, and J Karl Hedrick. A novel approach for vehicle inertial parameter identification using a dual Kalman filter. IEEE Transactions on Intelligent Transportation Systems, 16(1):151–161, 2015.

[31] Ardalan Vahidi, Anna Stefanopoulou, and Huei Peng. Recursive least squares with forgetting for online estimation of vehicle mass and road grade: Theory and experiments. Vehicle System Dynamics, 43(1):31–55, 2005.

[32] Hosam K Fathy, Dongsoo Kang, and Jeffrey L Stein. Online vehicle mass estimation using recursive least squares and supervisory data extraction. In 2008 American control conference, pages 1842–1848. IEEE, 2008.

[33] A Rezaeian, R Zarringhalam, S Fallah, W Melek, A Khajepour, S-Ken Chen, N Moshchuck, and B Litkouhi. Novel tire force estimation strategy for real-time implementation on vehicle applications. IEEE Transactions on Vehicular Technology, 64(6):2231–2241, 2015.

[34] Yoshimi Furukawa, Naohiro Yuhara, Shoichi Sano, Hideo Takeda, and Yoshinobu Matsushita. A review of four-wheel steering studies from the viewpoint of vehicle dynamics and control. Vehicle System Dynamics, 18(1-3):151–186, 1989.

[35] Shoichi Sano, Yoshimi Furukawa, and Yasuhei Oguchi. The effect of improved vehicle dynamics on drivers control performance. In 7th International Technical Conference on Experimental Safety Vehicles, Paris, 1979.

[36] Katsuhiko Fukui, Kazuo Miki, Yasutaka Hayashi, and Junzo Hasegawa. Analysis of driver and a four wheel steering vehicle system using a driving simulator. Technical Report 880641, SAE Technical Paper, 1988.

[37] Johannes Weichert Daniel Lunkeit. Performance oriented realisation of a rear wheel streering system for the Porsche 911 Turbo. Technical report.

[38] Jürgen Ackermann. Robust decoupling, ideal steering dynamics and yaw stabilization of 4WS cars. Automatica, 30(11):1761–1768, 1994.

[39] Yutaka Hirano and Katsumi Fukatani. Development of robust active rear steering control for automobile. JSME International Journal Series C, 40(2):231–238, 1997.

[40] Farbod Fahimi. Full drive-by-wire dynamic control for four-wheel-steer all-wheel-drive vehicles. Vehicle System Dynamics, 51(3):360–376, 2013.

[41] A El Hajjaji, A Ciocan, and D Hamad. Four wheel steering control by fuzzy approach. Journal of Intelligent and Robotic Systems, 41(2-3):141–156, 2005.

[42] Akira Higuchi and Yasushi Saitoh. Optimal control of four wheel steering vehicle. Vehicle System Dynamics, 22(5-6):397–410, 1993.

[43] Masao Nagai, Yutaka Hirano, and Sachiko Yamanaka. Integrated control of active rear wheel steering and direct yaw moment control. Vehicle System Dynamics, 27(5-6):357–370, 1997.

[44] Laszlo Palkovics. Effect of the controller parameters on the steerability of the four wheel steered car. Vehicle System Dynamics, 21(1):109–128, 1992.

[45] Masao Nagai, Etsuhiro Ueda, and Antonio Moran. Nonlinear design approach to four-wheel-steering systems using neural networks. Vehicle System Dynamics, 24(4-5):329–342, 1995.

[46] Feng Du, Ji-shun Li, Lun Li, Yu-jun Xue, Yong-gang Liu, and Xian-zhao Jia. Optimum control for active steering of vehicle based on H-infinity model following technology. In Informatics in Control, Automation and Robotics (CAR), 2010 2nd International Asia Conference on, volume 2, pages 341–344. IEEE, 2010.

[47] Eiichi Ono, Yoshikazu Hattori, Y Muragishi, and K Koibuchi. Vehicle dynamics integrated control for four-wheel-distributed steering and four-wheel-distributed traction/braking systems. Vehicle System Dynamics, 44(2):139–151, 2006.

[48] Masao Nagai, Yutaka Hirano, and Sachiko Yamanaka. Integrated robust control of active rear wheel steering and direct yaw moment control. Vehicle System Dynamics, 29(S1):416–421, 1998.

[49] TJ Veldhuizen. Yaw rate feedback by active rear wheel steering. Eindhoveñ Technische Univer-siteit Eindhoven, 2007.

[50] Nenggen Ding and Saied Taheri. An adaptive integrated algorithm for active front steering and direct yaw moment control based on direct Lyapunov method. Vehicle System Dynamics, 48(10):1193–1213, 2010.

[51] Leonardo De Novellis, Aldo Sorniotti, Patrick Gruber, Javier Orus, Jose-Manuel Rodriguez Fortun, Johan Theunissen, and Jasper De Smet. Direct yaw moment control actuated through electric drivetrains and friction brakes: Theoretical design and experimental assessment. Mechatronics, 26:1–15, 2015.

[52] Taeyoung Chung and Kyongsu Yi. Design and evaluation of side slip angle-based vehicle stability control scheme on a virtual test track. IEEE Transactions on Control Systems Technology, 14(2):224–234, 2006.

[53] C Ghike, T Shim, and J Asgari. Integrated control of wheel drive—brake torque for vehicle-handling enhancement. Proceedings of the Institution of Mechanical Engineers, Part D: Journal of Automobile Engineering, 223(4):439–457, 2009.

[54] Shuibo Zheng, Houjun Tang, Zhengzhi Han, and Yong Zhang. Controller design for vehicle stability enhancement. Control Engineering Practice, 14(12):1413–1421, 2006.

[55] D. Kasinathan, A. Kasaiezadeh, A. Wong, A. Khajepour, S. K. Chen, and B. Litkouhi. An optimal torque vectoring control for vehicle applications via real-time constraints. IEEE Transactions on Vehicular Technology, 65(6):4368–4378, June 2016.

[56] F Cheli, F Cimatti, P Dellachà, and A Zorzutti. Development and implementation of a torque vectoring algorithm for an innovative 4WD driveline for a high-performance vehicle. Vehicle System Dynamics, 47(2):179–193, 2009.

[57] Daniel Rubin and Shai A Arogeti. Vehicle yaw stability control using active limited-slip differential via model predictive control methods. Vehicle System Dynamics, 53(9):1315–1330, 2015.

[58] M Croft-White and M Harrison. Study of torque vectoring for all-wheel-drive vehicles. Vehicle System Dynamics, 44(sup1):313–320, 2006.

[59] Leonardo De Novellis, Aldo Sorniotti, and Patrick Gruber. Wheel torque distribution criteria for electric vehicles with torque-vectoring differentials. IEEE Transactions on Vehicular Technology, 63(4):1593–1602, 2014.

[60] Massimo Canale, Lorenzo Fagiano, Mario Milanese, and P Borodani. Robust vehicle yaw control using an active differential and IMC techniques. Control Engineering Practice, 15(8):923–941, 2007.

[61] Leonardo De Novellis, Aldo Sorniotti, Patrick Gruber, and Andrew Pennycott. Comparison of feedback control techniques for torque-vectoring control of fully electric vehicles. IEEE Transactions on Vehicular Technology, 63(8):3612–3623, 2014.

[62] Tommaso Goggia, Aldo Sorniotti, Leonardo De Novellis, Antonella Ferrara, Patrick Gruber, Johan Theunissen, Dirk Steenbeke, Bernhard Knauder, and Josef Zehetner. Integral sliding mode for the torque-vectoring control of fully electric vehicles: Theoretical design and experimental assessment. IEEE Transactions on Vehicular Technology, 64(5):1701–1715, 2015.

[63] Cong Geng, Lotfi Mostefai, Mouloud Denaï, and Yoichi Hori. Direct yaw-moment control of an in-wheel-motored electric vehicle based on body slip angle fuzzy observer. IEEE Transactions on Industrial Electronics, 56(5):1411–1419, 2009.

[64] Hiroshi Fujimoto, Akio Tsumasaka, and Toshihiko Noguchi. Direct yaw-moment control of electric vehicle based on cornering stiffness estimation. In 31st Annual Conference of IEEE Industrial Electronics Society, 2005. IECON 2005., pages 6–pp. IEEE, 2005.

[65] Efstathios Siampis, Matteo Massaro, and Efstathios Velenis. Electric rear axle torque vectoring for combined yaw stability and velocity control near the limit of handling. In 52nd IEEE Conference on Decision and Control, pages 1552–1557. IEEE, 2013.

[66] Russell P Osborn and Taehyun Shim. Independent control of all-wheel-drive torque distribution. Vehicle System Dynamics, 44(7):529–546, 2006.

[67] Ossama Mokhiamar and Masato Abe. Simultaneous optimal distribution of lateral and longitudinal tire forces for the model following control. Journal of dynamic systems, measurement, and control, 126(4):753–763, 2004.

[68] Qin Liu, Gerd Kaiser, Sudchai Boonto, Herbert Werner, Frederic Holzmann, Benoit Chretien, and Matthias Korte. Two-degree-of-freedom LPV control for a through-the-road hybrid electric vehicle via torque vectoring. In 2011 50th IEEE Conference on Decision and Control and European Control Conference, pages 1274–1279. IEEE, 2011.

[69] Francesco Braghin, Edoardo Sabbioni, Gabriele Sironi, and Michele Vignati. A feedback control strategy for torque-vectoring of IWM vehicles. In ASME 2014 International Design Engineering Technical Conferences and Computers and Information in Engineering Conference, pages V003T01A004–V003T01A004. American Society of Mechanical Engineers, 2014.

[70] Kaoru Sawase and Yuichi Ushiroda. Improvement of vehicle dynamics by right-and-left torque vectoring system in various drivetrains. Mitsubishi Motors Technical Review, 20:14, 2008.

[71] Yasuji Shibahata, K Shimada, and T Tomari. Improvement of vehicle maneuverability by direct yaw moment control. Vehicle System Dynamics, 22(5-6):465–481, 1993.

[72] Efstathios Siampis, Efstathios Velenis, and Stefano Longo. Rear wheel torque vectoring model predictive control with velocity regulation for electric vehicles. Vehicle System Dynamics, 53(11):1555–1579, 2015.

[73] Kerem Bayar, Junmin Wang, and Giorgio Rizzoni. Development of a vehicle stability control strategy for a hybrid electric vehicle equipped with axle motors. Proceedings of the Institution of Mechanical Engineers, Part D: Journal of automobile engineering, page 0954407011433396, 2012.

[74] Ossama Mokhiamar and Masato Abe. How the four wheels should share forces in an optimum cooperative chassis control. Control Engineering Practice, 14(3):295–304, 2006.

[75] Giancarlo Genta and Lorenzo Morello. The automotive chassis. Springer, 2009.

[76] Thomas D Gillespie. Fundamentals of vehicle dynamics. Technical Report R-114, SAE Technical Paper, 1992.

[77] Hans Pacejka. Tire and vehicle dynamics. Elsevier, 2005.

[78] Rajesh Rajamani. Vehicle dynamics and control. Springer Science & Business Media, 2011.

[79] David Kriesel. A Brief Introduction to Neural Networks. 2007.

[80] Pat Langley. The changing science of machine learning. Machine Learning, 82(3):275–279, 2011.

[81] Dean A Pomerleau. Efficient training of artificial neural networks for autonomous navigation. Neural Computation, 3(1):88–97, 1991.

[82] Arturo De La Escalera, Luis E Moreno, Miguel Angel Salichs, and José María Armingol. Road traffic sign detection and classification. IEEE Transactions on Industrial Electronics, 44(6):848–859, 1997.

[83] Jorge Moreno, Micah E Ortúzar, and Juan W Dixon. Energy-management system for a hybrid electric vehicle, using ultracapacitors and neural networks. IEEE Transactions on Industrial Electronics, 53(2):614–623, 2006.

[84] LiuWang Kang, Xuan Zhao, and Jian Ma. A new neural network model for the state-of-charge estimation in the battery degradation process. Applied Energy, 121:20–27, 2014.

[85] Mario Milanese, Diego Regruto, and Andrea Fortina. Direct virtual sensor (DVS) design in vehicle sideslip angle estimation. In American Control Conference, 2007. ACC'07, pages 3654–3658. IEEE, 2007.

[86] S Melzi and E Sabbioni. On the vehicle sideslip angle estimation through neural networks: Numerical and experimental results. Mechanical Systems and Signal Processing, 25(6):2005–2019, 2011.

[87] Haşim Sak, Andrew Senior, and Françoise Beaufays. Long short-term memory recurrent neural network architectures for large scale acoustic modeling. In Fifteenth Annual Conference of the International Speech Communication Association, 2014.

[88] Jürgen Schmidhuber. Deep learning in neural networks: An overview. Neural Networks, 61:85–117, 2015.

[89] Sepp Hochreiter and Jürgen Schmidhuber. Long short-term memory. Neural computation, 9(8):1735–1780, 1997.

[90] Alex Graves. Neural networks. In Supervised Sequence Labelling with Recurrent Neural Networks, pages 15–35. Springer, 2012.

[91] Tijmen Tieleman and Geoffrey Hinton. Lecture 6.5-RMSprop: Divide the gradient by a running average of its recent magnitude. COURSERA: Neural Networks for Machine Learning, 2012.

[92] William F Milliken and Douglas L Milliken. Race car vehicle dynamics. Society of Automotive Engineers Warrendale, 1995.

[93] S Foulard, M Ichchou, S Rinderknecht, and J Perret-Liaudet. Online and real-time monitoring system for remaining service life estimation of automotive transmissions–application to a manual transmission. Mechatronics, 30:140–157, 2015.

[94] Stephane Foulard. Online and real-time load monitoring for remaining service life prediction of automotive transmissions: damage level estimation of transmission components based on a torque acquisition. PhD thesis, Technische Universität Darmstadt, 2015.

[95] Lennart Ljung. System identification. In Signal Analysis and Prediction, pages 163–173. Springer, 1998.

[96] Sigurd Skogestad and Ian Postlethwaite. Multivariable feedback control: Analysis and design, volume 2. Wiley New York, 2007.

[97] Julian P Timings and David J Cole. Efficient minimum manoeuvre time optimisation of an oversteering vehicle at constant forward speed. In American Control Conference (ACC), 2011, pages 5267–5272. IEEE, 2011.

[98] Alessandro Rucco, Giuseppe Notarstefano, and John Hauser. Computing minimum lap-time trajectories for a single-track car with load transfer. In Decision and Control (CDC), 2012 IEEE 51st Annual Conference on, pages 6321–6326. IEEE, 2012.

[99] Robin Verschueren, Stijn De Bruyne, Mario Zanon, Janick V Frasch, and Moritz Diehl. Towards time-optimal race car driving using nonlinear MPC in real-time. In Decision and Control (CDC), 2014 IEEE 53rd Annual Conference on, pages 2505–2510. IEEE, 2014.

[100] A. Rucco, G. Notarstefano, and J. Hauser. An efficient minimum-time trajectory generation strategy for two-track car vehicles. IEEE Transactions on Control Systems Technology, 23(4):1505–1519, July 2015.

[101] VI-grade GmbH. VI-CarRealTime 17.2 Documentation, 2017.

[102] Jyotishman Ghosh, Andrea Tonoli, and Nicola Amati. A torque vectoring strategy for improving the performance of a rear wheel drive electric vehicle. In Vehicle Power and Propulsion Conference (VPPC), 2015 IEEE, pages 1–6. IEEE, 2015.

[103] Leonard Segel. Theoretical prediction and experimental substantiation of the response of the automobile to steering control. Proceedings of the Institution of Mechanical Engineers: Automobile Division, 10(1):310–330, 1956.

[104] VI Utkin. Sliding modes in control and optimization. New York, 1992.

[105] J.J. Rath, K.C. Veluvolu, and M. Defoort. Simultaneous estimation of road profile and tire road friction for automotive vehicle. IEEE Transactions on Vehicular Technology, 64(10):4461–4471, Oct 2015.

[106] C. Kim, J. Hahn, K. Hong, and W. Yoo. Estimation of tire-road friction based on onboard 6-DoF acceleration measurement. IEEE Transactions on Vehicular Technology, 64(8):3368–3377, Aug 2015.

[107] Jong Hyeon Park and Chan Young Kim. Wheel slip control in traction control system for vehicle stability. Vehicle System Dynamics, 31(4):263–278, 1999.

[108] Matteo Amodeo, Antonella Ferrara, Riccardo Terzaghi, and Claudio Vecchio. Wheel slip control via second-order sliding-mode generation. IEEE Transactions on Intelligent Transportation Systems, 11(1):122–131, 2010.

[109] Idar Petersen, Tor A Johansen, Jens Kalkkuhl, and J Ludemann. Wheel slip control using gain-scheduled LQ-LPV/LMI analysis and experimental results. In Proceedings of IEE European Control Conference, Cambridge, UK, September 1, volume 4. Citeseer, 2003.

[110] Takashi Nakakuki, Tielong Shen, and Katsutoshi Tamura. Adaptive control approach to uncertain longitudinal tire slip in traction control of vehicles. Asian Journal of Control, 10(1):67–73, 2008.

[111] Ricardo De Castro, Rui E Araujo, and David Freitas. Wheel slip control of EVs based on sliding mode technique with conditional integrators. IEEE Transactions on Industrial Electronics, 60(8):3256–3271, 2013.

[112] Kenneth R Buckholtz. Use of fuzzy logic in wheel slip assignment-part i: yaw rate control. Technical Report 2002-01-0301, SAE Technical Paper, 2002.

[113] Junmin Wang and Raul G Longoria. Coordinated and reconfigurable vehicle dynamics control. IEEE Transactions on Control Systems Technology, 17(3):723–732, 2009.

Appendix A

Tire Model

The tire model used for the EKF development is a Pacejka model obtained from [77]. The following parameters are used to define the tire model and their values are available from the vehicle manufacturer. They are defined as follows:
F_{ZO}- Nominal load on tire
$\lambda_{F_{ZO}}$- Scale factor of nominal (rated) load
λ_{Cy}- Scale factor of F_y shape factor
λ_{μ_Y}- Scale factor of F_y peak friction coefficient
λ_{Ey}- Scale factor of F_y curvature factor
λ_{Ky}- Scale factor of F_y cornering stiffness
λ_{Hy}- Scale factor of F_y horizontal shift
λ_{Vy}- Scale factor of F_y vertical shift
$\lambda_{\gamma y}$- Scale factor of camber for F_y
$\lambda_{y\kappa}$- Scale factor of alpha influence on F_x
$\lambda_{Vy\kappa}$- Scale factor of kappa induced F_y
p_{Cy1}- Shape factor C_y for lateral forces
p_{Dy1}- Lateral friction μ_y
p_{Dy2}- Variation of friction μ_y with load
p_{Dy3}- Variation of friction μ_y with squared camber
p_{Ey1}- Lateral curvature E_y at F_{ZO}
p_{Ey2}- Variation of curvature E_y with load
p_{Ey3}- Zero order camber dependency of curvature E_y
p_{Ey4}- Variation of curvature E_y with camber
p_{Ky1}- Maximum value of stiffness K_y/F_{ZO}

p_{Ky2}- Load at which K_y reaches maximum value
p_{Ky3}- Variation of K_y/F_{ZO} with camber
p_{Hy1}- Horizontal shift S_{hy} at F_{ZO}
p_{Hy2}- Variation of shift S_{hy} with load
p_{Hy3}- Variation of shift S_{hy} with camber
p_{Vy1}- Vertical shift in S_{vy}/F_{ZO}
p_{Vy2}- Variation of shift S_{vy}/F_z with load
p_{Vy3}- Variation of shift S_{vy}/F_z with camber
p_{Vy4}- Variation of shift S_{vy}/F_z with camber and load
r_{By1}- Slope factor for combined F_y reduction
r_{By2}- Variation of slope F_y reduction with alpha
r_{By3}- Shift term for alpha in slope F_y reduction
r_{Cy1}- Shape factor for combined F_y reduction
r_{Ey1}- Curvature factor of combined F_y
r_{Ey2}- Curvature factor of combined F_y with load
r_{Hy1}- Shift factor for combined F_y reduction
r_{Hy2}- Shift factor for combined F_y reduction with load
r_{Vy1}- Kappa induced side force $S_{vyk}/\mu_y F_z$ at F_{ZO}
r_{Vy2}- Variation of $S_{vyk}/\mu_y F_z$ with load
r_{Vy3}- Variation of $S_{vyk}/\mu_y F_z$ with camber
r_{Vy4}- Variation of $S_{vyk}/\mu_y F_z$ with alpha
r_{Vy5}- Variation of $S_{vyk}/\mu_y F_z$ with kappa
r_{Vy6}- Variation of $S_{vyk}/\mu_y F_z$ with $tan^{-1}(\kappa)$

$$F'_{ZO} = F_{ZO}.\lambda_{F_{ZO}} \tag{A.1}$$

$$dF_z = \frac{F_z - F'_{ZO}}{F'_{ZO}}; \tag{A.2}$$

$$\gamma_y = \gamma.\lambda_{\gamma y} \tag{A.3}$$

$$\mu_y = (p_{Dy1} + p_{Dy2}.dF_z)(1 - p_{Dy3}.\gamma_y^2)\lambda_{\mu_y} \tag{A.4}$$

$$D_y = \mu_y.F_z \tag{A.5}$$

$$C_y = p_{Cy1}.\lambda_{Cy} \tag{A.6}$$

$$K_{y0} = p_{Ky1}.F_{ZO}.sin[2tan^{-1}(\frac{F_z}{p_{Ky2}F_{ZO}\lambda_{F_{ZO}}})].\lambda_{F_{ZO}}.\lambda_{Ky} \tag{A.7}$$

$$Ky = K_{y0}(1 - p_{Ky3}.abs(\gamma_y)) \tag{A.8}$$

$$S_{Hy} = (p_{Hy1} + p_{Hy2}.dF_z)\lambda_{Hy} + p_{Hy3}\gamma_y \tag{A.9}$$

$$\alpha_y = \alpha + S_{Hy} \tag{A.10}$$

$$S_{Vy} = F_z((p_{Vy1} + p_{Vy2}.dF_z).\lambda_{Vy} + (p_{Vy3} + p_{Vy4}.dF_z)\gamma_y) * \lambda_{\mu_y} \tag{A.11}$$

$$E_y = min((PEy1 + p_{Ey2}.dF_z)(1 - (p_{Ey3} + p_{Ey4}\gamma_y).sign(\alpha_y))\lambda_{Ey}, 1) \tag{A.12}$$

$$B_y = \frac{K_y}{C_y.D_y} \tag{A.13}$$

$$F_y = D_y.sin(C_y.tan^{-1}(B_y.\alpha_y - E_y.(B_y.\alpha_y - tan^{-1}(B_y\alpha_y)))) + S_{Vy} \tag{A.14}$$

where γ is the camber angle, α is the tire sideslip angle. The tire lateral force in the presence of longitudinal acceleration is adapted as

$$F_{y,c} = kF_y, \tag{A.15}$$

where k is a tunable piecewise affine function of a_x and a_y.